ELSEVIER

Contents lists available at ScienceDirect

Electrochimica Acta

journal homepage: www.elsevier.com/locate/electacta



The influence of oxygen vacancy concentration in nanodispersed non-stoichiometric $CeO_{2-\delta}$ oxides on the physico-chemical properties of conducting polyaniline/ CeO_2 composites



Bojana Kuzmanović ^a, Milica J. Vujković ^{b, *}, Nataša Tomić ^c, Danica Bajuk-Bogdanović ^b, Vladimir Lazović ^c, Biljana Šljukić ^b, Nenad Ivanović ^a, Slavko Mentus ^{b, d}

- ^a Institute of Nuclear Sciences "Vinča", Mike Petrovića Alasa 12-14, 11001, Belgrade, University of Belgrade, Serbia
- ^b Faculty of Physical Chemistry, University of Belgrade, Studentski trg 12-16, 11158, Belgrade, Serbia
- ^c Institute of Physics Belgrade, University of Belgrade, Pregrevica 118, 11080, Belgrade, Serbia
- ^d Serbian Academy of Sciences and Arts, Knez Mihajlova 35, 11000, Belgrade, Serbia

ARTICLE INFO

Article history: Received 26 December 2018 Received in revised form 21 February 2019 Accepted 19 March 2019 Available online 22 March 2019

Keywords: Polyaniline Oxygen deficient cerium oxide PANI-CeO $_{2-\delta}$ interaction Supercapacitors

ABSTRACT

Cerium oxide $(CeO_{2-\delta})$ ultrafine nanoparticles, with the lower $(CeO_{2-\delta}-HT)$ and higher $(CeO_{2-\delta}-SS)$ fraction of oxygen vacancies, were used as anchoring sites for the polymerization of aniline in acidic medium. As a result, polyaniline-emeraldine salt (PANI-ES)-based composites (PANI-ES@CeO_{2-\delta}-HT and PANI-ES@CeO_{2-\delta}-SS) were obtained. The interaction between $CeO_{2-\delta}$ and PANI was examined by FTIR and Raman spectroscopy. The PANI polymerization is initiated via electrostatic interaction of anilinium cation and Cl^- ions (adsorbed at the protonated hydroxyl groups of $CeO_{2-\delta}$), and proceeds with hydrogen and nitrogen interaction with oxide nanoparticles. Tailoring the oxygen vacancy population of oxide offers the possibility to control the type of PANI-cerium oxide interaction, and consequently structural, electrical, thermal, electronic and charge storage properties of composite. A high capacitance of synthesized materials, reaching ~294 F g⁻¹ (PANI-ES), ~299 F g⁻¹ (PANI-ES@CeO_{2-\delta}-HT) and ~314 F g⁻¹ (PANI-ES@CeO_{2-\delta}-SS), was measured in 1 M HCl, at a common scan rate of 20 mV s⁻¹. The high adhesion of PANI with cerium oxide prevents the oxide from its slow dissolution in 1MHCl thus providing the stability of this composite in an acidic solution. The rate of electrochemical oxidation of emeraldine salt into pernigraniline was also found to depend on $CeO_{2-\delta}$ characteristics.

© 2019 Elsevier Ltd. All rights reserved.

1. Introduction

The linkage of diverse metal oxides (TiO_2 , CeO_2 , ZnO, graphene oxide, SiO_2 , Fe_xO_y , MnO_2 ...) with one of the oldest conducting polymers such as polyaniline (PANI) has been shown as an effective strategy for improving mechanical, thermal, dielectric, electrical and optical properties of this polymer [1–5]. An easy synthesis, environmental stability, and fast doping/dedoping process, make PANI very suitable matrix for the facile further fabrication. On the other hand, inorganic oxides easily interact with PANI chains, resulting in the synergistic behaviour. The versatile properties of these hybrid materials, achieved either through the different

E-mail address: milica.vujkovic@ffh.bg.ac.rs (M.J. Vujković).

degree of PANI's protonation or different oxide structures (obtained through numerous synthesis procedures), make their study inexhaustable.

While the investigations of composites with TiO₂ were quite diverse and numerous, the studies on PANI/CeO₂ nano-composites have mostly directed to the development of sensor technology including H₂O₂ sensors, humidity sensors, biosensors, gas sensing materials [6–11]. The positive influence of CeO₂ particles, incorporated into PANI chains, has been recognized in many sensor properties. Besides, the binding of cerium oxide with the polyaniline was found to improve thermal [12,13], corrosion protection [14] and electrochemical properties [15–17]. Still, the studies regarding the Ce-oxide's influence to the charge storage properties of polyaniline are quite rare. Recently, Fei et al. [17] showed that an indirect chemical bonding of PANI to CeO₂ surface via its –OH and –NCO functionalized groups improves both electrocatalytic and capacitive performance of PANI. By mixing CeO₂ with 10% of PANI,

^{*} Corresponding author.University of Belgrade, Faculty of Physical Chemistry, Studentski trg 12–14, 11158, Belgrade, Serbia.

Maheswari et al. [15] have significantly improved charge storage properties of oxide in HCl, from a very high value of $927 \,\mathrm{Fg}^{-1}$ (for pure oxide) to the extremely high one amounting to $1452 \,\mathrm{Fg}^{-1}$ for the CeO₂/PANI composite. Also, Gong et al. [16], have recently prepared nickel doped cerium oxide nanospheres at PANI (Ni-CeO₂@PANI) as an electrode material for supercapacitors. which provided a very high capacitance of $894 \,\mathrm{Fg^{-1}}$ (at $1 \,\mathrm{Ag^{-1}}$), thanks to the defective nature of Ni-CeO₂. The excess of reactive oxygen vacancies was achieved by doping CeO2 with nickel atoms, whereas the Ni-CeO₂@PANI nanocomposite was prepared by in situ chemical oxidative polymerization of aniline in presence of Ni-CeO₂ particles. Herein, polyaniline-cerium oxide composites have been synthesized by typical chemical polymerization of aniline (under highly acidic conditions), adsorbed on the surface of cerium-oxide nanoparticles, in order to examine its charge storage ability. The idea was to use the two types of $CeO_{2-\delta}$, containing different fraction of oxygen vacancies (without metal doping), in order to compare how the O-vacancy population influences the PANI-CeO₂ interaction. The oxide's particles were synthesized by two different methods: i) the solid-state method, yielding cerium-oxide with higher concentration of oxygen vacancies and ii) the hydrothermal method yielding oxide with lower concentration of oxygen vacancies. The influence of vacancy concentration of CeO_{2-\delta} oxides, in their composites with highly conductive emeraldine form of PANI, on the thermal, vibrational and electrochemical properties of composites, was thoroughly examined. The mechanism of PANI-CeO_{2-δ} interaction is proposed and discussed.

2. Experimental

2.1. Synthesis procedure

2.1.1. Synthesis of polyaniline emeraldine salt

Polyaniline, in the form of emeraldine salt (PANI-ES), was synthesized by typical chemical polymerization of aniline (Sigma Aldrich) in the presence of hydrochloric acid using ammonium persulfate (Sigma Aldrich) as an oxidant [18]. Briefly, 0.18 mL of two times distilled aniline monomer was injected into 7 mL of 2 M HCl solution. 0.45 g (NH₄)₂SO₄ (previously dissolved in 2 mL of deionized water) was dropped to the solution and stirred magnetically at 25 °C. After filtration, the precipitate was washed (with 2 M HCl and deionized water followed by ethanol) and dried at 60 °C in the oven for 36 h.

2.1.2. Hydrothermally synthesis of $CeO_{2-\delta}$

The $CeO_{2-\delta}$ nanoparticles with a lower amount of oxygen vacancies were prepared by the hydrothermal treatment (CeO_{2-δ}-HT), according to the procedure presented in Ref. [19]. In a typical synthesis, 2 g of polyvinylpyrrolidone (Sigma Aldrich) was dissolved in 40 mL of deionized water, continuously stirring on a magnetic stirrer (at room temperature T ≈ 25 °C) until a homogeneous solution was obtained. 6 mmol of Ce(NO₃)₃·6H₂O (Acros Organics 99.5%), previously dissolved in deionized water V = 40 mL, was slowly added to the resulting solution, with constant stirring. During the synthesis, the pH of the solution was not adjusted and value was pH \approx 4. The prepared solution was put into a Teflonlined stainless steel autoclave (capacity ~ 80 mL), and hydrothermally treated at 200 °C for 6 h. After synthesis, the autoclave was cooled down to room temperature naturally. The resulting precipitate was collected and washed several times with distilled water, and afterwards dried in a vacuum oven overnight at 105.5 °C.

2.1.3. Solid state synthesis of $CeO_{2-\delta}$

Solid-state reaction at room temperature was used for the

synthesis $CeO_{2-\delta}$ ultrafine particles with a higher amount of oxygen vacancies [20,21]. Cerium nitrate hexahydrate (Acros Organics 99.5%) and sodium hydroxide (Carlo Erba) were used as starting materials for this procedure. Synthesis involves manual mixing of the starting chemicals in mortar (~10 min) until the mixture becomes light brown. After exposure to the air (4 h), the sample was washed four times with distilled water and twice with ethanol to remove NaNO₃. The final product was transferred into petri dish using ethanol and dried at 60 °C in a drying oven overnight. The final result of the synthesis obtained is a light yellow powder $CeO_{2-\delta}$.

 $2[(Ce(NO_3)_3 \times 6H_2O] + 6NaOH + (1/2-\delta)O_2 \rightarrow 2CeO_{2-\delta} + 6NaNO_3 + 15H_2O$

2.1.4. PANI@CeO_{2- δ} synthesis procedure

The PANI@CeO $_{2-\delta}$ composites were prepared in the same way as PANI-ES, in presence of cerium oxide. Namely, 0.18 mL of distilled aniline monomer was injected into an aqueous solution of 2 M HCl, containing 50 mg of CeO $_{2-\delta}$ -SS or CeO $_{2-\delta}$ -HT ultrafine nanoparticles. The acidic solutions of cerium-oxide nanoparticles were previously treated by ultrasound to prevent aggregation of nano-CeO $_2$ particles. The oxidizing agent (NH $_4$) $_2$ S $_2$ O $_8$ (0.45 g), previously dissolved in 2 ml deionized water, was added to the solutions drop by drop. After mixing the solution for 6 h on a magnetic stirrer, at room temperature, the samples were filtered and washed. Afterwards, the obtained dark-green PANI@CeO $_{2-\delta}$ composites, labelled as PANI-ES@CeO $_{2-\delta}$ -SS and PANI-ES@CeO $_{2-\delta}$ -HT, were dried in the oven at 60° for 36 h to achieve the constant weight.

For the sake of comparison, the similar experiments using 100 mg of $CeO_{2-\delta}$ -SS and 9 mg, 50 mg and 100 mg of TiO_2 anatase (Sigma Aldrich) were also performed.

2.2. Characterization

The obtained powdered samples were pressed into pellets and their conductivity was measured between two stainless pistons using an ac bridge (Waynne Kerr Universal Bridge B 224) at 1.0 kHz, at room temperature and pressure of 375 MPa.

Thermogravimetric and differential thermal analysis (TG/DTA) were carried out simultaneously by an SDT 2960 Simultaneous DSC-TGA thermal analyzer, in air atmosphere with a flowing rate of $10\,\mathrm{C}$ min $^{-1}$.

The morphology of synthesized samples was observed by fieldemission scanning electron microscope (FESEM, Tescan MIRA3). PANI-based samples were clearly visible as such, while cerium oxide sample required vacuum decoration by gold.

The Raman spectra of samples were recorded on a DXR Raman microscope (Thermo Scientific) equipped with a research optical microscope and a CCD detector. A HeNe gas laser with an excitation wavelength of 633 nm was used for all measurements. The scattered light was analyzed by the spectrograph with a grating of 600 lines $\rm mm^{-1}$ and a spectrograph aperture of 50 μm slit. The laser power was kept at 0.5 mW on the sample. Each spectrum was measured with an exposure time of 30 s and number of exposures of 20.

The Infrared transmission spectra (FTIR) of the samples in the form of pellets with KBr, were recorded using an Avatar System 370 spectrometer (Thermo Nicolet), with 64 scans per sample and 2 cm⁻¹ resolution in the wavenumber range 4000–400 cm⁻¹.

2.3. Electrochemical measurements

Electrochemical measurements of examined samples were performed at Gamry PCI4/300 Potentiostat/Galvanostat, in the

typical three-electrode configuration. The reference electrode was a saturated calomel electrode (SCE), while the counter electrode was a wide Platinum foil (Pt). To prepare the working electrode the examined powder was mixed with the 5 wt% Nafion binder (Sigma Aldrich) in ethanol/water, in the 95:5 ratio. Several drops of ethanol were added in order to obtain the desired viscosity. After homogenization in an ultrasonic bath, the slurry was deposited over the rectangular glassy carbon support and dried at ambient temperature in order for ethanol to evaporate. The loading mass was $1.7~{\rm mg~cm^{-2}}$ for all examined electrodes. The electrolyte was $1~{\rm mol~dm^{-3}}$ HCl aqueous solution.

3. Results and discussion

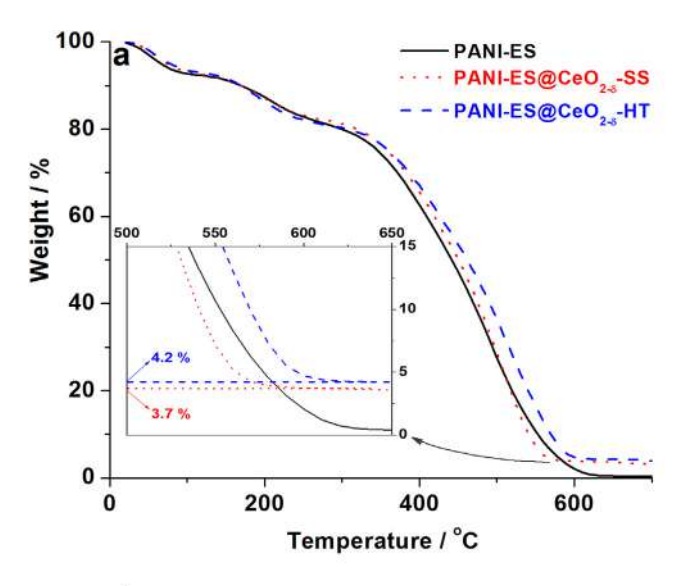
3.1. Conductivity measurements

The synthesized PANI-ES delivers a high value of electronic conductivity, amounting to ~0.6 S/cm. The incorporation of semi-conducting cerium-oxide, into polymer matrix, decreases the conductivity to ~0.5 S/cm and ~0.3 S/cm for PANI-ES@CeO_{2- δ}-SS and PANI-ES@CeO_{2- δ}-HT, respectively.

3.2. Thermal behavior

Thermal behavior of prepared samples was examined by simultaneous thermogravimetric/differential thermal analysis (TGA/DTA), in the temperature range 25-700 °C, under air atmosphere. The characteristic thermogram of conducting polymer [22], made of three separated weight loss steps, is observed (Fig. 1a). The first weight loss (about 7%) up to 100 °C, originates from desorption of adsorbed water molecules, while the second weight loss between 180 and 300 °C (about 13%) can be attributed to the elimination of protonating acid dopant (HCl) bound to the polymer chain. The third and the greatest weight loss (about 80% for pure PANI), within the temperature range 300–700 °C, corresponds to the structural degradation of the polymer backbone [22]. One can notice that both composites, unlike the pure PANI, did not lose the whole weight at 700 °C, but ~96.3% (PANI-ES@CeO_{2-δ}-SS) and ~95.8% (PANI-ES@CeO_{2-\delta}-HT) of its initial weight. It is due to a high thermal stability of inorganic cerium oxide. Based on this, the fraction of cerium-oxide in the composite could be determined and, relative to the mass of dried sample (taking into account the amount of adsorbed water), was found to be ~4% (PANI-ES@CeO_{2-δ}-SS) and 4.5% (PANI-ES@CeO_{2-δ}-HT). Somewhat higher content of hydrothermally synthesized oxide in the composite was obtained. This is in the correlation with the higher concentration of Ce⁴⁺ ions i.e. higher fraction of oxygen atoms in the $CeO_{2-\delta}$ -HT crystal lattice.

It can be seen that weight loss of samples, up to 300 °C (removal of water molecules and dopant), is insensitive to the presence of oxide (it is governed by the type of dopant). However, above ~300 °C, there are differences in the thermal decomposition of the polymer chain in examined samples, which are more visible in corresponding DTA curves (Fig. 1b). As our DTA curves show, two exothermic peaks follow the process of ES degradation within the temperature region 300-700 °C. The position of the first DTA peak (appearing at 384 °C) is the same for PANI-ES and PANI-ES@CeO_{2-δ}-SS, while its values for PANI-ES@CeO_{2-δ}-HT is slightly shifted towards higher temperature (393 °C). The second DTA peak, higher in the intensity, appears at ~489 °C (PANI-ES), 499 °C (PANI-ES@CeO₂- δ -SS), 512 °C (PANI-ES@ CeO_{2- δ}-HT). It can be concluded that the thermal resistance of PANI becomes higher by its binding with the cerium-oxide, especially when the chains grew on hydrothermally prepared oxide. This originates from its strong interaction with the oxide. The improved thermal stability of PANI in interaction with metal oxides has been already reported [12,13,17], but the opposite



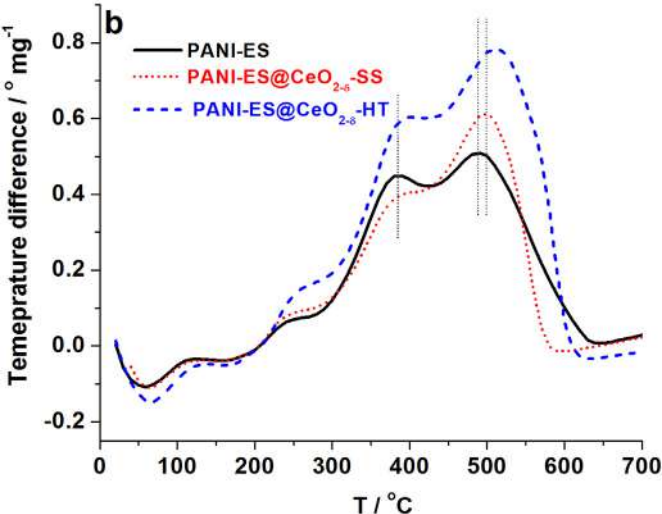


Fig. 1. TG (a) and DTA (b) curves of PANI-ES and PANI-ES@CeO $_{2\text{-}\delta}$ samples.

behavior [17] was also found. These variations can be explained in the different interactions of cerium oxide with polyaniline chains, which can be influenced by the synthesis of oxide, the type of PANI dopant and the doping level. Here, higher thermal stability of PANI was obtained for the composite containing $CeO_{2-\delta}$ with the lower fraction of oxygen vacancies. Furthermore, the declining slope of the PANI@ $CeO_{2-\delta}$ DTA curves is steeper than that of PANI-ES, which suggests that the cerium oxide acts as a catalyst of the combustion process of carbon, formed by the thermal decomposition of polymer.

3.3. Morphology

Ultrafine nanoparticles of $CeO_{2-\delta}$ -HT and $CeO_{2-\delta}$ -SS are shown in Fig. 2a and b. Nanodispersed, nearly spherical particles, 20—40 nm in diameter, prevail on the $CeO_{2-\delta}$ -SS surface (Fig. 2a) while the $CeO_{2-\delta}$ -HT sample is composed of monodispersed spherical particles, 0.7—1.1 μ m in diameter (Fig. 2b). Interestingly, these submicron/micron $CeO_{2-\delta}$ -HT spheres are huge agglomerates of nanoparticles 20—40 nm in diameter, which are similar to $CeO_{2-\delta}$ -SS particles. Representative FE-SEM micrograph of PANI-ES sample shows that the short nanofibers (~75 nm in diameter) can be perceived (Fig. 2c). The FE-SEM micrographs of PANI-ES@CeO₂-

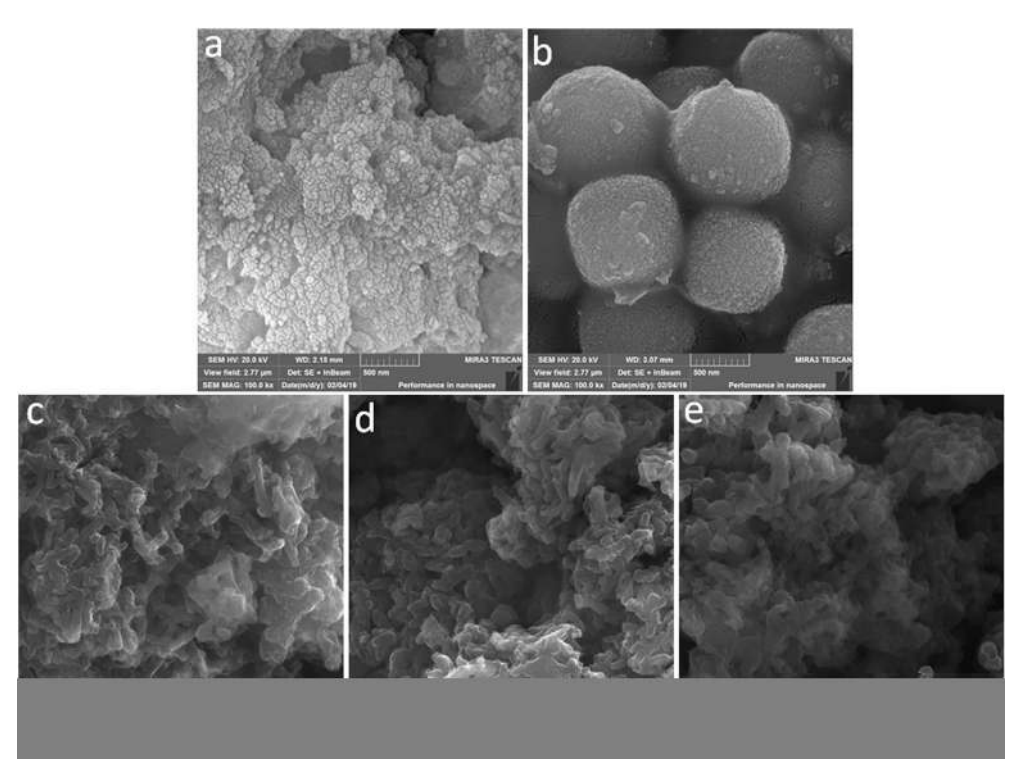


Fig. 2. SEM micrographs of CeO₂₋₈-SS (a), CeO₂₋₈-HT particles (b), PANI-ES (c), PANI-ES@CeO₂₋₈-SS (d) and PANI-ES@CeO₂₋₈-HT (e).

 $_{\delta}$ composites (Fig. 2d and e) indicate that the presence of ultrafine nanodispersed CeO_{2- $\delta}$ particles do not influence the original PANI-ES morphology.}

3.4. Vibrational spectroscopy study

3.4.1. Infrared spectroscopy

It is well known that FTIR spectrum of PANI is very sensitive to various experimental conditions such as humidity, temperature, pressure, storing and processing of samples and so on [23]. In order to avoid differences caused by the influence of the mentioned parameters we measured the spectra under the same conditions following recommendations by Trchova et al. [23].

Representative FTIR spectra of synthesized polyaniline-based samples are shown in Fig. 3. The characteristic spectrum of protonated emeraldine salt form can be recognized in all samples. The assignation of FTIR bands (well-documented in literature [23-30]), is presented in Supplementary Data. The spectrum of PANI-ES@CeO_{2-δ} sample is almost the same as the spectrum of pure PANI-ES since the characteristic CeO_{2-δ} vibrational modes (shown in inset of Fig. 3) cannot be distinguished. This can be associated to very intensive vibrational bands of protonated polyaniline as well as the low amount of cerium oxide in the composite. It can only be noticed that the intensity ratio of 1306/1244 cm⁻¹ bands (which are assigned to C-N stretching modes) changes in the presence of the oxide being 1.25, 1.28 and 1.29 for PANI-ES, PANI-ES@CeO_{2-δ}-SS, and PANI-ES@CeO $_{2-\delta}$ -HT, respectively. These changes are in correlation with the measured trend of electronic conductivity, and suggest the involvement of nitrogen from the polymer chain in the interaction with oxide.

3.4.2. Raman spectroscopy

The molecular structure of samples was studied also by Raman spectroscopy. The obtained Raman spectrum of PANI-ES (Fig. 4a) is typical for protonated emeraldine form, and its assignment is well-

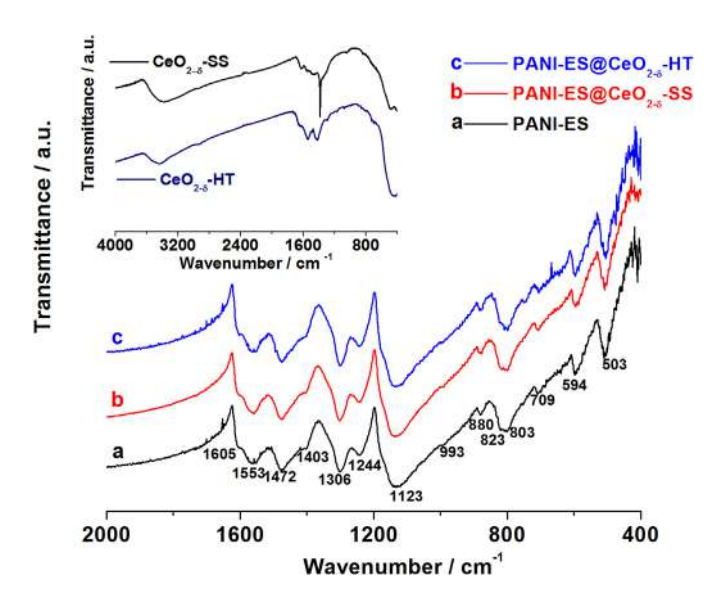


Fig. 3. FTIR spectrum of PANI-ES (a), PANI-ES@CeO_{2- δ}-SS (b) and PANI-ES@CeO_{2- δ}-HT (c). FTIR spectra of pure CeO_{2- δ}-SS and CeO_{2- δ}-HT are given in inset.

documented [27,31–36]. It can be seen in Supplementary Data.

Raman spectra of PANI@CeO_{2- δ} composites (Fig. 4b and c) show all characteristic modes of PANI-ES, but CeO_{2- δ} vibrations cannot be distinguished. The CeO_{2- δ} spectra are measured under the same experimental conditions as that of PANI-ES and presented in the inset of Fig. 4. The high intensity Raman band at ~463 cm⁻¹ corresponds to the F_{2g} vibrational mode of fluorite CeO_{2- δ} structure. Interestingly, this high intensity mode is not visible in the spectra of composites. This confirms that the CeO₂ is encapsulated into polymer chains thus forming the core-shell structure, via the polymerization of aniline adsorbed on the cerium oxide as a

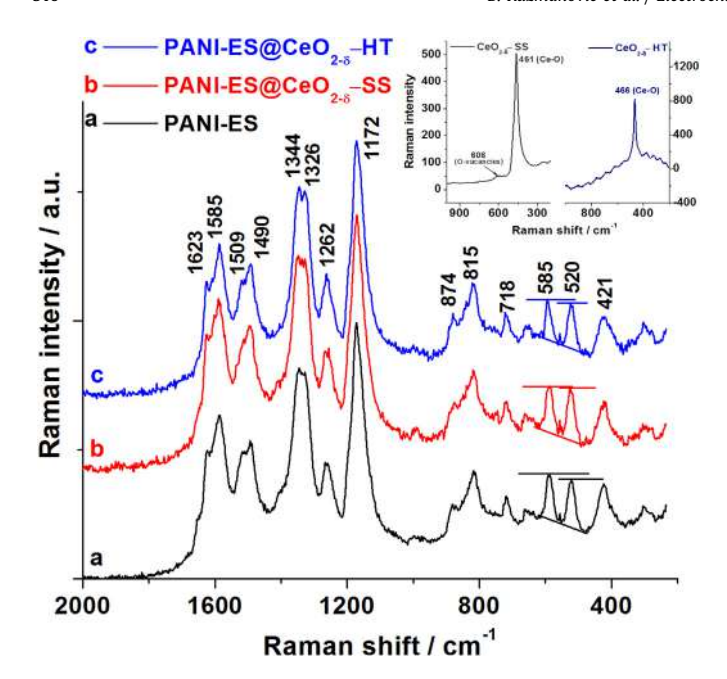


Fig. 4. Raman spectra of PANI-ES (a), PANI-ES@CeO $_{2-\delta}$ -SS (b) and PANI-ES@CeO $_{2-\delta}$ -HT in the normalized scale (c). Spectra of pure CeO $_{2-\delta}$ -SS and CeO $_{2-\delta}$ -HT oxides are given in inset.

nucleation core. A weak broadband (at ~ $606~cm^{-1}$) in the spectrum of $CeO_{2-\delta}$ -SS is related to the presence of oxygen vacancies. The use of more appropriate Raman conditions [35], provides more defined oxide modes, suggesting that both synthesized oxides investigated in this work actually possess a certain amount of vacancies, which is noticeable higher in the $CeO_{2-\delta}$ -SS sample.

The changes of the PANI-ES mode positions due to the presence of CeO_{2-δ} are not visible, but changes of the vibration modes intensity can be noticed. One can notice the $CeO_{2-\delta}$ influence on the band corresponding to the C~N⁺• stretching vibration of the delocalized polaronic structure, which is also identified by FTIR. Actually, the splitting of this band to ~1344 cm⁻¹ and ~1326 cm⁻¹ modes, which occurs in the pure PANI-ES, is more pronounced in the composites, especially in the PANI@CeO_{2-δ}-HT sample with the lower concentration of vacancies, and consequently, a higher degree of Ce⁴⁺ ions. It seems that the relative ratio of 1344 cm⁻¹/ 1326 cm⁻¹ bands decreases in the composite thus confirming the involvement of PANI's nitrogen in the interaction with cerium ions handing in electrons. By donating electrons to oxide, the C-N⁺ stretching bonds became weaker thus appearing at low wavenumbers which is reflected in the decreased intensity of $1344 \, \text{cm}^{-1}$ band on account of the increase of 1326 cm⁻¹ band intensity. The change in the 1509 cm⁻¹ mode, corresponding to N–H deformation vibrations, upon PANI-CeO_{2-δ} interaction, is also visible and is more pronounced in the composite containing $CeO_{2-\delta}$ -SS.

The PANI-CeO_{2- δ} interaction causes also pronounced changes of the vibrational modes intensity in the low-frequency region (in which the oxides modes appear). The relative intensity of the PANI's 421 cm⁻¹ band (which is positioned in the vicinity of the most intensive CeO_{2- δ} mode), is decreased in the composite. It can be correlated to the stronger F_{2g} vibrational mode of fluorite structure of CeO_{2- δ} which causes the strong interaction. Furthermore, the intensity ratio of bands at 585 cm⁻¹ (positioned in the vicinity of oxygen vacancy band) and 520 cm⁻¹ is decreased upon CeO_{2- δ} action (as indicated in Fig. 4), thus following the trend PANI-ES, PANI@CeO_{2- δ}-HT, PANI@CeO_{2- δ}-SS. So, this decrease is more pronounced for PANI@CeO_{2- δ}-SS, which could be related to the presence of higher concentration of oxygen vacancies. Also, the

change in the relative intensity of $718\,\mathrm{cm}^{-1}$ -assigned band to other bands follows this trend.

The observed changes in the Raman modes of polyaniline caused by the presence of cerium oxide indicates the existence of two types of PANI-CeO_{2- δ} interactions including the nitrogen-(from radical cation) and hydrogen (from amine of polarons and bipolarons) bonding. Unlike the interaction involved nitrogen atoms, it seems that the hydrogen bonding interaction is facilitated by oxygen vacancies in the oxide lattice.

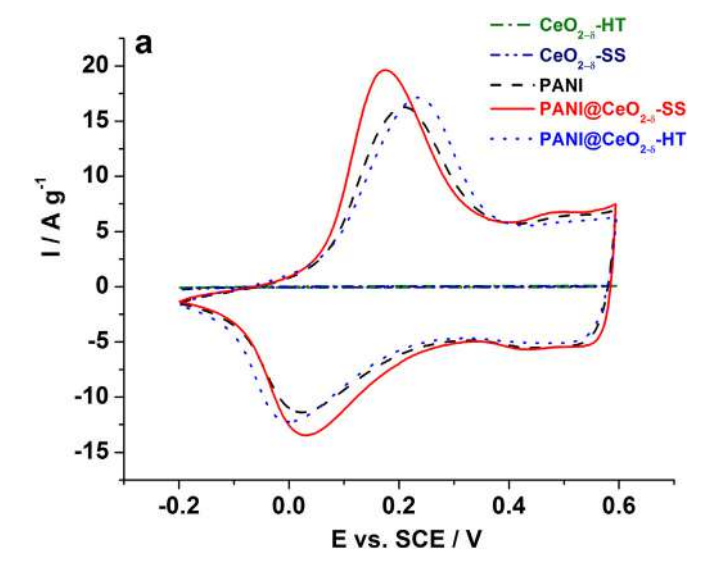
3.5. Electrochemical behavior

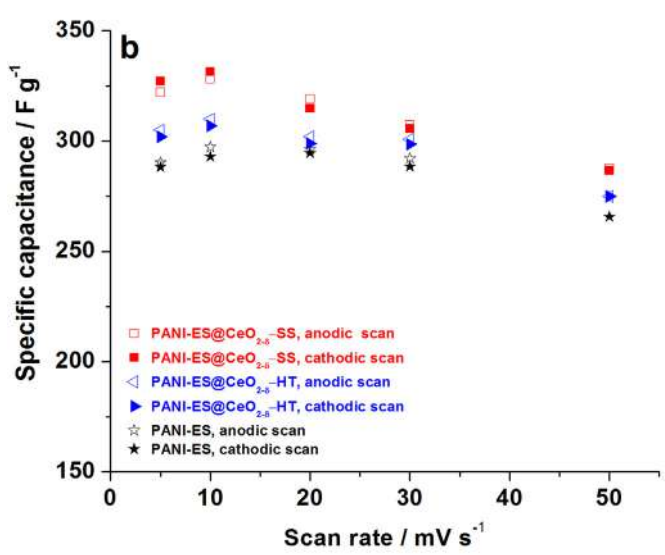
3.5.1. Narrower voltage interval

The influence of the cerium oxide to the charge storage behavior of PANI was studied by Cyclic Voltammetry. Typical redox pair of PANI, corresponding to the transition of leucoemeraldine to emeraldine salt, was observed in the potential range from $-0.2 \, \text{V}$ vs. SCE to 0.6 V vs. SCE (Fig. 5a) [37]. This redox process is sensitive to the presence and relative fraction of $CeO_{2-\delta}$ in the samples. As shown in Fig. 5a and Fig. S1, the current response of both ceriumoxides, in an acidic solution, is very poor, (below ~1 mA). On the other hand, PANI has more than twenty times higher current response. Theoretically, the ratio of active redox centers, such as Ce⁴⁺/Ce³⁺ and the amino/imino centers in the composite (wt%/M for CeO₂₋₈: wt%/M for C₆H₅NH), corresponds exactly to the ratio of 1:22, respectively. However, taking into account the mass ratio of individual components in the composite, the current ratio of PANI and oxide (in the composite) would be even higher in favor of PANI. Therefore, the slightly depressed current response of PANI-ES could be expected if the certain fraction of PANI was replaced with CeO_{2-δ}. However, the current response of PANI was somewhat increased after incorporation of cerium-oxide. This enhancement factor depends on the type of used oxide. Actually, the interaction of PANI with CeO_{2-δ}-HT leads to the very small increase of its current (which is practically negligible), while this response became somewhat higher in the presence of $CeO_{2-\delta}$ -SS (Fig. 5a and b). Charge/discharge capacitance expressed in F g^{-1} , were found to be $296/294 \, \text{F g}^{-1}$ for pure PANI, $302/299 \, \text{Fg}^{-1}$ for PANI@CeO_{2- δ}-HT and $319/314 \, F \, g^{-1}$ for PANI@CeO_{2- δ}-SS, at a common scan rate of $20 \, \text{mVs}^{-1}$.

Incorporation of $CeO_{2-\delta}$ into PANI-ES provides a slightly higher coulombic capacity despite the fact that the conductivity of composite was decreased by $CeO_{2-\delta}$ doping (although it decreased, the electronic conductivity of PANI-based composite is still very high). Therefore, the capability of polyaniline chains to attach/release electrolyte ions (without the charge transfer of protons) to compensate acceptance/liberation of electrons upon cycling can be limiting step. This process can be faster in the composite due to improved wettability caused by $CeO_{2-\delta}$ presence [38]. Better charge behavior of PANI@ $CeO_{2-\delta}$ -SS than PANI@ $CeO_{2-\delta}$ -HT can be attributed to the differences in wettability. $CeO_{2-\delta}$ -SS surface contains a higher amount of surface hydroxyl groups, compared to the one of $CeO_{2-\delta}$ -HT surface (Fig. 3). The presence of these groups improves the wettability of both PANI's surface at its boundary with $CeO_{2-\delta}$.

To summarize, both investigated PANI@CeO_{2- δ} composites present novel materials with a very large charge storage ability in an acidic solution. The synthesized PANI-ES@CeO_{2- δ} composites are also stable in 1 M HCl solution. This is confirmed by the stability of the charge storage of PANI-ES@CeO_{2- δ}-SS during the long cycling in this acidic electrolyte solution (Fig. S2, Supp.Data). Upon cycling, PANI@CeO_{2- δ}-SS electrode is kept in the electrolyte overnight, after which the same charge storage behavior was measured. TG curve of such cycled electrode powder was identical to the one for the raw powder, thus confirming the same oxide fraction in the composite. It can be concluded that a strong adhesion of PANI with the cerium





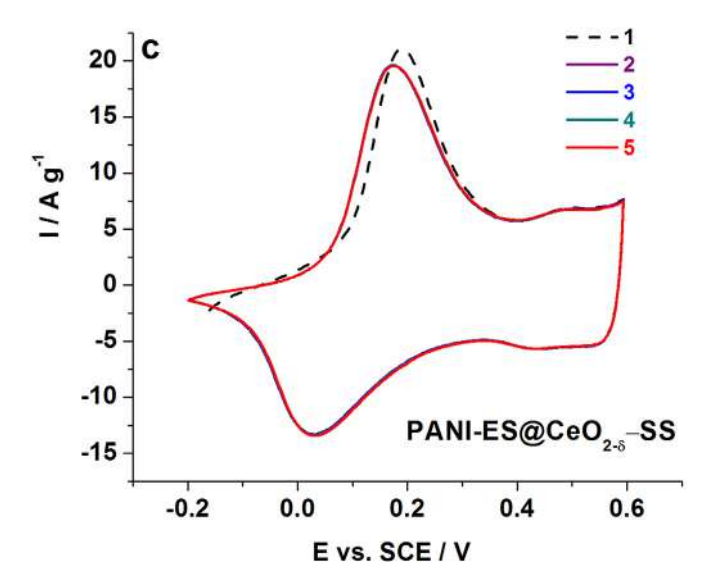


Fig. 5. a) Stabilized CVs of PANI-ES, $CeO_{2-\delta}$, and PANI-ES@ $CeO_{2-\delta}$ composites; b) Specific capacitance of PANI-ES, PANI-ES@ $CeO_{2-\delta}$ -HT, and PANI-ES@ $CeO_{2-\delta}$ -SS at different scan rates; c) The cyclic stability of PANI-ES@ $CeO_{2-\delta}$ -SS. The electrolyte was 1 M HCl. The voltage range was 0.2-0.6 V vs. SCE and the scan rate was 20 mV s $^{-1}$.

oxide surface prevents the oxide from its possible slow dissolution in 1 M HCl. The fact that the cerium oxide in the composite is encapsulated into the shell of polymer chains favors this assumption.

The higher capacitance was obtained for PANI-ES@CeO $_2$ - δ -SS, which makes this composite a very promising supercapacitor electrode. Its stable capacitance during consecutive cycling (Fig. 5c and Fig. S2) indicates the stable leucoemeraldine-emeraldine redox process. A small capacity decrease, with the increase of the scan rate, was measured (Fig. 5b).

3.5.2. Extended voltage interval

It is known that over-oxidation of PANI in an acidic solution by applying potentials above ~0.6–0.7 V vs. SCE, results in its capacity decrease. Because of that, the cycling behavior in the deeper positive-going scan (beyond 0.6 V vs. SCE) was rarely examined [39]. Among other things, the idea of this work is to see how the presence of nonstoichiometric cerium-oxide influences the electrochemical over-oxidation of polyaniline.

CVs of all three samples, measured in an extended potential range from -0.2-1 V vs. SCE during ten consecutive cycles were shown in Fig. 6. In the first cycle, beside the main redox couple I (positioned at 0.22/0.01 V vs. SCE), which originates from the oxidation of leucoemeraldine base (LM) to emeraldine salt, one can see another main redox pair (labeled as III) at 0.8/0.65 V vs. SCE, corresponding to the emeraldine/pernigraniline (EM/PN) salt transition. A small redox pair II (0.55/0.45 V vs. SCE) positioned between these two main redox pairs can be also observed. Although the nature of this peak depends on the experimental details of polyaniline synthesis, electrolyte, and pH, this peak is generally attributed to the formation of benzoquinone degradation products and formation of cross-linked polyaniline chains by direct reaction between parts of the polyaniline chain itself [39]. One can see that the current of this middle redox couple increases during consecutive cycling of PANI within the extended water stability window, while the current of both LE-EM and EM-PN redox process decreases. Actually, over-oxidation of polyaniline leads to the irreversible formation of electrochemically inactive structures, which causes the current decrease throughout the consecutive cycling [37,39]. During experiments we noticed that the current of the second redox couple became more pronounced as soon as the current of the third peak has increased. One can conclude that the redox process corresponding to the second peak is still associated with the emeraldine-pernigraniline transformation.

Interestingly, some differences of the relative ratio of anodic peaks I and III can be observed between PANI and the CeO_{2-δ}modified PANI. A similar current response of these anodic peaks is observed for PANI and PANI@CeO_{2-δ}-SS (Fig. 6a and b), indicating similar kinetics of the LE-EM and EM-PN redox processes in these samples. However, this is not the case for PANI-ES@CeO_{2-δ}-HT (Fig. 6c) where the first anodic peak is noticeable higher than the third one. The process of the PN formation during PANI's oxidation is aggravated by CeO_{2-δ}-HT action. The involvement of positively charged nitrogen in the interaction with cerium oxide impedes PANI-ES deprotonation, resulting in the lower fraction of formed PN upon the first anodic scan (Fig. 7a) and consequently the slower disappearance of the third peak after ten cycles (Fig. 7b). As a result, slightly better capacitance retention of PANI@CeO_{2-δ}-HT (83.4% after 10 cycles or 64.4% after 30 cycles) was observed with respect to the pure PANI (80.8% after 10 cycles or 60.5% after 30 cycles) and PANI@CeO_{2- δ}-SS (76.8% after 10 cycles and 55.6% after 30 cycles).

3.6. PANI-CeO_{2- δ} interaction

Polyaniline chains can change their redox state from a

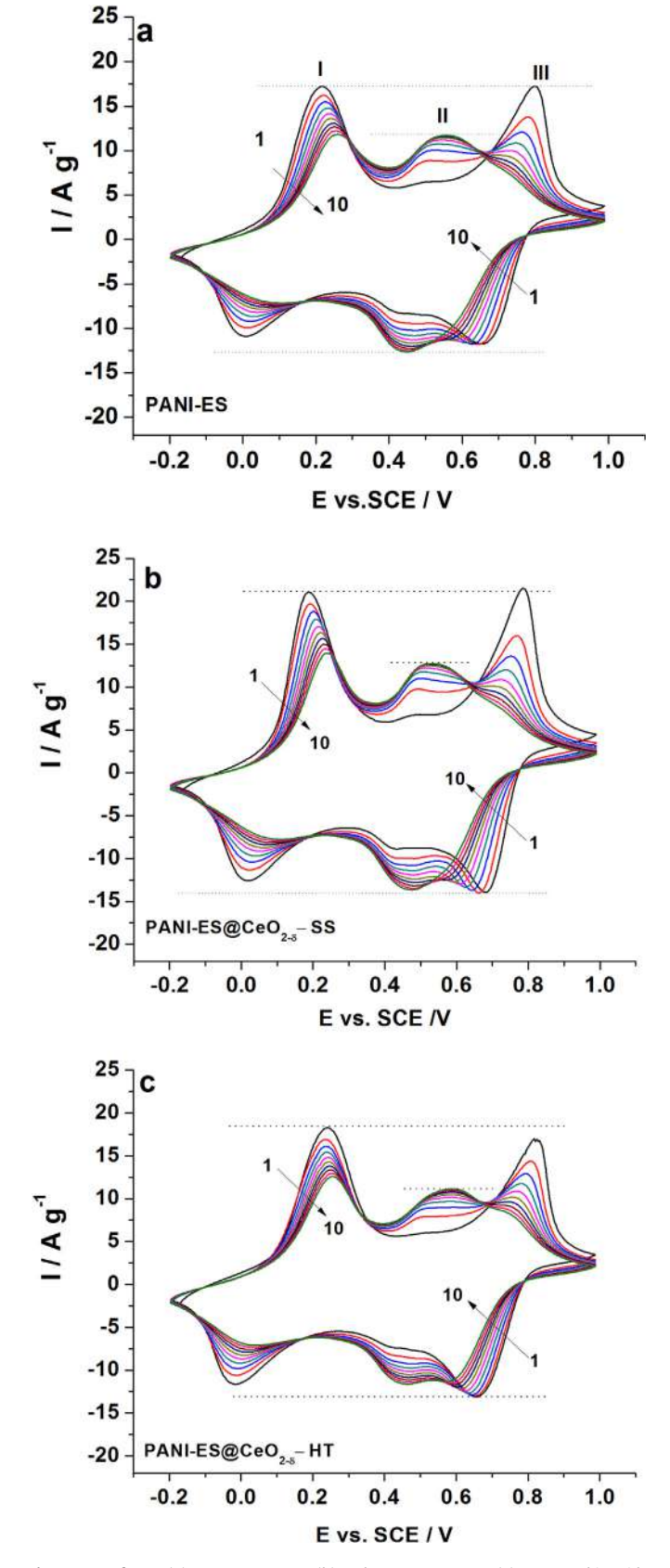
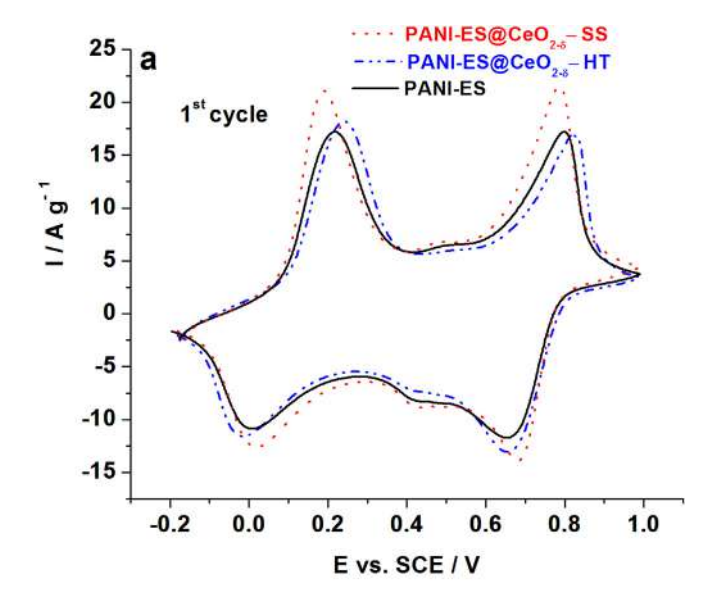


Fig. 6. CVs of PANI (a), PANI@CeO $_{2-\delta}$ -SS (b) and PANI@CeO $_{2-\delta}$ -HT (c) measured in wide potential interval from -0.2-1 V vs. SCE during 10 successive cycling, at a common scan rate at 20 mV s $^{-1}$.



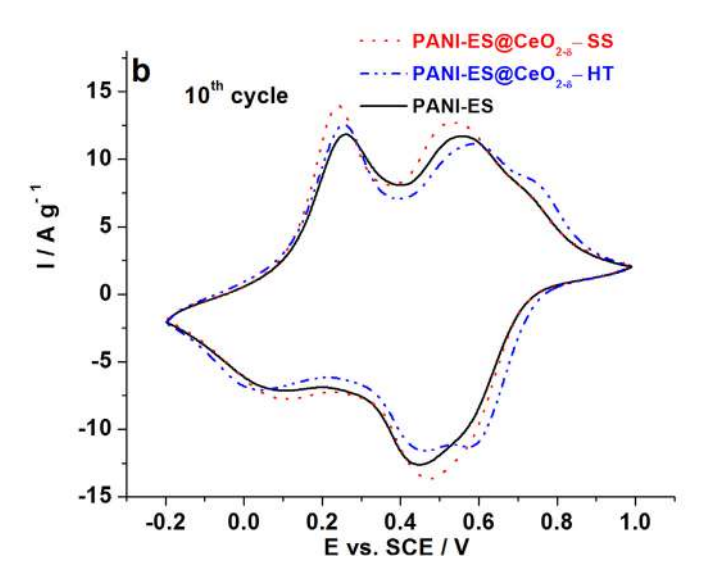


Fig. 7. CVs of PANI-ES, PANI-ES@CeO_{2- δ}-SS and PANI-ES@CeO_{2- δ}-HT samples measured in HCl at a common scan rate of 20 mV s⁻¹: a) the 1st cycle and b) 10th cycle.

completely reduced form (leucoemeraldine), composed of benzenoid units containing amine nitrogen atoms -NH-, to a fully oxidizied form (pernigraniline), composed of quinoid units containing imine nitrogen atoms -N=. A semi-oxidized form of polyaniline, known as emeraldine (either in the form of base or salt), is composed from equal numbers of reduced and oxidized polymer repeat units. The protonation of the emeraldine base, under acidic conditions, includes the addition of protons to imine nitrogen sites to generate radical cations (some amine nitrogen atoms can also be protonated to give NH_2^+ groups even if all the imines are not protonated), which can significantly increase the conductivity of polyaniline (up to 11 orders of magnitude) [25,40], reaching the metallic values.

On the other hand, cerium oxide crystallized in the fluorite type cubic crystal lattice where the Ce⁴⁺ cation is surrounded by eight O²⁻ anions, each of which is coordinated to four Ce⁴⁺ cations. Both theoretical and experimental results revealed that in oxygen deficient cerium oxide the adsorbed water molecules prefer to dissociate near the oxygen vacancy sites thus forming surface hydroxyl

groups [41,42]. Therefore, both chemisorbed H_2O and OH groups coexist at the reduced cerium oxide surface, so their presence can be expected at the surface of the $CeO_{2-\delta}$ -SS and $CeO_{2-\delta}$ -HT oxides, as confirmed by their FTIR spectra (inset in Fig. 3, O—H stretching vibrations around 3500 cm $^{-1}$). Their lower content in the $CeO_{2-\delta}$ -HT can be correlated to the lower reactivity of surface towards the water dissociation, due to the smaller fraction of oxygen vacancies.

The experimentally determined pH values of CeO_{2- δ}-SS, at zero point of charge (pH_{ZPC} = 6.3), showed that the oxide surface became positively charged in the reaction solution of HCl (Fig. 8). Namely, surface hydroxyl groups are protonated, according to the equation

$$Ce-OH + H^+ \leftrightarrow Ce-OH_2^+$$

Such formed positively charged cerium oxide nanoparticles can electrostatically attract Cl⁻ ions from the acidic solution (Fig. 8a).

The adsorbed Cl⁻ ions can easily attract the anilinium cation (formed by adding aniline into acidic solution) which undergoes further polymerization to the emeraldine salt when the oxidant is added in the acidic medium. Consequently, there is possibility that various oligomers with an active radical cation head (positive head) are adsorbed to the surface of CeO_{2-δ} particles as well, but this possibility is reduced by the fact that the adsorption centers of cerium oxide were previously saturated with protonated aniline species. In this way, CeO_{2-δ} particles become wrapped into PANI chains thus forming the "core-shell" nanostructure. This type of structure has been already recognized for polyaniline/cerium oxide system [6,7,12,43-45]. These data showed that the interaction of protonated form of polyaniline with CeO_{2-δ} is usually achieved through the formation of hydrogen bond between surface hydroxyl (-OH) groups of oxide and hydrogen of the polymer chain [6,44-46]. Based on both Raman and FTIR measurements, the similar type of interaction is also identified in as-synthesized PANI@CeO_{2-δ} composites. Namely, zeta potential-pH dependence, measured for oxygen deficient cerium oxide [21], revealed that the maximum positive charge, at the surface, was achieved for the pH solution of about 4-5. Besides, some of OH groups at the ceriumoxide surface can be found un-protonated, thus participating in the formation of hydrogen bonds, acting as the bridge between polymer and oxide (Fig. 8b). This type of interaction is more pronounced in the CeO_{2-δ}-SS since the higher fraction of oxygen vacancies (relative to CeO₂₋₀-HT) results in the higher amount of hydroxyl groups. Besides, another type of oxide-polyaniline interaction (Fig. 8c), involving positively charged nitrogen (-N°+H-), is identified by vibrational spectroscopy study. This interaction is found to be stronger in the case of composite with the hydrothermally synthesized oxide, which has the smaller oxygen vacancy population (i.e. higher concentration of Ce⁴⁺ ions). Theoretical study on $CeO_{2-\delta}$ revealed that the electrons can be localized at cerium ions or oxygen vacancies [35]. Having in mind, that the nitrogen-involved interaction is more manifested in $CeO_{2-\delta}$ -HT than in $CeO_{2-\delta}$ -SS, and easier reduction of Ce^{4+} to Ce^{3+} ions, one can assume that delocalized π electrons of polymer chains became localized at 4f states of cerium ions. This may result in the decreased of the electronic conductivity of PANI when bonded to cerium oxide, following the trend PANI, PANI-ES@CeO_{2- δ}-SS and PANI-ES@CeO_{2- δ}-HT. Also, it could be responsible for the higher amount of bonded $CeO_{2-\delta}$ -HT and consequently improved thermal stability of PANI-ES@CeO_{2- δ}-HT composite. The mechanism of PANI-CeO_{2- δ} interaction is illustrated in Fig. 9.

A small amount of oxide (about 4%wt), incorporated into the shell of conducting polymer, was found to decrease its conductive behavior (in the extent that depends on properties of the used oxides), but conversely to improve its charge storage capability. The interactions at the PANI@CeO_{2-δ} interface weakened the polymer interchain bonds providing an easier attraction of electrolyte ions. Whether the higher amount of $CeO_{2-\delta}$ can improve electrochemical performance even more is the main question which arises here? Our attempt to answer this question, by increasing the amount of doped CeO_{2-δ} oxide during the synthesis, failed. Interestingly, PANI was not capable to bind a higher amount of CeO_{2-δ} (under applied synthesis conditions) regardless to the increase of its initial amount into reaction medium. Actually, the doubling of the initial content of CeO_{2-δ} (from 50 mg to 100 mg) for the aniline oxidation did not increase the content of bonded-CeO $_{2-\delta}$ at all. Such behavior is opposite to the case of TiO2 added upon aniline oxidation, under completely same experimental conditions. In a set of separated experiments we showed that the initial amounts of 9 mg, 50 mg and 100 mg of TiO₂ (under same synthesis conditions), resulted in the ~4 wt%, ~18 wt% and ~34 wt% of oxide (calculated per mass of dried sample), in the composites (Fig. S3), respectively, which is in agreement with results of Bian et al. [18]. We try to explain this peculiar behavior using TG analysis. It can be seen from TG curves of composites, doped with a small percent (3–4%) of either CeO₂₋ δ (Fig. 1) or TiO₂ (Fig. S1), that the presence of such doped concentration did not change the final amount of internal dopant (HCl) in the composite. One can suggest that the type of interaction of these oxides in the case of their small doped fraction is similar i.e. both oxides coexist together with Cl⁻ ions (some of the Cl⁻ ions are adsorbed on the protonated hydroxyl groups) thus interacting also with hydrogen/nitrogen and weakening PANI's bonds with dopant. Furthermore, it can be seen that the amount of doped acid is noticeably decreased after mixing PANI with the higher percent (18% or 34%) of TiO₂ (Fig. 1). By competing with dopant ions for the positions of chains (close to the nitrogen atoms) during the synthesis, titanium oxide molecules (in higher concentration), are capable to eliminate some of dopant ions thus making complex

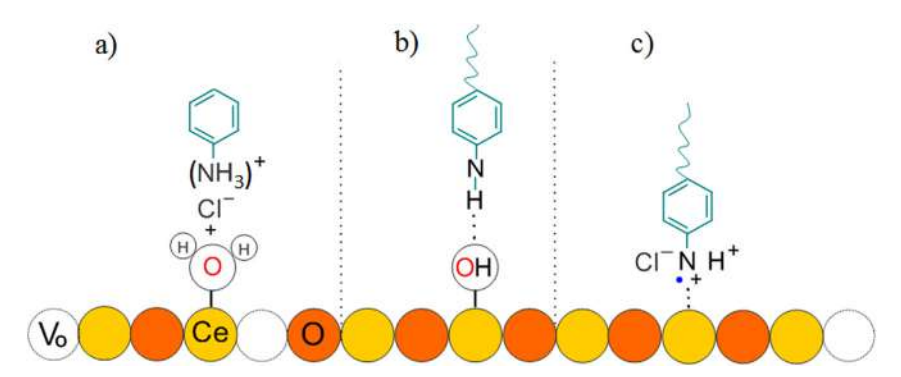


Fig. 8. The initial stage of polymerization (a) and hydrogen (b) and nitrogen-involved interactions (c).

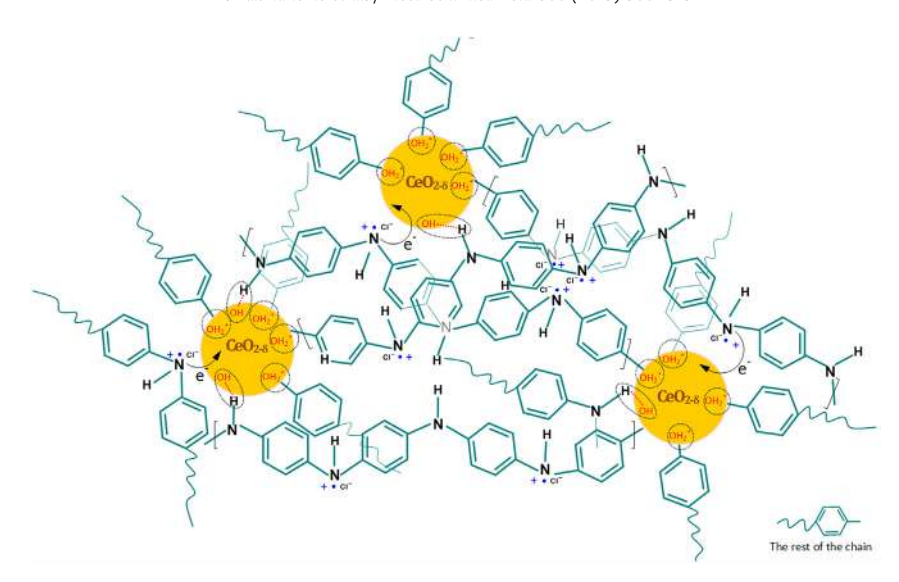


Fig. 9. Schematic illustration of the formation of PANI chains on the surface of $CeO_{2-\delta}$ nanoparticles (core-shell structure).

with nitrogen atoms of PANI. It could be related to a strong tendency of titanium to form coordination compounds with nitrogen [47]. On the other hand, nano-CeO $_{2-\delta}$, in spite of the higher concentration in the reaction solution, does not show this capability under the same experimental conditions, which resulted in its unsuccessful high-level bonding.

4. Conclusions

The use of non-stoichiometric cerium oxide as the adsorption center for the polymerization of aniline, in highly acidic conditions, influences thermal, electrical and charge storage properties of the formed emeraldine salt. These changes are the consequence of the strong interaction of polyaniline chains with cerium oxide ultrafine nanoparticles. The oxygen vacancies control indirectly the intensity of these interactions. A higher fraction of O-vacancies in CeO₂δ promotes the dissociation of chemisorbed H₂O to OH groups at the oxide's surface, which in the protonated form, play the role of chemically active sites for the growth of PANI chains. Besides, unprotonated hydroxyl groups of cerium oxide surface interact with the hydrogen of polymer chains through the formation of hydrogen bonds. A lower fraction of O-vacancies provides the higher concentration of Ce4+ ions into crystal lattice, thus intensifying the interaction of Ce⁴⁺ cation with the nitrogen of the polaron structure $(C \sim N^{\bullet +})$, through the trapping of electrons into localized 4f states of cerium ions.

By encapsulating small weight percent of oxygen deficient cerium oxide, into highly conductive emeraldine salt, the improvement of both thermal stability and charge storage behavior is achieved. The highest and stable capacitance, amounting to $314\,\mathrm{Fg}^{-1}$, was obtained for the oxide with the higher degree of deficient oxygen (PANI-ES@CeO_{2- δ}-SS), thus making this material promising as electrode for supercapacitors.

Acknowledgments

The Ministry of Education, Science and Technological Development of Republic of Serbia is acknowledged for funding support within projects III45014, III45003, III45018, OI172043, III45016 as well as through the bilateral projects Serbia-Slovenia entitled "Developments of novel materials for alkaline-ion batteries" and Serbia-Montenegro entitled "Development of ecological Li-ion

batteries". S.M. acknowledges Serbian Academy of Sciences and Arts for support of this investigation, too, through the project "Electrocatalysis in the contemporary process of energy conversion".

Appendix A. Supplementary data

Supplementary data to this article can be found online at https://doi.org/10.1016/j.electacta.2019.03.135.

References

- [1] H. Wang, J. Lin, Z.X. Shen, Polyaniline (PANi) based electrode materials for energy storage and conversion, J. Sci. Adv. Mater. Dev. 1 (2016) 225.
- [2] F.-Y. Chuang, S.-M. Yang, Cerium dioxide/polyaniline core—shell nanocomposites, J. Colloid Interface Sci. 320 (2008) 194.
- [3] S. Daikh, F.Z. Zeggai, A. Bellil, A. Benyoucef, Chemical polymerization, characterization and electrochemical studies of PANI/ZnO doped with hydrochloric acid and/or zinc chloride: differences between the synthesized nanocomposites, J. Phys. Chem. Solids 121 (2018) 78.
- [4] H. Wei, X. Yan, S. Wu, Z. Luo, S. Wei, Z. Guo, Electropolymerized polyaniline stabilized tungsten oxide nanocomposite films: electrochromic behavior and electrochemical energy storage, J. Phys. Chem. C 116 (2012) 25052.
- [5] C.-G. Wu, D.C. DeGroot, H.O. Marcy, J.L. Schindler, C.R. Kannewurf, Y.-J. Liu, W. Hirpo, M.G. Kanatzidis, Redox intercalative polymerization of aniline in V2O5 xerogel. The postintercalative intralamellar polymer growth in polyaniline/metal oxide nanocomposites is facilitated by molecular oxygen, Chem. Mater. 8 (1996) 1992.
- [6] C. Liu, H. Tai, P. Zhang, Z. Yuan, X. Du, G. Xie, Y. Jiang, A high-performance flexible gas sensor based on self-assembled PANI-CeO2 nanocomposite thin film for trace-level NH3 detection at room temperature, Sens. Actuators B Chem. 261 (2018) 587.
- [7] L. Wang, H. Huang, S. Xiao, D. Cai, Y. Liu, B. Liu, D. Wang, C. Wang, H. Li, Y. Wang, Q. Li, T. Wang, Enhanced sensitivity and stability of room-temperature NH3 sensors using core-shell CeO2 Nanoparticles@Cross-linked PANI with p—n heterojunctions, Appl. Mater. Interfaces 6 (2014) 14131.
- [8] A.A. Ansari, G. Sumana, R. Khan, B.D. Malhotra, Polyaniline-cerium oxide nanocomposite for hydrogen peroxide sensor, J. Nanosci. Nanotechnol. 9 (2009) 4679.
- [9] N. Parvatikar, S. Jain, S.V. Bhoraskar, M.V.N.A. Prasad, Spectroscopic and electrical properties of polyaniline/CeO2 composites and their application as humidity sensor, J. Appl. Polym. Sci. 102 (2006) 5533.
- [10] M. Singh, N. Nesakumar, S. Sethuraman, U. Maheswari, Journal of Colloid and Interface Science Electrochemical biosensor with ceria — polyaniline core shell nano-interface for the detection of carbonic acid in blood, J. Colloid Interface Sci. 425 (2014) 52.
- [11] M.B. Gumpu, N. Nesakumar, S. Sethuraman, U.M. Krishnan, J.B.B. Rayappan, Electrochemical biosensor with ceria-PANI core-shell nano-interface for the detection of histamine, Sens. Actuators B Chem. 199 (2014) 330.
- [12] H. Huang, Z. Guo, Preparation and characterization of conductive polyaniline/ cerium dioxide composites, Mater. Sci. Forum 663–665 (2011) 686.
- [13] S. Wang, Z. Huang, J. Wang, Y. Li, Z. Tan, Thermal stability of several

- polyaniline/rare earth oxide composites (I): polyaniline/CeO2 composites, J. Therm. Anal. Calorim. 107 (2012) 1199.
- [14] B. Ramezanzadeh, G. Bahlakeh, M. Ramezanzadeh, Polyaniline-cerium oxide (PAni-CeO2) coated graphene oxide for enhancement of epoxy coating corrosion protection performance on mild steel, Corros. Sci. 137 (2018) 111.
- [15] N. Maheswari, G. Muralidharan, Fabrication of CeO2/PANI composites for high energy density supercapacitors, Mater. Res. Bull. 106 (2018) 357.
- [16] Q. Gong, Y. Li, H. Huang, J. Zhang, T. Gao, G. Zhou, Shape-controlled synthesis of Ni-CeO2@PANI nanocomposites and their synergetic effects on supercapacitors, Chem. Eng. J. 344 (2018) 290.
- [17] Y. Fei, H. Huang, S. Song, L. Jin, X. Zhang, Z. Guo, Preparation of thermostable and electroconductive PANI/TDI-CeO2 composite by graft polymerization and its electrochemical properties, Int. J. Electrochem. Sci. 13 (2018) 1308.
- [18] C. Bian, Y. Yu, G. Xue, Synthesis of conducting polyaniline/TiO2 composite nanofibres by one-step in situ polymerization method, J. Appl. Polym. Sci. 104 (2007) 21.
- [19] S. Phokha, S. Pinitsoontorn, P. Chirawatkul, Y. Poo-arporn, S. Maensiri, Synthesis, characterization, and magnetic properties of monodisperse CeO 2 nanospheres prepared by PVP-assisted hydrothermal method, Nanoscale Ress. Lett. 7 (2012) 425.
- [20] X. Yu, F. Li, X. Ye, X. Xin, Synthesis of cerium(IV) oxide ultrafine particles by solid-state reactions, J. Am. Ceram. Soc. 83 (2000) 964.
- [21] N. Tomić, Z.D. Dohčević-Mitrović, N.M. Paunović, D.Ž. Mijin, N.D. Radić, B.V. Grbić, S.M. Aškrabić, B.M. Babić, D.V. Bajuk-Bogdanović, Nanocrystalline CeO2–δ as Effective Adsorbent of Azo Dyes 30 (2014) 11582.
- [22] Y. Wei, K.F. Hsueh, Thermal analysis of chemically synthesized polyaniline and effects of thermal aging on conductivity, J. Polym. Sci., Part A: Polym. Chem. 27 (1989) 4351.
- [23] M. Trchová, J. Stejskal, Polyaniline: the infrared spectroscopy of conducting polymer nanotubes, Pure Appl. Chem. 83 (2011) 1803—1817, https://doi.org/ 10.1351/PAC-REP-10-02-01.
- [24] M. Hasik, C. Paluszkiewicz, E. Bielánska, Reactions of Polyaniline with Transition Metal Ions in Nonaqueous Solutions, 2005, pp. 744–747, 677.
- [25] Z. Ping, In situ FTIR-attenuated total reflection spectroscopic investigations on the base-acid transitions of polyaniline, J. Chem. Soc., Faraday Trans. 92 (1996) 3063
- [26] M. Lohrasbi, N. Hedayat, S.S.C. Chuang, In-situ infrared study of the synthesis of polyaniline under acid and neutral pH, Top. Catal. 57 (2014) 1570.
- [27] M. Trchová, Z. Morávková, I. Šeděnková, J. Stejskal, Spectroscopy of thin polyaniline films deposited during chemical oxidation of aniline, Chem. Pap. 66 (2012) 415.
- [28] M. Hasik, A. Drelinkiewicz, E. Wenda, C. Paluszkiewicz, S. Quillard, FTIR spectroscopic investigations of polyaniline derivatives-palladium systems, J. Mol. Struct. 596 (2001) 89.
- [29] M. Trchová, I. Šeděnková, E.N. Konyushenko, J. Stejskal, P. Holler, G. Ćirić-Marjanović, Evolution of polyaniline nanotubes: the oxidation of aniline in water, J. Phys. Chem. B 110 (2006) 9461.
- [30] M.R. Devi, B. Lawrence, N. Prithivikumaran, N. Jeyakumaran, Synthesis and

- characterization of conducting polymer Polyaniline doped with Salicylic Acid, Int.J. ChemTech Res. 6 (2014) 5400.
- [31] G. Čirić-Marjanović, M. Trchová, J. Stejskal, The chemical oxidative polymerization of aniline in water: Raman spectroscopy, J. Raman Spectrosc. 39 (2008)
- [32] G.M. do Nascimento, V.R.L. Constantino, R. Landers, M.L.A. Temperini, Aniline polymerization into montmorillonite clay: a spectroscopic investigation of the intercalated conducting polymer, Macromolecules 37 (2004) 937.
- [33] M. Tagowska, B. Pałys, K. Jackowska, Polyaniline nanotubules anion effect on conformation and oxidation state of polyaniline studied by, Raman spectroscopy 142 (2004) 223.
- [34] B.Z. Wei, M. Wan, T. Lin, L. Dai, Polyaniline nanotubes doped with sulfonated carbon nanotubes made via a self-assembly, Adv. Mater. 15 (2003) 136.
- [35] M. Radović, B. Stojadinovic, N. Tomić, A. Golubović, B. Matovic, I. Veljković, Z. Dohčević-Mitrović, Investigation of surface defect states in CeO2-y nanocrystals by Scanning-tunneling microscopy/spectroscopy and ellipsometry, J. Appl. Phys. 116 (2014) 234305.
- [36] A. Drury, S. Chaure, M. Kröll, V. Nicolosi, N. Chaure, W.J. Blau, Fabrication and characterization of silver/polyaniline composite nanowires in porous anodic alumina, Chem. Mater. 19 (2007) 4252.
- [37] E. Song, J.-W. Choi, Conducting polyaniline nanowire and its applications in chemiresistive sensing, Nanomaterials 3 (2013) 498.
- [38] S. Popescu, M. Mîndroiu, D. Cabuzu, C. Pîrvu, The Roll of NaPSS Surfactant on the Ceria Nanoparticles Embedding in Polypyrrole Films, 2016, 2016, p. 1.
- [39] R. Pauliukaite, C.M.A. Brett, A.P. Monkman, Polyaniline fibres as electrodes, Electrochemical characterisation in acid solutions 50 (2004) 159.
- [40] A.G. MacDiarmid, A.J. Epstein, Conducting polymers: science and technology, in: P.N. Prasad (Ed.), Frontiers of Polymers and Advanced Materials, Plenum Press. New York. 1994. p. 251.
- Press, New York, 1994, p. 251.
 [41] Z. Yang, Q. Wang, S. Wei, D. Ma, Q. Sun, The effect of environment on the reaction of water on the ceria(111) surface: a DFT+U study, J. Phys. Chem. C 114 (2010) 14891.
- [42] Lj Kundakovic, D.R. Mullins, S.H. Overbury, Adsorption and reaction of H2O and CO on oxidized and reduced Rh/CeOx(111) surfaces, Surf. Sci. 457 (2000) 51
- [43] E. Kumar, P. Selvarajan, D. Muthuraj, Preparation and characterization of polyaniline/cerium dioxide (CeO2) nanocomposite via in situ polymerization, J. Mater. Sci. 47 (2012) 7148.
- [44] Y. Sasikumar, A.M. Kumar, Z.M. Gasem, E.E. Ebenso, Hybrid nanocomposite from aniline and CeO2 nanoparticles: surface protective performance on mild steel in acidic environment, Appl. Surf. Sci. 330 (2015) 207.
- [45] F. Liu, H. Yongjun-He, J.-S. Huh, Study on the synthesis and characterization of PANi/nano-CeO2 composites, Solid State Phenom. 124–126 (2007) 287.
- [46] Y. He, Synthesis of polyaniline/nano-CeO2 composite microspheres via a solid-stabilized emulsion route, Mater. Chem. Phys. 92 (2005) 134.
- [47] X. Li, G. Wang, X. Li, D. Lu, Surface properties of polyaniline/nano-TiO2 composites, Appl. Surf. Sci. 229 (2004) 395.

ORIGINAL PAPER



Atmospheric Plasma Supported by TiO₂ Catalyst for Decolourisation of Reactive Orange 16 Dye in Water

Tatjana Mitrović¹ · Nataša Tomić² · Aleksandra Djukić-Vuković³ · Zorana Dohčević-Mitrović⁴ · Saša Lazović²

Received: 8 July 2019 / Accepted: 30 December 2019 © Springer Nature B.V. 2020

Abstract

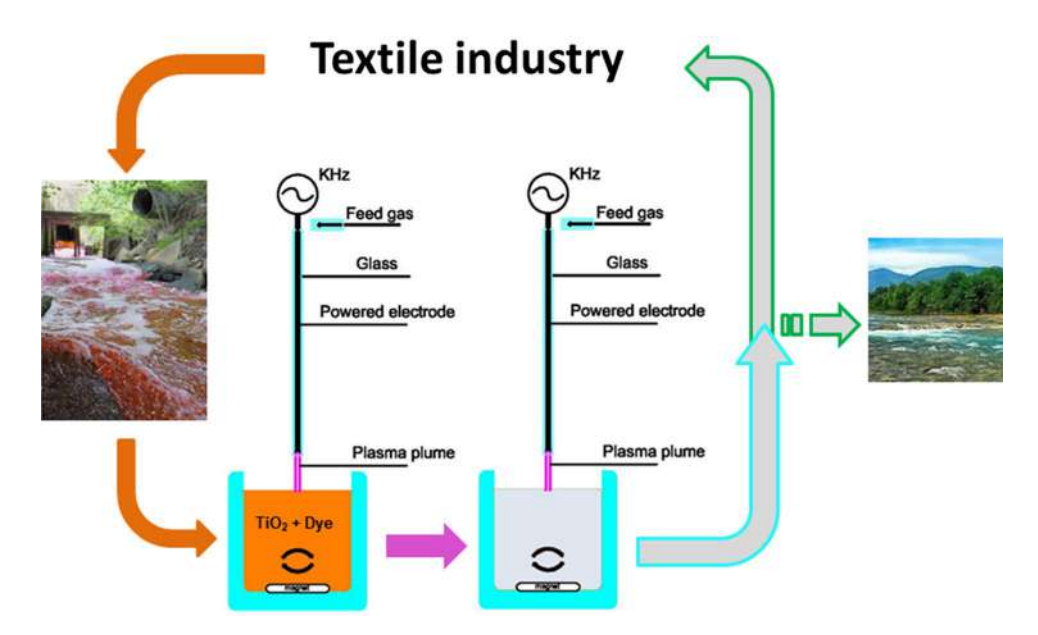
Purpose Every advanced oxidation process (AOP) has its limitations in water purification. Novel designs with simultaneous application of different AOPs can offer better solutions for cleaner water.

Methods We have comparatively studied two advanced oxidation processes (AOPs) on decolourisation of Reactive Orange 16 (RO 16) azo dye pollutant from water: gas plasma treatment by low power atmospheric pressure plasma using novel plasma needle configuration, and semiconductor heterogeneous photocatalysis using titanium dioxide (TiO₂) nanopowders. Additionally, simultaneous application of two advanced oxidation processes on azo dye decolourisation was studied.

Results It was found that plasma treatment is very efficient system for the dye removal even for low flow rates (1 slm) of the Ar as feed gas. The presence of 10% of O_2 in Ar flow intensified dye oxidation process and shortened required time for total decolourisation. When plasma and catalyst were simultaneously applied, TiO_2 was activated with a few Watts plasma source as well as 300 W UV lamp source. The synergic effect of two AOPs was more pronounced for higher feed gas flow rates, resulting in improved decolourisation efficiency.

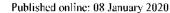
Conclusion Plasma needle can efficiently remove Reactive Orange 16 azo dye from water with a power consumption of only few Watts. With the addition of TiO₂ the removal efficiency is significantly improved.

Graphic Abstract



Keywords Advanced oxidation · Wastewater treatment · Plasma needle · Titanium dioxide · Azo dyes · Photocatalysis

Extended author information available on the last page of the article





Statement of Novelty

Textile industry consumes around 2000 L of water to produce a single pair of jeans. Ten to fifteen percent of the global production of dyes is discharged into the waterbodies. This is not sustainable. Treated wastewater has to be reused. We propose a novel and efficient method for treatment of textile industry wastewater. A combination of two advanced oxidation processes—low power atmospheric pressure plasma and ${\rm TiO_2}$ heterogeneous photocatalysis is used for decolourisation of Reactive Orange 16 azo dye pollutant.

Introduction

Since water is one of the most important resources, its availability and quality have become one of the biggest social priorities today. Increasing pollution of the water system, including textile industries and agriculture, affects ecosystem and human health directly and represent the widespread concern.

Textile and paper industries generate complex and diverse effluents and they belong to the most polluting industrial sectors [1]. Organic dyes as the main components of these effluents, are considered to be very toxic, mutagenic, and potentially carcinogenic [2, 3]. About 10-15% of the total world production of dyes are discharged into different waterbodies affecting directly aquatic life by disrupting the amount of dissolved O_2 and consequently photosynthesis and respiration processes [4-6].

Azo dyes are organic molecules generally with an azo bond (R-N=N-R') as main chromophore group. They are widely used in textile industry and because of their chemical complexity and low biodegradability; the wastewater treatment is very demanding. Different methods are applied to remove these organic compounds from the water sources: biological, physicochemical (adsorption, coagulation/flocculation, reverse osmosis) or chemical treatments (chlorination and ozonation). However, these methods have certain limitations. The biological treatments are not effective in the case of stable and resistant azo dyes. Only few unstable azo dyes can be degraded under aerobic conditions. On the other hand, anaerobic degradation causes aromatic amines generation which are toxic and carcinogenic [7]. The physicochemical treatments often cause formation of secondary pollution, generating large amounts of sludge and transferring pollutants from water to solid phase. Therefore, incomplete degradation and necessity for additional operations including final degradation of the waste and adsorbent regeneration limit the application of these treatments [8]. Chemical treatments like chlorination can result in complete decolourisation of dyes, but chlorinated organic by-products are very hazardous [9]. Ozone oxidizes dyes as well, but its extreme oxidizing effects can harm the atmosphere. Thus, ozonation system must include a control unit which prevents excessive use of chemicals [10].

Advanced oxidation processes (AOPs) have shown some advantages over the conventional water purification technologies. Based on the production of very strong and unselective oxidizing species (hydroxyl radicals—OH), these techniques are used in mineralization of soluble complex organic pollutants. The ultimate goal of this process is to decompose pollutants to CO₂, H₂O, and some inorganic ions. Most common AOPs are: gas plasma oxidation [11, 12], (heterogeneous) photocatalytic oxidation [13, 14], ultrasounds [15], photo Fenton oxidation [16, 17], etc.

Among above-mentioned treatments, gas plasma is a relatively novel AOP method for wastewater decontamination. The method is based on ionized gas produced by an electrical discharge, generating electrons, radicals (OH, H, O'), ions (OH–, H₂O+, H+, HO₂⁻) and neutrals (H₂O₂, O₃). Plasma systems can be generally divided into thermal or non-thermal plasma. Thermal plasma typically needs more power than non-thermal and creates high flux of heat, which can be used for degradation of very resistant organic molecules. In the case of non-thermal plasma, electrons are at temperatures as high as 11,000 K, and are colliding with gas molecules at temperatures as low as the room temperature, promoting the generation of chemically active species [18].

Previous studies reported that non-thermal plasma generated in the gas phase above the water surface initiates many chemical and physical effects including a high electric field, intense ultraviolet radiation, overpressure shock waves and, of particular importance, formation of various chemically strong oxidative species like radicals and molecules (OH, H, O₂, O, H₂O₂, O₃). These species, dissolved in water, initiate oxidation processes [19, 20].

Until now, various types of non-thermal plasma devices such as plasma jets [21, 22], plasma needle [23-25], gliding arc [26, 27], dielectric barrier discharge [28, 29], pulsed corona discharges [30, 31] have been developed. These systems have strong oxidizing ability and include simple feed conditions such as temperature and atmospheric pressure. During the treatment, various complex chemical reactions (collision, addition, dissociation and transformation reactions) can be initiated in the polluted solution [26]. Among above mentioned types of non-thermal plasma devices, plasma needle may be easily operated under atmospheric pressure and room temperature and do not require expensive vacuum systems. Its simple configuration provides very easy to work and it can be applied to a



wide range of vessels for treatment. Plasma needle is non-aggressive oxidation method which produces chemically active species at low gas temperature, thus meets all the necessary conditions for the treatment of organic materials, living tissues (wound sterilization, cancer treatment and other biomedical applications) and delicate materials which are unable to withstand vacuum or are thermally sensitive (heat- sensitive polymers, foodstuffs).

Liquid and gas plasma chemistry have been largely studied during the last decade and it is concluded that the degradation takes place mainly because of the formation of reactive radicals. The amount of radicals and their oxidation mechanisms depend on the discharge type and properties, such as the feed gas composition and flow rate, but also on the properties of the liquid [32]. Since the efficiency of non–thermal plasma treatment is highly dependent on the characteristics of both contaminant and liquid media, it is necessary to study and develop adequate treatment scheme for every pollutant/wastewater system.

Another most explored AOP is heterogeneous photocatalysis, because it is suitable for the destruction of resistant hazardous contaminants, as it uses inexpensive operational parameters such as light and semiconductors [33, 34]. It is based on the application of semiconductors and their capability to generate electron—hole pairs under light irradiation, which participate in different redox reactions on the catalyst surface leading to mineralization of the pollutant.

Nowadays, one of the most promising treatments for wastewater remediation combines plasma treatment with metal oxide catalysts [35]. The most common catalysts reported in literature are: TiO_2 [8, 36-38], ZnO [39], Fe_2O_3 [40], NiO [41], and Al_2O_3 [42]. It is expected that combined plasma—catalyst treatment can overcome drawbacks of individual plasma treatment and photocatalysis, preventing at the same time the electron–hole recombination at metal oxide surface and enhancing the mass transport of the reactants to the solid surface [18].

In this paper, we have investigated the decolourisation of toxic RO 16 azo dye through different treatments: low power atmospheric pressure gas plasma (plasma needle configuration); heterogeneous photocatalysis using TiO₂ as catalyst; and combined plasma—catalysis application. To the best of our knowledge, the joint application of plasma needle and catalyst employed for decolourisation of organic dye has not been studied yet. We have developed plasma needle setup to study the effects of flow rate, feed gas composition (Ar and Ar/O₂ mixture), and the eventual UV influence on the oxidation process. Furthermore, we attempted to enhance the efficiency of the decolourization process by combining plasma and TiO₂ photocatalyst and to evaluate the synergic effect of non—thermal plasma and TiO₂ for the decomposition of RO 16 in aqueous solution.

Experimental Section

Chemicals and Sample Preparation

RO 16 (C.I. 17,757; CAS 20262–58–2; $C_{20}H_{17}N_3O_{11}S_3Na_2$, Sigma Aldrich) was used as a model pollutant. The TiO₂nanopowders were prepared by a sol–gel method using tetrabutyltitanate (Ti (OBu)₄) as a precursor, hydrochloride acid as the catalyst, ethanol as the solvent and water for the hydrolysis. The hydrolysis and polycondensation reactions of Ti(OBu)₄ were carried out on the ice–bath. The reagent molar ratio was Ti(OBu)₄:HCl:EtO H:H₂O = 1:0.3:15:4 [43]. After the gelation, the wet gel was dried at 80 °C, and then calcinated at 500 °C for 1.5 h.

TiO₂ Characterization

Phase identification of TiO₂ sample was performed by X-ray powder diffraction (XRPD) (Ital Structures APD2000, Italy) using Cu–K α radiation ($\lambda = 1.5406 \text{ Å}$). The measurements were performed at room temperature in the 20 range from 20 to 80° in a continuous scan mode with a step width of 0.1° and the counting time of 0.5 s/step. Software MDI Jade 5.0 was used for the calculation of the structural and microstructural parameters. The powder specific surface area of the sample was calculated following the multipoint BET procedure on the Quantachrome ChemBet-3000 setup. The nitrogen adsorption-desorption isotherm was obtained at 77 K. Morphology of the synthesized nanopowders has been studied on a Tescan MIRA3 field emission gun scanning electron microscope (FE-SEM), at 20 kV in high vacuum. The infrared (IR) transmission spectrum of TiO₂ using the potassium bromide pellet was measured on a Thermo Nicolet 6700 Fourier transform infrared spectrophotometer at the room temperature.

Treatment Setups

In Fig. 1 five different treatment setups are presented: plasma treatment – PT (Fig. 1a), PT with quartz glass (Fig. 1b), heterogeneous photocatalysis–HP (Fig. 1c), plasma coupled with catalyst—PC (Fig. 1d) and PC with quartz glass (Fig. 1e).

The plasma needle setup, which we have adapted for this research (Fig. 1a), consists of a body made of Teflon and a central copper electrode inserted in the glass tube 1 mm above the sample. Its electrical properties are presented by Zaplotnik et al. [44]. Discharge is generated at the tip of a copper wire. Ar (5.0 purity) and a mixture of Ar and O_2 (Ar/ $10\%O_2$) are used as feed gases. The flow rates vary from



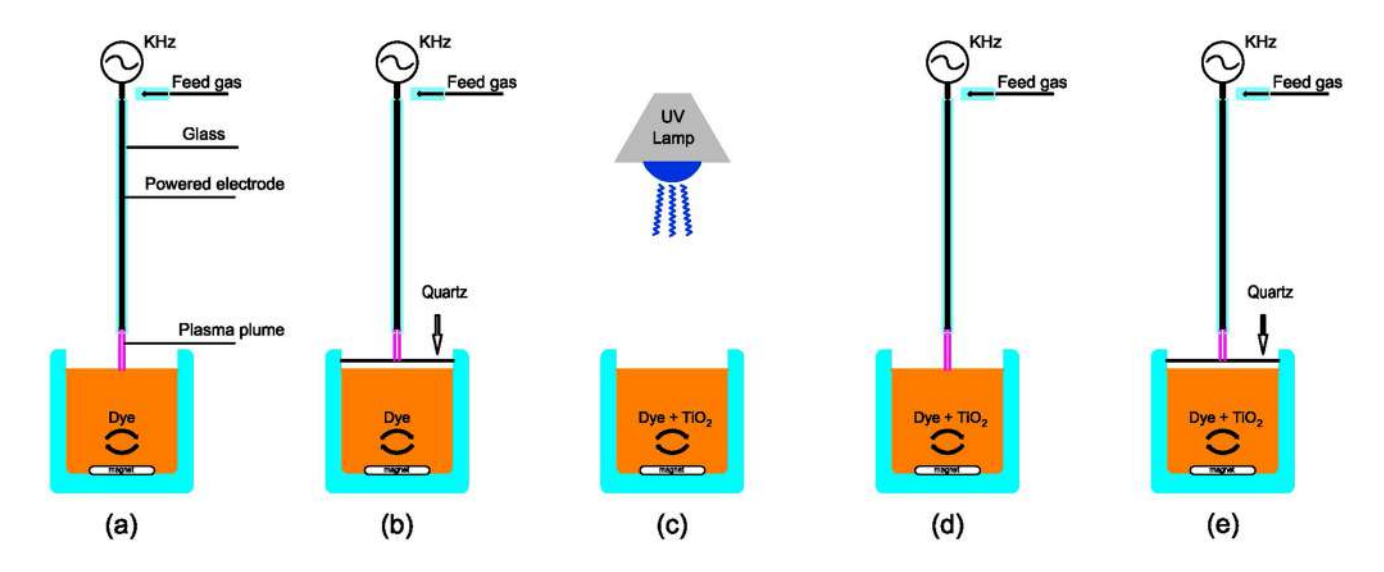


Fig. 1 Different treatment setups used in the study: a Plasma treatment (PT), b Plasma treatment (PT) with quartz glass, c semiconductor heterogeneous photocatalysis (HP), d plasma coupled with catalyst (PC), e plasma coupled with catalyst (PC) with quartz glass

1 to 4 slm. The exposure times for all treatments range from 5 to 150 min.

In the first set of experiments (PT, Fig. 1a) we have analysed the decolourisation effects of plasma needle on the RO 16 solution, by changing its flow rate and feed gas composition. UV contribution of plasma needle to decolourisation process was investigated by putting a quartz glass (190 to 2500 nm) between the sample and the plasma source (Fig. 1b). In such a way only UV contribution from plasma source to the decolourisation process can be estimated, as in this configuration reactive radicals generated in plasma are prevented to reach the sample surface and oxidize the dye.

The photocatalytic experiment (Fig. 1c) was performed as follows: TiO₂ (2 g/l as the optimal concentration for RO 16 photodegradation) [13] was added to the RO 16 solution and magnetically stirred for 30 min in the dark in order to uniformly disperse nanopowder and to achieve the adsorption–desorption equilibrium. Afterwards, a mercury lamp (300 W, UVA/UVB, Osram Vitalux) as a light source placed 40 cm above the sample was switched on in order to initiate the photocatalytic reaction.

In the third set of experiments, we have used plasma needle in the presence of TiO₂ (Fig. 1d) in order to examine whether there is a synergic oxidation outcome. The effects of plasma generated UV radiation on the TiO₂ activation was investigated by using quartz glass in order to restrict reactive radicals to participate in the dye oxidation process (Fig. 1e).

Decolourisation Measurements

The above-mentioned experiments were conducted in magnetically stirred thermostated glass vessel. The concentration of dye solution (c = 50 mg/l) and working volume

(V=25~ml) were kept fixed during all treatments. At certain time intervals, aliquots were withdrawn, centrifuged (in the case of TiO₂) and analysed on UV/VIS spectrophotometer (Varian Superscan 3, USA). RO 16 concentration was followed by measuring the variation of the intensity of main absorption band at 494 nm. This absorption band originates from $n\to\pi^*$ transition in the chromophore group (-N=N-) and its disappearance indicates that the main chromophores of the dye were destroyed. The measurements were repeated three times to check their reproducibility and the mean value was taken into consideration.

Detection of Reactive Hydroxyl Radicals

In order to detect the formation of free hydroxyl radicals, photoluminescence (PL) measurements were performed using terephthalic acid (TA), which in reaction with hydroxyl radicals induced on the photocatalysts surface produces highly fluorescent 2-hydroxyterephthalic acid. The experiment was carried out at room temperature, where 20 mL of working solution was prepared using distilled water in such a manner that the concentrations of the terephthalic acid (TA) and NaOH were 5×10^{-4} M and 2×10^{-3} M, respectively. The nanopowder TiO₂ (50 mg) was dispersed and solution was constantly stirred on a magnetic stirrer. A 300 W UV lamp, (Osram Vitalux) was used as a light source, placed 40 cm above the solution. At given time intervals (5, 10, 15, 20 and 30 min), aliquots were withdrawn, centrifuged and filtered to remove the catalyst particles. The room- temperature PL spectra at 425 nm of the supernatant were analyzed on the Fluorescence Spectrometer (Spex Fluorolog) using 320 nm as excitation light, in order to estimate the concentration of 2- hydroxyterephthalic acid.



Results and Discussion

The RO 16 decolourisation mechanism by plasma needle is dependent on the generation of plasma directly above the treated sample in the continuous gas phase simultaneously contacting molecules, clusters, aerosols, droplets, and planar surfaces of the liquid [45]. The complexity of physical and chemical phenomena, which appear during the discharges in both gas and liquid phase, is considerable. For this reason, we studied different plasma needle treatment parameters (e.g. feed gas flow rate and composition) and their influence on the RO 16 oxidation process (decolourisation). Later, we have also studied combined plasma-heterogeneous photocatalysis in order to examine the potential oxidation synergic effects of plasma and catalyst and to verify whether plasma UV radiation was adequate to activate the TiO₂ surface. The TiO₂ based heterogeneous photocatalysis on RO 16 degradation was used as a benchmark.

Effects of Plasma Treatment on the RO 16 Decolourisation

Producing concurrently large amount of active species with high reduction potential (Table 1) [46] UV radiation and shock waves, plasma decomposes organic matter with no additional procedures and no sludge production [47]. Chemically reactive radicals reach the liquid surface, diffuse into the bulk, and oxidize the hazardous component. Therefore, plasma chemistry, which occurs in these atmospheric and subsequently aqueous conditions, is highly relevant to the evolution of the reactive radicals and their influence on the target compound. Figure 2 illustrates the formation mechanisms of possible reactive species, whereas the oxidation potential of plasma reactive species are given in Table 1.

Key reactions from Fig. 2 which take place during the air discharge are described in the following sections.

Depending on the electron energies formed by electrical discharges, high–energy electrons collide with ambient molecules resulting in the several possible reactions such as excitation, dissociation, electron capture or ionization, (Eqs. 1–5):

$$e^{-*} + N_2 \rightarrow N^{\cdot} + N^{\cdot} + e^{-}$$
 (1)

$$e^{-*} + O_2 \rightarrow O' + O' + e^{-}$$
 (2)

Table 1 Oxidation potential of plasma reactive species

$OH^- + H^+ + e^- \rightarrow H_2O$	$\mathrm{E}_{\mathrm{OH/H_{2}O}}^{0}$	2.85 V
$O' + 2H^{+} + 2e^{-} \rightarrow 2H_{2}O$	E_{O/H_2O}^0	2.42 V
$O_3 + 2H^+ + 2e^- \rightarrow O_2 + H_2O$	E_{O_3/O_2}^0	2.07 V
$H_2O_2 + 2H^+ + 2e^- \rightarrow 2H_2O$	$E_{H_2O_2/H_2O}^0$	1.77 V
$O_2 + 4H^+ + 4e^- \rightarrow 2H_2O$	E_{O_2/H_2O}^0	1.23 V

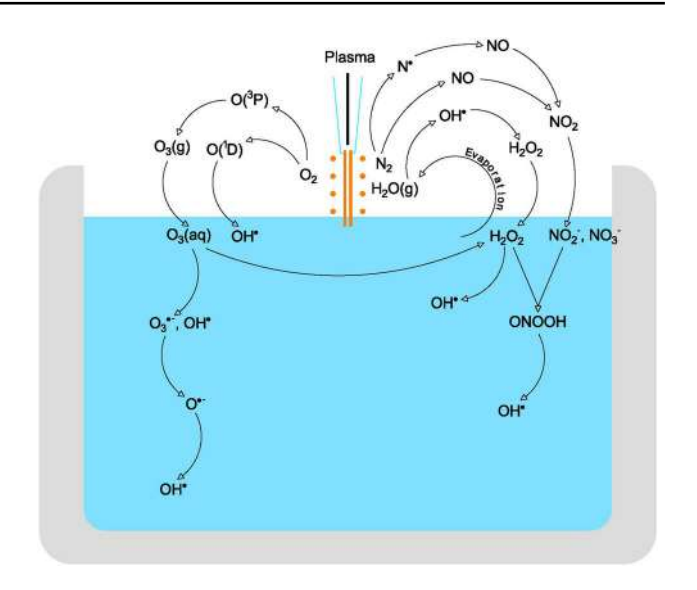


Fig. 2 Important chemical species in the gas and liquid phase induced by Ar fed plasma needle discharge

$$e^{-*} + H_2O \rightarrow O(^1D) + O' + e^{-}$$
 (3)

$$e^{-*} + H_2O \rightarrow OH^{\cdot} + H^{\cdot} + e^{-}$$
 (4)

$$e^{-*} + 2H_2O \rightarrow H_2O_2 + H_2 + e^{-}$$
 (5)

Further important reactions related to the formation of the primary long live reactive species $(O_3, H_2O_2, NO_3^-, NO_2^-)$ and their dissolution in water are described below. O generated in air plasma together with O_2 produce O_3 which reacting with water molecules forms H_2O_2 (Eqs. 6–7). Additional H_2O_2 generation mechanism is through the recombination reaction of OH radicals (Eq. 8).

$$O' + O_2 + M \rightarrow O_3 + M$$

 $\left(M - \text{third collision partner, which may be Ar, } O_2, \ N_2, \ \text{etc.}\right)$
 (6)

$$O_3 + H_2O \rightleftharpoons O_2 + H_2O_2$$
 (7)

$$OH^{\cdot} + OH^{\cdot} \rightarrow H_2O_2$$
 (8)

Nitrogen oxides (NO, NO_2) formed in air plasma through reactions between O_2 and N_2 dissolve in the solution creating nitrites and nitrates (Eqs. 9–10) and consequently forming the peroxynitrous acid through the reaction of nitrites with hydrogen peroxide (Eq. 11) [32].

$$2NO_2 + H_2O \rightarrow NO_2^- + NO_3^- + 2H^+$$
 (9)

$$NO + NO_2 + H_2O \rightarrow 2NO_2^- + 2H^+$$
 (10)



$$NO_2^- + H_2O_2 + H^+ \rightarrow O = NOOH + H_2O$$
 (11)

Occurrence of even more reactive species (OH, O, NO₂ etc.) (Eqs. 12–18) can be expected as well, but because of their short lifetime they can react directly with a pollutant only in its current encirclement where the reaction occurs [5, 48, 49]. Among them, the most influential reactive species found in electric discharges is OH. It is a very powerful oxidizing agent with a standard reduction potential of $E^0 = 2.8 \text{ V}$ [50] and lifetime ($\approx 200 \,\mu s$ in the gas phase and $10^{-9} \, s$ in an aqueous solution). Although it has very short lifetime there are additional OH formation mechanisms in the bulk as a consequence of the transformation of above-mentioned long lifetime species. Several mechanisms are responsible for the OH formation: electron impacts dissociation of H₂O (Eq. 4); ozone dissolution in water [51] (Eqs. 12–14); reactions of excited O atoms and O with water (Eqs. 15, 16); reaction of e and H₂O₂ (Eq. 17) or via reaction of peroxynitrous acid in water (Eq. 18).

$$O_3 + HO^- \rightarrow O_3^{-} + OH^-$$
 (12)

$$O_3^{-} \to O^{-} + O_2$$
 (13)

$$O^{-} + H_2O \rightleftharpoons OH^{-} + HO^{-}$$
(14)

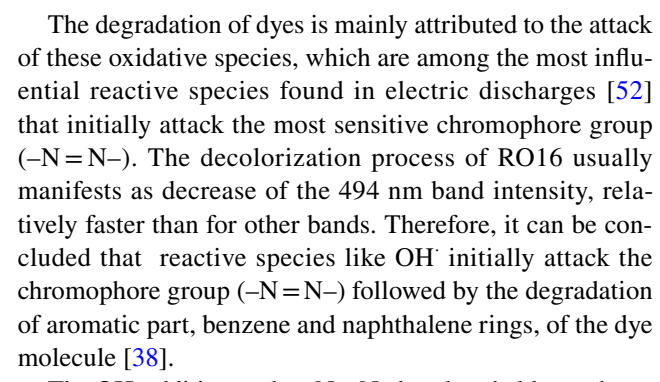
$$O(^{1}D) + H_{2}O \rightarrow 2OH$$
 (15)

$$O' + H_2O \rightarrow 2OH' \tag{16}$$

$$H_2O_2 + e^- \rightarrow OH^- + OH^-$$
 (17)

$$O = NOOH \rightleftharpoons NO_2^{\cdot} + OH^{\cdot}$$
 (18)

Fig. 3 Absorbance spectra of RO 16 for different PT times by using Ar(1slm) as feed gas



The OH addition to the -N=N- bond probably produces the hydrazyl type radical forms, -N-N(OH)- as reported in the literature [5], leading to the destruction of the colour in the visible range and finally mineralization into totally innocuous gaseous nitrogen [38]. The oxidation of nitrogen containing organic molecules leading to the NO_x generation is also reported [53], but in small quantities not harmful for the environment.

Influence of Different Flow Rates and Composition of Feed Gas on the Decolourisation Rate

The absorption spectral changes of RO 16 solution at different irradiation time during PT with Ar as feed gas (1 slm), are presented in Fig. 3. The intensity of absorption peaks in the visible region (494 and 386 nm), as well as the intensity of peaks in the ultraviolet region (297 and 254 nm), rapidly decreased in the initial stage of the PT and after 90 min none of the absorption peaks were observed.

The kinetics of RO 16 decolourisation under PT process at different flow rates of Ar is given in Fig. 4. C_0 and C_t represent the initial dye concentration and the dye concentration at reaction time t. The RO 16 concentration of each treated sample was determined using a calibration curve which is

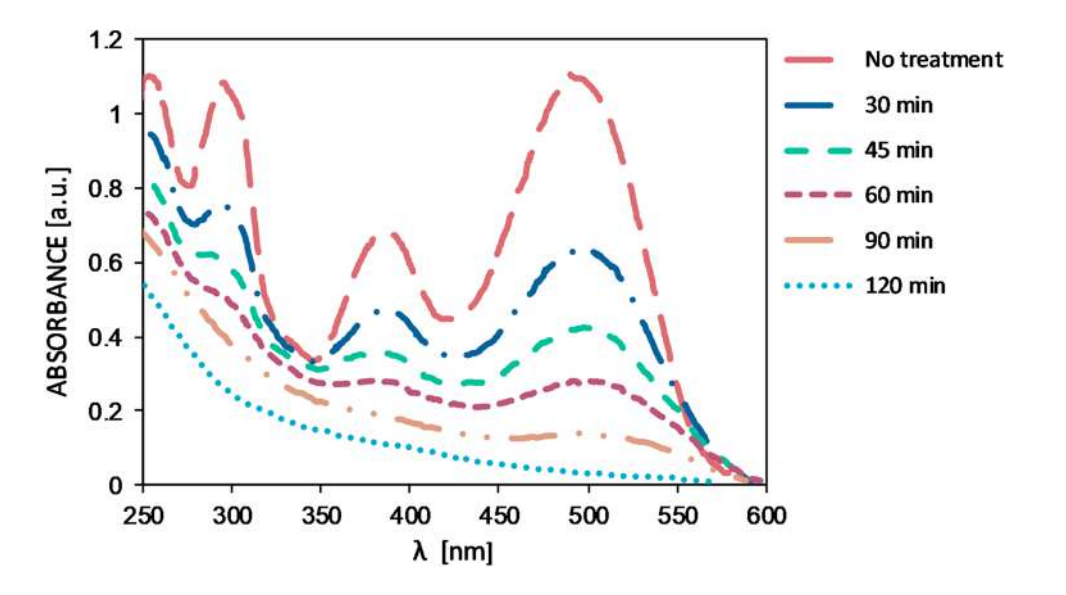
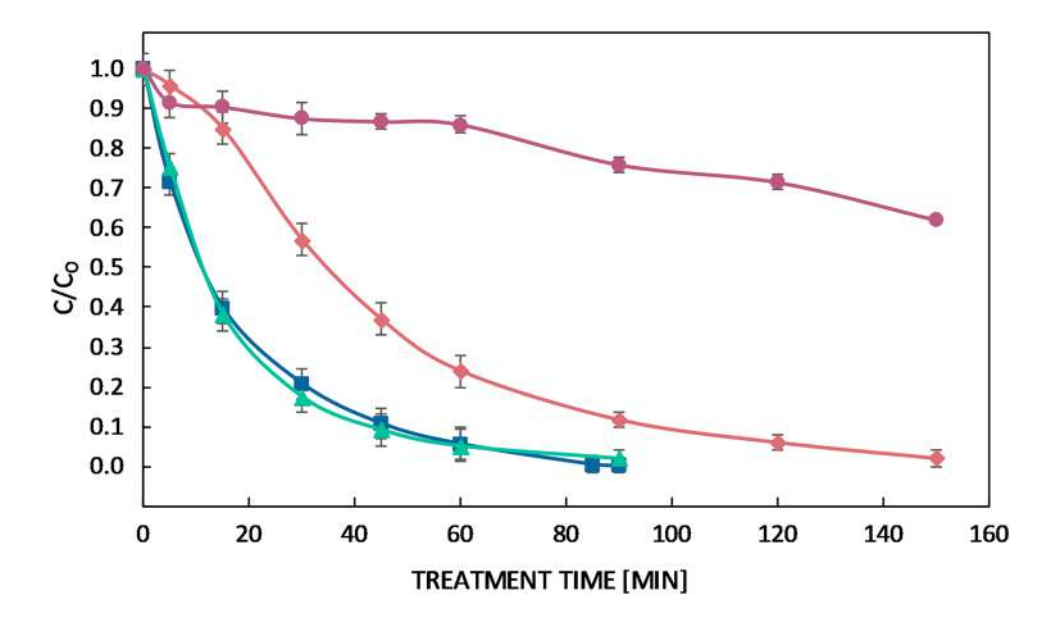




Fig. 4 Decolourisation of RO 16 (c=50 mg/L, V=25 mL) under PT treatment using Ar (1 and 4 slm); Ar/O₂ (1 slm) and Ar (4 slm+Quartz) as feed gas. Symbols: filled diamond- Ar 1 slm; filled rectangle- Ar 4 slm; filled triangle- Ar/O₂ 1 slm; filled circle – 4 slm with Quartz



previously established with prepared standards and theirs related absorbances. It can be observed that RO 16 decolourisation was faster for the increased flow rate of Ar (4 slm) and almost total decolourisation was achieved after 90 min. It is obvious that generation of radicals in plasma depends on gas flow rate. The higher is the flow rate, the faster is the decolourisation. However, the efficiency of radicals generation and plasma chemistry can be also tailored by changing the feed gas composition. For that purpose, in Fig. 4 is presented the kinetics of RO 16 decolourisation when $10\%~O_2$ was introduced into Ar flow rate of 1 slm.

The O_2 introduction into the feed gas has the similar decolourisation effect on RO 16 as increasing of Ar flow rate from 1 to 4 slm. It is evident that adding only 10% O_2 to the feed gas (Ar, 1slm) the decolourisation of RO 16 is faster, reaching almost complete decolourisation after 90 min.

The introduction of O₂ into the feed gas evidently influenced the oxidation process kinetics. The better efficiency of the RO 16 oxidation with the addition of O₂ can be a consequence of at least two reasons. The most apparent reason is that higher amount of active species, like OH, can be formed when O2 is introduced in Ar because of the lower energy of the first ionization of O₂ (12.1 eV) compared to Ar (15.8 eV). In their work, Gumuchian et al. [24] measured amount of OH in different compositions of feed gases and concluded that in Ar/O₂ feed gas mixture, the concentration of OH was the highest [24]. Beside this, atomic oxygen can react directly with organic pollutants, and together with O₂ can produce very reactive ozone (Eq. 6). Nevertheless, in the paper of Miyazaki et al. [54] it was shown that very small amount of ozone was produced if the Ar concentration in Ar/O₂ feed gas mixture is equal or higher than 80%. Since in our experiments 90% of Ar, was used, we suppose that ozone contribution in these experiments is not of great

importance. Evidently, the presence of O_2 in the feed gas significantly improves the oxidation potentials of plasma needle, presumably due to the formation of more reactive species (Eqs. 2, 15–16).

In order to investigate an isolated effect of plasma generated UV light on dye oxidation, the quartz glass was placed between plasma source and RO 16 solution to block plasma–generated species from reaching the surface, allowing only UV light to pass to the sample. Namely, for 1 slm of Ar flow rate there was no observed UV contribution, while for 4 slm Ar flow rate UV dependent decolourisation was less than 15% after 60 min of treatment. For that reason, it can be concluded that isolated UV light cannot be considered as significant contributing factor to decolourising process of the dye.

Effects of the Heterogeneous Photocatalysis on the RO 16 Removal

Among the semiconductors, titanium dioxide (TiO₂) is by far the most frequently studied photocatalyst, highly abundant in nature, photochemically very stable under ambient conditions and environmentally friendly. Among the three TiO₂ crystal phases: anatase, rutile and brookite, the anatase is the most frequently applied photocatalyst showing excellent photocatalytic activity, although its application is restricted to the utilization of UV light due to the large band gap ($E_g \sim 3.2 \; eV$).

The photochemical decolorization of RO 16 was studied by heterogeneous photocatalysis, using anatase TiO_2 nanopowders as catalyst and UV lamp as an excitation source. TiO_2 nanopowders were synthesized by sol–gel method and the XRPD pattern of TiO_2 is presented in Fig. 5a.



The main diffraction peaks correspond to the anatase crystallite phase (PDF card 782,486) and no other phases were detected. Characteristic Miller indices are denoted for the main diffraction peaks. The average crystallite size, <D> and average lattice strain of the prepared sample were calculated using Williamson–Hall Method and are presented in Table 2 together with cell parameters [55].

To determine the surface area of synthesized nanopowder the nitrogen adsorption—desorption isotherm at 77 K has been measured and shown in Fig. 5b. Prior to adsorption, the sample was outgassed for 1 h under vacuum at room temperature, and additionally for 16 h at 110 °C at the same residual pressure. The specific surface areas ($S_{\rm BET}$) of sample is calculated from the linear part of the adsorption isotherm by applying the Brunauer-Emmet-Teller (BET) equation [56]. The curves may be interpreted as type IV [57], typical for mesoporous materials, with an H2-type hysteresis loop,

Table 2 The unit cell parameters, average crystallite size < D> and micro strain values of TiO_2

Sample name	Unit cell parameters $a, c (\mathring{\mathbf{A}})$	Williamson-Hall method			
		< D > (nm)	Microstrain (%)		
TiO ₂	a=3.784(3) c=9.53(0)	24	0.301		

indicating the presence of pore networks. The reported value of the BET specific surface area (S_{RET}) is 52 m² g⁻¹.

 ${
m TiO_2}$ nanoparticles produced by sol-gel method are not porous itself, so the porous structure originates from interparticle voids. From the FE-SEM images given in the Fig. 5c, d, it is clear that we are dealing with spherical and agglomerated nonporous nanoparticles, where the particle size ranges from 30 to 100 nm.

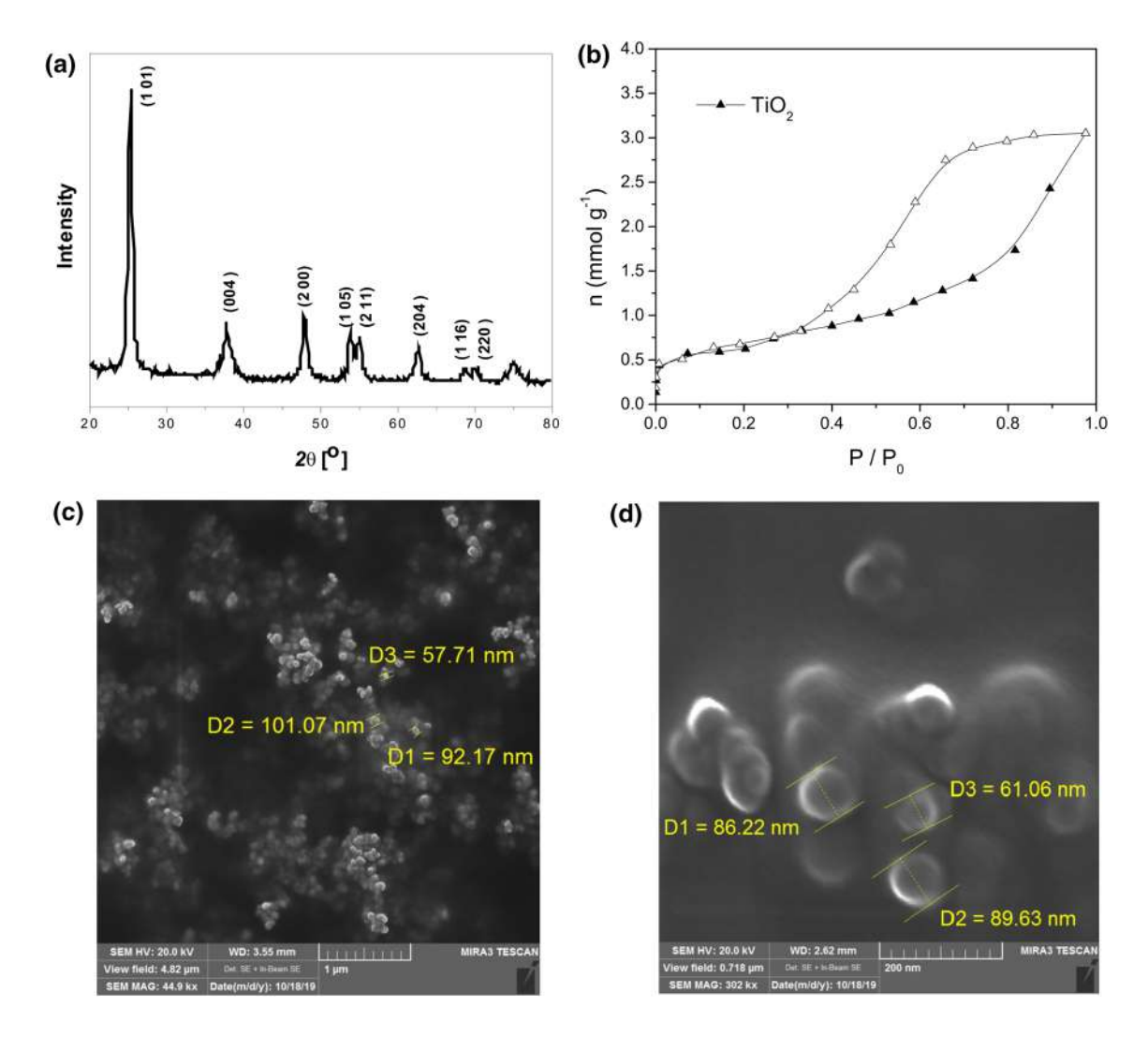


Fig. 5 XRPD pattern of TiO_2 nanopowder obtained by the sol-gel method (a); The nitrogen adsorption-desorption isotherm of synthesized TiO_2 nanopowder at 77 K (b); FE-SEM images of TiO_2 sample (c), (d)



When the RO 16–TiO₂ solution is illuminated with UV irradiation, main processes, which take place on the nanoparticles surface are illustrated in Fig. 6.

When TiO_2 solution is illuminated with light having energy greater than the band gap of the semiconductor, photogenerated electron (e_{cb}^-) –hole (h_{vb}^+) pairs are formed (Eq. 19). These pairs can be recombined within the bulk of the material or at the particle surface. Furthermore, the (e_{cb}^-) and (h_{vb}^+) can migrate to the semiconductor surface [38, 58] and react with adsorbed reactants leading to increased photocatalytic efficiency. The photodegradation mechanism can be summarized as follows:

$$TiO_2 + h\nu \xrightarrow{\text{energy}} e_{cb}^- + h_{vb}^+$$
 (19)

$$e_{cb}^- + h_{vb}^+ \rightarrow \text{thermal energy}$$
 (20)

$$h_{vb}^+ + dye \rightarrow oxidation of organic molecule$$
 (21)

$$h_{vh}^{+} + H_2O \rightarrow H^{+} + OH^{-}$$
 (22)

$$h_{vh}^{+} + OH^{-} \rightarrow OH^{-}$$
 (23)

$$e_{ch}^- + O_2 \rightarrow O_2^{--}$$
 (24)

The direct oxidation of organic substances is possible since the holes (h_{vb}^+) have high oxidative potential (Eq. 21), or they can also react with H_2O (Eq. 22) and OH^- (Eq. 23) producing very active and unselective OH radicals [14, 38, 58]. On the other hand, photogenerated electrons can react with O_2 molecules dissolved in water forming superoxide

radical anion (O_2^-) (Eq. 24) leading to the production of other very reactive species as follows:

$$O_2^{-} + H^+ \rightarrow HO_2^{-}$$
 (25)

$$O_2^{-} + HO_2^{-} + H^+ \rightarrow H_2O_2 + O_2$$
 (26)

Figure 7 shows the decolourisation rate of RO 16 for TiO_2 nanopowder activated by UV lamp. As can be seen from Fig. 7, photodegradation of the dye reached about 90% after 90 min of treatment, similar to the decolourisation effects of plasma needle for Ar 1 slm (Fig. 4). No detectable degradation of RO 16 was registered without the presence of TiO_2 sample (triangles on Fig. 7).

The presence of H₂O and O₂ molecules is crucial for generation of very reactive radicals. In the presence of H₂O and O₂ molecules, highly reactive radicals such as OH', O2' and HO2', generated through processes of photodegradation, substantially contribute to the degradation of organic molecules/pollutants. However, the most important contribution and benefits among these processes arise from reactions accompanying generation of hydroxyl radicals. These radicals are considered as very strong and nonselective oxidizing species [59, 60]. The presence of functional groups at the surface of TiO2 affects the formation of hydroxyl radicals. Infrared spectroscopy is used to analyse the surface of TiO₂. The IR spectrum of TiO₂ nanopowder is presented in Fig. 8a in the range from 500 to 4000 cm⁻¹. The main bands of O-H groups and H₂O are denoted with arrows. Namely, a wide band around ~ 3400 cm⁻¹, corresponds to stretching vibration of the O-H bond involved in hydrogen bonding O-H···O, whereas the band around ~ 1600 cm⁻¹ can be ascribed to the bending mode of the water molecules H-O-H.

Fig. 6 Formation of e^-/h^+ pars in TiO_2 nanoparticles and catalytic processes on TiO_2 surface

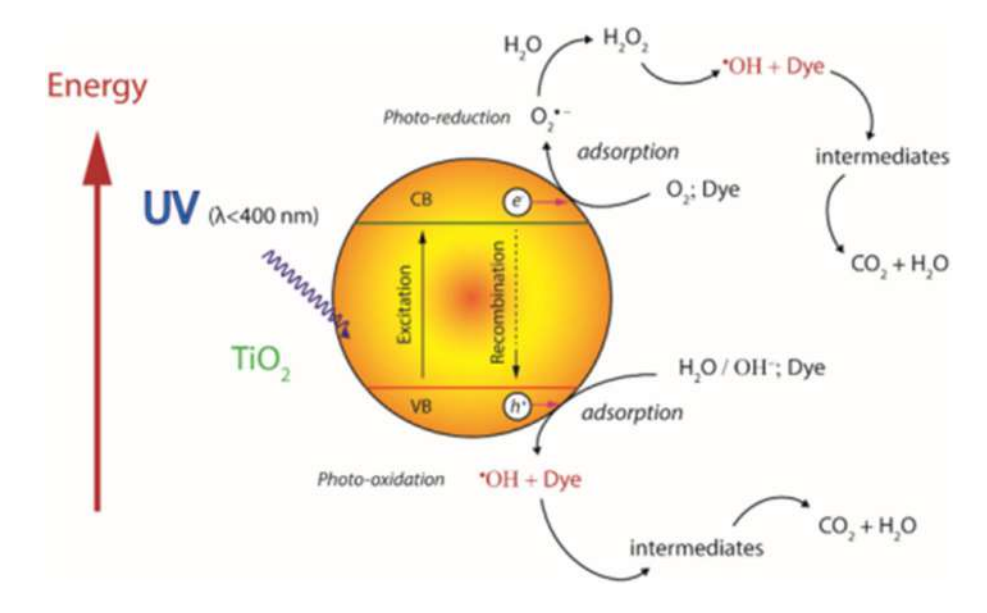
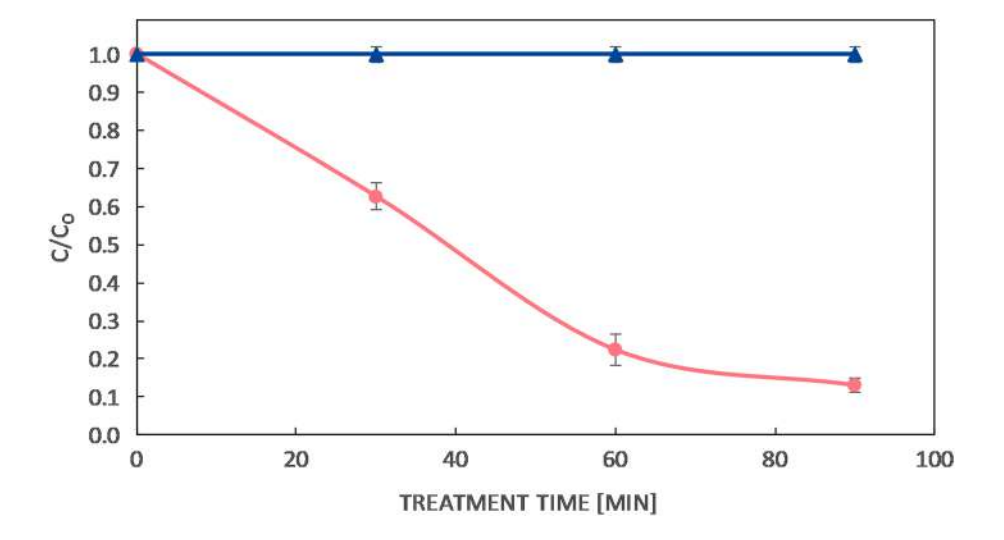




Fig. 7 Decolourisation efficiency of RO 16 (c=50 mg/l, V=25 ml) by using TiO_2 (c=2 g/l) under UV irradiation. Symbols: filled circle- RO $16+UV+TiO_2$; filled triangle RO 16+UV



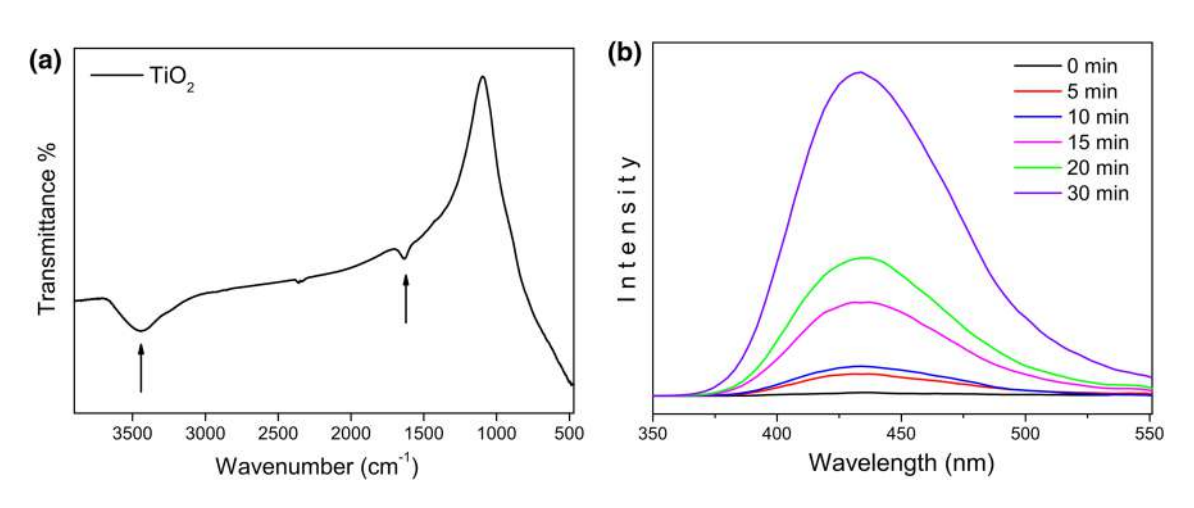


Fig. 8 IR spectrum of TiO₂ nanopowder (a), PL spectral changes of a TA-OH solution generated by TiO₂ under UV light irradiation (b)

The IR spectrum confirmed existence of O–H groups and water molecules (H_2O), on the surface of TiO_2 nanopowder (Fig. 8a), implying that generation of OH radicals in high concentration is likely to occur.

Since the hydroxyl radicals are considered the primary oxidizing species their presence on the surface of the UV illuminated photocatalyst can be confirmed in reaction with terephthalic acid (TA) as a probe molecule. This acid reacts with OH radicals, generated at the water/TiO₂ interface, forming a highly fluorescent product: 2-hydroxy-terephthalic acid (TA-OH), with intensive peak at about 425 nm [61]. Since PL peak intensity is proportional to the amount of generated OH radicals, by monitoring the changes in the intensity of 425 nm peak the hydroxyl radicals could be detected indirectly. From the Fig. 8b, it can be observed that the intensity of 425 nm peak increases in time, meaning that the concentration of hydroxyl radicals also increases [61, 62]. The spectrum labelled as "0 min" represents the pure TA solution recorded prior the UV

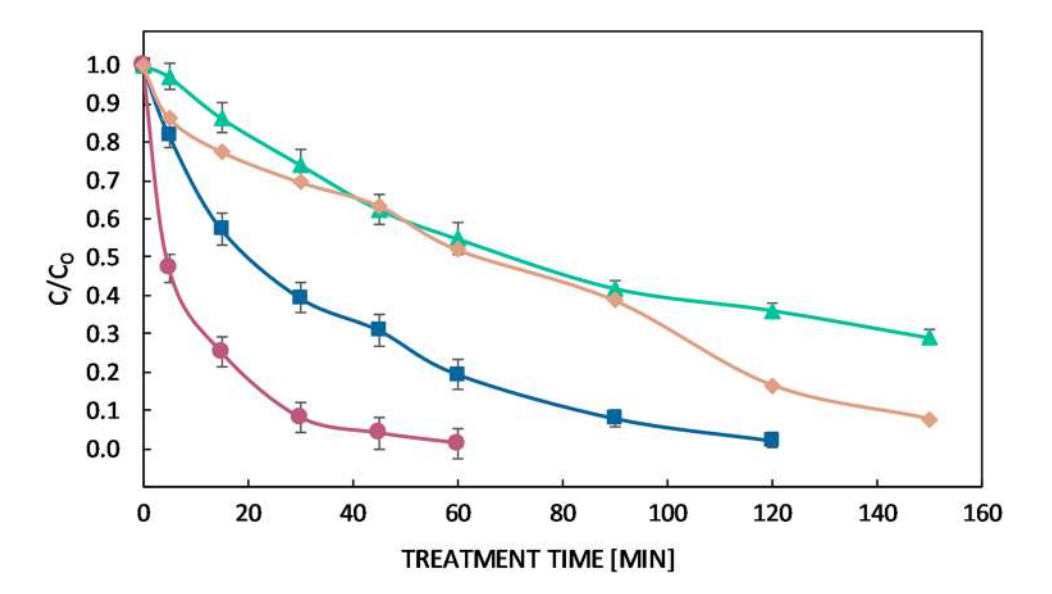
irradiation source. These results clearly demonstrated that with increasing illumination time the increasing amount of OH radicals are formed at TiO₂/water interface, responsible for dye degradation.

Effects of the Plasma–Tio₂ Catalyst Treatment on the RO 16 Removal

Figure 9 illustrates the degradation kinetics of RO 16 during the combined TiO₂ and non-thermal plasma treatment—PC treatment. As can be seen from Fig. 9, PC treatment is more efficient than PT (Fig. 4) for the same Ar flow rate of 1 slm. Namely, after 15 min more than 40% of dye was degraded under the PC treatment, whereas under PT the photodegradation of dye reached only15%. It is also evident that the time for complete decolourisation reduced from 150 to 120 min. Similar effect was observed with increased feed gas flow rate (4 slm) when the time for complete RO 16 decolourisation was shortened from 90 min (PT) to 60 min (PC). Improved



Fig. 9 Decolourisation of RO 16 (c=50 mg/L, V=25 mL) under PC treatment by using TiO₂ (c=2 g/L) and Ar (1, 4 slm) as feed gas. Symbols: filled diamond- Ar 4 slm+Quartz+TiO₂; filled rectangle- Ar 1 slm+TiO₂; filled triangle- Ar 1 slm+Quartz+TiO₂; filled circle -Ar 4 slm+TiO₂



decolourization of RO 16 can be ascribed to the synergic effect of plasma–photocatalysis process.

In order to investigate an isolated effect of plasma generated UV light on dye degradation during the PC treatment, we placed a quartz glass between plasma source and ${\rm TiO_2}$ –dye solution, allowing only UV light to pass to the solution. From Fig. 9 it is evident that the dye degradation process was much slower compared to the PC experiment without quartz glass. Hence, it is clear that UV emission from the plasma needle activates ${\rm TiO_2}$ leading to enhanced synergic effects for pollutant removal.

The oxygen addition (10%) to the feed gas (1 slm of Ar) further improved the PC decolourisation process, i.e. the synergic effect between plasma and photocatalyst was more pronounced, as the total decolourisation was achieved after 60 min (Fig. 10).

The experimental kinetic data for all presented treatments followed pseudo first—order kinetics and were fitted by pseudofirst—order reaction, $ln(C/C_o) = kt$ where k is pseudo—first order constant rate, t the treatment time. The constant rates and correlation coefficient (\mathbb{R}^2) for different treatment setups (PT, heterogenous photocatalysis and PC) are presented in Table 3.

In the case of PT treatment, with increasing Ar flow rate from 1 to 4 slm, the constant rate k increases from 24.5 to 51.8×10^{-3} min⁻¹. The k values for Ar 4 slm ($k = 51.8 \times 10^{-3}$ min⁻¹) and mixture of Ar/O₂ 1 slm ($k = 47.4 \times 10^{-3}$ min⁻¹) are comparable implying similar final oxidation effect. PT treatment with Ar 1 slm ($k = 24.5 \times 10^{-3}$ min⁻¹) manifest almost the same oxidation degree as heterogeneous photocatalysis ($k = 22.8 \times 10^{-3}$ min⁻¹). This is very important knowing that

Fig. 10 Decolourisation of RO 16 (c=50 mg/L, V=25 mL) under the PC treatment using $TiO_2 (c=2 \text{ g/L})$ and Ar (1slm) and Ar/O₂ (1slm) as feed gas. Symbols: filled diamond- Ar/O₂ $1 \text{ slm} + TiO_2$; filled rectangle- Ar $1 \text{ slm} + TiO_2$

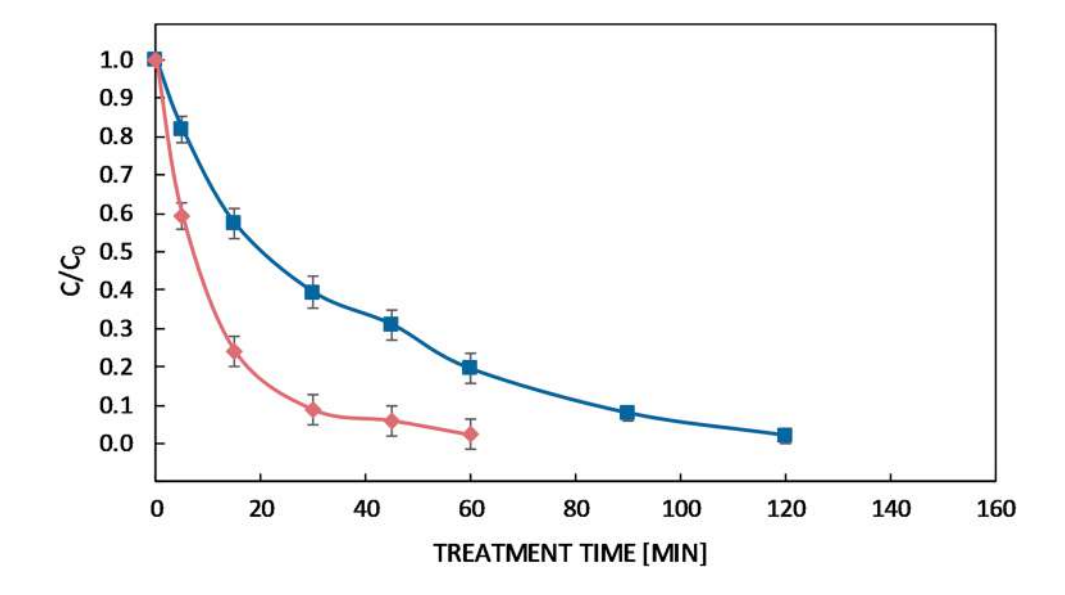




Table 3 Constant rates for different treatment setups

Treatment setup	S	Constant rates, $k \times 10^{-3} (min^{-1})$	R ²
PT	1 slm (Ar)	24.5	0.988
PT	4 slm (Ar)	51.8	0.993
PT	1 slm (Ar/O ₂)	47.4	0.970
HP	$TiO_2 + UV 300 W$	22.8	0.975
PC	$1 \text{ slm (Ar)} + \text{TiO}_2$	30.1	0.986
PC	$1 \operatorname{slm} (Ar/O_2) + \operatorname{Ti}O_2$	66.2	0.953
PC	$4 \text{ slm (Ar)} + \text{TiO}_2$	73.1	0.971
PC with quartz	$1 \text{ slm } (Ar) + TiO_2 + Quartz$	8.9	0.986
PC with quartz	$4 \text{ slm } (Ar) + TiO_2 + Quartz$	15.5	0.943

plasma needle needs smaller power consumption for ${\rm TiO_2}$ activation than UV lamp.

In the case of PT treatment with quartz glass, the UV radiation emitted from the 1 slm plasma needle was not enough to decolourise RO 16 dye by itself. For increased Ar flow rate (4 slm) low value of constant rate ($k = 3.1 \times 10^{-3} \, \mathrm{min}^{-1}$) confirmed that UV light cannot be considered as significant factor during the process of decolourisation.

As expected, the best removal efficiency was obtained with combined plasma/TiO₂ process (PC). Namely, among all experiments with different setups (HP, PT and PC), the PC rate constants are the highest (see Table 3).

This is particularly evidenced for increased Ar flow rate (4 slm) when the rate constant is almost 50% higher for PC than for PT treatment ($k = 73.1 \times 10^{-3} \, \text{min}^{-1} \, \text{vs.}$ $k = 51.8 \times 10^{-3} \, \text{min}^{-1}$). Therefore, it can be concluded that the synergic effect of two AOPs is evident and very dependent on the flow rate of feed gas and gas mixture. PC experiment with quartz glass demonstrated that UV radiation from the plasma needle source evidently has influence on the TiO₂ photolytic activity and contribute to the RO 16 decolourisation process. Further investigations will be directed to the estimation of the optimal TiO₂ concentration, identification of RO 16 oxidation by–products and determination of their levels of toxicity.

Conclusions

In this paper, we investigated the RO 16 decolourisation process by using two advanced oxidation processes (plasma discharge process and heterogenous photocatalysis), as well as combined plasma/TiO₂ process. For that purpose, we have developed a low power atmospheric pressure plasma source (plasma needle). The anatase TiO₂ nanopowders, used in experiments, were synthetized by sol–gel method. In the case of only plasma treatment, it was demonstrated that both flow rate and feed gas composition had significant effect on

dye removal. The presence of $\rm O_2$ in the feed gas, as well as, increased feed gas flow rate significantly improved the process of RO16 decolourisation as compared with the $\rm TiO_2$ based heterogenous photocatalysis.

The RO 16 degradation efficiency significantly improved when plasma was combined with TiO₂ photocatalyst. Such an improvement can be attributed to synergic effects of radicals generated by the plasma in the gas phase and delivered to the liquid and radicals generated directly in the liquid on the surface of TiO₂. The synergic effect of two AOPs was more pronounced at higher flow rate of the plasma feeding gas. Accordingly, we can conclude that simultaneous application of different AOPs can offer better solution for wastewater treatment and improves energy utilization efficiency when using plasma needle as UV source.

Acknowledgements Authors acknowledge the support of the Ministry of Education, Science, and Technological Development of the Republic of Serbia, Project Numbers: III43007, OI171032 and Bilateral Project No.39 Serbia/Slovenia (2018–2019). This work is a part of PhD thesis of T.M. under the supervision of S.L.

Compliance with Ethical Standards

Conflict of interest The authors declare that they have no conflict of interest.

References

- Bizani, E., Fytianos, K., Poulios, I., Tsiridis, V.: Photocatalytic decolorization and degradation of dye solutions and wastewaters in the presence of titanium dioxide. J. Hazard. Mater. 136, 85–94 (2006)
- de Lima, R.O.A., Bazo, A.P., Salvadori, D.M.F., Rech, C.M., de Palma, O.D., de Aragão, U.G.: Mutagenic and carcinogenic potential of a textile azo dye processing plant effluent that impacts a drinking water source. Mutat. Res. Genet. Toxicol. Environ. Mutagen. 626(1-2), 53-60 (2007)
- Gao, J., Zhang, Q., Su, K., Chen, R., Peng, Y.: Biosorption of Acid Yellow 17 from aqueous solution by non-living aerobic granular sludge. J. Hazard. Mater. 174, 215–225 (2010)
- Dutta, S., Saha, R., Kalita, H.: Rapid reductive degradation of azo and anthraquinone dyes by nanoscale zero-valent iron. Environ. Technol. Innov. 5, 176–187 (2016)
- Dojčinović, B.P., Roglić, G.M., Obradović, B.M., Kuraica, M.M., Kostić, M.M., Nešić, J., Manojlović, D.D.: Decolorization of reactive textile dyes using water falling film dielectric barrier discharge. J. Hazard. Mater. 192, 763–771 (2011)
- Chandanshive, V.V., Kadam, S.K., Khandare, R.V., Kurade, M.B., Jeon, B.H., Jadhav, J.P., Govindwar, S.P.: In situ phytoremediation of dyes from textile wastewater using garden ornamental plants, effect on soil quality and plant growth. Chemosphere 210, 968–976 (2018)
- Pandey, A., Singh, P., Iyengar, L.: Bacterial decolorization and degradation of azo dyes. Int. Biodeterior. Biodegrad. 59, 73–84 (2007)
- 8. Ghezzar, M.R., Abdelmalek, F., Belhadj, M., Benderdouche, N., Addou, A.: Enhancement of the bleaching and degradation of



- textile wastewaters by Gliding arc discharge plasma in the presence of TiO2 catalyst. J. Hazard. Mater. **164**(2–3), 1266–1274 (2009)
- Tichonovas, M., Krugly, E., Racys, V., Hippler, R., Kauneliene, V., Stasiulaitiene, I., Martuzevicius, D.: Degradation of various textile dyes as wastewater pollutants under dielectric barrier discharge plasma treatment. Chem. Eng. J. 229, 9–19 (2013)
- Tijani, J.O., Fatoba, O.O., Madzivire, G., Petrik, L.F.: A review of combined advanced oxidation technologies for the removal of organic pollutants from water. Water Air Soil Pollut. 225(9), 2102 (2014)
- Foster, J.E.: Plasma-based water purification: challenges and prospects for the future. Phys. Plasmas 24(5), 055501 (2017)
- Wang, T., Qu, G., Ren, J., Sun, Q., Liang, D., Hu, S.: Organic acids enhanced decoloration of azo dye in gas phase surface discharge plasma system. J. Hazard. Mater. 302, 65–71 (2016)
- Mijin, D., Radulovic, M., Zlatic, D., Jovancic, P.: Photocatalytic degradation of textile dye RO 16 in TiO₂ water suspension by simulated solar light. Chem. Ind. Chem. Eng. Q. 13, 179–185 (2007)
- Mijin, D., Zlatic, D., Uscumlic, G., Jovancic, P.: Solvent effects on photodegradation of CI reactive orange 16 by simulated solar light. Hem. Ind. 62, 275–281 (2008)
- Khan, M.A.N., Siddique, M., Wahid, F., Khan, R.: Removal of reactive blue 19 dye by sono, photo and sonophotocatalytic oxidation using visible light. Ultrason. Sonochem. 26, 370–377 (2015)
- Basturk, E., Karatas, M.: Advanced oxidation of Reactive Blue 181 solution: a comparison between Fenton and Sono-Fenton process. Ultrason. Sonochem. 21, 1881–1885 (2014)
- Becelic-Tomin, M., Dalmacija, M., Dalmacija, B., Rajic, L., Tomasevic, D.: Degradation of industrial azo dye in aqueous solution by heterogeneous Fenton process (fly ash/H₂O₂). Hem. Ind. 66, 487–496 (2012)
- Jiang, B., Zheng, J., Qiu, S., Wu, M., Zhang, Q., Yan, Z., Xue, Q.: Review on electrical discharge plasma technology for wastewater remediation. Chem. Eng. J. 236, 348–368 (2014)
- Lukes, P., Clupek, M., Babicky, V., Janda, V., Sunka, P.: Generation of ozone by pulsed corona discharge over water surface in hybrid gas—liquid electrical discharge reactor. J. Phys. D 38, 409–416 (2005)
- Sun, Y., Liu, Y., Li, R., Xue, G., Ognier, S.: Degradation of reactive blue 19 by needle-plate non-thermal plasma in different gas atmospheres: kinetics and responsible active species study assisted by CFD calculations. Chemosphere 155, 243–249 (2016)
- McKay, K., Salter, T.L., Bowfield, A., Walsh, J.L., Gilmore, I.S., Bradley, J.W.: Comparison of three plasma sources for ambient desorption/ionization mass spectrometry. J. Am. Soc. Mass Spectrom. 25, 1528–1537 (2014)
- Dünnbier, M., Schmidt-Bleker, A., Winter, J., Wolfram, M., Hippler, R., Weltmann, K.D., Reuter, S.: Ambient air particle transport into the effluent of a cold atmospheric-pressure argon plasma jet investigated by molecular beam mass spectrometry. J. Phys. D 46(43), 435203 (2013)
- Puač, N., Maletić, D., Lazović, S., Malović, G., Dordević, A., Petrović, Z.L.: Time resolved optical emission images of an atmospheric pressure plasma jet with transparent electrodes. Appl. Phys. Lett. 101(2), 024103 (2012)
- Gumuchian, D., Cavadias, S., Duten, X., Tatoulian, M., Da Costa, P., Ognier, S.: Organic pollutants oxidation by needle/plate plasma discharge: on the influence of the gas nature. Chem. Eng. Process 82, 185–192 (2014)
- Robert, E., Darny, T., Dozias, S., Iseni, S., Pouvesle, J.M.: New insights on the propagation of pulsed atmospheric plasma streams: from single jet to multi jet arrays. Phys. Plasmas 22(12), 122007 (2015)

- Ghezzar, M.R., Saïm, N., Belhachemi, S., Abdelmalek, F., Addou, A.: New prototype for the treatment of falling film liquid effluents by gliding arc discharge part I: application to the discoloration and degradation of anthraquinonic Acid Green 25. Chem. Eng. Process. 72, 42–50 (2013)
- Kim, H.S., Wright, K.C., Hwang, I.H., Lee, D.H., Rabinovich, A., Fridman, A.A., Cho, Y.I.: Effects of H2O2 and low pH produced by gliding arc discharge on the inactivation of Escherichia coli in water. Plasma Med. 1(3–4), 295–307 (2011)
- Hijosa-Valsero, M., Molina, R., Schikora, H., Müller, M., Bayona, J.M.: Removal of priority pollutants from water by means of dielectric barrier discharge atmospheric plasma. J. Hazard. Mater. 262, 664–673 (2013)
- Pavlovich, M.J., Chang, H.-W., Sakiyama, Y., Clark, D.S., Graves, D.B.: Ozone correlates with antibacterial effects from indirect air dielectric barrier discharge treatment of water. J. Phys. D 46, 145202 (2013)
- Lukes, P., Clupek, M., Babicky, V., Sunka, P.: Ultraviolet radiation from the pulsed corona discharge in water. Plasma Sources Sci. Technol. 17, 024012 (2008)
- Lukes, P., Aoki, N., Spetlikova, E., Hosseini, S.H.R., Sakugawa, T., Akiyama, H.: Effects of pulse frequency of input power on the physical and chemical properties of pulsed streamer discharge plasmas in water. J. Phys. D 46, 125202 (2013)
- Lukes, P., Dolezalova, E., Sisrova, I., Clupek, M.: Aqueous-phase chemistry and bactericidal effects from an air discharge plasma in contact with water: evidence for the formation of peroxynitrite through a pseudo-second-order post-discharge reaction of H2O2 and HNO2. Plasma Sources Sci. Technol. 23(1), 015019 (2014)
- Garcia-Segura, S., Brillas, E.: Applied photoelectrocatalysis on the degradation of organic pollutants in wastewaters. J. Photochem. Photobiol. C 31, 1–35 (2017)
- Spasiano, D., Marotta, R., Malato, S., Fernandez-Ibañez, P., Di Somma, I.: Solar photocatalysis: materials, reactors, some commercial, and pre-industrialized applications. A comprehensive approach. Appl. Catal. B 170, 90–123 (2015)
- Whitehead, J.C.: Plasma—catalysis: the known knowns, the known unknowns and the unknown unknowns. J. Phys. D 49, 243001 (2016)
- Parvulescu, V.I., Magureanu, M., Lukes, P., Liu, J., Bruggeman, P.J., et al.: Pulsed discharge purification of water containing nondegradable hazardous substances. J. Phys. D 33, 145202 (2011)
- Wang, T.C., Lu, N., Li, J., Wu, Y.: Plasma-TiO₂ catalytic method for high-efficiency remediation of p-nitrophenol contaminated soil in pulsed discharge. Environ. Sci. Technol. 45, 9301–9307 (2011)
- Ghezzar, M.R., Abdelmalek, F., Belhadj, M., Benderdouche, N., Addou, A.: Gliding arc plasma assisted photocatalytic degradation of anthraquinonic acid green 25 in solution with TiO2. Appl. Catal. B 72(3–4), 304–313 (2007)
- Evgenidou, E., Fytianos, K., Poulios, I.: Photocatalytic oxidation of dimethoate in aqueous solutions. J. Photochem. Photobiol. A 175, 29–38 (2005)
- Chen, L., Zhang, X., Huang, L., Lei, L.: Application of in-plasma catalysis and post-plasma catalysis for methane partial oxidation to methanol over a Fe₂O₃-CuO/γ- Al₂O₃ catalyst. J. Nat. Gas Chem. 19, 628–637 (2010)
- Gallon, H.J., Tu, X., Twigg, M.V., Whitehead, J.C.: Plasmaassisted methane reduction of a NiO catalyst-low temperature activation of methane and formation of carbon nanofibres. Appl. Catal. B 106, 616–620 (2011)
- Tu, X., Gallon, H.J., Whitehead, J.C.: Plasma-assisted reduction of a NiO/Al2O3 catalyst in atmospheric pressure H₂/Ar dielectric barrier discharge. Catal. Today. 211, 120–125 (2013)
- Du, Y.L., Deng, Y., Zhang, M.S.: Variable-temperature Raman scattering study on anatase titanium dioxide nanocrystals. J. Phys. Chem. Solids. 67, 2405–2408 (2006)



- Zaplotnik R, Kregar Z, Bišćan M, Vesel A, Cvelbar U, Mozetič M, Milošević S (2014) Multiple vs. single harmonics AC-driven atmospheric plasma jet. EPL 106(2):25001.
- 45. Parvulescu, V., Magureanu, M., Lukes, P.: Plasma chemistry and catalysis in gases and liquids. Wiley, New Jersey (2012)
- Chen, Q., Li, J., Li, Y.: A review of plasma—liquid interactions for nanomaterial synthesis. J. Phys. D 48, 424005 (2015)
- 47. Malik, P.: Kinetics of decolourisation of azo dyes in wastewater by UV/H₂O₂ process. Sep. Purif. Technol. **36**, 167–175 (2004)
- Malik, M.A., Ghaffar, A., Malik, S.A.: Water purification by electrical discharges. Plasma Sources Sci. Technol. 10, 82–91 (2001)
- Liu, D.X., Liu, Z.C., Chen, C., Yang, A.J., Li, D., Rong, M.Z., Chen, H.L., Kong, M.G.: Aqueous reactive species induced by a surface air discharge: heterogeneous mass transfer and liquid chemistry pathways. Sci. Rep. 6, 23737 (2016)
- Ay, F., Kargi, F.: Advanced oxidation of amoxicillin by Fenton's reagent treatment. J. Hazard. Mater. 179, 622–627 (2010)
- Bruggeman, P., Leys, C.: Non-thermal plasmas in and in contact with liquids. J. Phys. D 42(5), 053001 (2009)
- Puač, N., Miletić, M., Mojović, M., Popović-Bijelić, A., Vuković, D., Miličić, B., Maletić, D., Lazović, S., Malović, G., Petrović, Z.L.: Sterilization of bacteria suspensions and identification of radicals deposited during plasma treatment. Open Chem. 13, 332–338 (2015)
- Garcia-Segura, S., Mostafa, E., Baltruschat, H.: Could NOx be released during mineralization of pollutants containing nitrogen by hydroxyl radical? Ascertaining the release of N-volatile species. Appl. Catal. B 207, 376–384 (2017)
- Miyazaki, Y., Satoh, K., Itoh, H.: Pulsed discharge purification of water containing nondegradable hazardous substances. Electr. Eng. Japan. 174, 1–8 (2011)

- Williamson, G.K., Hall, W.H.: X-ray line broadening from filed aluminium and wolfram. Acta Metall. 1, 22 (1953)
- Brunauer, S., Emmett, P.H., Teller, E.: Adsorption of gases in multimolecular layers. J. Am. Chem. Soc. 60(2), 309–319 (1938)
- Rouquerol, J., Avnir, D., Fairbridge, C.W., Everett, D.H., Haynes, J.H., Pernicone, N., Ramsay, J.D., Sing, K.S.W., Unger, K.K.: Recommendations for the characteruzation of porous solids. Pure Appl. Chem. 66, 1739–1758 (1994)
- 58. Ribeiro, A.R., Nunes, O.C., Pereira, M.F.R., Silva, A.M.T.: An overview on the advanced oxidation processes applied for the treatment of water pollutants defined in the recently launched Directive 2013/39/EU. Environ. Int. **75**, 33–51 (2015)
- Daneshvar N, Rasoulifard MH, Khataee AR, Hosseinzadeh F (2007) Removal of C.I. acid orange 7 from aqueous solution by UV irradiation in the presence of ZnO nanopowder. J. Hazard. Mater. 143(1–2), 95–101.
- Turchi, C.S., Ollis, D.F.: Photocatalytic degradation of organic water contaminants: mechanisms involving hydroxyl radical attack. J. Catal. 122, 178–192 (1990)
- Yu, J., Wang, W., Cheng, B., Su, B.L.: Enhancement of photocatalytic activity of mesporous TiO₂ powders by hydrothermal surface fluorination treatment. J. Phys. Chem. C. 113, 6743–6750 (2009)
- Su, T.M., Liu, Z.L., Liang, Y., Qin, Z.Z., Liu, J., Huang, Y.Q.: Preparation of PbYO composite photocatalysts for degradation of methyl orange under visible-light irradiation. Catal. Commun. 18, 93–97 (2012)

Publisher's Note Springer Nature remains neutral with regard to jurisdictional claims in published maps and institutional affiliations.

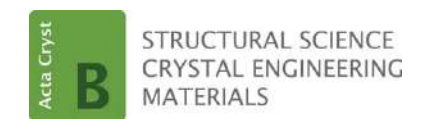
Affiliations

Tatjana Mitrović¹ · Nataša Tomić² · Aleksandra Djukić-Vuković³ · Zorana Dohčević-Mitrović⁴ · Saša Lazović²

- Saša Lazović lazovic@ipb.ac.rs
- ¹ "Jaroslav Černi" Water Institute, Jaroslava Černog 80, 11226 Belgrade, Serbia
- Institute of Physics Belgrade, University of Belgrade, Pregrevica 118, 11080 Belgrade, Serbia
- Faculty of Technology and Metallurgy, University of Belgrade, Karnegijeva 4, 11000 Belgrade, Serbia
- ⁴ Nanostructured Matter Laboratory, Institute of Physics Belgrade, University of Belgrade, Pregrevica 118, 11080 Belgrade, Serbia







issn: 2052-5206 journals.iucr.org/b

Size—strain line-broadening analysis of anatase/brookite (TiO₂)-based nanocomposites with carbon (C): XRPD and Raman spectroscopic analysis

Aleksandar Kremenović, Mirjana Grujić-Brojčin, Nataša Tomić, Vladimir Lazović, Danica Bajuk-Bogdanović, Jugoslav Krstić and Maja Šćepanović

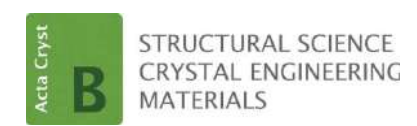
Acta Cryst. (2022). B78, 214–222



Author(s) of this article may load this reprint on their own web site or institutional repository provided that this cover page is retained. Republication of this article or its storage in electronic databases other than as specified above is not permitted without prior permission in writing from the IUCr.

For further information see https://journals.iucr.org/services/authorrights.html

research papers



ISSN 2052-5206

Received 4 August 2021 Accepted 15 February 2022

Edited by R. Černý, University of Geneva, Switzerland

Keywords: anatase; brookite; TiO₂; size-strain line broadening; XRPD; Raman spectra; phonon confinement model.

Supporting information: this article has supporting information at journals.iucr.org/b

Size—strain line-broadening analysis of anatase/ brookite (TiO₂)-based nanocomposites with carbon (C): XRPD and Raman spectroscopic analysis

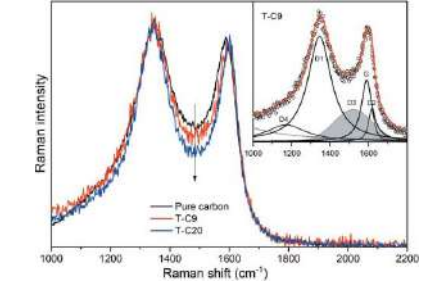
Aleksandar Kremenović, a* Mirjana Grujić-Brojčin, Nataša Tomić, Vladimir Lazović, Danica Bajuk-Bogdanović, Jugoslav Krstić and Maja Šćepanović

^aFaculty of Mining and Geology, University of Belgrade, Dušina 7, Belgrade 11000, Serbia, ^bCenter for Solid State Physics and New Materials, Institute of Physics, University of Belgrade, Pregrevica 118, Belgrade 11000, Serbia, ^cPhotonics Center, Institute of Physics, University of Belgrade, Pregrevica 118, Belgrade 11000, Serbia, ^dFaculty of Physical Chemistry, University of Belgrade, Studentski Trg 12-16, Belgrade 11000, Serbia, and ^cDepartment of Catalysis and Chemical Engineering, Institute of Chemistry, Technology and Metallurgy, University of Belgrade, Njegoševa 12, Belgrade 11000, Serbia. *Correspondence e-mail: akremenovic@rgf.bg.ac.rs

A size-strain line-broadening analysis of the XRPD patterns and Raman spectra for two anatase/brookite (TiO₂)-based nanocomposites with carbon (C) was carried out and the results compared with those of a similar sample free of carbon. The crystal structures and microstructures of anatase and brookite, as well as their relative abundance ratio, have been refined from XRPD data by the Rietveld method (the low amount of carbon is neglected). The XRPD sizestrain analysis resulted in reliable structure and microstructure results for both anatase and brookite. The experimental Raman spectra of all the samples in the region 100-200 cm⁻¹ are dominated by a strong feature primarily composed of the most intense modes of anatase (E_g) and brookite (A_{1g}) . The anatase crystallite sizes of 14-17 nm, estimated by XRPD, suggest the application of the phonon confinement model (PCM) for the analysis of the anatase E_{g} mode, whereas the relatively large brookite crystallite size (27–29 nm) does not imply the use of the PCM for the brookite A_{1g} mode. Superposition of the anatase E_g mode profile, calculated by the PCM, and the Lorentzian shape of the brookite A_{1g} mode provide an appropriate simulation of the change in the dominant Raman feature in the spectra of TiO₂-based nanocomposites with carbon. Raman spectra measured in the high-frequency range (1000–2000 cm⁻¹) provide information on carbon in the investigated nanocomposite materials. The results from field-emission scanning electron microscope (SEM), thermogravimetric analysis (TGA), Fourier transform infrared (FTIR) spectroscopy and nitrogen physisorption measurements support the XRPD and Raman results.

1. Introduction

Titanium dioxide (TiO₂) is the most commonly used photocatalyst because of its high efficiency, nontoxicity, chemical and biological stability, and low cost. Among the three natural crystalline modifications (anatase, rutile and brookite) of TiO₂, anatase and rutile are the most common and have been extensively investigated due to their excellent photoactivity. However, little has been reported for the brookite modification. Investigation of the properties and applications was limited due to the difficulty in producing pure brookite (Di Paola *et al.*, 2008, 2013; Xie *et al.*, 2009; Iliev *et al.*, 2013; Lee *et al.*, 2006; Bhave & Lee, 2007; Lee & Yang, 2006). It was also reported that hydrothermal synthesis is necessary to obtain brookite as a major phase (Bhave & Lee, 2007). The control of pH is very important, as high basicity is required for the



formation of brookite (Yanqing et al., 2000; Zheng et al., 2000; Okano et al., 2009). Also, the control of the synthesis parameters, such as the hydrothermal temperature and reaction time, is of great importance (Nguyen-Phan et al., 2011; Lin et al., 2012; Tomić et al., 2015).

Modifications of metal oxide nanoparticles with carbonaceous materials have attracted much attention over the past decade. Carbon materials, such as graphene, carbon nanotubes and carbon black, having unique structures, morphology, good conductivity and large surface area appear to be good candidates to be involved in the synthesis procedure with nanomaterials (Zhang, Lv et al., 2010; Zhong et al., 2010; Xie et al., 2010; Cong et al., 2015). This kind of composite is showing improvement in different application areas, such as water splitting for hydrogen generation and the degradation of various pollutants in wastewater, as well as air purification (Fan et al., 2011; Sun et al., 2014; Zhang, Tang et al., 2010; Xie et al., 2010). In this regard, it is beneficial to design composites that can provide higher adsorptivity, extended light absorption and good charge separation and transportation (Zhang, Lv et al., 2010). Among the mentioned materials, carbon is easily affordable due to its low cost (Cong et al., 2015).

This article is devoted to an investigation of the features and distinctions of XRPD and Raman scattering in the microstructure characterization of nanomaterials. XRPD and Raman spectroscopy results have been analysed and compared for pure TiO₂ and TiO₂ nanocomposites with carbon. The results of scanning electron microscopy (SEM), thermogravimetric analysis (TGA), Fourier transform infrared (FTIR) spectroscopy and nitrogen physisorption measurements support the XRPD and Raman results, and provide additional insight into the microstructure of the samples and their carbon content.

2. Materials synthesis

TiO₂ nanoparticles based on the brookite phase were synthesized using the sol-gel hydrothermal method. In a typical procedure, an appropriate amount of TiCl₄ (99.9% pure, Acros Organic) was dissolved in distilled water (150 ml) in an ice bath. In order to obtain the hydrogel, an aqueous solution of NaOH was added after careful control of the pH of the solution (pH \sim 9). After aging in the mother liquor for 5 h, the hydrogel was placed in a steel pressure vessel (autoclave, V =50 ml) at a controlled temperature. After treatment at 200°C for 24 h, filtration and washing (rinsing) with distilled water until complete removal of chloride ions were carried out. The last step was drying at 105.5°C for 72 h. For the purposes of preparing the composites of TiO₂ with carbon, a different amount of carbon black was added together with the hydrogel to an autoclave. As well as the pure TiO₂ sample (T-AB), samples with 9 and 20 wt% carbon black in the nanocomposite were prepared and are denoted T-C9 and T-C20, respectively. The carbon black content in these nanocomposites was estimated using thermogravimetric analysis (TGA) (see §1 of the supporting information).

3. Experimental methods

X-ray powder diffraction (XRPD) measurements were carried out on a Philips PW1710 diffractometer employing Cu $K\alpha_{1,2}$ radiation. Data were collected every 0.06° in the $10\text{--}110^{\circ}$ 2θ angular range in step scan mode using a counting time of 12.5 s per step. The instrumental resolution function was obtained by parameterizing the profiles of the diffraction pattern of an LaB₆ (NIST SRM660a) standard specimen. Details of the XRPD line-broadening analysis are presented in §S2.1 of the supporting information.

Raman scattering measurements were performed using the TriVista TR557 triple spectrometer system equipped with a nitrogen-cooled CCD detector. The samples were excited in backscattering micro-Raman configuration by a Coherent Verdi G optically pumped semiconductor laser operating at 532 ± 2 nm with a minimal output laser power of about 20 mW. The Raman scattering measurements of nanopowders pressed into pellets were performed in the air, at room temperature, using an objective lens with 50× magnification and a 0.75 numerical aperture to focus the laser to a spot size of around 2 µm. To avoid local heating of the sample surface due to laser irradiation, neutral density filters transmitting 10 or 1% of the incident light were used to additionally reduce the laser power at the entrance of the optical system of the Raman spectrometer to less than 1 mW. To reveal the local heating effects on the Raman spectra of the investigated samples with a high carbon content, the output laser power was varied from 20 to 400 mW. In order to record the spectra with relatively high resolution in a lower frequency range, a 1800/1800/2400 grooves/mm diffraction grating combination was used in the TriVista system, whereas for the measurements in a wide wavenumber range with lower resolution, a 300/300/500 grooves/mm grating combination was used. In order to analyze the experimental results, the Raman spectra are fitted by the sum of the Lorentzian profiles and the profile obtained by Phonon Confinement Method (PCM) (see §S3.1 in the supporting information).

The morphologies of the synthesized nanopowders were studied on a Tescan MIRA3 field emission gun scanning electron microscope (FESEM) at 20 kV in a high vacuum. Powdered samples were sonicated in ethanol for 10 min, then a drop of the solution was applied to 'kish' graphite (crystals of natural graphite) and the sample was degassed in a low vacuum for an hour.

The loading percentage of C in TiO_2 was checked by TGA in air by scanning the temperature from 30 to $700^{\circ}C$ at a rate of $10^{\circ}C$ min⁻¹ on an SDT 2960 TA instrument.

The IR transmission spectra of T-AB, T-C9 and T-C20 pellets before and after the introduction of carbon black were measured on a Thermo Nicolet 6700 FTIR spectrophotometer at room temperature in the range from 4000 to 400 cm⁻¹.

The textural properties of the nanocomposites were analyzed by nitrogen physisorption at -196° C using a Sorptomatic 1990 Thermo Finnigan device. Prior to adsorption, the samples were outgassed for 1 h in a vacuum at room temperature and, additionally, at 110° C and the same residual

research papers

pressure for 16 h. The specific surface areas ($S_{\rm BET}$) of the samples were calculated from the linear part of the adsorption isotherm by applying the Brunauer–Emmet–Teller (BET) equation (Brunauer *et al.*, 1938).

4. Results and discussion

Results concerning composite materials of similar composition, TiO₂:Fe, are reported in Kremenović et al. (2011, 2013). In relation to the TiO₂:C composite materials presented in this article, the amount of Fe in TiO2:Fe was significantly lower than the amount of C in TiO₂:C. Heterogeneity (phase and spatial), disorder, morphology and crystal structure were investigated for TiO2:Fe. Only phase heterogeneity and not spatial heterogeneity is shown in TiO2:C. The presence of three polymorphic modifications of TiO2 (rutile, anatase and brookite), as well as amorphous TiO2, was confirmed in TiO₂:Fe. The presence of Fe in TiO₂:Fe composites was confirmed only by SQUID magnetic measurements, but was not located in TiO₂ (rutile, anatase, brookite or amorphous) by XRPD (WPPF and PDF fit), high-resolution transmission electron microscopy (HRTEM) or Raman spectroscopy. SQUID magnetic measurements defined only the type of Fe distribution in the composite material. In the composite materials TiO₂:C, the presence of only two polymorphic modifications of TiO2 (brookite and anatase) was confirmed, as well as amorphous C, but not amorphous TiO2. The effect of Fe on the heterogeneity and disorder of TiO2:Fe composites has not been studied, but the effect of C on TiO₂:C composites has been investigated. The aim of the study of TiO₂:C composite materials presented in this article is focused primarily on comparing the results of diffraction line/vibration mode broadening analysis using XRPD and Raman spectroscopic techniques. Also, during the investigation of TiO₂:Fe composite materials, the XRPD and Raman results were analyzed routinely. The XRPD and Raman results for TiO2:C composite materials presented here have been analyzed and compared in much more detail. Such an analysis is necessary to determine the agreement/mutual support of the XRPD and Raman results. In this way, these two methods show a common/synergistic series of effects, which the individual methods alone cannot completely resolve.

4.1. XPRD

The XRPD patterns of the investigated samples are presented in Fig. S2 (see §S2.2 of the supporting information). In all three samples, the most intense diffraction peaks in the XRPD patterns can be ascribed to the two polymorph phases of TiO₂ brookite (PDF card 29-1360) and anatase (PDF card 78-2486). For the carbon-containing samples (T-C9 and T-C20), low-intensity diffraction peaks that correspond to carbon, *i.e.* the graphite 2H pattern (PDF card 89-7213), could be hardly distinguished due to extensive peak overlap with peaks from the brookite and anatase patterns. However, the 101 reflection at \sim 44.5° 2 θ that corresponds to the graphite 2H pattern could be recognized if the y axis is represented as a

Table 1
Refined unit-cell, structure and microstructural parameters (average apparent crystallite size and average maximal strain), quantitative phase analysis results, *i.e.* contents of anatase and brookite, as well as reliability factors of the refinements for T-AB, T-C9 and T-C20.

Sample	T-AB	T-C9	T-C20
Brookite (space group <i>Pbca</i> , No. 61)			
a (°)	9.1747 (2)	9.1850 (3)	9.1837 (2)
b (°)	5.4518 (1)	5.4579 (2)	5.4568 (1)
c (°)	5.1428 (1)	5.1488 (1)	5.1472 (1)
$\alpha = \beta = \gamma$ (°)	90	90	90
$V(\mathring{A}^3)$	257.24(1)	258.11(1)	257.94(1)
⟨Ti−O⟩ (Å)	1.963 (5)	1.967 (6)	1.965 (5)
Average appar. size (nm)	29 (3)	27 (6)	29 (4)
Average max. strain ×10 ⁻⁴	11(1)	7(2)	9(1)
%	74(1)	83 (1)	77 (1)
$R_{ m B}$ (%)	1.95	2.71	2.27
Anatase (space group I4 ₁ /amd, No. 141)		
a (°)	3.7898 (2)	3.7939 (3)	3.7930(2)
c (°)	9.4954 (6)	9.508(1)	9.5089 (7)
$\alpha = \beta = \gamma$ (°)	90	90	90
$V(\mathring{A}^3)$	136.38 (1)	136.86 (2)	136.81 (1)
$\langle Ti - O \rangle$ (Å)	1.955 (2)	1.962 (4)	1.957 (3)
Average appar. size (nm)	17 (2)	14 (5)	15 (7)
Average max. strain ×10 ⁻⁴	27 (3)	17 (6)	11 (5)
%	26(1)	17(1)	23(1)
R _B (%)	1.79	3.10	1.74
Reliability factors of the refinements			
R_{wp} (%)	6.51	8.41	6.96
$R_{\rm p}$ (%)	4.71	6.52	5.36
$R_{\text{exp}}^{\text{F}}$ (%)	4.70	4.63	4.41
R_{exp} (%) χ^2	1.97	3.38	2.55

logarithm of diffraction intensity (insets of Fig. S2 in §S2.2 of the supporting information). The XRPD patterns indicate the microcrystalline to amorphous character of carbon black (see Fig. S3 in §S2.3 of the supporting information). The abovementioned 101 reflection that corresponds to the graphite 2H pattern indicates a slight change of the carbon black crystalline structure during synthesis.

Structure models for the Rietveld (1969) refinements are taken from Meagher & Lager (1979) for brookite and from Horn et al. (1972) for anatase. Some of the results from the Rietveld refinements are presented in Table 1 and Fig. 1. Refined values of the atomic coordinates and the corresponding interatomic distances and angles are in good agreement with the literature data. For all three samples, the refined values of the interatomic Ti—O distances for brookite and anatase are in excellent agreement with the values obtained by Meagher & Lager (1979) and Horn et al. (1972) (Table 1). The same is true for the refined unit-cell parameters when compared to the values obtained by Meagher & Lager (1979) for brookite and Horn et al. (1972) for anatase. This is clear evidence that C atoms did not enter in significant amounts into the brookite and anatase crystal structures.

The contents of the brookite phase in the samples T-AB, T-C9 and T-C20 are 74 (1), 83 (1) and 77 (1)%, respectively (values in parentheses represent estimated standard deviations). A somewhat higher brookite content in the TiO₂-based nanocomposite samples (T-C9 and T-C20) in comparison to pure TiO₂ (T-AB) indicates that the presence of carbon may

have an influence on the brookite/anatase phase ratio. The quantity of crystalline carbon could not be refined due to its low abundance (probably less than 2%) and large diffraction peak overlap.

The refined average apparent crystallite size and average maximal strain in brookite are similar for all samples, indicating that the average crystallite size radius is about 30 nm and the average maximal strain is about 1×10^{-3} (Table 1).

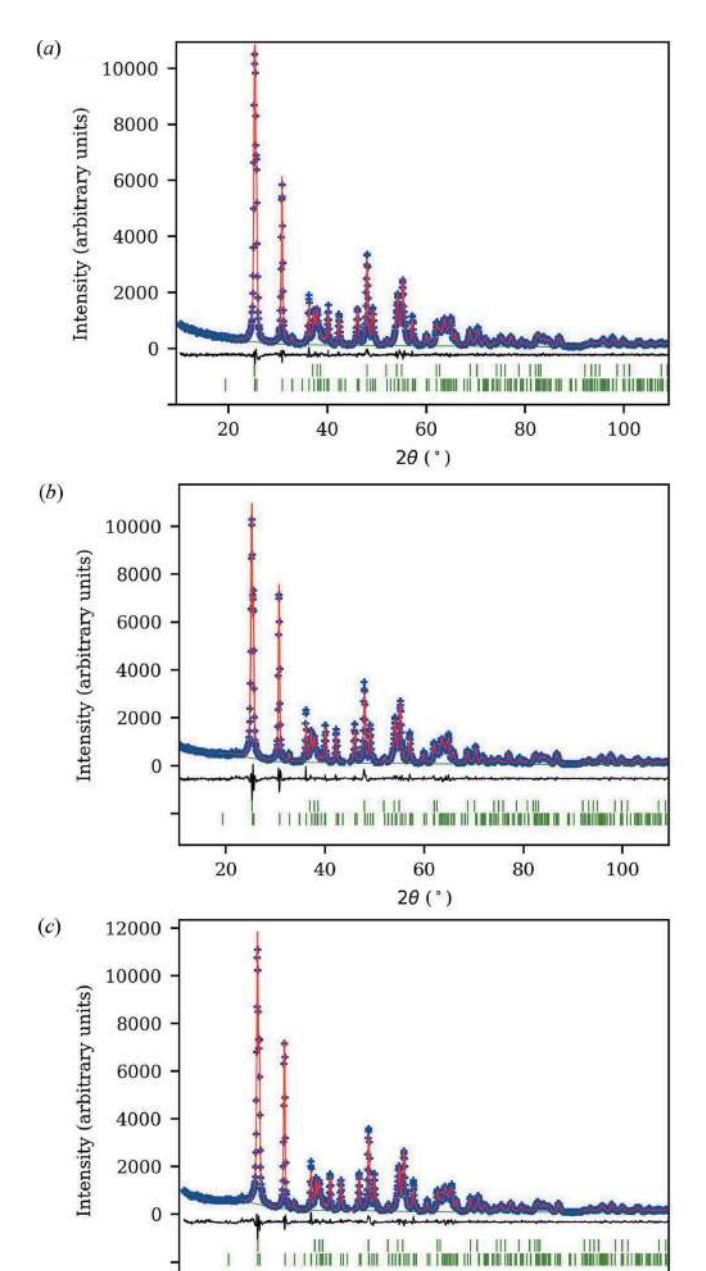


Figure 1 Final Rietveld plots for (a) T-AB, (b) T-C9 and (c) T-C20. Blue crosses denote observed step intensities and the red line represents the corresponding calculated values. The difference curve between the observed and calculated values is given at the bottom (black line). Vertical green bars represent diffraction line positions; the upper bars correspond to brookite and the lower bars to anatase.

60

2θ (°)

80

100

40

20

The refined average apparent crystallite size and average maximal strain in anatase are similar for all samples, with the exception of the strain in T-AB (27×10^{-4}), indicating that the average crystallite size radius is about 15 nm and the average strain is about 15×10^{-4} (Table 1).

4.2. Raman scattering

The Raman spectra of all the synthesized samples are dominated by the features of anatase and brookite (shown and assigned in §S3.2 of the supporting information). The spectra taken in the region from 100 to 230 cm⁻¹, usually used as a reliable titania fingerprint (Tomić *et al.*, 2015), are shown in Fig. 2. Characteristic Raman modes at ~126 $[A_{1g}(B)]$, 130 $[B_{1g}(B)]$, 143 $[E_g(A)]$, 153 $[A_{1g}(B)]$, 160 $[B_{1g}(B)]$, 172 $[B_{1g}(B)]$, 197 $[E_g(A) + A_{1g}(B)]$ and 212 cm⁻¹ $[A_{1g}(B)]$ are assigned to the anatase (A) and brookite (B) phases (Iliev *et al.*, 2013; Ohsaka *et al.*, 1978; Tomić *et al.*, 2015; Šćepanović *et al.*, 2007), as denoted in Fig. 2. Since the average crystallite sizes in anatase are estimated by XRPD to be from ~14 to ~17 nm (Table 1), it is expected that phonon confinement and other effects relevant for nanomaterials may have an impact on the most intense anatase E_g mode (Šćepanović *et al.*, 2007;

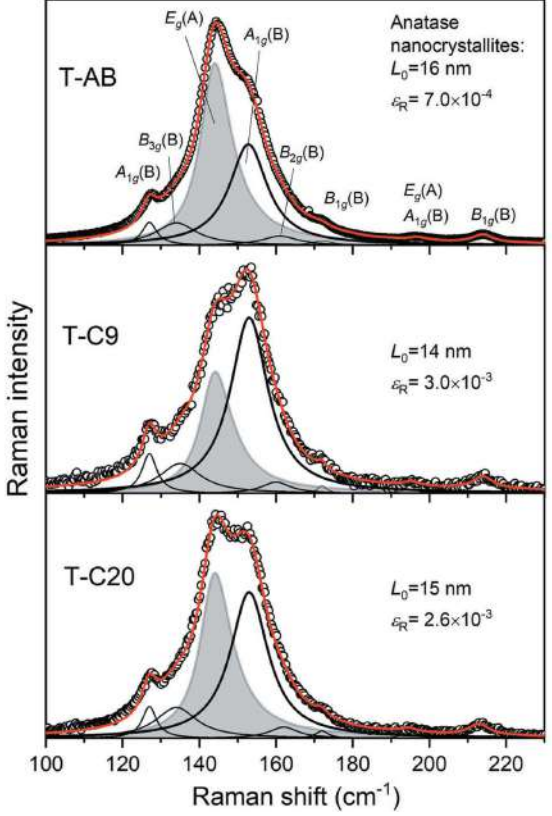
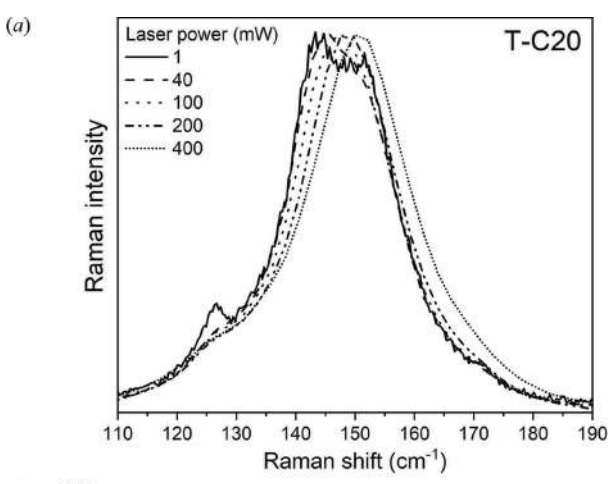


Figure 2 Experimental Raman spectra of T-AB, T-C9 and T-C20 in the titania fingerprint region (100–230 cm⁻¹), with the modes assigned, together with the corresponding calculated results, given as the sum of the most intense anatase mode, $E_g(A)$, obtained by the PCM, other anatase (A) and all brookite (B) modes fitted by the Lorentzians. The values of the reduced chi-squared (χ^2) and adjusted *R*-squared (R^2) parameters: T-AB ($\chi^2=1.98\times 10^{-5}, R^2=0.9964$), T-C9 ($\chi^2=4.55\times 10^{-4}, R^2=0.9928$) and T-C20 ($\chi^2=1.24\times 10^{-4}, R^2=0.9982$).

Kremenović *et al.*, 2013). On the other hand, for the crystallite size of brookite, estimated to be close to 29 nm (Table 1), the effect of phonon confinement (shift and broadening of the Raman mode) on the A_{1g} mode is not expected, as can be seen in previous work related to mixed-phase titania (Kremenović *et al.*, 2013; Tomić *et al.*, 2015). Therefore, all the modes shown in Fig. 2 are fitted by the Lorentzian profiles, except the most intense anatase E_g mode, which is simulated by the PCM (defined in §S3.1 of the supporting information).

The phonon confinement due to the nanosize effect causes asymmetrical broadening and a shift of the most intense anatase E_g mode to higher frequencies (blue-shift) in comparison to the corresponding bulk values. The influence of strain on the mode position is simulated in the PCM by Equations S11 and S12 (see §S3.1 in the supporting information), proposed by Gouadec & Colomban (2007) and Kibasomba *et al.* (2018). The values of the average correlation length L_0 and the so-called Raman strain (ε_R) in anatase, both obtained as fitting parameters in the numerical adjustment of the spectrum calculated by PCM to the experimental spectrum, are shown in Fig. 2. A good agreement between the



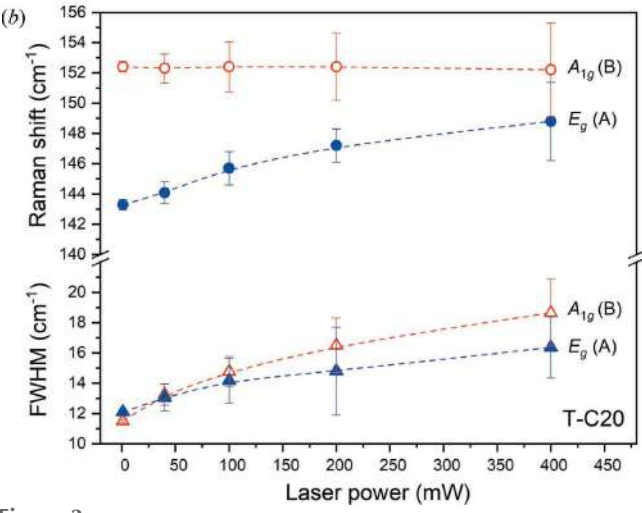


Figure 3 (a) Normalized Raman spectra of the TiO_2 -based nanocomposite with 20% C (T-C20) taken at different laser powers in the range 1–400 mW. (b) The dependence of the Raman shift and the FWHM of the most intense anatase E_g (A) and brookite A_{1g} (B) modes on laser power.

simulated and experimental E_g mode, with a similar Raman shift (\sim 144 cm⁻¹) and broadening (\sim 10–11 cm⁻¹) in all the investigated samples, could be obtained by using a parameter choice reflecting the compensation of the blue-shift due to a decrease of nanocrystallite size and the red-shift due to tensile Raman strain (see §S3.1 in the supporting information). Namely, the effects of tensile strain partially compensate for the effect of phonon confinement in such a way as to produce similar Raman positions in the spectra of all the samples in spite of their different correlation lengths.

The brookite modes are simulated by Lorentzian profile, with the position $\sim 153~{\rm cm}^{-1}$ and linewidth $\sim 12~{\rm cm}^{-1}$ of the most intense brookite A_{1g} mode similar for all the samples, which relies on the similar crystalline structure of brookite (Table 1). Therefore, the proposed fitting procedure is appropriate for an analysis of the changes in the position and shape of the dominant Raman features with C content in TiO_2 -based nanocomposites.

The strong impact of different laser powers (1–400 mW) during the Raman measurements on the spectra of TiO₂-based nanocomposites with carbon has been noticed and analyzed for sample T-C20. The Raman feature shown in Fig. 3(a) is blue-shifted and becomes more symmetric with increasing laser power. The decomposition of the spectra with a procedure similar to that described above shows that the anatase E_g mode is blue-shifted (from 144.0 to 148.8 cm⁻¹) and broadened (from 10.5 to 18 cm⁻¹) with increasing laser power, whereas the brookite A_{1g} mode is less influenced; it is slightly red-shifted (by less than 1 cm⁻¹) and less broadened (by 12 to 16.5 cm⁻¹) in comparison to the anatase E_g mode [Fig. 3(b)]. This is in accordance with literature data (Šćepanović et al., 2007, 2019; Du et al., 2006) and indicates the increase of the local temperature at the sample surface up to 277°C at maximal laser power (400 mW) (Du et al., 2006). This analysis also reveals that the Raman spectrum of the TiO₂ nanopowder

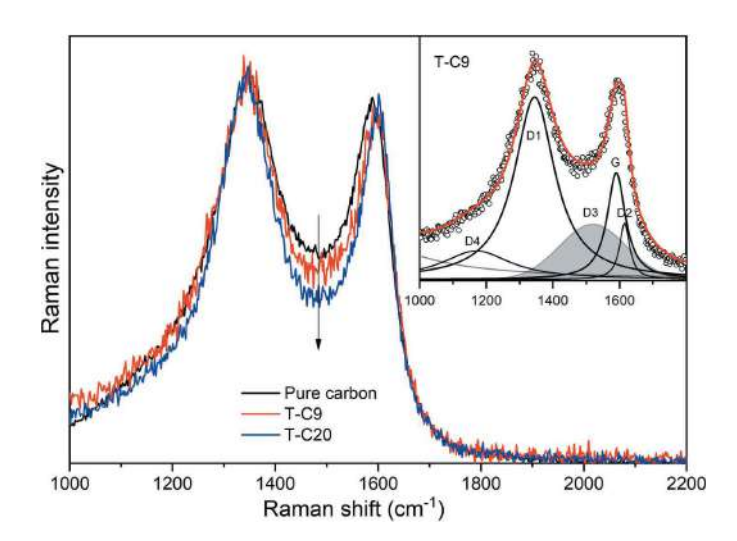


Figure 4
The Raman spectra of pure carbon and TiO₂-based nanocomposites T-C9 and T-C20, taken in the fingerprint carbon region and normalized to the G mode. Inset: the Raman spectra of nanocomposite sample T-C9, fitted by the sum of the corresponding Lorentzian and Gaussian profiles.

 Table 2

 The frequencies of the first-order Raman modes of carbon, together with relevant mode intensity ratios and the statistics of fit.

The intensities are denoted as: $vs = \text{very strong } s = \text{strong } m = \text{medium and } w = \text{weak FWHM is full width at half maximum}$	

Band	Vibrational mode (Sadezky <i>et al.</i> , 2005)	Pure C		T-C9		T-C20	
		Raman shift (cm ⁻¹)	FWHM (cm ⁻¹)	Raman shift (cm ⁻¹)	FWHM (cm ⁻¹)	Raman shift (cm ⁻¹)	FWHM (cm ⁻¹)
G	E_{2g} Graphitic structure (s)	1582	68	1590	67	1596	60
D1	A_{1g} Disordered graphitic lattice (vs)	1343	193	1345	148	1345	140
D2	E_{2g} Disordered graphitic lattice (s)	1610	39	1615	37	1615	37
D3	Amorphous carbon (Gaussian shape) (m)	1513	220	1520	200	1530	160
D4	A_{1g} Disordered graphitic lattice (w)	1177	318	1170	255	1170	300
Mode intensity ratio							
I(D1)/I(G)		2.3		3.6		3.9	
I(D3)/I(G)		1.8		1.2		0.8	
Goodness-of-fit							
Reduced χ^2 Adjusted R^2		3.40×10^{-4} 0.9958		8.82×10^{-4} 0.9906		$4.91 \times 10^{-4} \\ 0.9943$	

composed of anatase and brookite phases, in the spectral range presented in Fig. 3(a), is mostly influenced by the behaviour of the anatase E_g mode.

Besides the TiO₂ modes discussed above, in the Raman spectra of the TiO₂-based nanocomposites (T-C9 and T-C20), features related to carbon are detected. In Fig. 4, the variations of the Raman spectra of pure carbon black and TiO₂-based nanocomposite samples are shown in the carbon fingerprint range (1000–2200 cm⁻¹). It can be seen that the central part of the normalized spectrum (around 1500 cm⁻¹) decreases from the pure carbon sample to T-C20. To relate the observed variations in the spectra to variations of the carbon structure due to hydrothermal synthesis conditions, the spectra have been fitted by the sum of the Lorentzians (denoted D1, D2 and G) and Gaussian (D3), according to the methodology optimized by Sadezky *et al.* (2005) and Pawlyta *et al.* (2015). The decomposed spectrum of T-C9 is given in the inset as an example, and the results are summarized in Table 2.

The D1 band, ascribed to the disordered graphitic lattice (Sadezky et al., 2005), is located at a similar position in pure carbon and the TiO₂ nanocomposites. However, the G band, related to the graphitic structure (Sadezky et al., 2005), is shifted in T-C9 and T-C20 towards higher frequencies in comparison to pure carbon. Such a shift, together with the narrowing of the D1 and G bands (see Table 2), indicates a decrease of the amorphous carbon content in the nanocomposite samples (Ferrari et al., 2000; Pawlyta et al., 2015). Also, the narrowing and shift to higher frequencies of the D3 band, related to amorphous carbon (Merlen et al., 2017; Sadezky et al., 2005; Pawlyta et al., 2015), supports the conclusion that the content of amorphous carbon decreases when carbon is subjected to a hydrothermal procedure, which is more pronounced in the nanocomposites with a higher carbon content.

Note that bands D3 and D4 (related to the disordered graphite lattice) may also originate from hydrogenation (CH)

and oxidation (CO), respectively (Karlin *et al.*, 1997; Merlen *et al.*, 2017), but in the nanocomposite samples investigated here, we have not detected CH and CO vibrations in the relevant regions of the FTIR spectra (see §S5 in the supporting information).

The ratios of the integrated intensities of the different Raman bands in the first-order spectral region have been used to perform further analysis of carbon crystalline and amorphous phases (Sadezky *et al.*, 2005; Pawlyta *et al.*, 2015). The increase of the integrated intensity ratio $I_{\rm Dl}/I_{\rm G}$ and the decrease of $I_{\rm D3}/I_{\rm G}$ (Table 2) both point to a slightly higher content of the crystalline carbon phase and a lower amount of the amorphous carbon phase in the nanocomposites (especially in sample T-C20) than in pure carbon.

Although the refined unit-cell parameters obtained from XRPD analysis have shown that C atoms did not enter in significant amounts into the brookite and anatase crystal structures, the results of both characterization methods imply that carbon could influence the formation of brookite and anatase phases in TiO₂-based nanocomposites synthesized by the hydrothermal method. This is also supported by our wider research, where we have investigated the influence of carbon content in the range from 0.3 to 20% on the formation of titania phases by this synthesis method. The Raman results, presented in §S3.2 in the supporting information, show that the addition of a small amount of carbon suppresses the formation of brookite, so that the synthesized sample with a low carbon content is dominated by the anatase phase. An increase in the carbon content is followed by the formation of brookite in preference to the anatase phase. However, it seems that this transformation may be partially suppressed at a higher percent of carbon (as in sample T-C20), which may be a consequence of a different manner of formation of the composite with the highest carbon content (for an analysis of nitrogen physisorption, see §S7 of the supporting information). Recent research shows that the influence of carbon content on the brookite-to-anatase ratio in TiO₂-based nanomaterials depends on the carbon source, the type of synthesis and the starting TiO₂ phase (Li *et al.*, 2013; Cano-Casanova *et al.*, 2021), but this subject still needs further study.

4.3. XRPD versus Raman scattering

Both XRPD and Raman scattering analyses have shown that TiO_2 consists of a combination of anatase and brookite phases in all samples investigated in this work. This is also supported by the SEM measurements (see §S6 in the supporting information), revealing two different types of particles: spherical, ascribed to anatase, and spindle-like, characteristic for brookite (Tomić *et al.*, 2015). The spindle-like particles of brookite in sample T-AB are elongated by up to \sim 200 nm, with the shorter dimension estimated at less than 40 nm. By comparing size values for brookite obtained from XRPD (Table 1) and SEM measurements, one can conclude that on average one particle is composed from 6–7 crystallites.

It is known that the Raman modes in nanocrystalline oxide materials are very sensitive to disorder, caused by nonstoichiometry due to the nanometric crystallite size or thermal effects. In that sense, the correlation length is introduced in the PCM to define the mean size of the homogeneous regions in a material (Kosacki et al., 2002). The correlation length may be influenced by many factors, such as the level of disorder due to the presence of point defects, dislocations and voids, as well as a disturbance in the long-range order, due to doping or the creation of solid solutions, so the PCM analysis of the Raman spectra may provide important information about lattice disorder (Šćepanović et al., 2010). Having in mind that in this work the correlation lengths of the anatase phase used in the PCM simulations match the anatase crystallite size estimated by XRPD, the crystallites are suggested to have little disorder.

The analysis of the Raman spectra, performed in §4.2, has shown that the most intense brookite Raman A_{1g} mode is not significantly shifted and broadened in comparison to the bulk values (Iliev *et al.*, 2013). This fact, together with the brookite crystallite size (according to XRPD) being too big for phonon confinement effects, excludes the PCM analysis in the case of the brookite phase.

Regarding the amorphous TiO₂ phase, the Raman and XRPD analyses have given similar results. Namely, an analysis of the Raman spectra, decomposed by the combination of the PCM and Lorentzian profiles (§4.2), did not show the presence of modes which could be assigned to this phase (Kremenović *et al.*, 2013), either in pure TiO₂ or in the nanocomposites.

Besides giving insight into the nanocrystalline structures of the anatase and brookite phases in pure ${\rm TiO_2}$ and nanocomposites, XRPD and Raman scattering may also provide information on their content ratio (see §S4 in the supporting information).

The carbon content, which contributes to the very dark colour of the sample (in comparison to the white of pure TiO_2), has little influence on the XRPD measurements, but in the Raman scattering causes a significant increase in the

absorption of laser energy, which can induce local heating. This makes the nanocomposites with carbon extremely sensitive to laser power, which requires additional attention during the Raman measurements (careful choice of parameters and equipment). However, this allows an investigation of the behaviour of the Raman spectra of complex materials with local heating. The observed variation of the Raman spectra with increasing laser power (see Fig. 3) may even be used to estimate the level of heating and local temperature.

It appears that XRPD is not very useful for the investigation of carbon in the crystalline and especially amorphous state when it is present in small amounts. The intensities of the diffraction maxima depend on the number of electrons of the atoms that make up the crystal and XRPD barely detects carbon (carbon has only six electrons; we had to show the diffraction intensity on a logarithmic scale in order for the strongest carbon reflection to be visible) in samples T-C9 and T-C20. Note also that the results of XRPD analysis show that initial carbon is mostly amorphous (see §S2.3 of the supporting information). In contrast, the intensity of Raman scattering is proportional to the change in the polarizability of molecules; the atoms in carbon are tightly bound by strong covalent bonds and the Raman spectra show clearly defined carbon bands which do not overlap with the anatase and brookite modes. This allows a detailed analysis to be made of the variation of carbon structure due to hydrothermal synthesis by Raman scattering measurements (presented in Fig. 4 and Table 2). These results show that, during hydrothermal synthesis, the amorphous carbon phase is reduced in the nanocomposites in comparison to this phase in initial carbon. This is even more pronounced in sample T-C20, which may indicate that higher carbon content probably enhances the carbon crystallization during the hydrothermal process.

5. Conclusions

The compatibility, synergy and limits of XRPD and Raman scattering measurements have been established by investigating pure TiO₂ nanopowder and two TiO₂-based nanocomposites with different amounts of carbon, fabricated by the sol-gel hydrothermal method. To assure proper correlation between the XRPD and Raman results, several analytical techniques (TGA, SEM, FTIR and nitrogen physisorption) have also been used. Both XRPD and Raman scattering, together with SEM results, have shown that, in all the samples, brookite is a major phase with good crystallinity. Matching anatase crystallite sizes were determined by XRPD and PCM analysis of the anatase Raman E_g mode, confirming the low disorder of this phase. Amorphous TiO₂ has not been detected by either Raman scattering or XRPD. XRPD analysis could not detect whether significant amounts of carbon had been incorporated into the brookite and anatase crystal structures, whereas the Raman results revealed a decreasing content of amorphous carbon when subjected to the hydrothermal procedure, which is more pronounced in the nanocomposite with the higher carbon content. The brookite-to-anatase ratios estimated by the XRPD and Raman measurements imply that carbon could influence the formation of the brookite phase in preference to the anatase phase in the TiO₂-based nanocomposites synthesized by the hydrothermal method.

6. Related literature

The following references are cited in the supporting information: Barrett *et al.* (1951); Campbell & Fauchet (1986); Dubinin (1975); Gregg & Sing (1982); Grujić-Brojčdin *et al.* (2009); Hearne *et al.* (2004); Mikami *et al.* (2002); Richter *et al.*, 1981; Rodríguez-Carvajal (1993, 2001, 2016); Spanier *et al.* (2001); Stokes & Wilson (1944); Thompson *et al.* (1987); Wang *et al.* (2007).

Acknowledgements

The authors acknowledge funding provided from the Faculty of Mining and Geology, Faculty of Physical Chemistry, University of Belgrade, Institute of Physics Belgrade, Institute of Chemistry, Technology and Metallurgy, and Ministry of Education, Science and Technological Development of the Republic of Serbia. The authors appreciate advice given by Ljiljana Karanović, Professor Emeritus since 2016, and Predrag Dabić, Faculty of Mining and Geology, University of Belgrade.

Funding information

Funding for this research was provided by: Faculty of Mining and Geology, University of Belgrade, Serbia (contract No. 451-03-68/2022-14/200126).

References

- Barrett, E. P., Joyner, L. G. & Halenda, P. P. (1951). *J. Am. Chem. Soc.* **73**, 373–380.
- Bhave, R. C. & Lee, B. I. (2007). *Mater. Sci. Eng. A*, **467**, 146–149.
- Brunauer, S., Emmett, P. H. & Teller, E. (1938). *J. Am. Chem. Soc.* **60**, 309–319.
- Campbell, I. H. & Fauchet, P. M. (1986). Solid State Commun. 58, 739–741.
- Cano-Casanova, L., Amorós-Pérez, A., Ouzzine, M., Román-Martínez, M. C. & Lillo-Ródenas, M. A. (2021). J. Environ. Chem. Eng. 9, 104941.
- Cong, Y., Li, X., Dong, Z., Yuan, G., Cui, Z. & Zhang, J. (2015). Mater. Lett. 138, 200–203.
- Di Paola, A., Bellardita, M. & Palmisano, L. (2013). *Catalysts*, **3**, 36–73.
- Di Paola, A., Cufalo, G., Addamo, M., Bellardita, M., Campostrini, R., Ischia, M., Ceccato, R. & Palmisano, L. (2008). Colloids Surf. A Physicochem. Eng. Asp. 317, 366–376.
- Du, Y. L., Deng, Y. & Zhang, M. S. (2006). J. Phys. Chem. Solids, 67, 2405–2408.
- Dubinin, M. M. (1975). Prog. Surface Membrane Sci. 9, 1-70.
- Fan, W., Lai, Q., Zhang, Q. & Wang, Y. (2011). J. Phys. Chem. C, 115, 10694–10701.
- Ferrari, A. C. & Robertson, J. (2000). *Phys. Rev. B*, **61**, 14095–14107.
- Gouadec, G. & Colomban, Ph. (2007). Prog. Cryst. Growth Charact. Mater. 53, 1–56.
- Gregg, S. J. & Sing, S. J. (1982). Adsorption, Surface Area and Porosity. London: Academic Press.

- Grujić-Brojčin, M., Šćepanović, M. J., Dohčević-Mitrović, Z. D. & Popović, Z. V. (2009). *Acta Phys. Pol.* **A116**, 51–54.
- Hearne, G. R., Zhao, J., Dawe, A. M., Pischedda, V., Maaza, M., Nieuwoudt, M. K., Kibasomba, P., Nemraoui, O., Comins, J. D. & Witcomb, M. J. (2004). *Phys. Rev. B*, **70**, 134102.
- Horn, M., Schwebdtfeger, C. F. & Meagher, E. P. (1972). Z. Kristallogr. Cryst. Mater. 136, 273–281.
- Iliev, M. N., Hadjiev, V. G. & Litvinchuk, A. P. (2013). Vib. Spectrosc. 64, 148–152.
- Karlin, S. & Colomban, Ph. (1997). J. Raman Spectrosc. 28, 219-228
- Kibasomba, P. M., Dhlamini, S., Maaza, M., Liu, C.-P., Rashad, M. M., Rayan, D. A. & Mwakikunga, B. W. (2018). *Results Phys.* **9**, 628–635.
- Kosacki, I., Suzuki, T., Anderson, H. U. & Colomban, Ph. (2002). Solid State Ionics, 149, 99–105.
- Kremenović, A., Antić, B., Blanuša, J., Čomor, M., Colomban, Ph., Mazerolles, L. & Bozin, E. S. (2011). *J. Phys. Chem. C*, **115**, 4395–4403.
- Kremenovic, A., Grujic Brojcin, M., Welsch, A.-M. & Colomban, P. (2013). J. Appl. Cryst. 46, 1874–1876.
- Lee, B. I., Wang, X., Bhave, R. & Hu, M. (2006). *Mater. Lett.* **60**, 1179–1183.
- Lee, J. H. & Yang, Y. S. (2006). J. Mater. Sci. 41, 557-559.
- Li, K., Xiong, J., Chen, T., Yan, L., Dai, Y., Song, D., Lv, Y. & Zeng, Z. (2013). *J. Hazard. Mater.* **250–251**, 19–28.
- Lin, H., Li, L., Zhao, M., Huang, X., Chen, X., Li, G. & Yu, R. (2012).
 J. Am. Chem. Soc. 134, 8328–8331.
- Meagher, E. P. & Lager, G. A. (1979). Can. Mineral. 17, 77-85.
- Merlen, A., Buijnsters, J. G. & Pardanaud, C. (2017). Coatings, 7, 153
- Mikami, M., Nakamura, S., Kitao, O. & Arakawa, H. (2002). *Phys. Rev. B*, **66**, 155213.
- Nguyen-Phan, T.-D., Kim, E. J., Hahn, S. H., Kim, W.-J. & Shin, E. W. (2011). *J. Colloid Interface Sci.* **356**, 138–144.
- Ohsaka, T., Izumi, F. & Fujiki, Y. (1978). *J. Raman Spectrosc.* **7**, 321–324.
- Okano, S., Yamamuro, S. & Tanaka, T. (2009). Sci. China Ser. E-Technol. Sci. 52, 190–192.
- Pawlyta, M., Rouzaud, J.-N. & Duber, S. (2015). Carbon, 84, 479-
- Richter, H., Wang, Z. P. & Ley, L. (1981). Solid State Commun. 39, 625–629.
- Rietveld, H. M. (1969). J. Appl. Cryst. 2, 65-71.
- Rodríguez-Carvajal, J. (1993). Physica B, 192, 55-69.
- Rodríguez-Carvajal, J. (2001). *IUCr Commission on Powder Diffraction Newsletter*, **26**, 12–19.
- Rodríguez-Carvajal, J. (2016). *FullProf* computer program (https://www.ill.eu/sites/fullprof/)
- Sadezky, A., Muckenhuber, H., Grothe, H., Niessner, R. & Pöschl, U. (2005). *Carbon*, **43**, 1731–1742.
- Šćepanović, M., Grujić-Brojčin, M., Lazarević, N. & Popović, Z. V. (2019). *Phys. Status Solidi A*, **216**, 1800763.
- Šćepanović, M., Grujić-Brojčin, M., Vojisavljević, K., Bernik, S. & Srećković, T. (2010). *J. Raman Spectrosc.* **41**, 914–921.
- Šćepanović, M. J., Grujić-Brojčin, M., Dohčević-Mitrović, Z. D. & Popović, Z. V. (2007). Appl. Phys. A, 86, 365–371.
- Spanier, J. E., Robinson, R. D., Zhang, F., Chan, S.-W. & Herman, I. P. (2001). Phys. Rev. B, 64, 245407.
- Stokes, A. R. & Wilson, A. J. C. (1944). Proc. Phys. Soc. 56, 174– 181.
- Sun, H., Liu, S., Liu, S. & Wang, S. (2014). Appl. Catal. Environ. 146, 162–168.
- Thompson, P., Cox, D. E. & Hastings, J. B. (1987). *J. Appl. Cryst.* **20**, 79–83
- Tomić, N., Grujić-Brojčin, M., Finčur, N., Abramović, B., Simović, B., Krstić, J., Matović, B. & Šćepanović, M. (2015). *Mater. Chem. Phys.* 163, 518–528.

research papers

- Wang, D., Chen, B. & Zhao, J. (2007). J. Appl. Phys. 101, 113501.
 Xie, J., Lü, X., Liu, J. & Shu, H. (2009). Pure Appl. Chem. 81, 2407–2415.
- Xie, Y., Heo, S. H., Yoo, S. H., Ali, G. & Cho, S. O. (2010). *Nanoscale Res. Lett.* **5**, 603–607.
- Yanqing, Z., Erwei, S., Suxian, C., Wenjun, L. & Xingfang, H. (2000). J. Mater. Sci. Lett. 19, 1445–1448.
- Zhang, H., Lv, X., Li, Y., Wang, Y. & Li, J. (2010). ACS Nano, 4, 380–386.
- Zhang, Y., Tang, Z.-R., Fu, X. & Xu, Y.-J. (2010). ACS Nano, 4, 7303–7314.
- Zheng, Y., Shi, E., Cui, S., Li, W. & Hu, X. (2000). *J. Am. Ceram. Soc.* **83**, 2634–2636.
- Zhong, J., Chen, F. & Zhang, J. (2010). J. Phys. Chem. C, 114, 933–939.





Article

Photocatalytic Activity of the V₂O₅ Catalyst toward Selected Pharmaceuticals and Their Mixture: Influence of the Molecular Structure on the Efficiency of the Process

Sanja J. Armaković ^{1,*}, Aleksandra Jovanoski Kostić ¹, Andrijana Bilić ¹, Maria M. Savanović ¹, Nataša Tomić ², Aleksandar Kremenović ³, Maja Šćepanović ², Mirjana Grujić-Brojčin ², Jovana Ćirković ⁴ and Stevan Armaković ⁵

- University of Novi Sad, Faculty of Sciences, Department of Chemistry, Biochemistry and Environmental Protection, 21000 Novi Sad, Serbia
- ² Center for Solid State and New Materials, Institute of Physics Belgrade, 11000 Belgrade, Serbia
- ³ Laboratory of Crystallography, Faculty of Mining and Geology, University of Belgrade, Đušina 7, 11000 Belgrade, Serbia
- ⁴ Institute for Multidisciplinary Research, University of Belgrade, 11000 Belgrade, Serbia
- University of Novi Sad, Faculty of Sciences, Department of Physics, 21000 Novi Sad, Serbia
- Correspondence: sanja.armakovic@dh.uns.ac.rs; Tel.: +381-21-485-2754

Abstract: Due to the inability of conventional wastewater treatment procedures to remove organic pharmaceutical pollutants, active pharmaceutical components remain in wastewater and even reach tap water. In terms of pharmaceutical pollutants, the scientific community focuses on β -blockers due to their extensive (over)usage and moderately high solubility. In this study, the photocatalytic activity of V₂O₅ was investigated through the degradation of nadolol (NAD), pindolol (PIN), metoprolol (MET), and their mixture under ultraviolet (UV) irradiation in water. For the preparation of V₂O₅, facile hydrothermal synthesis was used. The structural, morphological, and surface properties and purity of synthesized V₂O₅ powder were investigated by scanning electron microscopy (SEM), X-ray, and Raman spectroscopy. SEM micrographs showed hexagonal-shaped platelets with welldefined morphology of materials with diameters in the range of 10-65 µm and thickness of around a few microns. X-ray diffraction identified only one crystalline phase in the sample. The Raman scattering measurements taken on the catalyst confirmed the result of XRPD. Degradation kinetics were monitored by ultra-fast liquid chromatography with diode array detection. The results showed that in individual solutions, photocatalytic degradation of MET and NAD was relatively insignificant (<10%). However, in the PIN case, the degradation was significant (64%). In the mixture, the photodegradation efficiency of MET and NAD slightly increased (15% and 13%). Conversely, it reduced the PIN to the still satisfactory value of 40%. Computational analysis based on molecular and periodic density functional theory calculations was used to complement our experimental findings. Calculations of the average local ionization energy indicate that the PIN is the most reactive of all three considered molecules in terms of removing an electron from it.

Keywords: β-blocker; nadolol; pindolol; metoprolol; photocatalysis; nanomaterial characterization; DFT analysis



Citation: Armaković, S.J.;
Jovanoski Kostić, A.; Bilić, A.;
Savanović, M.M.; Tomić, N.;
Kremenović, A.; Šćepanović, M.;
Grujić-Brojčin, M.; Ćirković, J.;
Armaković, S. Photocatalytic Activity
of the V₂O₅ Catalyst toward Selected
Pharmaceuticals and Their Mixture:
Influence of the Molecular Structure
on the Efficiency of the Process.

Molecules 2023, 28, 655. https://
doi.org/10.3390/molecules28020655

Academic Editor: Wanhong Ma

Received: 8 December 2022 Revised: 4 January 2023 Accepted: 5 January 2023 Published: 9 January 2023



Copyright: © 2023 by the authors. Licensee MDPI, Basel, Switzerland. This article is an open access article distributed under the terms and conditions of the Creative Commons Attribution (CC BY) license (https://creativecommons.org/licenses/by/4.0/).

1. Introduction

The World Health Organization noted in its reports that pharmaceuticals are present in natural and treated water in concentrations from 0.1 to 0.05 mg/L [1]. Among all pharmaceuticals, a large increase was noted for β -blockers due to an increase in cardiovascular diseases [2]. Because of their moderately high solubility [3] and incomplete removal by wastewater treatment plants, β -blockers are persistent in water environments and they may show potential toxic properties against nontarget organisms, i.e., aquatic organisms

Molecules **2023**, 28, 655 2 of 18

and even human health. For example, metoprolol (MET, Figure 1) is one of the most used medicines in this class, and its usage increased four times in recent years [4]. Pindolol (PIN, Figure 1) possesses lipophilic properties and at natural pH is almost completely insoluble in water [5,6]. Nadolol (NAD, Figure 1) is another medicine from the β -blockers class, which is highly soluble in water and hydrolytically stable, and thanks to that property, is highly bioavailable in the environment [7,8]. Usually, β -blockers are present in the environment in combination with other β -blockers and various organic pollutants. Their mutual reactions may manifest additional health and environmental risks caused by unexpected interactions between them.

Figure 1. Structural formulas of studied beta blockers.

Conventional water treatment plants (WWTPs) lack the potential to remove emerging pollutants, such as pharmaceuticals, especially β-blockers [9]. The poor efficiency of conventional WWTPs in removing β -blockers is proven by the presence of β -blockers in various water organisms [10]. The average removal efficiency of these compounds is around 30–40% [11]. The degradation of individual β -blockers depends on various factors, such as temperature, pH value, compound's polarity, cation-exchange properties, biodegradability, etc. [12]. Multiple strategies have been applied in their removals, such as adsorption [13], chemical treatment for tackling water contamination, and advanced oxidation processes (AOPs) [14,15]. However, to achieve easy operation, low equipment cost, and cheap raw materials, AOPs are highly desirable. In addition, AOP, such as photodegradation, is considered most commonly used due to its ability to remove most organic pollutants from water [16]. To prevent and eliminate their unexpected toxic properties, there is a need for new efficient methods and materials for β -blockers removal from the water environment. A slow degradation rate during photolysis requires catalysts activated by interaction with light, after which the degradation process is more efficient [8]. For more than ten years, semiconductor-based photocatalysts have focused on water purification because of their high potential for the degradation of pollutants [17]. Some latest photocatalysts used are nanocrystalline M-type hexaferrite Ca_{0.5}Pb_{0.5}-xYb_xZn_vFe_{12-v}O₁₉ synthesized by sol–gel autocombustion method [15], the $C_3N_{4x}/AgO_y@Co_{1-x}Bi_{1-y}O_7$ synthesized by the combination of sol-gel and annealing approaches [14], porous methacrylic organosilica materials (Ag@PMOS) synthesized by reducing the silver moieties on and in the surfaces of porous methacrylic organic silicates [18], V_2O_5 nanoparticles [19], V_2O_5 nanorods [20], etc.

Vanadium oxide is a compound with colossal potential in water treatment because of its capability of light absorption, lower bandgap (2.3 eV) than TiO_2 and ZnO, chemical stability, and surface catalytic properties [21–25]. Following previously obtained results (Table 1), the V_2O_5 catalyst showed significant photocatalytic activity toward various organic pollutants [21,23–27]. Most studied molecules are branched with at least one aromatic ring and nitrogen and oxygen atoms in their structure. Degradation pathways and degra-

Molecules **2023**, 28, 655 3 of 18

dation rate is determined by the nature of substituents on aromatic rings [25]. For example, Fu et al. noted that surface OH groups play a vital role in increasing the degradation rate of nitrobenzene and methylene blue after introducing Al_2O_3 particles. The structural similarity of previously investigated compounds and selected β -blockers and obtained results in those experiments served as a starting point for this research.

Table 1. Some	previous resear	ch on the	photocatal	vtic activit	v of V2O5 towa	ard organic pollutants.

Synthesis Method	Compounds	Irradiation	Efficiency	Reference
Hydrothermal method V_2O_5 pure vanadium pentoxide nanoparticles	Methyl orange (MO) Congo red (CR)	Visible light	After 180 min degradation of MO was 82% and CR was 99.61%	[21]
Coprecipitation—calcination V_2O_5/Al_2O_3 composite photocatalyst The highest activities were obtained for the sample with the V/Al ratio of 1:1	Reduction of Cr(VI), nitrobenzene (NB), and degradation of methylene blue (MB)	UV	After irradiation for 20, 300, and 20 min, the highest removal (or conversion) efficiencies for Cr(VI), NB, and MB over the optimal sample were found to be 79%, 67%, and 31%, respectively	[23]
Ultrasound-assisted V_2O_5 nanoparticles	Rose Bengal dye (RB)	Solar light	After 150 min degradation of RB was around 99%	[24]
Chemical precipitation from ammonium metavanadate using Triton X-100 as surfactant V_2O_5 powder	Phenol and derivatives	Natural sunlight	No contribution to the photocatalytic process	[25]
Growing radially on PET fibers V_2O_5 nanoflakes	Rhodamine B (RhB)	Visible light	After 60 min degradation of RhB was around 50%	[26]
Simple thermal decomposition method V ₂ O ₅ /ZnO nanocomposites	MB	Visible light	After 120 min degradation of MB was around 97%	[27]

In this paper, we investigate the photocatalytic properties of V_2O_5 nanopowder for the degradation of three β -blockers (MET, NAD, and PIN) separately and in a mixture. Several methods of characterization, such as X-ray powder diffraction (XRPD), scanning electron microscopy (SEM), energy-dispersive X-ray spectroscopy (EDS), Brunauer–Emmett–Teller (BET) measurements, Fourier transform infrared (FTIR) and Raman spectroscopy, are employed to correlate structural and morphological properties of synthesized nanopowders and their photocatalytic activity under ultraviolet (UV) irradiation. The efficiency of the photodegradation process was compared with the efficiency of direct photolysis (DF). The experimentally obtained results were correlated with the molecular and periodic DFT analysis to explain the influence of molecular structure on the efficiency of the degradation process.

2. Results and Discussion

2.1. XRPD

Only one crystalline phase Shcherbinaite, V_2O_5 (PDF card no. 01-072-0433; orthorhombic Pmnm space group) could be identified in the sample, Figure 2. Refined unit cell parameter values (a = 11.506 (2), b = 4.3708 (6), c = 3.5627 (4) Å, V = 179.17 (4) ų) are in good agreement with reference values reported in upper mentioned PDF card (a = 11.5100, b = 4.3690, c = 3.5630 Å, V = 179.173 ų). The significant presence of an amorphous component is not evident. Crystallite-sized (1251(35) Å) and lattice strain (0.16(2)%) values point to well crystalline material with important lattice strain.

Molecules **2023**, 28, 655 4 of 18

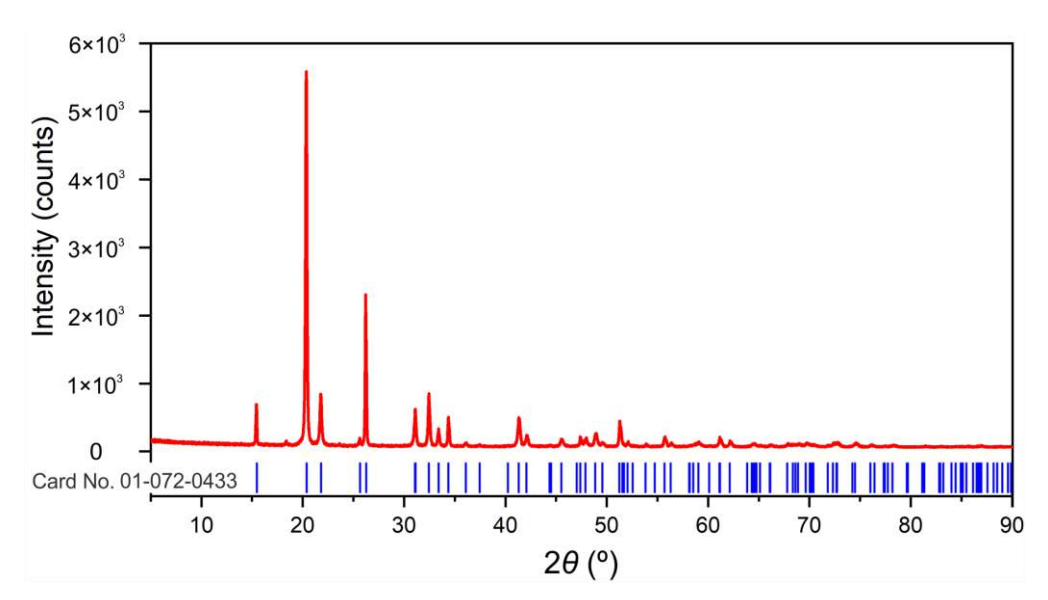


Figure 2. Experimental XRPD pattern in red. Peak positions for Shcherbinaite, V_2O_5 (card number 01-072-0433; ICDD (PDF-2 Release 2016 RDB)) in blue are shown below the experimental pattern.

2.2. SEM/EDS

By applying the hydrothermal method, where ammonium metavanadate was used as a precursor in an acidic media, hexagonal-shaped platelets with well-defined morphology were obtained as a major entity (Figure 3). The diameters of the platelets are in the range of $10\text{--}65~\mu m$, whereas their thickness may be estimated to be a few microns. Rashed et al. [28] obtained similar information regarding the morphology, where the cetyltrimethylammonium bromide (CTAB) was used as a surfactant. Due to this, the thinner nanoflake particles were formed with an average diameter of ~70 nm for the sample annealed at 500 °C for 2 h. A similar procedure was conducted by Abdullah et al. [29] with the same surfactant: after annealing at 500 °C for 4 h, the nanoflakes with thicknesses close to 65–80 nm were obtained.

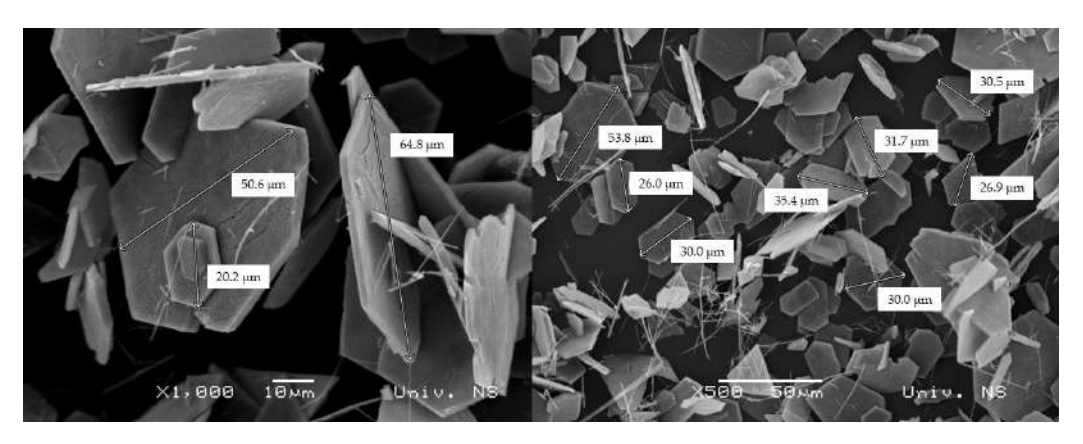


Figure 3. SEM micrographs of V₂O₅ powder with different magnifications.

The EDS analysis indicates that the main elements of the catalyst are vanadium and oxygen, and no other impurity elements could be detected (Figure 4). The atomic percentage of V and O in Spectrum 1 is estimated as 39.86% and 60.14%, respectively, indicating possible oxygen deficiency on the edge of the platelet. The values obtained in Spectrum 2, at the flat surface of the platelet, estimated as 25.47% for V and 74.53% for O, are close to the values of stoichiometric V_2O_5 .

Molecules **2023**, 28, 655 5 of 18

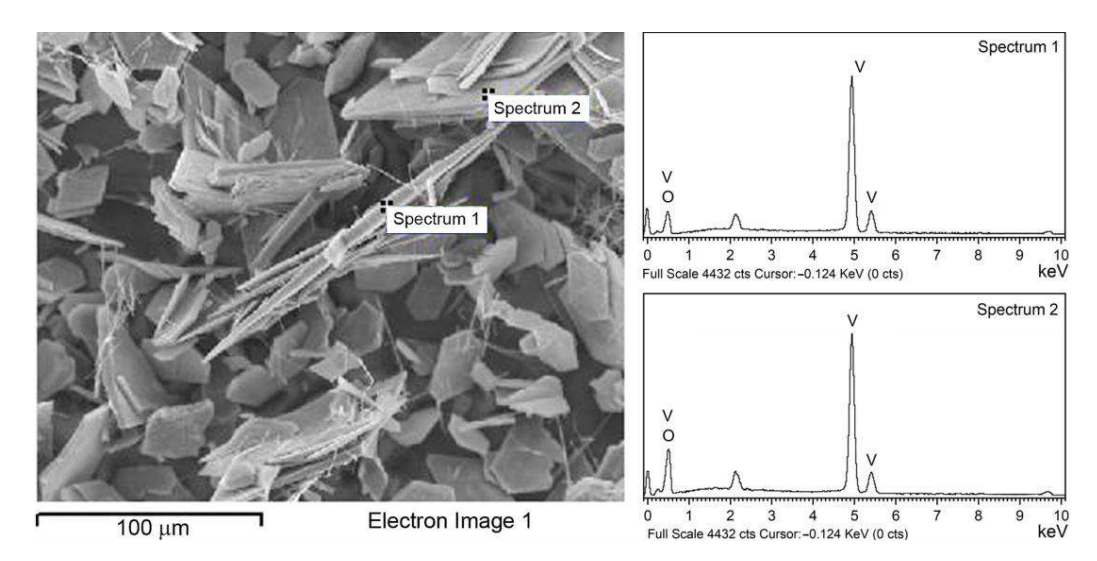


Figure 4. SEM image (left) with corresponding EDS spectra (right) of V₂O₅ catalyst.

2.3. Raman Scattering Measurements

The Raman scattering measurements taken on the catalyst sample have confirmed the results of XRPD regarding orthorhombic α -V₂O₅ structure with Pmnm symmetry. This structure is associated with 21 Raman active modes ($7_{Ag} + 3B_{1g} + 7B_{2g} + 4B_{3g}$) [30], 10 of which are registered in the spectrum shown in Figure 5. These modes are unambiguously assigned to α -V₂O₅ structure [30,31]: ~104(A_g), 146(B_{1g}/B_{3g}), 198 (A_g/B_{2g}), 285 (B_{1g}/B_{3g}), 306 (A_g), 406 (A_g), 483 (A_g), 528 (A_g), 701 (B_{1g}/B_{2g}), and 995 cm⁻¹ (A_g). A good agreement of the position of the Raman mode at 995 cm⁻¹ with corresponding bulk value, together with the absence of ~840 cm⁻¹ mode in the spectra of the catalyst, reveals a good crystallinity of the V₂O₅ phase [30–32]. A broad feature at ~1020 cm⁻¹ may be ascribed to surface VO_x species on V₂O₅ [33].

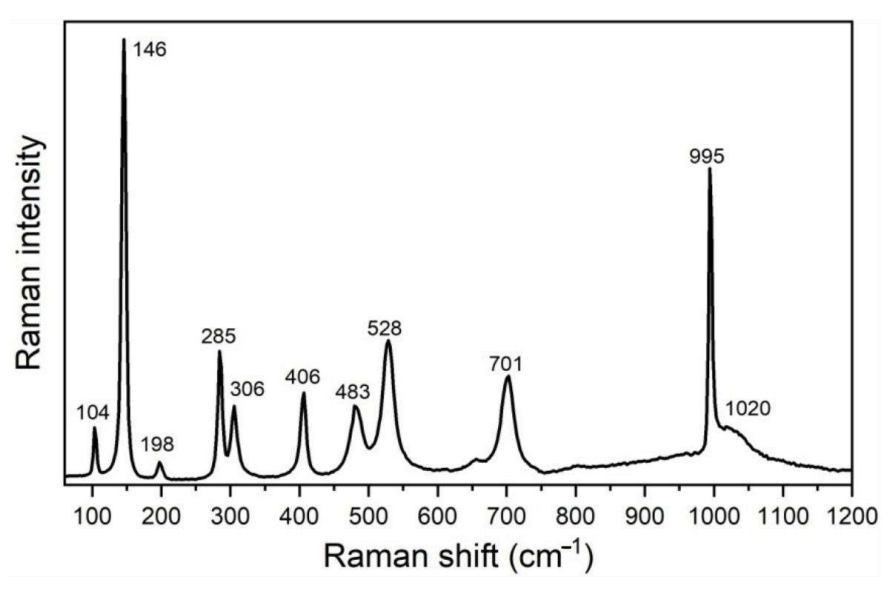


Figure 5. Experimental Raman spectrum of V₂O₅ catalyst (after a baseline correction).

2.4. UV-Vis

In order to estimate the energy bandgap of V_2O_5 powder, Kubelka–Munk functions F(R) [34] were calculated as $F(R) = (1 - R)^2 / 2R$, where R is the diffuse reflectance of the

Molecules **2023**, 28, 655 6 of 18

 V_2O_5 sample. Taking into account that F(R) is proportional to the absorption coefficient α , the Tauc plot [35] was obtained by using the following equation:

$$(h\nu F(R))^{1/n} = A(h\nu - E_g)$$

where h is Planck's constant, ν —photon's frequency, E_g —bandgap, A—proportional constant, and the n factor depends on the nature of the electron transition. They equal 1/2 or 2 for allowed direct and indirect transition band gaps [36]. The band gap values were deduced by extrapolating the linear portion of the curves to the energy axis, as shown in Figure 6. According to this procedure, the bandgap energy E_g values, assuming the allowed direct and indirect transitions, are estimated as ~2.24 and ~2.11 eV, respectively.

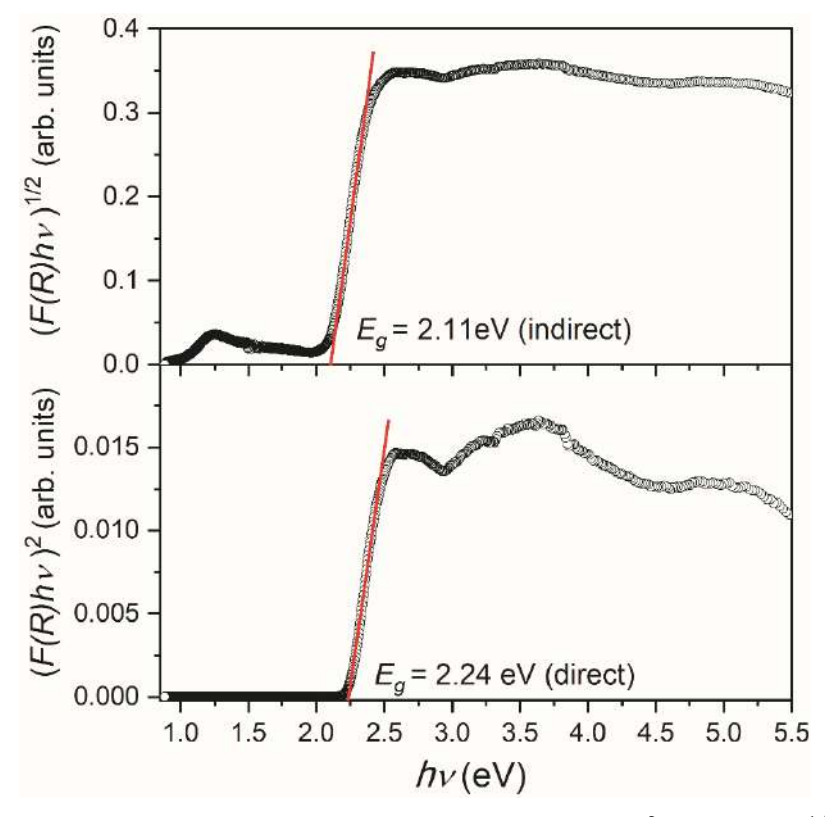


Figure 6. Transformed Kubelka–Munk functions $(F(R) hv)^2$ and $(F(R) hv)^{1/2}$ assuming direct and indirect energy bandgap in the V₂O₅ sample, respectively.

It should be noted that different V_2O_5 structures may undergo direct and indirect transitions, and it is not often easy to decide which type of electron inter-band transition is predominant [37]. According to a detailed analysis of available literature data and the film properties, Schneider concluded that the direct allowed transition could be considered the most probable in investigated V_2O_5 films [37]. Conversely, Mousavi et al. [38] have suggested the direct bandgap in the V_2O_5 nanoparticles based on the best line fitting of Kubelka–Munk functions. Still, in our case, it is impossible to decide the character of the allowed transition, considering the good quality of line fitting (Figure 6).

In this work, the DFT approach was used to perform band structure calculations to complement our experimental observations and to compare band gaps. The model of V_2O_5 was generated according to the previously mentioned information regarding the crystal structure of V_2O_5 . The model of V_2O_5 was first subjected to geometrical optimization, followed by band structure calculations, using the PBE-D3 level of theory with Hubbard U value set to 3.5 eV for vanadium 3d states, a value reported to produce excellent results in terms of band gap for this material [39]. The obtained band structure is presented in Figure 7.

Molecules **2023**, 28, 655 7 of 18

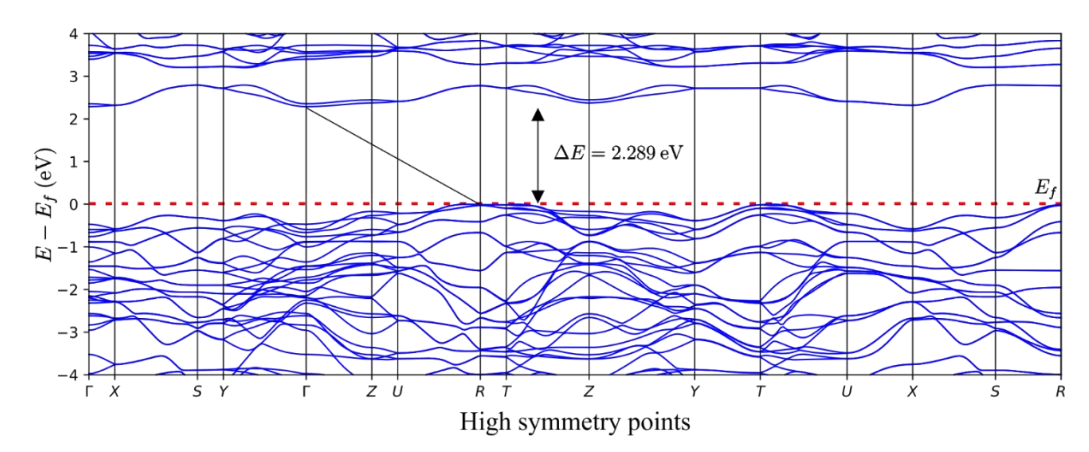


Figure 7. Band structure of $V_2O_{5.}$ The red dotted line denotes the Fermi level. The black line connects the top of the valence and the bottom of the conduction zones.

As presented in Figure 7, it can be seen that the DFT calculations lead to excellent matching between experimental and computational results. Our DFT calculations indicate that an indirect band gap characterizes the V_2O_5 . Additionally, the DFT + U approach utilized in this work yielded a band gap value of 2.289 eV, which is in excellent agreement with our experimental observations and reports of other research groups [40,41]. The importance of Hubbard U correction was essential for reaching this level of agreement. However, it is also interesting to note that the absence of Hubbard U correction led to a reasonably decent band gap value equal to 1.880 eV (again, with the indirect band gap type).

2.5. Photocatalytic Application

The photocatalytic activity of the V_2O_5 catalyst was studied through the photocatalytic degradation of NAD, PIN, and MET and their mixture. The results of the degradation efficiency were compared with the efficiency of DF.

Since light absorption is an important parameter influencing the degradation efficiency, we have also analyzed the excitations within studied pharmaceutical molecules. For these purposes, we have performed TD-DFT calculations with CAM-B3LYP functional and 6-311++G(d,p) basis set, which enabled us to simulate the UV spectra of the compounds mentioned above (Figure 8). The obtained results agree with the investigated compounds' experimental spectra.

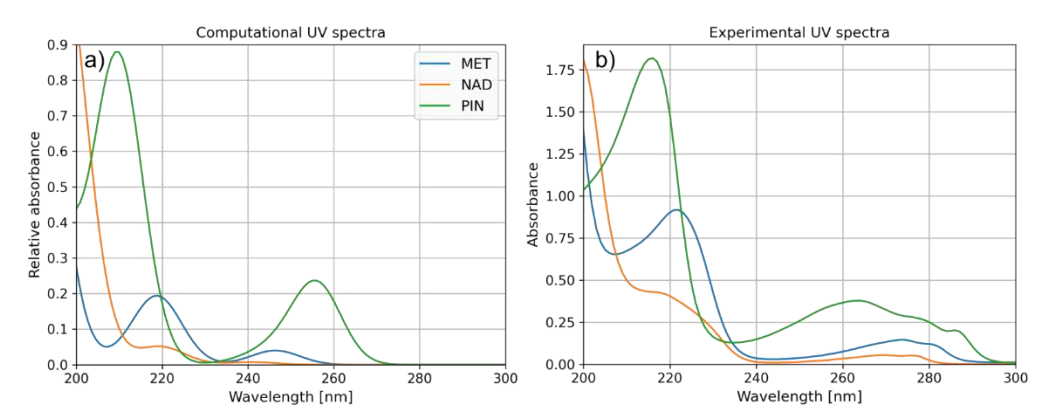


Figure 8. (a) Computational and (b) experimental UV spectra of MET, NAD, and PIN.

UV spectra presented in Figure 8 indicate one more interesting property of the PIN molecule, in line with the experimentally observed degradation efficiencies. Namely, aside from the excitations at wavelengths around 200 nm, the PIN molecule is also characterized by relatively strong light absorption at 260 nm. The stronger light absorption of the

Molecules **2023**, 28, 655 8 of 18

molecule is significant for photocatalytically assisted degradation and, in the case of the present study, may be a crucial factor leading to the superior degradation efficiency of PIN over other molecules (Figure 9).

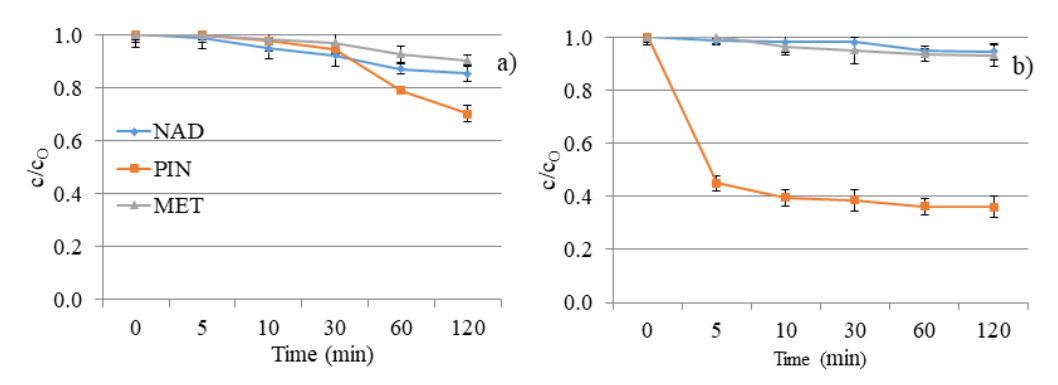


Figure 9. NAD, PIN, and MET degradation kinetics under UV irradiation: (a) without V_2O_5 and (b) with V_2O_5 catalyst.

The poor degradation efficiency of investigated compounds was expected, considering the investigated compounds' absorption maxima and the UV lamp's characteristics. Namely, the absorption maximum of the used lamp corresponds to the UV/A-B region of the spectrum. As shown in Figure 9a, MET and NAD expressed 10% and 15% degradation after 120 min. DF of separate solutions offers slight removal of NAD and MET and a two- to three-times higher degradation rate for PIN (30%). The nature of the substituents attached to the aromatic ring and the secondary interaction of released ions have significant roles in the degradation progress and regulate the degradation pathways. The obtained results can be explained based on the structural characteristics of the tested compounds.

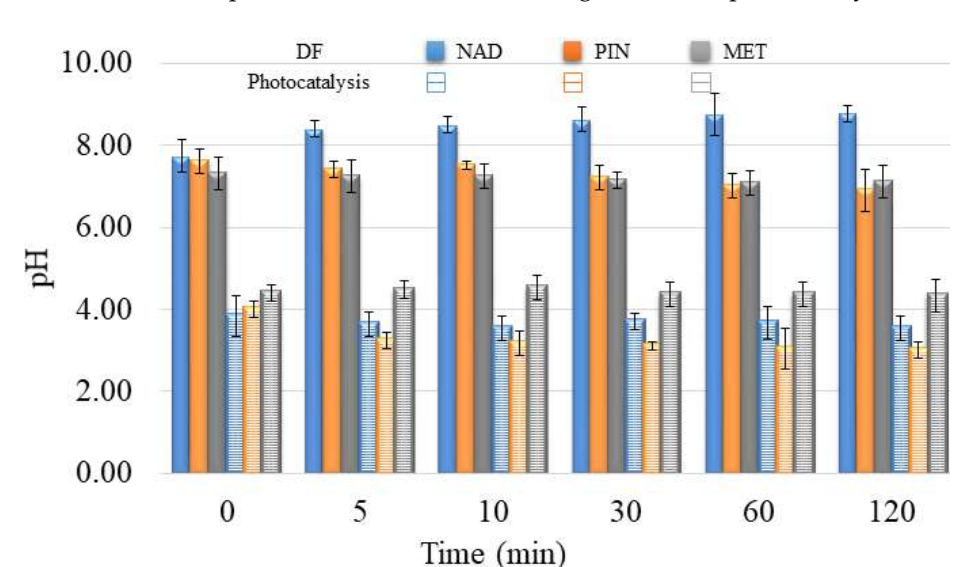
The efficiency of DF is usually improved when irradiation is combined with a photocatalyst. However, V_2O_5 did not show a positive effect on the removal of NAD and MET from the aqueous solution (Figure 9b). Moreover, the efficiency of the process has decreased in comparison to DF. We can conclude that the turbidity of the solution resulting from the presence of nanomaterials decreased the removal efficiency of the mentioned two beta blockers. However, PIN showed higher efficiency than MET and NAD in the presence and absence of a V_2O_5 catalyst. Namely, 64% of PIN was eliminated by photocatalytic degradation within 120 min.

In addition to the fact that it is necessary to overlap at least partially the radiation spectrum and the compounds that DF decomposes, the pH of the solution plays a vital role in the creation of reactive oxygen species and the further interaction of released ions and radicals. The pH value of the aqueous solutions for DF was about 7.5 ± 1.0 (Figure 10). At the specified pH value of the aqueous solution, reactive oxygen species can be created in the water, contributing to the degradation efficiency.

In the presence of V_2O_5 , the pH values of water suspensions were around 4.0 ± 0.5 (Figure 10). The effect of pH solution on photocatalytic degradation is complex due to the electrostatic interaction between the semiconductor surface, solvent molecules, substrate, and radicals formed during the photodegradation reaction.

 V_2O_5 is a transition metal oxide of vanadium that has a narrow band gap (2.3 eV) [22,24]. It can capture a significant fraction of the UV spectrum to generate active redox centers. Photoactivation happens with wavelengths less than 443 nm [42]. Catalyst also accelerated the degradation of PIN two times compared to the DF study within 120 min (64% and 30%, respectively). However, the catalyst did not have expected behavior towards MET and NAD, wherein the degradation rate was almost the same for these two β -blockers (7% and 5%, respectively). Differences between the efficiency of PIN removal and removal of MET and NAD result from differences in these compounds' structural and electronic properties. With the addition of V_2O_5 , the pH value of NAD and PIN solutions decreased from 8.0 to

Molecules **2023**, 28, 655 9 of 18



around 3.5. There was no significant change in pH value for the MET solution after V_2O_5 addition, and the pH value was about 4.4 during 120 min of photocatalysis.

Figure 10. pH value during degradation of selected pharmaceuticals under UV irradiation without V_2O_5 (DF) and with V_2O_5 catalyst (Photocatalysis).

When the pH is ≥ 7 OH radicals are the main reactive species, while at lower pH values, the reactive species are h⁺ [43,44]. Based on pH value, it can be determined through which reactive species the process takes place in the presence of V_2O_5 . Since the pH value is less than 7 for all three β -blockers, the reactive species are h^+ . However, because the efficiency for MET and NAD is low in the presence of V₂O₅, it implies that degradation did not occur via h⁺. In contrast, the degradation of PIN takes place via h⁺. To better understand the interaction between MET and the *OH radicals, Armaković et al. [45] have conducted a DFT computational analysis. The interaction of *OH radicals with MET formed a new bond. It was concluded that *OH binds to the aromatic ring of MET. Moreover, the structural properties of MET indicated the highest interaction of MET and *OH, compared to other radicals and h⁺. These data are essential, considering that MET and NAD are similar β-blockers, concluding that NAD will also interact with *OH radicals. Data obtained in this work also supported similar behavior of MET and NAD in reaction with V_2O_5 . Armaković et al. [46] have determined the Fukui f_0 function of the PIN molecule, which provides information about the sensitivity towards radical attacks. Since positive values of Fukui f_0 were mainly located at the PIN rings, they suggested that this molecular site is the most sensitive to radical attacks. However, they emphasized that the h⁺ generated during the photocatalytic process significantly increases degradation efficiency. Jovanoski Kostić et al. [47] have stated that the influence of h⁺ on the photodegradation of PIN is favored in acidic conditions. The obtained pH value (Figure 10) within the photo degradation of PIN using V_2O_5 indicated that the mechanism of degradation of PIN occurs mainly via h⁺.

To explain the observed difference in degradation efficiencies, we performed a computational analysis of all molecules in the framework of the DFT approach. Since the degradation efficiency generally depends on the reactivity of molecules and photophysical properties of the catalyst, we decided to compare the reactivity of considered molecules by calculating the average local ionization energy (ALIE), a well-known quantum molecular descriptor. The analysis of the ALIE quantum-molecular descriptor precisely identifies the PIN molecule as the most reactive of all three considered, see Figure 11.

Molecules **2023**, 28, 655

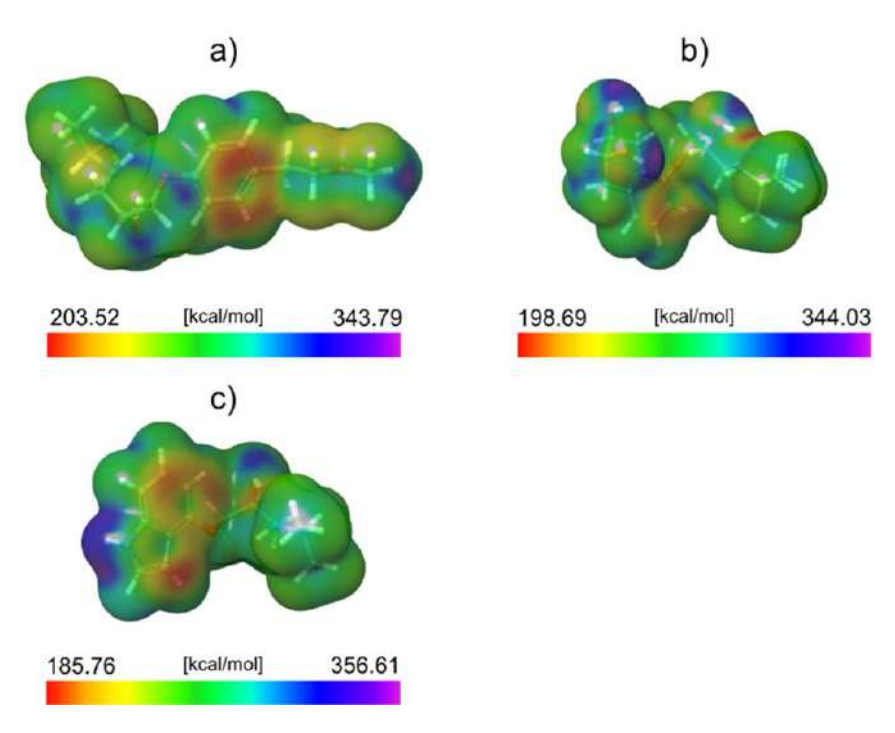


Figure 11. ALIE surfaces of (a) MET, (b) NAD, and (c) PIN.

This work visualized the ALIE descriptor as an electron density surface mapped with the ALIE values. ALIE values indicate the energy required to remove an electron from a certain point around the molecule. The lower this energy is, the easier it is to remove an electron from a certain point around the molecule. The results presented in Figure 11 indicate that the PIN is by far the most reactive of all three considered molecules in terms of how easy it is to remove an electron from it. Both MET and NAD have relatively similar lowest values of the ALIE descriptor (the difference is ~4 kcal/mol). On the other side, the PIN has around 14 kcal/mol lower minimal ALIE value than NAD and about 19 kcal/mol lower minimal ALIE value than MET.

This significant difference in ALIE indicates that the PIN molecule is much more sensitive to the influence of positive charge than the other two molecules. This also suggests that the positively charged h⁺ might be responsible for the efficient degradation of the PIN. Since, according to the ALIE descriptor, the other two molecules are not sensitive to positive charge as the PIN is, their degradation efficiency is very low. The distribution of ALIE values on the electron density surface leads to one more important conclusion regarding the PIN's degradation efficiency. Namely, the lowest ALIE values are delocalized to a much greater extent over the PIN molecule than the MET and NAD. This means that a much higher surface area of the PIN molecule is sensitive toward the positive charge compared to the MET and NAD.

Further, the mixture of NAD, PIN, and MET was subjected to DF and a photocatalytic reaction with V_2O_5 to study their degradation when coexisting in environmental waters, as it occurs in nature. As seen in Figure 12a, exposure of the NAD, PIN, and MET mixture to UV did not cause a higher degradation efficiency of these three compounds. The DF of the separate solution of each β -blocker was a more efficient process. The reason may be caused by the additive or synergistic effects of the structures of these three β -blockers and the same amount of UV energy distributed over all three compounds [11]. Moreover, the pH value during decomposition (Figure 13) was constant and slightly basic (around 7.7 ± 0.2), indicating no changes in the aqueous solution.

Molecules **2023**, 28, 655 11 of 18

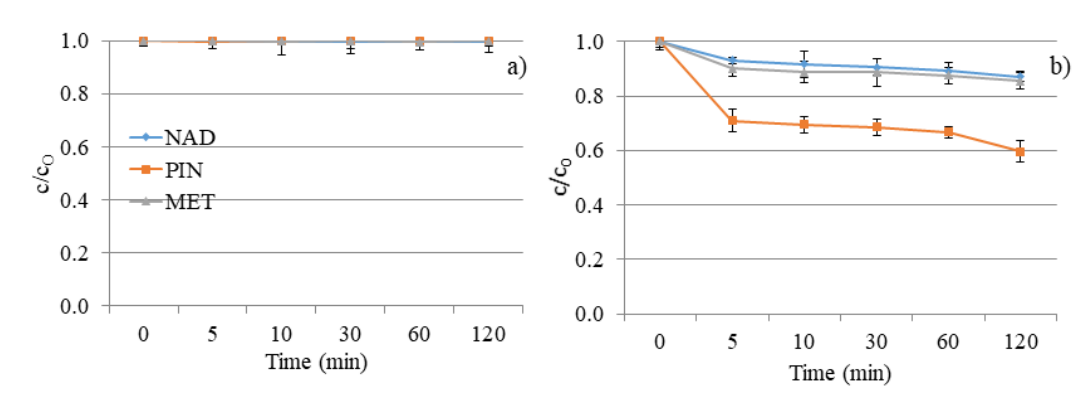


Figure 12. NAD, PIN, and MET mixture degradation kinetics under UV irradiation: (a) without V_2O_5 and (b) with V_2O_5 catalyst.

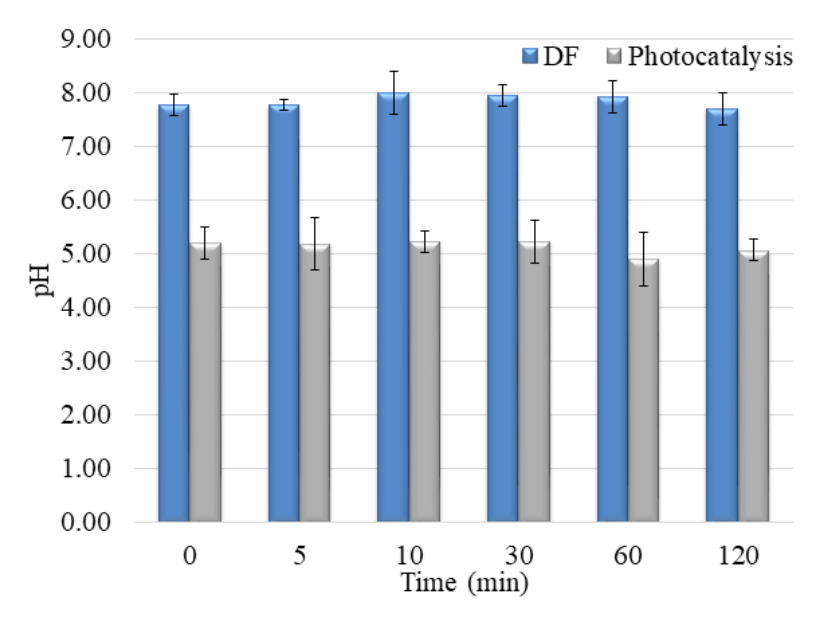


Figure 13. pH values during NAD, PIN, and MET mixture degradation under UV irradiation without/with V_2O_5 catalyst.

The lower photocatalytic efficiency of the PIN removal was achieved in a mixture with NAD and MET than in an individual solution. However, a much more interesting result is the increase in the degradation rate of NAD and MET in the presence of PIN (Figures 9b and 12b). One of the possible reasons for the acceleration of the decomposition process of NAD and MET in the mixture with PIN could be the higher concentration of NAD and MET molecules on the surface of the catalyst, which is also an explanation for the lower decomposition efficiency of PIN. Namely, 5 min after the beginning of UV irradiation, a certain amount of each compound was removed, and it continued to slightly increase up to a degradation rate of 13% for NAD, 40% for PIN, and 15% for MET within 120 min.

The mixture solution's pH was also acidic, but a 1.0 value higher than in the separate pharmaceuticals solutions (around 5.0 ± 0.2). These results also indicate that the presence of all three compounds in water changes starting pH. Moreover, the changing pH during degradation is different, showing the other degradation mechanism and the generation of various intermediates during the degradation process (Figures 10 and 13).

3. Materials and Methods

3.1. Chemicals and Solutions

The active components of β -blockers, NAD (\geq 99%, Sigma-Aldrich, Hamburg, Germany), PIN (\geq 99%, Sigma-Aldrich, Hamburg, Germany), and MET (\geq 99%, Sigma-Aldrich,

Molecules **2023**, 28, 655

Hamburg, Germany) were used as received. All three solutions were made using ultrapure water (UPW, $\kappa = 0.055 \,\mu\text{S/cm}$, pH 6.6).

As the catalyst, V_2O_5 was used at a concentration of 1.0 mg/cm³. Detailed information about the V_2O_5 synthesis is given in Sections 3.2 and 3.3.

Ammonium metavanadate (NH $_4$ VO $_3$, ACS reagent, \geq 99.0%, Sigma-Aldrich, Hamburg, Germany), acetic acid (glacial) 100% (CH $_3$ CO $_2$ H) anhydrous for analysis (EMSURE ACS, ISO, Reag. Ph Eur, Supelco, Bellefonte, PA, USA), ethanol absolute (CH $_3$ CH $_2$ OH, ACS reagent absolute, Supelco) were used as received.

3.2. Powder Synthesis

The facile hydrothermal synthesis method was used to prepare V_2O_5 powders [14,48]. For that purpose, 0.1 M ammonium metavanadate (NH₄VO₃) was dissolved in 80 mL of distilled water, resulting in a pale yellow solution. To adjust the pH of the reaction solution to about 4, the diluted acetic acid (CH₃COOH/H₂O = 1:1 v/v) was added drop-wise. The final orange solution was placed into a Teflon-lined stainless steel autoclave and kept at 180 °C for 24 h and then naturally cooled down to room temperature. The orange product was centrifuged with distilled water and absolute ethanol and dried at 80 °C for 12 h. The as-prepared sample was annealed at 500 °C for 2 h in air.

3.3. Characterization

The catalyst was investigated by X-ray powder diffraction (XRPD). Measurements were conducted on a Rigaku Smartlab X-ray diffractometer in θ - θ geometry (the sample in horizontal position) in part focusing on Bragg–Brentano geometry using a D/teX Ultra 250 strip detector in 1D standard mode with a CuK $\alpha_{1,2}$ radiation source (U = 40 kV and I = 30 mA). The XRPD patterns were collected in the 4–90° 2 θ range, with a step of 0.01°, and a data collection speed of 5.1 °/min. The low background single crystal silicon sample holder minimizes the background. Unit cell parameters and average crystallite size and lattice strain values were obtained by PDXL2 integrated X-ray powder diffraction software (Version 2.8.30; Rigaku Corporation, Tokyo, Japan).

The morphology and composition/quality of the catalyst were analyzed on SEM (JEOL JSM-6460LV, with the operating voltage of 20 keV) equipped with an EDS INCAx-sight detector and an "INAx-stream" pulse processor (Oxford Instruments, Abingdon, UK).

The Raman scattering spectra of the catalyst were taken in the backscattering geometry at room temperature in the air using Jobin-Yvon T64000 triple spectrometer (with 1800 grooves $\rm mm^{-1}$ grating) equipped with a confocal microscope and a nitrogen–cooled charge-coupled device detector. The spectra were excited by a 514.5 nm line of $\rm Ar^+/Kr^+$ ion laser with an output power of less than 10 mW.

The UV–vis diffuse reflectance (UV–vis DR) spectrum was recorded in the wavelength range of 200-1400 nm using the Shimadzu UV-2600 spectrophotometer equipped with an integrated sphere. The reflectance spectra were measured relative to a reference sample of $BaSO_4$.

3.4. Photodegradation Experiments

Photocatalytic degradation experiments were conducted through NAD, PIN, and MET solutions (0.05 mmol/dm³) exposed to UV irradiation in the presence of catalyst V_2O_5 (1.0 mg/cm³). In the case of the DF study, solutions were exposed to UV irradiation without a catalyst. Each solution, separately (in the volume of $20~\text{cm}^3$), and then a mixture of all three β -blockers, was placed in a cell made of Pyrex glass (total volume ca. $40~\text{cm}^3$, liquid layer thickness 35~mm) with a water circulating jacket. The cell was then placed in an ultrasonic bath, and suspensions were sonicated for 15~min. Afterward, a magnetic stir was added to the cell and placed on a magnetic stirrer in the stream of O_2 , thermostated at $25~\pm~0.5~\text{°C}$. The cell has a plain window on which the UV light beam was focused. The UV radiation source was a 125~W high-pressure mercury lamp (emission bands at 290,

Molecules **2023**, 28, 655

293, 296, 304, 314, 335, and 366 nm, with maximum emission at 366 nm and intensity of 2.6×10^{-3} W/cm² in the visible region and 1.4×10^{-2} W/cm² in the UV region).

In order to investigate the adsorption of selected β -blockers on the surface of the material, a solution of the corresponding compound was analyzed in the presence of V_2O_5 under identical conditions as photocatalytic degradation but without irradiation of the solution. The results showed negligible adsorption (less than 1% in 120 min in all three cases).

3.5. Analytical Procedure

For each solution (NAD, PIN, and MET) the sample was collected before cell exposure to the UV irradiation, filtered through a Millipore membrane filter (Milex-GV, $0.22~\mu m$), and placed in a chromatographic vial. Then, the samples were collected and filtered after 5, 10, 30, 60, and 120 min from the beginning of exposure to the UV irradiation. At each sample point, the pH value was measured.

In order to study the degradation kinetics, 20 μ L of the filtrate was analyzed by Shimadzu UFLC-PDA (Shimadzu Scientific Instruments, Columbia, Maryland, USA) Eclipse XDB-C18 column, 1550 mm \times 4.6 mm i.d., particle size 5 μ m, 30 °C). The UV/Vis PDA detector was set at wavelengths of maximum absorption of each β -blocker: 210 nm (for NAD), 217 nm (for PIN), and 223 nm (for MET). To achieve better peak separation, gradient elution was used (flow rate 0.7 mL min⁻¹, ACN, and water mixture—15% ACN at the beginning increased to 25% ACN at 6 min, and after that, it was constant for the next 2 min; post time 1 min).

3.6. Computational Details

All molecular DFT calculations were performed using the B3LYP density functional [49–52] in combination with a 6-31G(d,p) basis set [53–55]. All molecules were subjected to frequency calculations to check that geometrical optimizations identified the true ground states. Frequency calculations yielded only positive values. During geometrical optimizations, frequency, and property calculations, solvent effects (water) were considered in the Poisson–Boltzmann solver framework. Molecular DFT calculations were performed with the Jaguar program [56–59], as implemented in the Schrödinger Materials Science Suite 2022-2. TD-DFT analyses were performed using the long-range corrected version of B3LYP, namely the CAM-B3LYP density functional [60], together with the 6-311++G(d,p) basis set [61,62]. TD-DFT calculations were performed with ORCA 5.0.3. molecular modeling package developed by Prof. Frank Neese and coworkers [63–70]. Input files for TD-DFT analyses were prepared with the online ORCA input generator of the atomistica.online web application [71], available at https://atomistica.online.

All periodic DFT calculations were performed using the PBE density functional [72], including the empirically derived correction (D3 variant) developed by Prof. Stefan Grimme and coworkers [73–77]. Additionally, we included the Hubbard U correction for vanadium atoms to consider the underestimation of the band gap by the DFT approach [78]. In this case, we set the U value for vanadium to be 3.5 eV [39]. All periodic DFT calculations were performed with the Quantum Espresso program [79–82], as implemented in the Schrödinger Materials Science Suite 2022-2.

4. Conclusions

For the preparation of V_2O_5 , facile hydrothermal synthesis was used. X-ray diffraction identifies only one crystalline phase in the sample, which is proven by the fact that the crystallite size (1251(35) Å) and lattice strain (0.16(2)%) values point to well-crystallized material with a significant lattice strain. SEM micrographs show that hexagonal-shaped platelets with well-defined morphology were obtained as substantial entities with diameters in the range of 10–65 μ m and thicknesses of around a few microns, following previously conducted similar procedures available in the literature. EDS spectra indicate that the main elements of the catalyst are vanadium and oxygen with no other impurities, and the

Molecules **2023**, 28, 655 14 of 18

estimated contribution of each component is close to stoichiometric V_2O_5 . The Raman scattering measurements taken on the catalyst confirmed the result of XRPD.

The efficiency of DF of the individual solutions was poor, except for PIN (10% for MET, 15% for NAD, and 30% for PIN). Adding a catalyst in the water solution of MET and NAD did not improve the degradation. However, the degradation efficiency of PIN increased up to 64% within 120 min. This study considered various perspectives to determine why PIN showed the highest efficiency. The fact that PIN absorbs light at a wavelength of around 200 nm and has relatively strong light absorption at 260 nm may indicate its superior degradation efficiency over the other two molecules. Calculations of ALIE indicate that the PIN is by far the most reactive of all three considered molecules in terms of how easy it is to remove an electron from it. MET and NAD have similar minimal ALIE values, and PIN has around 14 kcal/mol lower minimal ALIE value than NAD and about 19 kcal/mol more down minimal ALIE value than MET. Moreover, the pH value indicated different intermediates of photocatalysis. Namely, following the fact that PIN degradation was at a pH value below 4, it can be concluded that PIN degradation occurs via h⁺.

A photocatalytic study of a mixture of NAD, MET, and PIN, as they occur in nature, shows that the degradation processes for MET and NAD were accelerated compared to individual solutions of these two compounds. This can be explained by a higher concentration of NAD and MET molecules on the surface of the catalyst, which also explains the lower decomposition efficiency of PIN. Conditions in the mixture were acidic, with a pH value higher than in individual solutions. pH values were changing differently, indicating the other degradation mechanism and generation of various intermediates during the degradation process.

This and other research demonstrated that V_2O_5 has a significant potential for practical applications to eliminate organic pollutants from the most precious natural resource—water. However, an extensive literature survey performed for this research has indicated several more essential facts regarding the potential of V_2O_5 for practical applications. One of the most important facts concerns bandgap engineering in the case of the V_2O_5 . Namely, it was demonstrated that the bandgap value can be efficiently tuned, either by manipulating the structure of V_2O_5 or by applying an external stimulus. It has been reported that the band gap of V_2O_5 can either be decreased or increased, depending on the selected technique. The ability to finely tune the band gap of V_2O_5 is essential for its practical application as a photocatalyst. Finally, the readily available synthesis of this material is one more factor determining the bright future of the material.

Author Contributions: Conceptualization, S.J.A.; data curation, S.J.A., A.J.K., A.B., M.M.S., N.T., M.Š., M.G.-B. and S.A.; formal analysis, S.J.A., A.J.K., A.B., M.M.S., N.T., A.K., M.Š., M.G.-B. and S.A.; funding acquisition, S.J.A.; investigation, S.J.A., A.J.K., A.B., M.M.S., N.T., A.K., M.Š., M.G.-B. and S.A.; methodology, S.J.A., M.Š. and S.A.; project administration, S.J.A. and N.T.; resources, S.A.; software, S.J.A. and S.A.; supervision, S.J.A. and S.A.; validation, S.J.A., A.B., M.M.S., M.G.-B. and S.A.; visualization, S.J.A., A.J.K., A.B., M.M.S., N.T., M.Š., M.G.-B. and S.A.; writing—original draft, S.J.A., A.J.K., A.B., M.M.S., N.T., M.Š., writing—revision, S.J.A., A.J.K., A.B., M.M.S., N.T., M.Š., M.G.-B. and S.A.; writing—revision, S.J.A., A.J.K., A.B., M.M.S., N.T., M.Š., M.G.-B., J.Ć. and S.A. All authors have read and agreed to the published version of the manuscript.

Funding: This research was funded by the Ministry of Education, Science and Technological Development of the Republic of Serbia (grant no. 451-03-68/2022-14/200125 and grant no. 451-03-68/2022-14/200126), Innovation Fund of the Republic of Serbia—Proof of Concept (PoC) ID5619, the Institute of Physics, University of Belgrade, Serbia.

Institutional Review Board Statement: Not applicable.

Informed Consent Statement: Not applicable.

Data Availability Statement: Not applicable.

Molecules **2023**, 28, 655 15 of 18

Acknowledgments: S.J.A., S.A. and M.M.S. thank the Association of the International Development of Academic and Scientific Collaboration (www.aidasco.org) for providing the computational resources necessary for the first principles calculations.

Conflicts of Interest: The authors declare no conflict of interest.

Sample Availability: Samples of the compounds are not available from the authors.

References

1. Fallah, Z.; Zare, E.; Ghomi, M.; Ahmadijokani, F.; Amini, M.; Tajbakhsh, M.; Arjmand, M.; Sharma, G.; Ali, H.; Ahmad, A. Toxicity and remediation of pharmaceuticals and pesticides using metal oxides and carbon nanomaterials. *Chemosphere* **2021**, 275, 130055. [CrossRef]

- 2. Ali, I.; Alothman, Z.; Alwarthan, A. Uptake of propranolol on ionic liquid iron nanocomposite adsorbent: Kinetic, thermodynamics and mechanism of adsorption. *J. Mol. Liq.* **2017**, 236, 205–213. [CrossRef]
- 3. Kibbey, T.; Paruchuri, R.; Sabatini, D.; Chen, L. Adsorption of beta blockers to environmental surfaces. *Environ. Sci. Technol.* **2007**, 41, 5349–5356. [CrossRef] [PubMed]
- 4. Alder, A.; Schaffner, C.; Majewsky, M.; Klasmeier, J.; Fenner, K. Fate of β-blocker human pharmaceuticals in surface water: Comparison of measured and simulated concentrations in the Glatt Valley Watershed, Switzerland. *Water Res.* **2010**, *44*, 936–948. [CrossRef]
- 5. Kim, K.; Cho, E.; Choi, J.; Kim, H.; Jang, A.; Choi, Y.; Yu, J.-H.; Jung, S. Intermolecular complexation of low-molecular-weight succinoglycans directs solubility enhancement of pindolol. *Carbohydr. Polym.* **2014**, *106*, 101–108. [CrossRef]
- 6. Perlovich, G.; Volkova, T.; Bauer-Brandl, A. Thermodynamic study of sublimation, solubility, solvation, and distribution processes of atenolol and pindolol. *Mol. Pharm.* **2007**, *4*, 929–935. [CrossRef] [PubMed]
- 7. Hernando, M.; Gómez, M.; Agüera, A.; Fernández-Alba, A. LC-MS analysis of basic pharmaceuticals (beta-blockers and anti-ulcer agents) in wastewater and surface water. *TrAC Trends Anal. Chem.* **2007**, *26*, 581–594. [CrossRef]
- 8. Dhangar, K.; Kumar, M. Tricks and tracks in removal of emerging contaminants from the wastewater through hybrid treatment systems: A review. *Sci. Total Environ.* **2020**, *738*, 140320. [CrossRef] [PubMed]
- 9. Bijlsma, L.; Pitarch, E.; Fonseca, E.; Ibanez, M.; Botero, A.; Claros, J.; Pastor, L.; Hernandez, F. Investigation of pharmaceuticals in a conventional wastewater treatment plant: Removal efficiency, seasonal variation and impact of a nearby hospital. *J. Environ. Chem. Eng.* **2021**, *9*, 105548. [CrossRef]
- 10. Ye, Y.; Feng, Y.; Bruning, H.; Yntema, D.; Rijnaarts, H. Photocatalytic degradation of metoprolol by TiO₂ nanotube arrays and UV-LED: Effects of catalyst properties, operational parameters, commonly present water constituents, and photo-induced reactive species. *Appl. Catal. B Environ.* **2018**, 220, 171–181. [CrossRef]
- 11. Stankiewicz, A.; Giebułtowicz, J.; Stankiewicz, U.; Wroczyński, P.; Nałęcz-Jawecki, G. Determination of selected cardiovascular active compounds in environmental aquatic samples–methods and results, a review of global publications from the last 10 years. *Chemosphere* 2015, 138, 642–656. [CrossRef] [PubMed]
- Radjenović, J.; Petrović, M.; Barceló, D. Fate and distribution of pharmaceuticals in wastewater and sewage sludge of the conventional activated sludge (CAS) and advanced membrane bioreactor (MBR) treatment. Water Res. 2009, 43, 831–841.
 [CrossRef]
- 13. Liu, H.; Chen, M.; Wei, D.; Ma, Y.; Wang, F.; Zhang, Q.; Shi, J.; Zhang, H.; Peng, J.; Liu, G. Smart removal of dye pollutants via dark adsorption and light desorption at recyclable Bi₂O₂CO₃ nanosheets interface. *ACS Appl. Mater. Interfaces.* **2020**, 12, 20490–20499. [CrossRef] [PubMed]
- 14. Kumar, O.; Shahzad, K.; Nazir, M.; Farooq, N.; Malik, M.; Shah, S.; ur Rehman, A. Photo-Fenton activated C₃N_{4x}/AgO_y@Co_{1-x}Bi_{0.1-y}O₇ dual s-scheme heterojunction towards degradation of organic pollutants. *Opt. Mater.* **2022**, *126*, 112199. [CrossRef]
- 15. Jamshaid, M.; Nazir, M.; Najam, T.; Shah, S.; Khan, H.; ur Rehman, A. Facile synthesis of Yb³⁺-Zn²⁺ substituted M type hexaferrites: Structural, electric and photocatalytic properties under visible light for methylene blue removal. *Chem. Phys. Lett.* **2022**, *805*, 139939. [CrossRef]
- 16. Oluwole, A.O.; Omotola, E.O.; Olatunji, O.S. Pharmaceuticals and personal care products in water and wastewater: A review of treatment processes and use of photocatalyst immobilized on functionalized carbon in AOP degradation. *BMC Chem.* **2020**, *14*, 62. [CrossRef]
- 17. Soares, S.F.; Simoes, T.; Antonio, M.; Trindade, T.; Daniel-da-Silva, A.L. Hybrid nanoadsorbents for the magnetically assisted removal of metoprolol from water. *Chem. Eng. J.* **2016**, *302*, 560–569. [CrossRef]
- 18. Shahzad, K.; Khan, M.I.; Shanableh, A.; Elboughdiri, N.; Jabeen, M.A.; Nazir, M.; Farooq, N.; Ali, H.; Abdelfattah, A.U.; ur Rehman, A. Silver supported-Ag@ PMOS onto thumb structured porous organosilica materials with efficient hetero-junction active sites for photo-degradation of methyl orange dye. *Inorg. Nano-Met. Chem.* **2022**, *52*, 407–416.
- 19. Suresh, R.; Giribabu, K.; Manigandan, R.; Munusamy, S.; Kumar, S.; Muthamizh, S.; Stephen, A.; Narayanan, V. Doping of Co into V_2O_5 nanoparticles enhances photodegradation of methylene blue. *J. Alloys Compd.* **2014**, 598, 151–160. [CrossRef]
- Jayaraj, S.; Sadishkumar, V.; Arun, T.; Thangadurai, P. Enhanced photocatalytic activity of V₂O₅ nanorods for the photodegradation of organic dyes: A detailed understanding of the mechanism and their antibacterial activity. *Mater. Sci. Semicond. Process.* 2018, 85, 122–133. [CrossRef]

Molecules **2023**, 28, 655 16 of 18

21. Sajid, M.; Shad, N.; Javed, Y.; Khan, S.; Zhang, Z.; Amin, N.; Zhai, H. Preparation and characterization of Vanadium pentoxide (V₂O₅) for photocatalytic degradation of monoazo and diazo dyes. *Surf. Interfaces* **2020**, *19*, 100502. [CrossRef]

- 22. Sun, J.; Li, X.; Zhao, Q.; Ke, J.; Zhang, D. Novel V2O5/BiVO4/TiO2 nanocomposites with high visible-light-induced photocatalytic activity for the degradation of toluene. *J. Phys. Chem. C* 2014, 118, 10113–10121. [CrossRef]
- 23. Fu, X.; Tang, W.; Ji, L.; Chen, S. V₂O₅/Al₂O₃ composite photocatalyst: Preparation, characterization, and the role of Al₂O₃. *Chem. Eng. J.* **2012**, *180*, 170–177. [CrossRef]
- Karthik, K.; Nikolova, M.; Phuruangrat, A.; Pushpa, S.; Revathi, V.; Subbulakshmi, M. Ultrasound-assisted synthesis of V₂O₅ nanoparticles for photocatalytic and antibacterial studies. *Mater. Res. Innov.* 2020, 24, 229–234. [CrossRef]
- 25. Aslam, M.; Ismail, I.; Salah, N.; Chandrasekaran, S.; Qamar, M.; Hameed, A. Evaluation of sunlight induced structural changes and their effect on the photocatalytic activity of V₂O₅ for the degradation of phenols. *J. Hazard. Mater.* **2015**, 286, 127–135. [CrossRef]
- Chan, Y.-L.; Pung, S.-Y. Sreekantan, Synthesis of V₂O₅ nanoflakes on PET fiber as visible-light-driven photocatalysts for degradation of RhB dye. J. Catal. 2014, 2014, 370696.
- Saravanan, R.; Gupta, V.; Mosquera, E.; Gracia, F. Preparation and characterization of V₂O₅/ZnO nanocomposite system for photocatalytic application. J. Mol. Liq. 2014, 198, 409–412. [CrossRef]
- 28. Rasheed, R.; Mansoor, H.; Abdullah, T.; Juzsakova, T.; Al-Jammal, N.; Salman, A.D.; Al-Shaikhly, R.R.; Le, P.; Domokos, E.; Abdulla, T.A. Synthesis, characterization of V₂O₅ nanoparticles and determination of catalase mimetic activity by new colorimetric method. *J. Therm. Anal. Calorim.* **2021**, 145, 297–307. [CrossRef]
- Abdullah, T.; Juzsakova, T.; Rasheed, R.; Mallah, M.; Salman, A.; Cuong, L.; Jakab, M.; Zsirka, B.; Kułacz, K.; Sebestyén, V. V₂O₅, CeO₂ and Their MWCNTs Nanocomposites Modified for the Removal of Kerosene from Water. *Nanomaterials* 2022, 12, 189. [CrossRef] [PubMed]
- 30. Shvets, P.; Dikaya, O.; Maksimova, K.; Goikhman, A. A review of Raman spectroscopy of vanadium oxides. *J. Raman Spectrosc.* **2019**, *50*, 1226–1244. [CrossRef]
- 31. Ureña-Begara, F.; Crunteanu, A.; Raskin, J.-P. Raman and XPS characterization of vanadium oxide thin films with temperature. *Appl. Surf. Sci.* **2017**, 403, 717–727. [CrossRef]
- 32. Ilahi, B.; Abdel-Rahman, M.; Zaaboub, Z.; Zia, M.; Alduraibi, M.; Maaref, H. Thermal annealing induced multiple phase in V/V₂O₅ alternating multilayer structure. *Int. J. Mod. Phys. B* **2016**, *30*, 1650210. [CrossRef]
- 33. Wang, Y.; Rosowski, F.; Schlögl, R.; Trunschke, A. Oxygen Exchange on Vanadium Pentoxide. *J. Phys. Chem. C* **2022**, 126, 3443–3456. [CrossRef]
- 34. Kubelka, P. New contributions to the optics of intensely light-scattering materials. Part I. *Josa* **1948**, *38*, 448–457. [CrossRef] [PubMed]
- 35. Tauc, J. Optical properties and electronic structure of amorphous Ge and Si. Mater. Res. Bull. 1968, 3, 37–46. [CrossRef]
- 36. Makuła, P.; Pacia, M.; Macyk, W. How to correctly determine the band gap energy of modified semiconductor photocatalysts based on UV–Vis spectra. *J. Phys. Chem. Lett.* **2018**, *9*, 6814–6817. [CrossRef]
- 37. Schneider, K. Optical properties and electronic structure of V₂O₅, V₂O₃ and VO₂. *J. Mater. Sci. Mater. Electron.* **2020**, 31, 10478–10488. [CrossRef]
- 38. Mousavi, M.; Yazdi, S.T.; Khorrami, G. Structural, Optical and Magnetic Characterization of Vanadium Pentoxide Nanoparticles Synthesized in a Gelatin Medium. *J. Nanostruct.* **2021**, *11*, 105–113.
- 39. Das, T.; Tosoni, S.; Pacchioni, G. Structural and electronic properties of bulk and ultrathin layers of V₂O₅ and MoO₃. *Comput. Mater. Sci.* **2019**, *163*, 230–240. [CrossRef]
- 40. Khyzhun, O.; Strunskus, T.; Grünert, W.; Wöll, C. Valence band electronic structure of V₂O₅ as determined by resonant soft X-ray emission spectroscopy. *J. Electron Spectrosc. Relat. Phenom.* **2005**, 149, 45–50. [CrossRef]
- 41. Srilakshmi, P.; Maheswari, A.; Sajeev, V.; Sivakumar, M. Tuning the optical bandgap of V₂O₅ nanoparticles by doping transition metal ions. *Mater. Today Proc.* **2019**, *18*, 1375–1379. [CrossRef]
- 42. Karunakaran, C.; Senthilvelan, S. Vanadia-catalyzed solar photooxidation of aniline. *J. Colloid Interface Sci.* **2005**, 289, 466–471. [CrossRef] [PubMed]
- 43. Konstantinou, I.; Albanis, T. TiO₂-assisted photocatalytic degradation of azo dyes in aqueous solution: Kinetic and mechanistic investigations: A review. *Appl. Catal. B Environ.* **2004**, *49*, 1–14. [CrossRef]
- 44. Faisal, M.; Tariq, M.; Muneer, M. Photocatalysed degradation of two selected dyes in UV-irradiated aqueous suspensions of titania. *Dyes Pigments* **2007**, *72*, 233–239. [CrossRef]
- 45. Armaković, S.; Armaković, S.; Finčur, N.; Šibul, F.; Vione, D.; Šetrajčić, J.; Abramović, B. Influence of electron acceptors on the kinetics of metoprolol photocatalytic degradation in TiO₂ suspension. A combined experimental and theoretical study. *RSC Adv.* **2015**, *5*, 54589–54604. [CrossRef]
- 46. Armaković, S.; Armaković, S.; Šibul, F.; Četojević-Simin, D.; Tubić, A.; Abramović, B. Kinetics, mechanism and toxicity of intermediates of solar light induced photocatalytic degradation of pindolol: Experimental and computational modeling approach. *J. Hazard. Mater.* **2020**, 393, 122490. [CrossRef]
- 47. Kostić, A.J.; Kanas, N.; Rajić, V.; Sharma, A.; Bhattacharya, S.; Armaković, S.; Savanović, M.; Armaković, S. Evaluation of Photocatalytic Performance of Nano-Sized Sr_{0.9}La_{0.1}TiO₃ and Sr_{0.25}Ca_{0.25}Na_{0.25}Pr_{0.25}TiO₃ Ceramic Powders for Water Purification. *Nanomaterials* **2022**, *12*, 4193. [CrossRef]

Molecules **2023**, 28, 655 17 of 18

48. Li, B.; Xu, Y.; Rong, G.; Jing, M.; Xie, Y. Vanadium pentoxide nanobelts and nanorolls: From controllable synthesis to investigation of their electrochemical properties and photocatalytic activities. *Nanotechnology* **2006**, *17*, 2560. [CrossRef]

- 49. Stephens, P.; Devlin, F.; Chabalowski, C.; Frisch, M. Ab Initio Calculation of Vibrational Absorption and Circular Dichroism Spectra Using Density Functional Force Fields. *J. Phys. Chem.* **1994**, *98*, 11623–11627. [CrossRef]
- 50. Vosko, S.H.; Wilk, L.; Nusair, M. Accurate spin-dependent electron liquid correlation energies for local spin density calculations: A critical analysis. *Can. J. Phys.* **1980**, *58*, 1200–1211. [CrossRef]
- 51. Becke, A. Density-functional thermochemistry. III. The role of exact exchange. J. Chem. Phys. 1993, 98, 5648–5652. [CrossRef]
- 52. Lee, C.; Yang, W.; Parr, R. Development of the Colle-Salvetti correlation-energy formula into a functional of the electron density. *Phys. Rev. B* **1988**, *37*, 785. [CrossRef] [PubMed]
- 53. Rassolov, V.; Pople, J.; Ratner, M.; Windus, T.L. 6-31G* basis set for atoms K through Zn. J. Chem. Phys. 1998, 109, 1223–1229. [CrossRef]
- 54. Rassolov, V.; Ratner, M.; Pople, J.; Redfern, P.; Curtiss, L. 6-31G* basis set for third-row atoms. *J. Comput. Chem.* **2001**, 22, 976–984. [CrossRef]
- 55. Ditchfield, R.; Hehre, W.; Pople, J. Self-Consistent Molecular-Orbital Methods. IX. An Extended Gaussian-Type Basis for Molecular-Orbital Studies of Organic Molecules. *J. Chem. Phys.* **1971**, *54*, 724–728. [CrossRef]
- 56. Jacobson, L.; Bochevarov, A.; Watson, M.; Hughes, T.; Rinaldo, D.; Ehrlich, S.; Steinbrecher, T.; Vaitheeswaran, S.; Philipp, D.; Halls, M. Automated transition state search and its application to diverse types of organic reactions. *J. Chem. Theory Comput.* 2017, 13, 5780–5797. [CrossRef]
- 57. Cao, Y.; Hughes, T.; Giesen, D.; Halls, M.; Goldberg, A.; Vadicherla, T.; Sastry, M.; Patel, B.; Sherman, W.; Weisman, A.; et al. Highly efficient implementation of pseudospectral time-dependent density-functional theory for the calculation of excitation energies of large molecules. *J. Comput. Chem.* **2016**, *37*, 1425–1441. [CrossRef]
- 58. Bochevarov, A.; Harder, E.; Hughes, T.; Greenwood, J.; Braden, D.; Philipp, D.; Rinaldo, D.; Halls, M.; Zhang, J.; Friesner, R. Jaguar: A high-performance quantum chemistry software program with strengths in life and materials sciences. *Int. J. Quantum Chem.* 2013, 113, 2110–2142. [CrossRef]
- 59. Cao, Y.; Halls, M.; Vadicherla, T.; Friesner, R.A. Pseudospectral implementations of long-range corrected density functional theory. *J. Comput. Chem.* **2021**, 42, 2089–2102. [CrossRef]
- 60. Yanai, T.; Tew, D.; Handy, N. A new hybrid exchange–correlation functional using the Coulomb-attenuating method (CAM-B3LYP). *Chem. Phys. Lett.* **2004**, 393, 51–57. [CrossRef]
- 61. McLean, A.; Chandler, G. Contracted Gaussian basis sets for molecular calculations. I. Second row atoms, Z = 11–18. *J. Chem. Phys.* **1980**, 72, 5639–5648. [CrossRef]
- 62. Krishnan, R.; Binkley, J.; Seeger, R.; Pople, J.A. Self-consistent molecular orbital methods. XX. A basis set for correlated wave functions. *J. Chem. Phys.* **1980**, 72, 650–654. [CrossRef]
- 63. Liakos, D.; Guo, Y.; Neese, F. Comprehensive Benchmark Results for the Domain Based Local Pair Natural Orbital Coupled Cluster Method (DLPNO-CCSD(T)) for Closed- and Open-Shell Systems. *J. Phys. Chem. A* **2020**, 124, 90–100. [CrossRef]
- 64. Neese, F.; Wennmohs, F.; Hansen, A.; Becker, U. Efficient, approximate and parallel Hartree–Fock and hybrid DFT calculations. A 'chain-of-spheres' algorithm for the Hartree–Fock exchange. *Mov. Front. Quantum Chem.* **2009**, 356, 98–109. [CrossRef]
- 65. Guo, Y.; Riplinger, C.; Liakos, D.; Becker, U.; Saitow, M.; Neese, F. Linear scaling perturbative triples correction approximations for open-shell domain-based local pair natural orbital coupled cluster singles and doubles theory [DLPNO-CCSD(T0/T)]. *J. Chem. Phys.* **2020**, *152*, 024116. [CrossRef]
- 66. Neese, F. Software update: The ORCA program system—Version 5.0. WIREs Comput. Mol. Sci. 2022, 12, e1606. [CrossRef]
- 67. Neese, F. Software update: The ORCA program system, version 4.0. WIREs Comput. Mol. Sci. 2018, 8, e1327. [CrossRef]
- 68. Neese, F. The ORCA program system. WIREs Comput. Mol. Sci. 2012, 2, 73–78. [CrossRef]
- 69. Neese, F.; Wennmohs, F.; Becker, U.; Riplinger, C. The ORCA quantum chemistry program package. *J. Chem. Phys.* **2020**, 152, 224108. [CrossRef] [PubMed]
- 70. Neese, F. The SHARK integral generation and digestion system. J. Comput. Chem. 2022, 44, 381–396. [CrossRef]
- 71. Armaković, S.; Armaković, S. Atomistica.online—Web application for generating input files for ORCA molecular modelling package made with the Anvil platform. *Mol. Simul.* **2023**, 49, 117–123. [CrossRef]
- 72. Perdew, J.; Burke, K.; Ernzerhof, M. Generalized Gradient Approximation Made Simple. *Phys. Rev. Lett.* **1996**, 77, 3865–3868; Erratum in *Phys. Rev. Lett.* **1997**, 78, 1396. [CrossRef]
- 73. Grimme, S.; Antony, J.; Ehrlich, S.; Krieg, H. A consistent and accurate ab initio parametrization of density functional dispersion correction (DFT-D) for the 94 elements H-Pu. *J. Chem. Phys.* **2010**, *132*, 154104. [CrossRef] [PubMed]
- 74. Caldeweyher, E.; Ehlert, S.; Hansen, A.; Neugebauer, H.; Spicher, S.; Bannwarth, C.; Grimme, S. A generally applicable atomic-charge dependent London dispersion correction. *J. Chem. Phys.* **2019**, *150*, 154122. [CrossRef] [PubMed]
- 75. Grimme, S.; Ehrlich, S.; Goerigk, L. Effect of the damping function in dispersion corrected density functional theory. *J. Comput. Chem.* **2011**, 32, 1456–1465. [CrossRef] [PubMed]
- 76. Caldeweyher, E.; Bannwarth, C.; Grimme, S. Extension of the D3 dispersion coefficient model. *J. Chem. Phys.* **2017**, 147, 034112. [CrossRef]
- 77. Smith, D.; Burns, L.; Patkowski, K.; Sherrill, C.D. Revised Damping Parameters for the D3 Dispersion Correction to Density Functional Theory. *J. Phys. Chem. Lett.* **2016**, 7, 2197–2203. [CrossRef] [PubMed]

Molecules **2023**, 28, 655 18 of 18

78. Anisimov, V.; Zaanen, J.; Andersen, O.K. Band theory and Mott insulators: Hubbard U instead of Stoner I. *Phys. Rev. B* **1991**, 44, 943–954. [CrossRef] [PubMed]

- 79. Giannozzi, P.; Andreussi, O.; Brumme, T.; Bunau, O.; Nardelli, M.B.; Calandra, M.; Car, R.; Cavazzoni, C.; Ceresoli, D.; Cococcioni, M.; et al. Advanced capabilities for materials modelling with Quantum ESPRESSO. *J. Phys. Condens. Matter.* **2017**, 29, 465901. [CrossRef] [PubMed]
- 80. Scandolo, S.; Giannozzi, P.; Cavazzoni, C.; de Gironcoli, S.; Pasquarello, A. Baroni, First-principles codes for computational crystallography in the Quantum-ESPRESSO package. *Z. Krist. Cryst. Mater.* **2005**, 220, 574–579. [CrossRef]
- 81. Giannozzi, P.; Baseggio, O.; Bonfà, P.; Brunato, D.; Car, R.; Carnimeo, I.; Cavazzoni, C.; de Gironcoli, S.; Delugas, P.; Ruffino, F.F.; et al. Quantum ESPRESSO toward the exascale. *J. Chem. Phys.* **2020**, *152*, 154105. [CrossRef] [PubMed]
- 82. Giannozzi, P.; Baroni, S.; Bonini, N.; Calandra, M.; Car, R.; Cavazzoni, C.; Ceresoli, D.; Chiarotti, G.L.; Cococcioni, M.; Dabo, I.; et al. QUANTUM ESPRESSO: A modular and open-source software project for quantum simulations of materials. *J. Phys. Condens. Matter.* 2009, 21, 395502. [CrossRef] [PubMed]

Disclaimer/Publisher's Note: The statements, opinions and data contained in all publications are solely those of the individual author(s) and contributor(s) and not of MDPI and/or the editor(s). MDPI and/or the editor(s) disclaim responsibility for any injury to people or property resulting from any ideas, methods, instructions or products referred to in the content.



Contents lists available at ScienceDirect

Journal of Physics and Chemistry of Solids

journal homepage: www.elsevier.com/locate/jpcs





Composite nanofibers electrospun from cerium, titanium, and zinc precursors

L.R. Padilla Jr. ^a, N. Stojilovic ^{a,b,*}, M. Grujić-Brojčin ^c, M. Šćepanović ^c, N. Tomić ^c, B. Simović ^d, G.R. Potratz ^a, G. Gopalakrishnan ^e

- ^a Department of Chemistry, University of Wisconsin Oshkosh, Oshkosh, WI, 54901, USA
- ^b Department of Physics and Astronomy, University of Wisconsin Oshkosh, Oshkosh, WI, 54901, USA
- ^c Institute of Physics Belgrade, University of Belgrade, Pregrevica 118, Belgrade, 11080, Serbia
- ^d Institute for Multidisciplinary Research, University of Belgrade, Kneza Višeslava 1, Belgrade, 11030, Serbia
- ^e Department of Engineering Physics, University of Wisconsin Platteville, WI, 53818, USA

ARTICLE INFO

Keywords: Electrospinning Nanofibers Ceria Zinc oxide Zinc titanate

ABSTRACT

Non-woven fibers were produced by sol-gel and electrospinning methods, from a solution containing cerium nitrate, zinc acetate, titanium isopropoxide, polyvinylpyrrolidone, acetic acid, ethanol, and water. The fibers were calcined at various temperatures ranging from 300 to 900 °C and were characterized using Scanning Electron Microscopy (SEM), X-Ray diffraction (XRD), Brunauer-Emmett-Teller (BET) surface area analysis, Energy Dispersive X-ray (EDX), Raman spectroscopy, Thermogravimetric analysis (TGA) and differential scanning calorimetry (DSC). Structural characterization revealed the fluorite nanocrystalline phase of ceria (CeO₂) at all temperatures, the wurtzite zinc oxide (ZnO) phase in the 300–500 °C range, and a variety of zinc titanate phases (such as ZnTiO₃, Zn₂Ti₃O₈ and Zn₂TiO₄) at higher temperatures. Titania (TiO₂) phases were not observed following calcination up to 900 °C. The average ceria nanocrystallite size increases with calcination temperature, as revealed by XRD and confirmed by the Phonon Confinement Model (PCM) of Raman spectra. The opposite trend is observed for the BET specific surface area of the nanofibers, where this value decreases with calcination temperatures above 400 °C. These nanofibers containing ceria and zinc titanates are potential candidates for photocatalytic applications.

1. Introduction

Electrospinning is a relatively inexpensive and simple method for making non-woven nanofibers [1–3]. One of the notable advantages of this method is the ability to tailor the chemical composition, and thus the properties of the fibers, through the choice of polymer and inorganic components. The electrospinning method is typically coupled with the sol-gel preparation process. A sol-gel is prepared by mixing a polymer with inorganic precursor and solvents, until a desired rheology for electrospinning is achieved. Electrospinning the solution under high voltage (typically between 10 and 20 kV) produces fibers containing an amorphous mixture of polymer and inorganic material, which, after calcination at high temperatures, results in the formation of metal-oxide nanofibers. Calcination of as-spun nanofibers first removes moisture and solvents, followed by removal of polymer at temperatures between 400 °C and 500 °C, and results in the formation of metal-oxides

nanofibers.

Composite metal-oxide nanofibers have potential applications ranging from environmental [4], to catalysis and energy storage [5]. Many of these potential applications are based on the relatively large surface area-to-volume ratios, high porosity, and various functionalities [6] of these nanofibers. Ceria or cerium dioxide (CeO₂) nanostructures have potential applications in fuel cells [7,8], optical devices [9], and in high-storage capacitors [10], to name a few. Ceria nanostructures have been made using various methods including hydrothermal [11], spray pyrolysis [12], electrosynthesis [13], and sol-gel and electrospinning [14]. Yang et al. studied the effect of calcination temperature on morphology, structure and photocatalytic activity of electrospun ceria nanofibers, reporting an increased photodegradation rate for methylene blue from 500 to 800 °C [15]. The wide band gap of ceria and its high electron-hole recombination rates reduce its photocatalytic efficiency; however, combining ceria with other metal oxides holds great promise

^{*} Corresponding author. Department of Physics and Astronomy, University of Wisconsin Oshkosh, Oshkosh, WI, 54901, USA. *E-mail address:* stojilovicn@uwosh.edu (N. Stojilovic).

for making novel materials with enhanced photocatalytic properties [16,17]. For example, electrospun cerium-based titania nanofibers are potential candidates for photocatalytic oxidation applications [18]. Li et al. [19] produced electrospun CeO₂–ZnO composite nanofibers using zinc acetate and cerium nitrate precursors, with poly(vinylpyrrolidone) fiber template, and investigated their photocatalytic properties. They calcined fibers at 600 °C for 3 h, and observed almost complete decomposition of the Rhodamine B, making these composite nanofibers good candidates for use in the purification of organically polluted water.

 TiO_2 –ZnO composite nanofibers have been fabricated by electrospinning a solution based on tetraisopropyl titanate, zinc acetate dihydrate, and polyvinylpyrrolidone (PVP). The resulting nanofibers exhibited three different crystalline phases (anatase and rutile titania (TiO_2), and wurtzite ZnO) [20]. In another study, it has been reported that TiO_2 binds ZnO and decreases its sublimation rate [21]. Zn–Ti composite oxides can also exist in Zn₂TiO₄ (cubic), ZnTiO₃ (hexagonal), and Zn₂Ti₃O₈ (cubic) structures [22]. For example, Cai et al. [23] produced the zinc titanate composite nanofibers using sol-gel and electrospinning methods, followed by calcination. They synthesized ZnO–TiO₂ ceramic nanofibers including ZnTiO₃, Zn₂TiO₄, and rutile phases by calcination at 700 °C. Pinto et al. [24] fabricated Zn–Zn₂TiO₄ nanocomposites from zinc hydroxide nitrate and proposed them as promising materials for photocatalytic degradation of complex organic compounds.

The main goal of this study is to produce novel, composite, metaloxide nanofibers by calcining an electrospun sol-gel from relatively inexpensive Ce, Ti, Zn precursors, and to understand how calcination temperature affects their physical properties and the formation of crystalline phases. The resulting nanofibers are characterized using Scanning Electron Microscopy (SEM), X-Ray diffraction (XRD), Brunauer-Emmett-Teller (BET) surface area analysis, Energy Dispersive X-ray (EDX), Raman spectroscopy, Thermogravimetric analysis (TGA) and differential scanning calorimetry (DSC).

2. Experimental procedures

2.1. Materials and methods

Acetic acid, ethanol, zinc acetate dihydrate (Zn(CH₃COO)₂·2H₂O), titanium (IV) isopropoxide (Ti(OCH(CH₃)₂)₄), and polyvinylpyrrolidone (PVP) ($M_w=1\,300\,000$) were purchased from Sigma-Aldrich, while cerium(III) nitrate hexahydrate (Ce(NO₃)₃·6H₂O) was purchased from Alfa Aesar. All of the materials were used without further purification.

2.2. Preparation of solutions and electrospinning

In a typical experiment, 0.28 g of zinc acetate and 0.42 g of cerium nitrate were dissolved in 12 mL of a 2:1 (v/v) ethanol/water mixture. The solution was transferred into an Erlenmeyer flask containing 0.24 g of titanium isopropoxide and 0.5 mL of acetic acid. Then, 1.3 g of polyvinylpyrrolidone (PVP) was added to the flask. The flask was capped with a rubber stopper, and the solution was stirred for 3 h. After stirring, 5 mL of the solution was transferred into a 5 mL plastic syringe for electrospinning.

An electrospinning apparatus, consisting of a syringe pump (WPI SP101I), a high voltage supply (Gamma High Voltage Research ES), a 5 mL plastic syringe connected to a 30 cm plastic tube, a metallic needle (inner diameter =0.8 mm), and grounded aluminum foil for collecting fibers, was used to produce composite nanofibers. The sol-gel was electrospun at 18 kV, with a working distance between the tip of the needle to the aluminum foil of 15 cm, a 10 $\mu L/min$ pumping rate, and at standard temperature and pressure. The as-spun fibers were calcined in air, in a tube furnace (Blue M Minimite) at a rate of $1^{\circ}/min$, at temperatures ranging between 300 $^{\circ}C$ and 900 $^{\circ}C$. The fibers were calcined for 5 h at each temperature.

2.3. Characterization

2.3.1. Scanning Electron Microscopy and energy dispersive X-ray spectroscopy

The surface morphologies of the nanofibers were studied using a scanning electron microscope (SEM, Hitachi S–3000 N), operating at 28 kV. Before imaging, the fibers were sputter coated with precious metals using a Denton Desk 2 Sputter/Etch Unit, to reduce charging effects. The elemental composition of the nanofibers was analyzed using Bruker QUANTAX 100, operating at 15 kV.

2.3.2. Nitrogen physisorption at 77 K

Specific surface area and pore size distribution of the calcined composite nanofibers were obtained using Brunauer–Emmett–Teller (BET) [25] and Barrett–Joyner–Halenda (BJH) [26] methods, respectively. The samples were degassed at 290 $^{\circ}\text{C}$ for 3 h and then analyzed using NOVA 4200e Surface Area & Pore Size Analyzer (Quantachrome Instruments). The measurements were performed using N_2 adsorption at 77 K (-196 $^{\circ}\text{C}$). The BET experiments were performed several times on each sample to confirm reproducibility.

2.3.3. X-ray diffraction

Structural properties of the fibers were characterized by powder X-ray diffraction (XRD, Rigaku D/Max 2200), operating at 40 kV and 40 mA, with $\lambda=0.154$ nm X-rays. The step size was 0.02° , and the scan speed was 1° per minute. The fibers were ground into powders for XRD analysis.

2.3.4. Raman spectroscopy

Raman scattering spectra were recorded with backscattering geometry at room temperature in open air. A Jobin-Yvon T64000 triple spectrometer (gratings with 1800 grooves/mm) equipped with a confocal microscope and a nitrogen–cooled charge-coupled device detector was used. The samples were excited by a 514.5 nm line of Ar^+/Kr^+ ion laser with an output power of $\sim\!10$ mW.

2.3.5. Thermogravimetric analysis (TGA) and differential scanning calorimetry (DSC)

TGA/DCS analysis was performed using a SDT Q600 instrument (TA Instruments) from room temperature up to 1000 °C, under a dynamic air atmosphere (heating rate: 20 °C/min, flow rate: 100 ml/min).

3. Results and discussion

3.1. SEM

Scanning electron microscopy (SEM) was used to confirm the fibrous nature of the electrospun material and to probe the surface morphology of the fibers. Fig. 1 displays SEM images of the composite nanofibers before calcination (left panel), and the fibers after calcination at 600 °C for 5 h (right panel). The images were taken using a beam operating at 28 kV, and the scale bars are 5 μm . The thickness of the nanofibers depends on different experimental parameters. The diameter of the asspun fibers was 290 \pm 40 nm and after calcination it decreased to 180 \pm 10 nm. The decrease in the thickness of the fibers after calcination reflects the removal of the PVP polymer template. The nanofibers become harder and more brittle with increase in calcination temperature.

3.2. EDX

The representative energy dispersive X-ray (EDX) spectrum of the composite nanofibers calcined at 600 °C for 5 h is shown in Fig. 2. The atomic percentages were obtained using C–K, O–K, Ti–K, Zn–K, and Ce-L signals. The carbon and part of the oxygen signals originate from the sample mounting assembly. The elemental composition (in at. %) of the

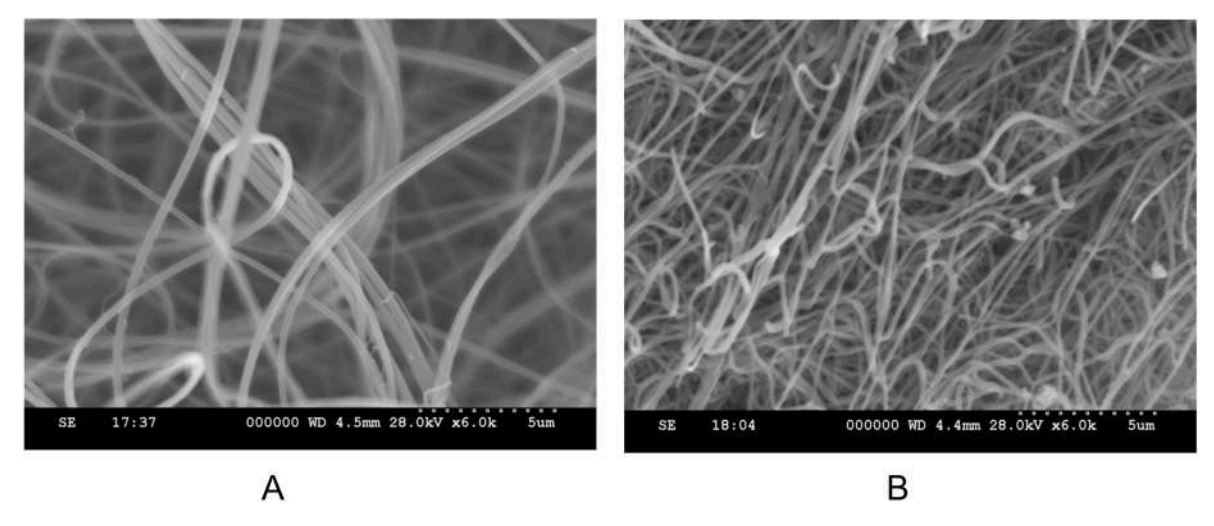


Fig. 1. SEM images of as-spun nanofibers (left panel), and fibers calcined at 600 °C for 5 h (right panel).

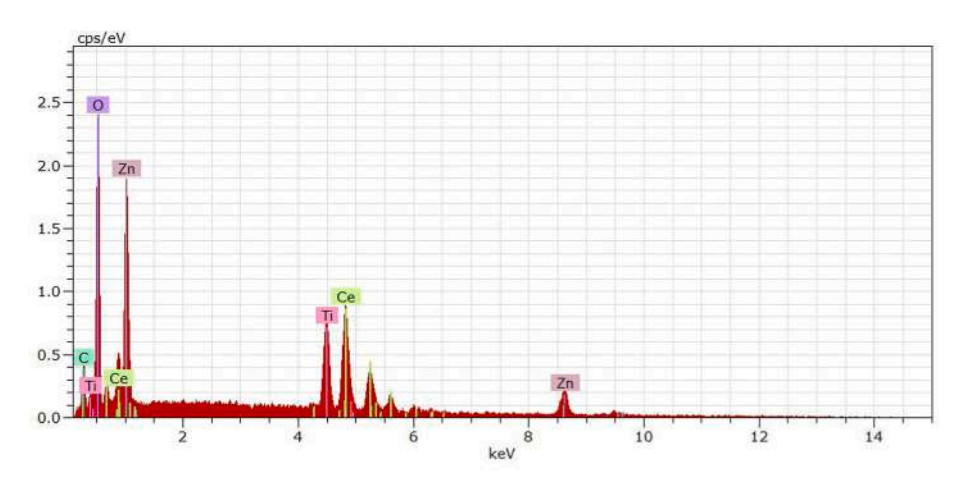


Fig. 2. EDX spectrum of composite nanofibers calcined at 600 °C for 5 h, recorded at 15 kV excitation.

calcined composite nanofibers, corresponding to Fig. 2, are: 60% O, 17% Zn, 12% Ti, and 11% Ce. Carbon was not included in the calculation. Similar compositions were observed for other samples calcined between 300 and 900 °C. The measured percentages are consistent (within experimental uncertainty) with the values calculated based on the amount of chemical used.

3.3. BET

The BET [25] experiments were performed using N2 physisorption under isothermal (77 K) conditions. Fig. 3 shows the specific surface area ($S_{\rm BET}$) of composite nanofibers as a function of calcination temperature. Nanofibers calcined at 400 °C exhibit the largest specific surface area, $S_{\rm BET} = 74 \text{ m}^2/\text{g}$, and as the size of the CeO₂ crystallites increases, the specific surface area of the nanofibers decreases. Effect of calcination temperature on morphology and structure of electrospun CeO₂ nanofibers was also investigated by Yang et al. [15]. It was reported that the specific surface area decreased from 56.3 to $3.3 \text{ m}^2/\text{g}$ as temperature increased from 500 to 800 $^{\circ}\text{C}.$ In the same study, it was found that the photodegradation rate of methylene blue was increased from 67 to 98% for ceria calcined at 500 and 800 $^{\circ}\text{C},$ revealing that the photocatalytic activity of ceria nanofibers is not only related to the specific surface area, and that increasing the calcination temperature increases crystallinity, providing conditions for improved photocatalytic activity. They reported the greatest specific surface area for a calcination

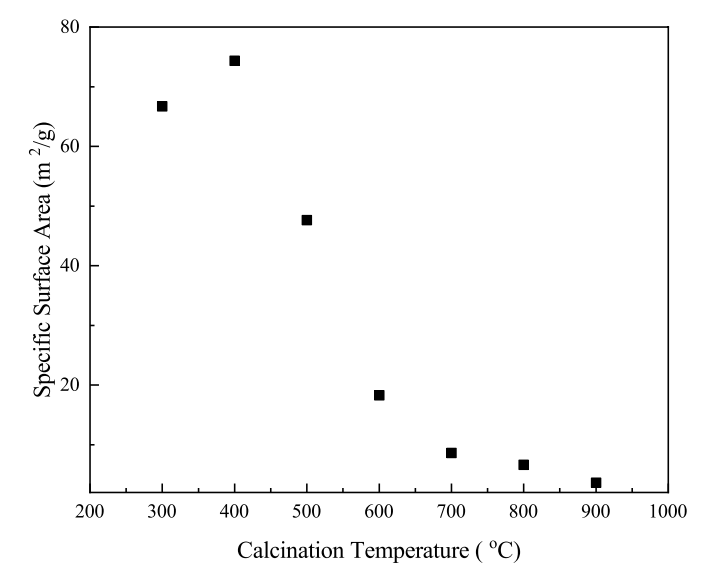


Fig. 3. BET specific surface area of the composite metal oxide nanofibers as a function of calcination temperature.

temperature of 500 °C. In our study, the greatest specific surface area was found after calcinations at 400 °C. The $S_{\rm BET}$ increases from 300 to 400 °C and then drops as the calcination temperature is raised to 900 °C. Using the BJH method [26], the pore volume was estimated at 0.05 cm³/g and pore radius was 1.5 nm. The value of $S_{\rm BET}$ is an important parameter in catalysis, and it typically increases with decrease in particle size and decreases with increase in calcination temperature. Our BET results reveal that ceria-based nanofibers have greater values of $S_{\rm BET}$ below 500 °C than above this temperature. It is thus important to compare the temperature trend of specific surface area with the temperature trend of average CeO₂ particle size estimated from XRD and Raman analysis.

3.4. XRD

The XRD patterns of the composite metal-oxide nanofibers (as-spun and calcined at temperatures in the range of 300–900 °C) are shown in Fig. 4. The diffraction peaks observed at $\sim\!31.8,\,34.4,\,36.3$ and $63.0^{\rm o}$ in diffractograms of nanofibers calcined in the 300–500 °C temperature range are ascribed to wurtzite ZnO (JCPDS card 36–1451, space group P63mc). Although the formation of oxides within the nanofiber structures at temperatures below 400 °C is rare, in a related study Turinske et al. [27] observed the formation of ZnO within polymer-based fibers after calcination at 120 °C.

The peaks at ~28.5, 33.1, 47.5, 56.5, 59.1, 69.4, 76.8, 79.1, and 88.4°, noticed in the diffractograms of nanofibers calcined from 300 to 900 °C, have revealed formation of CeO₂ fluorite crystalline structure (JCPDS card 34–0394, space group Fm3m). The CeO₂ diffraction peaks sharpen and increase in intensity with temperature up to 900 °C as a result of CeO₂ crystallization, which remains in its fluorite phase in whole temperature range. The average crystallite size, d, of the CeO₂ crystalline phase was estimated using the Scherrer formula, $d = K\lambda/\beta\cos\theta$, where K is the shape factor, β is the full width at half maximum (FWHM) of the (111) diffraction peak, λ is the wavelength, and θ is the Bragg's angle. The value of d is not greater than the grain size. The calcination temperature of 300 °C results in the CeO₂ average crystallite size of 4 nm, and further increase in temperature increases the crystallite size, with 900 °C calcination corresponding to a size of approximately 52 nm.

Fig. 4 shows that beside the peaks, which may be assigned to ZnO and CeO₂, there are no other phases formed in the samples calcined in

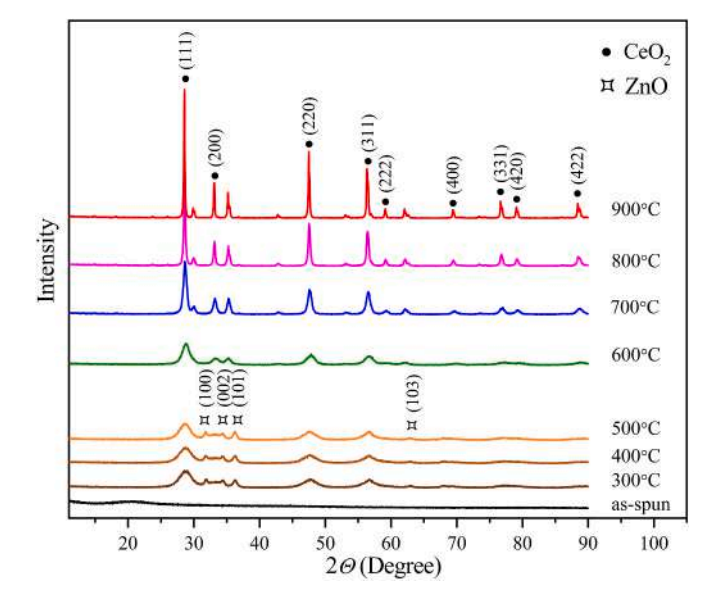


Fig. 4. XRD pattern of as-spun and fibers calcined for 5 h, at temperatures ranging from 300 to 900 $^{\circ}$ C (CeO₂ and ZnO peaks denoted by "•" and " \square " respectively, together with corresponding reflections).

the temperature range of 300–500 °C. However, in patterns of samples calcined at 600–900 °C, in addition to CeO $_2$, the peaks which could be related to zinc titanates phases appear [28–30]. Having in mind that titanium oxide (TiO $_2$) phases were not detected in XRD patterns in Fig. 4 up to 900 °C, this means that titanium combines with zinc and oxygen to form zinc titanate, instead of going through any titania phase. Note that doubling the concentration of titanium isopropoxide in the initial solution did not result in the formation of titanium dioxide within the composite nanofibers either.

In order to analyze zinc titanate peaks more thoroughly, the diffractograms of composite metal-oxide nanofibers calcined at $600-900\,^{\circ}\text{C}$ are shown in Fig. 5(a), at an enlarged scale.

Broad diffraction peaks noticed at ~35.3, 42.8, 53.1, and 62.1° in the difractogram of the nanofibers calcined at 600 °C could be ascribed to (311), (400), (422) and (440) reflections of cubic ZnTiO₃ and/or $Zn_2Ti_3O_8$ according to JCPDS cards 39–0190 and 87–1781, respectively. As pointed out by Budigi et al. [29], it is difficult to differentiate cubic phase ZnTiO₃ and cubic phase Zn₂Ti₃O₈ because they have similar crystal structure and lattice parameters [31]. From 600 °C to 700 °C, the crystallinity of these cubic phases increases, as evidenced from the increase in the mentioned XRD peaks, as well as from the appearance of several lower intensity peaks (as shown in Fig. 5(a)). In the pattern of nanofibers calcined at 800 °C, each of the peaks located at ~18.1, 30.0, 35.2, 42.9, 53.2, and 62.1° split into two. This splitting is more pronounced at 900 °C, which suggests the appearance of a different cubic phase, Zn₂TiO₄ (JCPDS card 25–1164), at these temperatures (see Fig. 5 (a)). The evolution of cubic zinc titanate phases with temperature (Fig. 5 (b)) is followed through the analysis of shift and shape of the (311) reflection peak. The broadening and low intensity of the peak at $\sim 35.3^{\circ}$ points to the coexistence of cubic Zn₂Ti₃O₈ and ZnTiO₃ in nanofibers calcined at 600 °C. This peak (denoted by "1") is narrowing and growing in nanofibers calcined at 700 °C, and a second peak ("2") corresponding to Zn₂TiO₄ appears at a lower diffraction angle. The second peak is narrowing, and its intensity increases relative to the intensity of the first peak, becoming dominant in the sample calcined at 900 °C. At the same temperature, the first peak is narrowed and slightly shifted to a higher angle, suggesting that it originates only from Zn₂Ti₃O₈. Note that the presence of hexagonal ZnTiO3 phase cannot be unambiguously established, because most of its diffraction peaks overlap with the peaks of the mentioned cubic zinc titanate phases. Moreover, detection of hexagonal ZnTiO₃ in the XRD patterns shown in Fig. 5(a) is made even more difficult because it is the most intensive, distinctive peak (104) located at 32.8° is overlapped with higher intensity (200) peak of CeO₂.

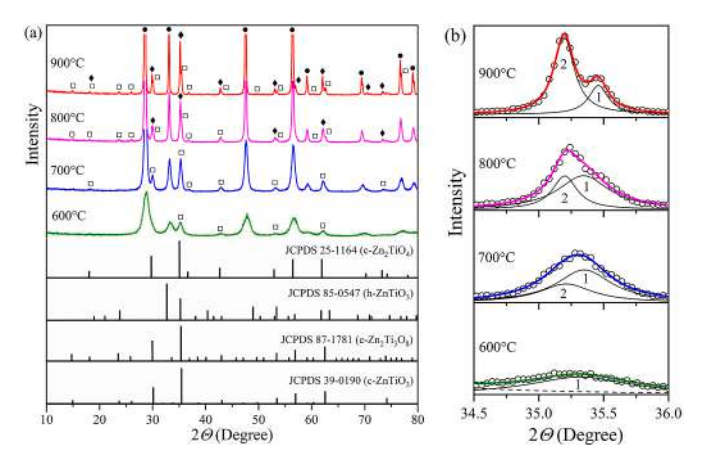


Fig. 5. (a) XRD pattern of nanofibers calcined at temperatures ranging from 600 to 900 °C (phases denoted by: "•" - CeO₂, "•" - Zn₂TiO₄ and "□" - Zn₂Ti₃O₈). The JCPDS cards of cubic and hexagonal ZnTiO₃, as well as cubic Zn₂Ti₃O₈ and Zn₂TiO₄, are shown. (b) Shift in (311) reflection for the cubic zinc titanate nanofibers calcined at 600–900 °C (fitted by Lorentzians: "1" - Zn₂Ti₃O₈/ZnTiO₃, "2" - Zn₂TiO₄).

Therefore, the presence of hexagonal phase can neither be confirmed nor excluded.

3.5. Raman scattering measurements

The Raman spectra of composite metal-oxide nanofibers calcined at 400, 500, 600, 700, and 900 °C are shown in Fig. 6. In the spectra of the sample calcined at 400 °C, no relevant Raman features were noticed, due to the strong background signal. All other spectra are dominated by the Raman mode at \sim 465 cm⁻¹ ascribed to the first order F_{2g} mode of CeO₂ fluorite structure [14]. In the spectra of the sample calcined at 900 °C, the position and linewidth of F_{2g} mode correspond to values that are characteristic to bulk CeO₂ [32]. This mode is significantly shifted and asymmetrically broadened to lower frequencies (redshift) in the spectra of samples calcined at lower temperatures. The Phonon Confinement Model (PCM) is used to analyze this Raman shift and broadening.

The PCM is phenomenological method often used to simulate experimental Raman spectra by considering different nanoscale effects [33]. In this model, several independent factors (phonon confinement, strain, non-homogeneity of the size distribution and variations in phonon relaxation with crystallite size decrease) contribute to the changes in the position and linewidth of calculated Raman modes [34–38]. Due to crystallite size decrease, the phonons are confined, and optical phonons over the entire Brillouin zone contribute to the first-order Raman spectra. The Raman intensity $I(\omega)$ for effective crystallite size and Gaussian confinement function is calculated as a superposition of weighted Lorentzian contributions over the whole Brillouin zone [34–36]:

$$I(\omega) \propto \sum_{i=1}^{n} \int_{0}^{\infty} \rho(L) dL \int_{BZ} \frac{exp\left(\frac{-q^{2}L^{2}}{8\beta}\right) d^{3}q}{\left(\omega - \left(\omega_{i}(q) + \Delta\omega\right)\right)^{2} + \left(\frac{\Gamma}{2}\right)^{2}}$$
(1)

with $\rho(L)$ – distribution of crystallite size L, q - wave vector, β - confinement strength and Γ - the intrinsic mode linewidth. The Brillouin

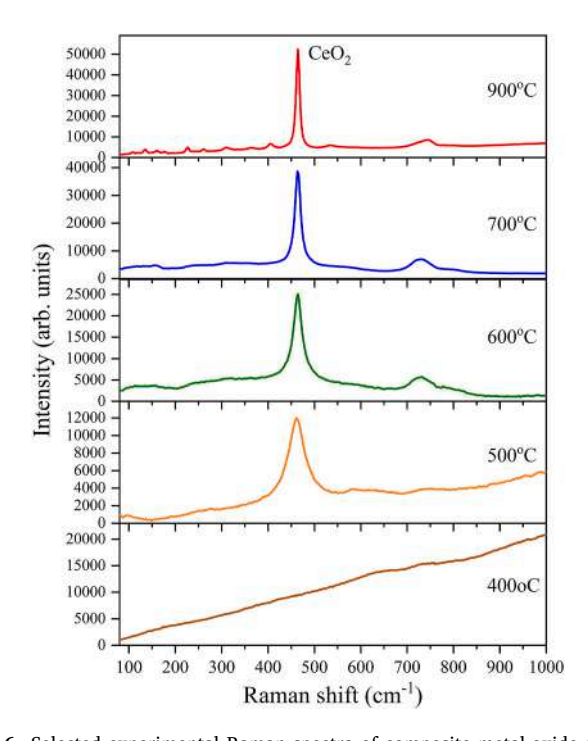


Fig. 6. Selected experimental Raman spectra of composite metal-oxide nanofibers calcined at different temperatures (the spectra of the samples calcined at 500, 600 and 700 $^{\circ}$ C were collected with an accumulation time of 200 s, whereas the accumulation time for those at 400 and 900 $^{\circ}$ C were 2 and 30 s, respectively).

zone is approximated as a sphere, and the sum is carried over n phonon dispersion curves $\omega_i(q)$, with mode degeneracy and symmetry of zone directions taken into account. The dispersions are taken from corresponding bulk counterparts, due to lack of appropriate experimental and theoretical dispersions of nanocrystalline materials [36,38,39]. The additional shift of Raman mode $\Delta\omega$ may appear due to relative variation of lattice parameters. The crystallite size distribution in Eq. (1) is defined by Gaussian distribution

$$\rho(L) = \frac{1}{\sigma\sqrt{2\pi}} exp\left(-\frac{(L-L_0)^2}{2\sigma^2}\right)$$
 (2)

with effective crystallite size, L_0 , and standard deviation, σ .

Simulated spectra obtained by PCM are shown in the range of 350–550 cm $^{-1}$ in Fig. 7(a), together with normalized Raman spectra of nanofibers calcined at 500, 600, 700 and 900 °C. The following room-temperature parameters have been used in PCM: the phonon strength $\beta=2\pi^2$ [35], intrinsic linewidth $\Gamma=9$ cm $^{-1}$, and phonon dispersion functions taken in the polynomial form, based on the data given by Nakajima et al. [32,37,38], with the frequency of the F_{2g} mode at the Brillouin zone center, corresponding to bulk value (465 cm $^{-1}$) [32]. The integration is performed along the weighted high-symmetry directions in the Brillouin zone (Δ , Σ , and Δ) [32,36–39]. Average nanocrystallite size L_0 and standard deviation σ were numerically adjusted to achieve the best agreement between experimental and simulated spectra.

The Raman shift and broadening of F_{2g} mode in the spectra simulated by PCM corresponding to experimental spectra of samples calcined at different temperatures are shown in Fig. 7(b). These results show that Raman shift gradually increases from 462 cm⁻¹ in the spectrum corresponding to the sample calcined at 500 °C to 464.5 cm⁻¹(close to the bulk value) in the spectra of sample calcined at 900 °C. On the other hand, the F_{2g} mode linewidth drastically decreases (from 41.5 to \sim 9 cm⁻¹) with the increase of calcination temperature. These trends are the result of a variation in nanocrystallite size with temperature. Namely, with the increase of calcination temperature from 500 to 900 °C, the average crystallite size estimated by PCM increases from 6 to 50 nm. This behavior agrees well with the results obtained by XRD, as shown in Fig. 7(c).

In order to analyze the Raman features other than the ceria F_{2g} mode, the spectra of composite metal-oxide nanofibers calcined at 500, 600, 700 and 900 °C are shown in Fig. 8, at an enlarged scale. The shape of the spectra, with a broad hump in the region of 100-700 cm⁻¹, may point to the presence of some amorphous phases, probably amorphous titania [40]. The only crystalline phase, beside nanocrystalline ceria, which could be identified by the spectra of nanofibers calcined at 500 °C is wurtzite ZnO (with P63mc space group). The features located at \sim 96, 382 and 582 cm⁻¹may be assigned to the first order wurtzite Raman modes E_2^{low} , $A_1(\text{TO})$ and $A_1(\text{LO})/E_1(\text{LO})$, respectively. The wurtzite $\it E_{2}^{high}$ mode, expected at \sim 438 cm $^{-1}$ [41], is not noticed, probably due to overlap with the more intense ceria F_{2g} mode. A mode registered at \sim 276 cm $^{-1}$ may also be ascribed to the ZnO phase. This additional mode in the ZnO spectrum may be related to intrinsic host lattice defects, but its origin is still under debate [42,43]. None of these ZnO related modes are seen in the spectra of samples calcined at higher temperatures.

In the Raman spectra of samples calcined above 400 °C, a broad feature is noticed in the range of 650–850 cm⁻¹. Beside this, low intensity features at ~160 and 310 cm⁻¹ were recognized in the spectra of samples calcined at 600 and 700 °C. On the other side, well resolved Raman modes in the spectrum of the sample calcined at 900 cm⁻¹ are registered at ~160, 177, 225, 260, 310, 363, 406, 532 cm⁻¹. These modes may be related to some of the cubic zinc titanate structures. Specifically, the cubic ZnTiO₃ phase (space group $Pm\overline{3}m$) has 10 Raman active modes (5 A_g and 5 E_g) usually registered at the following positions: 152, 188, 230, 262, 348, 403, 472, 486, 622, and 717 cm⁻¹ [28]. The Zn₂TiO₄ phase has a cubic inverse spinel structure (space group $Fd\overline{3}m$)

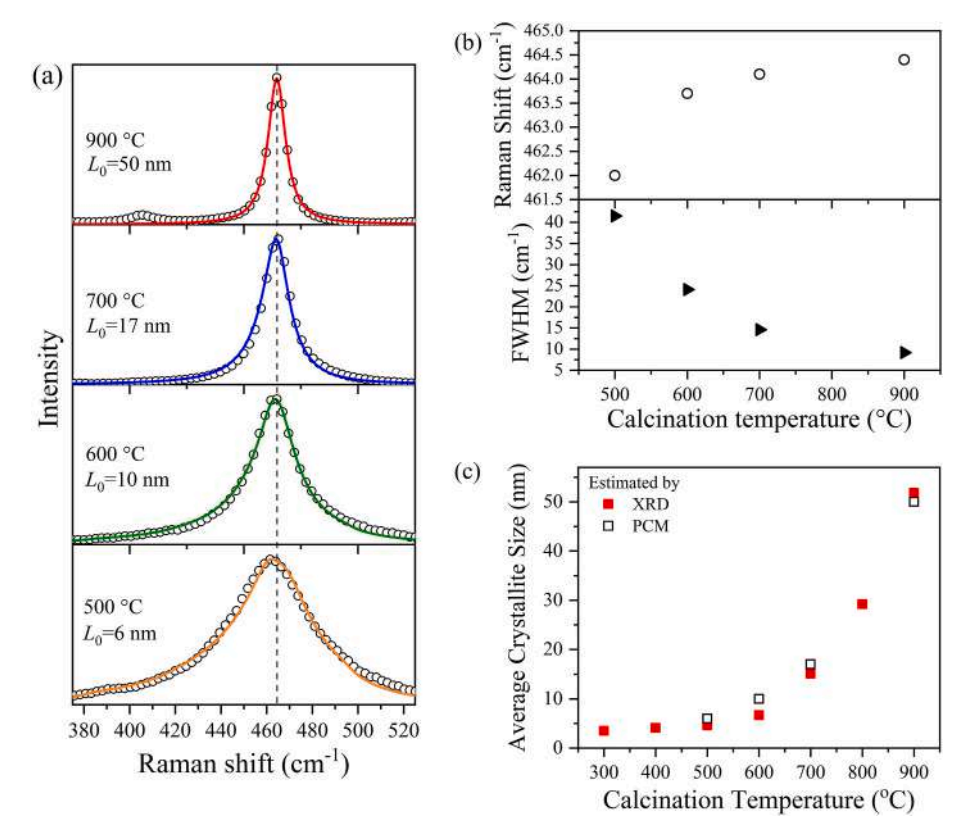


Fig. 7. (a) Experimental Raman mode assigned to the first order CeO_2 F_{2g} mode (open circles) together with PCM simulation (solid line) at different calcination temperatures; The L_0 represents the value of average nanocrystallite size estimated by PCM. (b) The dependence of the F_{2g} Raman shift and FWHM (full width at half maximum) obtained by PCM on calcination temperature. (c) The average ceria crystallite size estimated by XRD and PCM at different calcination temperatures.

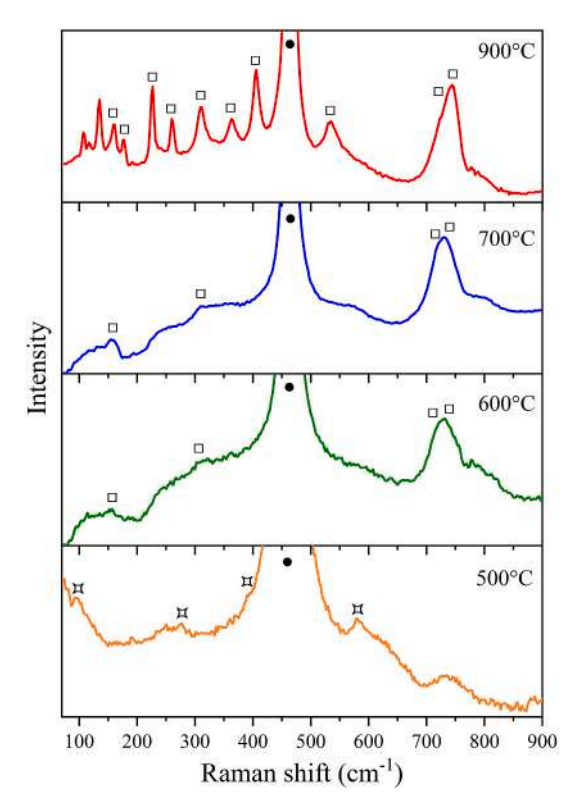


Fig. 8. Experimental Raman spectra of composite metal-oxide nanofibers calcined at 500, 600, 700 and 900 °C at an enlarged scale (wurtzite ZnO Raman modes are denoted by \Box , central position of the ceria F_{2g} mode by \blacksquare , whereas the modes ascribed to cubic zinc titanates are marked by \Box).

with 5 Raman active modes $(3F_{2g}, E_g, \text{ and } A_{1g})$ usually found around 245, 310, 470, 520, and 718 cm^{-1} [28,44]. The same space group is usually assigned to a cubic defect spinel Zn₂Ti₃O₈ [28,45]. Although there is limited Raman data related to this structure [28,45-47], the features registered at about 229, 264, 311, 366, 409, 445, 462, 536 and 751 cm⁻¹ are assigned to Zn₂Ti₃O₈ [45]. Therefore, the Raman mode in composite metal-oxide nanofibers calcined at temperatures of 600 and 700 °C, located at ~160 and 310 cm⁻¹ could be ascribed to cubic ZnTiO₃ and $Zn_2Ti_3O_8$ (and/or Zn_2TiO_4), respectively. According to the literature data listed above, in the spectrum of the sample calcined at 900 °C, the modes at \sim 160 and 177 cm⁻¹ are close to cubic ZnTiO₃ modes. Also, the modes at \sim 225, 260 and 406 cm⁻¹ could be ascribed to both cubic ZnTiO₃ and Zn₂Ti₃O₈, the mode at 310 cm⁻¹ to both Zn₂TiO₄ and $Zn_2Ti_3O_8$ and the modes at ~363 and 532 cm⁻¹ to $Zn_2Ti_3O_8$. By comparison of our experimental Raman spectra to literature data, we notice at least two zinc titanate phases with cubic structure in the nanofiber samples calcined at 600 °C and higher temperatures. In addition, even the presence of the hexagonal ZnTiO₃ phase cannot be excluded, because characteristic Raman modes of this phase (~263, 341, 530 and 709 cm^{-1}) [29,48,49] are very close to the modes of the cubic phases.

In order to analyze the presence of different zinc titanate phases in calcined nanofibers, the Raman spectra in the region from 650 to 850 cm $^{-1}$ have been fitted to the sum of four Lorentzian peaks (Fig. 9(a)). The Lorentzian centered at around 723 cm $^{-1}$ has been attributed to the A_g mode of cubic ZnTiO $_3$ [28], and/or the A_{1g} mode of Zn_TiO $_4$ structures [28,45], whereas the one at \sim 740 cm $^{-1}$ has been assigned to the A_{1g} mode of Zn_TiO $_8$ [45,46]. Beside the modes ascribed to cubic structures, the low intensity peak at \sim 710 cm $^{-1}$ could be related to hexagonal ZnTiO $_3$. Since low frequency carbon–carbon (C–C) vibrations appear at around 800 cm $^{-1}$, the peak at \sim 795 cm $^{-1}$ may be attributed to the presence of organic residuals.

The temperature dependance of Raman shift, linewidth and

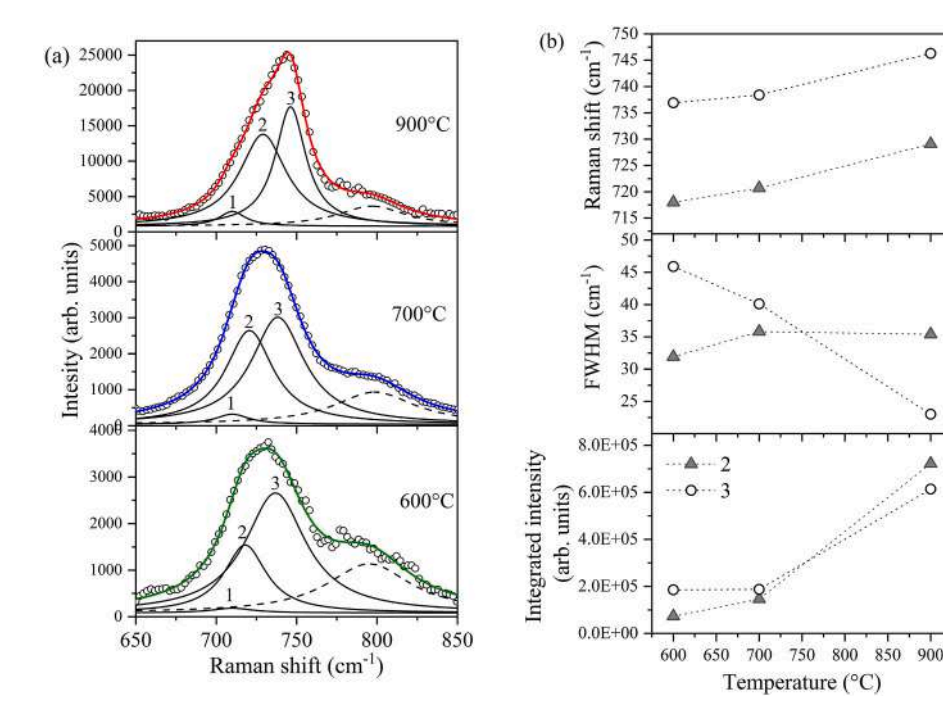


Fig. 9. (a) Experimental Raman spectra of nanofibers calcined at 600, 700 and 900 °C fitted by a sum of Lorentzian peaks in the region of 650–850 cm $^{-1}$ (the Lorentzian peaks presented by a full line correspond to: "1" – hexagonal ZnTiO₃, "2" – cubic ZnTiO₃ and/or Zn₂TiO₄, and "3" – Zn₂Ti₃O₈). (b) Variation of Raman shift, linewidth and integrated intensity of Lorentzian peaks (denoted in (a) as "2" and "3") with calcination temperature.

integrated intensity of the two modes originating from cubic zinc titanate structures is presented in Fig. 9(b). The increase of intensity, decrease of linewidth and shift towards higher frequencies of the mode at $\sim\!740~{\rm cm}^{-1}$ could be the consequence of the improved crystalline character of $\rm Zn_2Ti_3O_8$ at higher calcination temperatures. On the other hand, the variation of the mode at $\sim\!723~{\rm cm}^{-1}$, together with its broadening, may point to the partial transition of cubic $\rm Zn_2TiO_4$ at higher temperatures. Also, the increasing integrated intensity of this peak with calcination temperature, relative to intensity of the peak at $740~{\rm cm}^{-1}$, may point to $\rm Zn_2Ti_3O_8$ as a dominant phase at lower temperatures, whereas other phases (most probably $\rm Zn_2TiO_4$) become dominant at 900 °C. Note that the mode corresponding to hexagonal $\rm ZnTiO_3~(\sim\!710~{\rm cm}^{-1})$ is almost negligible at 600 °C, slightly increased at 700 °C, narrower and more pronounced at 900 °C, but still significantly less intensive than the modes of the cubic zinc titanate phases.

The analysis of the Raman results shown above confirms the findings from the XRD data. Crystalline CeO2 was observed in the Raman spectra of the nanofibers calcined at temperatures higher than 400 °C. PCM analysis of the ceria F_{2g} Raman mode has shown that the average ceria nanocrystallite size increases with calcination temperature, following the same trend estimated by XRD. The wurtzite ZnO was only detected in the Raman spectra of the nanofibers calcined at 500 °C. Raman features of any crystalline titania phase were absent in the fibers calcined in the 300-900 °C temperature range. The Raman spectra of the nanofibers calcined at 600 and 700 °C primarily point to the presence of cubic Zn₂Ti₃O₈. Detailed analysis of the spectral region of 650–850 cm⁻¹ have shown that the Zn₂Ti₃O₈ phase dominated at calcinations temperatures of 600 and 700 °C and that its crystallinity improved with the temperature increase. This analysis also shows that some combination of ZnTiO₃ and Zn₂TiO₄, both cubic phases, are present in the nanofibers calcined at 600 and 700 °C, whereas the cubic Zn₂TiO₄ phase becomes dominant at calcinations temperature of 900 °C. Also, the low intensity Raman mode at ~710 cm⁻¹ points to the low content of hexagonal ZnTiO₃ in the fibers calcined at 700 and 900 °C.

The combination of XRD and Raman spectroscopy results evidences the mixture of different zinc titanate phases in the metal-oxide nanofibers calcined at 600–900 $^{\circ}\text{C}.$ These results show that in the presence of

excess Zn relative to Ti (as determined by EDX), wurtzite ZnO is the dominant crystalline structure during the early stages of crystallization (300-500 °C), Zn₂Ti₃O₈ is preferentially formed as the calcination temperature increases, and partially transformed into Zn₂TiO₄ at 800 °C. Zn₂TiO₄ becomes the dominant zinc titanate phase at 900 °C. Similar complex temperature-dependent phase transitions have been observed in sol-gel-synthesized zinc titanates (with zinc acetate dihydrate and titanium tetraisopropoxide used as precursors) calcined at temperatures in the range of 400–1000 °C, as reported by Nolan et al. [47]. According to that study, in the presence of excess zinc (specifically, when the ratio of Zn to Ti is 4:3), a cubic defect spinel Zn₂Ti₃O₈ structure is dominant at 700-900 °C, a hexagonal ZnTiO₃ appears in small percentage (up to 10%) at calcination temperatures 800 and 900 °C, whereas direct transformation of Zn₂Ti₃O₈, as a metastable phase, into Zn₂TiO₄ occurs at temperatures above 900 °C [47]. The comparison of our findings to those related to nanofibers without ceria component, reported by Nolan at al. [47], indicates that solid-state reactions which result in the formation of zinc titanate phases are not affected by the presence of ceria. However, the decrease of specific surface area of nanofibers calcined above 400 °C (Fig. 3) could be related to the increase of average CO₂ particle size with temperature (Fig. 7(c)).

3.6. Thermogravimetric analysis (TGA) and differential scanning calorimetry (DSC)

Simultaneous thermal analysis measurements (thermogravimetric analysis - TGA and differential scanning calorimetry - DSC) are typically used to investigate the surface hydration, decomposition processes, and thermal stability. We have employed these methods primarily to investigate the formation of different crystalline phases of zinc titanates in the calcined composite nanofibers. Fig. 10 shows the TGA/DSC of the sample calcined at 500 °C. The endothermic peak in the DSC curve is related to the loss of residual chemisorbed water [50] up to 200 °C (1.61 wt%). The second weight loss (1.32 wt%) in the TGA curve between 200 and 450 °C, accompanied by an exothermic peak in the DSC curve at 235 °C, could also be related to the removal OH groups on the material, but mainly corresponds to the combustion decomposition of the organic

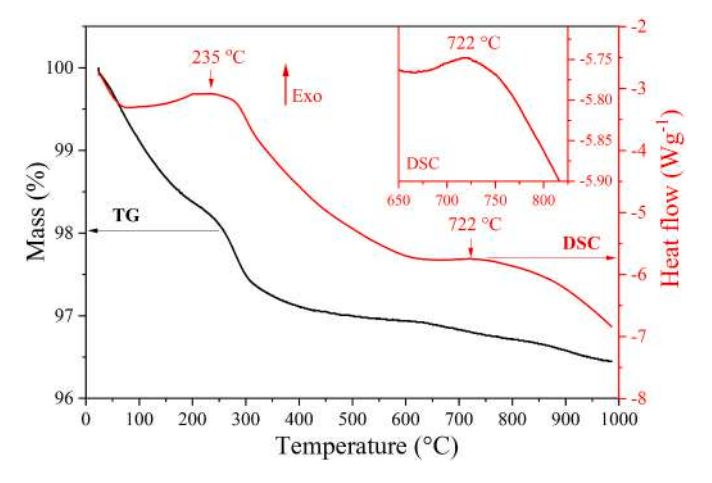


Fig. 10. TGA and DSC curves of the sample calcined at 500 °C.

residues [50]. Note that these small amounts of organic residues in the nanofibers calcined at 500 °C, may partially originate from PVP polymer, as its complete combustion in oxide nanofibers produced by electrospinning should be finished at 650 °C [51]. The third weight loss (\sim 0.5 wt%) is evident in the TGA curve between 600 and 1000 °C, and in the shape of the DSC curve in this temperature range, with a broad exothermic peak at around 722 °C (see the inset in Fig. 10). This very likely points to the formation of some zinc titanate crystalline phases.

The XRD and Raman results are supported and complemented by the TGA/DSC analysis. The TGA and DSC curves between 600 and 1000 °C point to some changes in crystallization (Fig. 10), which may be related to the formation of different crystalline phases of zinc titanates, revealed by the XRD and Raman analysis. Namely, the observed splitting of some diffraction peaks in the pattern of the nanofibers calcined at 800 °C (Fig. 5(a)), points to the appearance of the cubic phase, Zn₂TiO₄, between 700 and 800 °C. The Raman scattering data have also confirmed additional crystallization at temperatures higher than 700 °C (Fig. 8). Accordingly, the broad exothermic peak in the DSC curve, located at ~722 °C (Fig. 10), most probably corresponds to the formation of high-temperature zinc titanate crystalline phase (Zn₂TiO₄). The DSC analysis has provided a more precise insight into the temperature at which the Zn₂TiO₄ crystallization starts.

4. Conclusions

Novel composite metal oxide nanofibers were successfully synthesized from a solution containing Ce-Ti-Zn ions, using sol-gel and electrospinning methods, followed by calcination at temperatures ranging from 300 to 900 °C. The fibers were characterized using SEM, XRD, EDX, Raman scattering, BET and TGA/DSC measurements, and, to the best of our knowledge, this is the first composite electospun metal-oxide nanofibers composed of ceria, zinc oxide, and zinc titanates. The diameter of the fibers after calcination was estimated to be ~ 180 nm. The specific surface area of nanofibers exhibits the greatest value at 400 $^{\circ}\text{C}$ and decreases with further increase in calcination temperature up to 900 °C. The formation of crystalline CeO2 was observed after calcination at 300 °C, wurtzite ZnO phase existed in all samples with calcination temperatures in the range of 300–500 °C, whereas no crystalline titania phases were observed. The increase of calcination temperature above 500 °C facilitates solid-state reactions of Zn, Ti, O to form zinc titanates. At 600 $^{\circ}\text{C}$ and 700 $^{\circ}\text{C}$, cubic $\text{Zn}_{2}\text{Ti}_{3}\text{O}_{8}$ was found to be the dominant zinc titanate phase, while cubic Zn₂TiO₄ becomes dominant at 900 $^{\circ}$ C. The particle size analysis of XRD data, as well as PCM modeling of the ceria F_{2g} Raman feature, have shown that the average nanocrystallite size of ceria increases with calcination temperature. Regardless of the presence of ceria, the complex temperature-dependent phase transitions revealed by both XRD and Raman scattering measurements are in accordance with literature data obtained under similar synthesis conditions. These nanofibers show complex dependence of crystalline phases on calcination temperature. The presence of more than two oxide phases within fibers provides an opportunity for tailoring their properties for use in numerous technological applications.

Author statement

All authors who met the criteria to be authors are listed, and they all made significant contributions.

Declaration of competing interest

The authors declare that they have no known competing financial interests or personal relationships that could have appeared to influence the work reported in this paper.

Data availability

Data will be made available on request.

Acknowledgements

We thank Dr. Lee Farina at the University of Wisconsin Platteville for assistance with acquiring EDX data, and the University of Wisconsin Oshkosh Biology and Geology Departments for access to SEM and XRD systems, respectively. The authors also acknowledge funding provided from Institute of Physics Belgrade (University of Belgrade, Serbia) and UW Oshkosh FDR1409 grant.

References

- [1] D.H. Reneker, I. Chun, Nanotechnology 7 (1996) 216.
- [2] D. Li, Y. Xia, Adv. Mater. 16 (2004) 1151.
- [3] C. Burger, B.S. Hsiao, B. Chu, Annu. Rev. Matter. Res. 36 (2006) 333.
- [4] V. Thavasi, G. Singh, S. Ramakrishna, Energy Environ. Sci. 1 (2008) 205.
- [5] S. Li, Z. Cui, D. Li, G. Yue, J. Liu, H. Ding, S. Gao, Y. Zhao, N. Wang, Y. Zhao, Compos. Commun. 13 (2019) 1.
- [6] Q. Liu, J. Zhu, L. Zhang, Y. Qiu, Renew. Sustain. Energy Rev. 81 (2018) 1825.
- [7] K. Kendall, M. Palin, J. Power Sources 71 (1998) 268.
- [8] C. Kleinlogel, L.J. Gauckler, Adv. Mater. 13 (2001) 1081.
- [9] P. Patsalas, S. Logothetidis, C. Metaxa, Appl. Phys. Lett. 81 (2002) 466.
- [10] Y. Namai, K.I. Fukui, Y. Iwasawa, J. Phys. Chem. B 107 (2003), 11666.
- [11] H.C. Wang, C.H. Lu, Mater. Res. Bull. 37 (2002) 783.
- [12] H. Wang, J.J. Zhu, J.M. Zhu, X.H. Liao, S. Xu, T. Ding, H.Y. Chen, Phys. Chem. Chem. Phys. 4 (2002) 3794.
- [13] N. Guillou, L.C. Nistor, H. Fuess, H. Hahn, Nanostruct. Mater. 8 (1997) 545.
- [14] X. Yang, C. Shao, Y. Liu, R. Mu, H. Guan, Thin Solid Films 478 (2005) 228.
- [15] X. Yang, Y. Liu, J. Li, Y. Zhang, Mater. Lett. 241 (2019) 76.
- [16] P. Lu, B. Qiao, N. Lu, D.C. Hyun, J. Wang, M.J. Kim, J. Liu, Y. Xia, Adv. Funct. Mater. 25 (2015) 4153.
- [17] D. Channei, A. Nakaruk, S. Phanichphant, Mater. Lett. 209 (2017) 43.
- [18] L. Wang, Y. Zha, J. Zhang, Chemosphere 185 (2017) 690.
- [19] C. Li, R. Chen, X. Zhang, S. Shu, J. Xiong, Y. Zheng, W. Dong, Mater. Lett. 65 (2011) 1327.
- [20] A.F. Lotus, S.N. Tacastacas, M.J. Pinti, L.A. Britton, N. Stojilovic, R.D. Ramsier, G. G. Chase, Physica E 43 (2011) 857.
- [21] U. Steinike, B. Wallis, Cryst. Res. Technol. 32 (1997) 187.
- [22] Y.-S. Chang, Y.-H. Chang, I.-G. Chen, G.-J. Chen, Y.-L. Chai, T.-H. Fang, S. Wu, Ceram. Int. 30 (2004) 2183.
- [23] Z. Cai, J. Li, Y. Wang, J. Alloys Compd. 489 (2010) 167.
- [24] R.B. Pinto, P. Peralta-Zamora, F. Wypych, J. Photochem. Photobiol., A: Chem 353 (2018) 46.
- [25] S. Brunauer, P.H. Emmett, E. Teller, J. Am. Chem. Soc. 60 (1938) 309.
- [26] E.P. Barrett, L.G. Joyner, P.P. Halenda, J. Am. Chem. Soc. 73 (1951) 373.
- [27] A.J. Turinske, S.A. Nelson, N. Stojilovic, S.B. Ali, S.V. Dordevic, E.A. Evans, J. Sol. Gel Sci. Technol. 65 (2013) 283.
- [28] J. Arin, S. Thongtem, A. Phuruangrat, T. Thongtem, Res. Chem. Intermed. 43 (2017) 3183.
- [29] L. Budigi, M.R. Nasina, K. Shaik, S. Amaravadi, J. Chem. Sci. 127 (2015) 509.
- [30] M. Gabal, Y.M. Al Angari, Mater. Res. Express 9 (2022), 025010.
- [31] S.K. Manik, S.K. Pradhan, Physica E 33 (2006) 69.
- [32] A. Nakajima, A. Yoshihara, M. Ishigame, Phys. Rev. B 50 (18) (1994), 13297.
- [33] G. Gouadec, Ph Colomban, Prog. Cryst. Growth Char. Mater. 53 (2007) 1.
- [34] H. Richter, Z.P. Wang, L. Ley, Solid State Commun. 39 (1981) 625.
- [35] I.I. Campbell, P.M. Fauchet, Solid State Commun. 58 (10) (1986) 739.

- [36] J.E. Spanier, I.P. Herman, Phys. Rev. B61 (2000), 10437.
- [37] Z.D. Dohčević-Mitrović, M.J. Šćepanović, M.U. Grujić-Brojčin, Z.V. Popović, S. B. Bošković, B.M. Matović, M.V. Zinkevich, F. Aldinger, Solid State Commun. 137 (2006) 387.
- [38] M. Grujić-Brojčin, M.J. Šćepanović, Z.D. Dohčević-Mitrović, Z.V. Popović, Acta Phys. Pol. A116 (2009) 51.
- [39] M.J. Šćepanović, M. Grujić-Brojčin, Z. Dohčević-Mitrović, Z.V. Popović, Phys. A 86 (2007) 365.
- [40] A. Kremenovic, M. Grujic Brojcin, P. A.-M. Welsch, Colomban, J. Appl. Crystallogr. 46 (2013) 1874.
- [41] M. Šćepanović, M. Grujić-Brojčin, K. Vojisavljević, S. Bernik, T. Srećković, J. Raman Spectrosc. 41 (9) (2010) 914.
- [42] Z. Yao, K. Tang, Z. Xu, J. Ma, S. Gu, Opt. Mater. Express 9 (2019) 652.

- [43] K. Vojisavljević, M. Šćepanović, T. Srećković, M. Grujić-Brojčin, Z. Brankovic, G. Brankovic, J. Phys. Condens. Matter 20 (2008), 475202.
- [44] L. Li, F. Li, T. Cui, Q. Zhou, D. Xu, Phys. Status Solidi A 209 (2012) 2596.
- [45] J. Lu, D. Li, Y. Chai, L. Li, M. Li, Y. Zhang, J. Liang, Appl. Catal. B Environ. 256 (2019), 117800.
- [46] R. Helmy, G.A. El-Inany, H.S. Seleem, M.O. Abdel-Salam, T. Yoon, M. Saif, J. Alloys Compd. 907 (2022), 164487.
- [47] N.T. Nolan, M.K. Seery, S.C. Pillai, Chem. Mater. 23 (2011) 1496.
- [48] T. Surendar, S. Kumar, V. Shanker, Phys. Chem. Chem. Phys. 16 (2014) 728.
- [49] L. Hou, Y.-D. Hou, M.-K. Zhu, J. Tang, J.-B. Liu, H. Wang, H. Yan, Mater. Lett. 59 (2005) 197.
- [50] S. Prabhu, T. Viswanathan, K. Jothivenkatachalam, K. Jeganathan, Indian J. Mater. Sci. 2014 (2014) 1.
- [51] A. Mahapatra, B.G. Mishra, G. Hota, Ceram. Int. 37 (2011) 2329.

ELSEVIER

Contents lists available at ScienceDirect

Ceramics International

journal homepage: www.elsevier.com/locate/ceramint





From mixed brookite/anatase TiO₂ nanopowder to sodium titanates: Insight into morphology, structure, and photocatalytic performance

Nataša Tomić^{a,*}, Mirjana Grujić-Brojčin^a, Aleksandar Kremenović^b, Mirjana Novaković^c, Vladimir Lazović^d, Maja Šćepanović^a

- ^a Center for Solid State Physics and New Materials, Institute of Physics, University of Belgrade, Serbia
- b Faculty of Mining and Geology, University of Belgrade, Serbia
- ^c Department of Atomic Physics, Vinča Institute of Nuclear Sciences National Institute of The Republic of Serbia, University of Belgrade, Serbia
- ^d Photonics Center, Institute of Physics, University of Belgrade, Serbia

ARTICLE INFO

Handling Editor: Dr P. Vincenzini

Keywords:
Nanostructured materials
Chemical synthesis
X-ray diffraction
Scanning electron microscopy
Crystal structure
Catalysis

ABSTRACT

A method to obtain sodium titanate nanoribbons starting from a mixture of brookite and anatase TiO_2 nanopowder is described. As-prepared TiO_2 nanopowder with a major brookite phase was used as a precursor in an alkaline hydrothermal approach, where the temperature was kept at 200 °C. The influence of hydrothermal treatment and consequent annealing temperature (T=500 °C) on the crystal structure, phase composition, and morphology of samples were investigated by X-ray powder diffraction (XRPD), Raman and FTIR spectroscopy, and electron microscopy techniques (FESEM, HRTEM). All these methods point out that the hydrothermally treated sample, containing the NaTi₃O₆(OH)(H₂O)₂, Na₂Ti₃O₇, and Na₂Ti₉O₁₉, is dominated by layer-structured sodium hydroxititanate dihydrate. The annealing leads to the formation of rare sodium titanates, Na₃Ti₆O₁₃ and Na₂Ti₉O₁₉, with tunnel structures where the hexatitanate with increased sodium content prevails. The photocatalytic activity of synthesized nanostructures was tested in the degradation process of Reactive Orange (RO16) azo-dye upon UV excitation. It appears that photocatalytic activity is lower after hydrothermal treatment, but subsequent annealing makes sodium titanate nanoribbons faster in the degradation of RO16. The research implies that these sodium titanate nanostructures are promising photocatalytic materials and should be considered in the future for removing different pollutants from water.

1. Introduction

Titanium dioxide (TiO_2) represents the most commonly used photocatalyst because of its high efficiency, nontoxicity, chemical and biological stability, as well as low cost. The photocatalytic activity is well known and studied for the anatase phase, but little has been reported for the photocatalytic properties of the pure brookite or the mixed TiO_2 phases with brookite as the major phase [1–7]. It was also reported that hydrothermal synthesis is necessary to obtain brookite as a major phase [6]. The control of pH value (high basicity is required), as well as the temperature and reaction time, are of great importance in the formation of brookite as a major phase in hydrothermal synthesis with titanium tetrachloride as a precursor [8–13].

Furthermore, different kinds of titanates have been synthesized by using ${\rm TiO_2}$ as a precursor. These species consist of negatively charged layered sheets constructed with corner and edge shared ${\rm TiO_6}$ octahedra,

while alkali and alkaline earth metal ions (Na, Li, K, etc.) in the interlayers of the titanates compensate for the negative charge of the ${\rm TiO_6}$ sheets [14]. The influence of temperature on the structural properties is of great importance since practical performance can be directly influenced by these properties. The physicochemical characteristics of alkali titanates make them suitable for use in different fields such as photocatalysis, lithium/sodium ion batteries, humidity sensors, cation exchangers, dye-sensitized solar cells, and biosensors [15–19].

Tetragonal anatase and rutile phases of TiO_2 (as well as their commercial mixture P25 Degussa) were often used as a starting material to the obtained titanates by hydrothermal synthesis [15,17,20–27], whereas the use of orthorhombic brookite for this purpose was less common [16]. The variations in obtained titanates depend not only on the crystalline phase of the starting material but also on grain size in the same phase of the starting material [15]. Besides, the comparative analysis of hydrothermally synthesized sodium titanates with nanowire

E-mail address: natasat@ipb.ac.rs (N. Tomić).

^{*} Corresponding author.

morphology conducted by Meng et al. [16] has shown that the amount of intercalated Na is different in the case of anatase and brookite as precursors. Since titanate nanotubes, nanowires, and nanoribbons are the products of hydrothermal reactions, it is important to point out that the morphological transition between these species depends on synthesis parameters [20,23]. It has been reported that the increase in time or temperature treatment will favor the formation of nanoribbons [19, 22,24]. Besides this, Morgan et al. revealed that the contribution of high NaOH concentration is a crucial factor in order to achieve exclusively nanoribbon morphology [25].

All of this implies that the influence of the synthesis parameters as well as the nature of the starting material on the structure, morphology, and application of titanates represents a huge playground and is still under investigation. Moreover, it was found that photocatalytic rate varied with structural parameters and was also correlated with the crystallite size of prepared titanates [26]. To the best of our knowledge, a mixed TiO_2 phase consisting of brookite and anatase was not used as a starting material for the preparation of sodium titanates, nor were the photocatalytic properties of the resulting products estimated.

Water pollution is one of the biggest environmental pollutants. The dyes that are found in water as a waste product from industries can cause serious environmental problems due to their nonbiodegradability, toxicity, and potential carcinogenic nature [27–30]. Since these problems have become increasingly serious and environmental awareness continues to rise, a need for developing methods for low-cost and simple photocatalytic active materials is required. Besides the reported photocatalytic activity of ${\rm TiO}_2$ nanoparticles, these sodium titanate nanoribbons are considered suitable materials for removing a number of pollutants from water.

In this study, we present the path to design sodium titanate nanoribbons via the hydrothermal method, using titanium dioxide nanopowder as a precursor synthesized on purpose with brookite to anatase ratio very close to 3:1. The impact of the nature of this precursor on the morphology and phase composition of the obtained sodium titanate has been investigated. Furthermore, the properties of sodium titanates obtained after annealing at T = 500 °C have also been analyzed. Several methods of characterization have been employed: XRPD, Raman and Fourier transform infrared (FTIR) spectroscopy, FESEM and TEM/HRTEM. The photocatalytic activity of synthesized sodium titanates, as well as of TiO₂ precursor, has been investigated through the degradation of a representative azo dye (RO16) under ultraviolet (UV) irradiation.

2. Experimental

2.1. Synthesis of TiO2 materials

 ${
m TiO_2}$ nanopowder with mixed brookite and anatase phase was synthesized using the sol-gel hydrothermal method. In a typical procedure, an appropriate amount of ${
m TiCl_4}$ (99.9 % pure, Acros Organic) was dissolved in 150 ml of distilled water in the ice-bath. In order to obtain the hydrogel, the aqueous solution of NaOH was added under careful control of the pH value of the solution (pH \sim 9). After aging in the mother liquor for 5 h, the hydrogel was placed in an autoclave at a controlled temperature. After treatment at 200 °C for 24 h, filtration andrinsing with distilled water until complete removal of chloride ions were carried out. The last step was drying at 105.5 °C for 72 h. This procedure is also described in detail in the paperwork [31].

For the purpose of preparing the nanoribbons, a hydrothermal treatment starting with as-prepared TiO $_2$ was applied. Namely, 1 g of this nanopowder was added into 50 mL of 10 M solution NaOH and stirred on a magnetic stirrer for 1 h in order to uniformly disperse the nanoparticles. The solution was then transferred into an autoclave, where the temperature was T = 200 °C and the time of treatment t = 24 h. After the autoclave was cooled down to room temperature, the obtained white precipitate was washed several times with distilled water and dried at 105.5 °C over the night. The part from the batch of dried

samples was subjected to annealing temperature ($T=500~^{\circ}$ C). Besides the influence of hydrothermal treatment on starting TiO₂ nanopowder, the annealing process is also additionally investigated regarding the morphology and photocatalytic efficiency of the catalysts.

2.2. Characterization methods

The morphology of the synthesized nanostructures has been studied on a Tescan MIRA3 field emission gun scanning electron microscope (FE-SEM) at 20 kV in high vacuum. Prior to the measurements, samples were ultrasonically dispersed in ethanol.

XRPD measurements were conducted on a Rigaku Smartlab X-ray diffractometer in $\theta\text{-}\theta$ geometry (the sample in horizontal position) in parafocusing Bragg-Brentano geometry using a D/teX Ultra 250 strip detector in 1D standard mode with a $\text{CuK}\alpha_{1,2}$ radiation source (U = 40 kV and I = 30 mA). The XRPD patterns were collected in the 5–70/90° 20 range, with a step of 0.01° and a data collection speed of $5.1^\circ/\text{min}$. The low background single crystal silicon sample holder minimizes the background. PDXL2 integrated X-ray powder diffraction software (Version 2.8.30; Rigaku Corporation) was used for phase identifications, phase abundances (RIR method) calculation, and unit cell parameter refinements.

The morphology, chemical composition, and crystal structure of the samples were analyzed by a transmission electron microscope (TEM), FEI Talos F200X, operated at 200 keV. Conventional and high-resolution transmission electron microscopy analyses (TEM/HRTEM), together with high-angle annular dark-field (HAADF) examination, were carried out. The scanning transmission (STEM) mode with the energy-dispersive X-ray spectrometry (EDS) method, using four silicon detectors integrated into the Talos microscope, was used for spatially resolved EDS imaging. The phase composition of the samples was probed by the selected area electron diffraction(SAED) method and Fast Fourier Transform (FFT) analysis. The samples for TEM observation were prepared by standard procedure, where the solid powder was first dispersed into ethanol, and then a drop of the solution was placed on a carbon-coated copper grid, which was allowed to dry in the air.

Raman scattering spectra were taken in backscattering geometry employing a Jobin-Yvon T64000 triple spectrometer with gratings of 1800 grooves/mm. The setup included a confocal microscope and a nitrogen-cooled, charge-coupled device detector. The samples were excited using a 514.5 nm line of Ar $^+/Kr^+$ ion laser with a power of $\sim\!400~\mu W$ under an objective of $50~\times$ magnification. The measurements were performed at room temperature in the open air.

The infrared (IR) transmission spectra of the as-prepared ${\rm TiO_2}$ pellet together with un-annealed and annealed sodium titanate nanoribbons were measured on a Nicolet (NEXUS 470) Fourier transform infrared spectrophotometer at room temperature. The KBr pellet technique was used for this purpose, and the applied range was from 4000 cm $^{-1}$ to 400 cm $^{-1}$.

The thermal behavior of the material was examined by TGA/DTA thermogravimetric analyzer. The measurements were performed in air atmosphere with heating rate of 10° min⁻¹ in the temperature range from 30 to 600 °*C* on an SDT 2960 TA instruments.

2.3. Photocatalytic measurements

The photocatalytic activity of all samples was evaluated by photodegradation of Reactive Orange 16 solution. The photodegradation reaction was conducted in a batch Pyrex reactor equipped with a magnetic stirring bar and a water-circulating jacket. The initial concentration of RO 16was 50 mg L $^{-1}$ while the catalyst loading was 2 g L $^{-1}$. Irradiation in the UV range was performed using a 125 W mercury lamp. Experiments were carried out using 25 mL of dye solution. Prior to radiation, the suspensions were stirred in the dark for 60 min to uniformly disperse the photocatalyst particles and attain adsorption-desorption

equilibrium. At given time intervals, aliquots were taken and centrifuged to remove the catalyst particles. The supernatant was then analyzed on the UV–VIS spectrophotometer (DU 720) in order to monitor the concentration at the wavelength of 494 nm, corresponding to the maximum absorbance of RO16.

3. Results and discussion

3.1. Investigation of morphology, phase composition, and crystal structure

3.1.1. FESEM

The SEM image of the as-prepared TiO_2 nanopowder sample is presented in Fig. 1(a). Two different types of particles are noticed: spherical, ascribed to anatase, and spindle-like particles, characteristic of brookite [13,31]. These spindle-like particles of brookite in TiO_2 are elongated up to $\sim\!200$ nm, with a shorter dimension estimated as less than 40 nm.

From Fig. 1(b), it could be noticed that a nanoribbon shape was obtained where some structures aggregated into bundles. By comparing Fig. 1(b) and (c), it is clear that the annealing processing resulted in the formation of larger nanoribbons at the expense of smaller ones. Additionally, the somewhat shorter length of these elongated structures was noticed. Furthermore, in Fig. 1(d), where the stage was tilted for 60° , it has been proven that we are not dealing with nanotubes. Instead, completely closed nanostructures were produced by a hydrothermal procedure and annealing treatment. Nanoribbons are described as much longer structures with very good crystallinity and well-defined edges [19].

3.1.2. XRPD

The XRPD patterns of the as-prepared TiO_2 nanopowder and sodium titanate nanoribbon samples before and after annealing are shown in Fig. 2. The comprehensive XRPD analysis of TiO_2 nanopowder with dominant brookite phase has been reported previously [31]. According to the results of the quantitative phase analysis presented there, the sample consisted of 74 % brookite and 26 % anatase, with refined

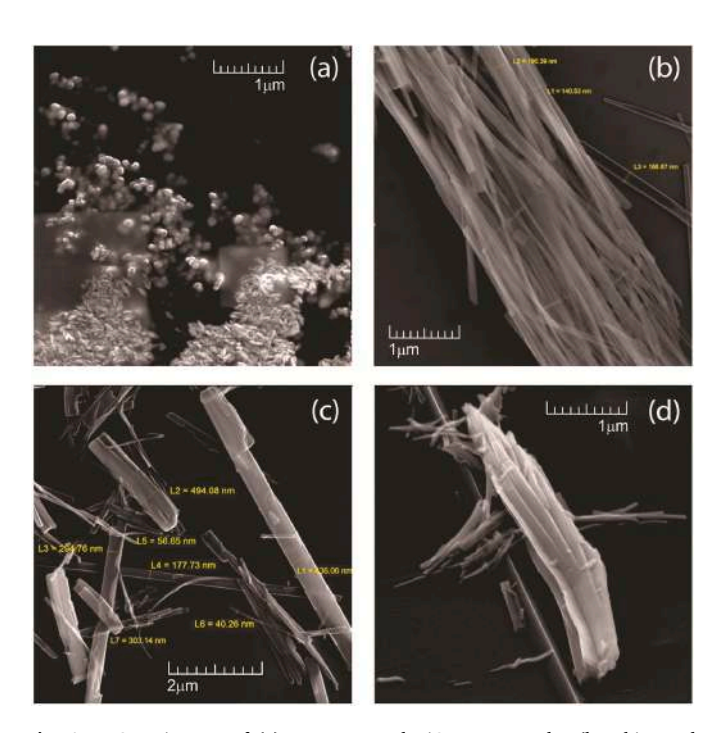


Fig. 1. FESEM images of (a) as - prepared TiO_2 nanopowder (brookite and anatase), (b) nanoribbons obtained after hydrothermal treatment, (c) subsequently annealed sample, and (d) cross-section of annealed sample (stage was tilted for 60°).

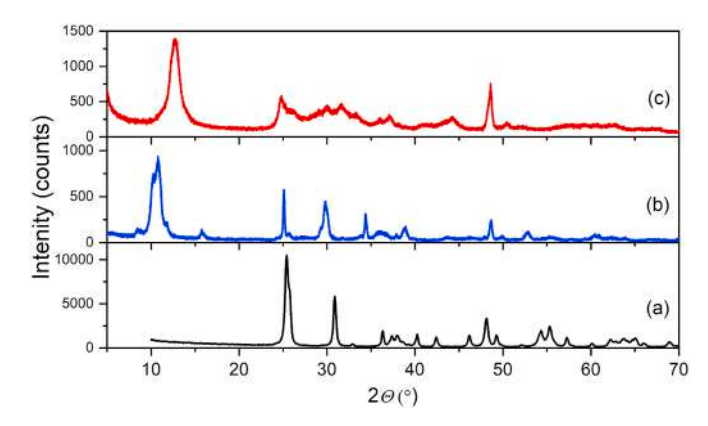


Fig. 2. XRPD patterns of (a) mixed-phase ${\rm TiO_2}$ nanopowder precursor and sodium titanate samples (b) before and (c) after annealing.

average apparent crystallite sizes of $\sim\!29$ and 17 nm estimated, respectively.

The XRPD pattern of the sodium titanate nanoribbon samples before annealing, using TiO_2 nanopowder with major brookite phase as a precursor, is presented in Fig. 3. The analysis of XRPD data has shown that different kinds of titanates are formed: $NaTi_3O_6(OH)(H_2O)_2$, $Na_2Ti_3O_7$, and $Na_2Ti_9O_{19}$, with the dominant presence of sodium hydroxititanate dihydrate (Table 1). The refined lattice parameters are in good agreement with unit cell parameter values reported in PDF cards. Due to overlapping diffraction peaks (see Fig. 3), it is difficult to reliably determine the anisotropic character of the crystallites of all three present crystal phases. For crystal phases with a low fraction ($Na_2Ti_3O_7$ and $Na_2Ti_9O_{19}$) the analysis of diffraction line broadening is not reliable. For the $NaTi_3O_6(OH)(H_2O)_2$, a crystal phase with the highest percentage, the analysis of diffraction line broadening shows that the dimensions of the crystallites calculated from the reflections (001), (200) and (020) are 193, 114 and 309 Å, respectively.

From the XRPD pattern shown in Fig. 4, it can be assumed that after annealing at 500 °C of the sodium titanate nanoribbon sample, two

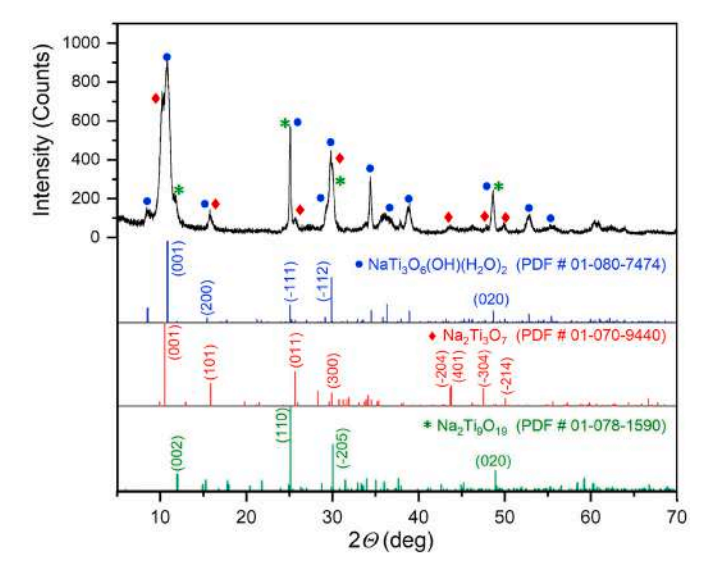


Fig. 3. Experimental XRPD pattern of sodium titanate nanopowder before annealing. Peak positions and intensities for $NaTi_3O_6(OH)(H_2O)_2$ (card number 01-080-7474), $Na_2Ti_3O_7$ (card number 01-070-9440) and $Na_2Ti_9O_{19}$ (card number 01-078-1590) (ICDD (PDF-2 Release 2016 RDB)) in blue, red and green, respectively, are shown below the experimental pattern. The most prominent peaks are denoted by symbols. (For interpretation of the references to color in this figure legend, the reader is referred to the Web version of this article.)

Table 1Phase composition, abundance, and unit cell parameters for crystaline phases in sodium titanate before annealing.

Formula/PDF #	%	a (Å)	b (Å)	c (Å)	α (°)	β (°)	γ (°)	$V(\mathring{A}^3)$
NaTi ₃ O ₆ (OH)(H ₂ O) ₂	86.5(8)	21.71(5)	3.75(1)	11.94(2)	90	136.79(7)	90	666(3)
PDF # 01-080-7474		21.5550	3.7583	11.9260	90	136.140	90	669.428
Na ₂ Ti ₃ O ₇	10.3(8)	9.24(3)	3.85(1)	8.60(3)	90	102.1(2)	90	299(1)
PDF # 01-070-9440		9.1330	3.8060	8.5660	90	101.570	90	291.706
Na ₂ Ti ₉ O ₁₉ ^a	3.2(1)	12.0799	3.7428	15.4464	90	105.0	90	675

^a Not refined due to low abundance.

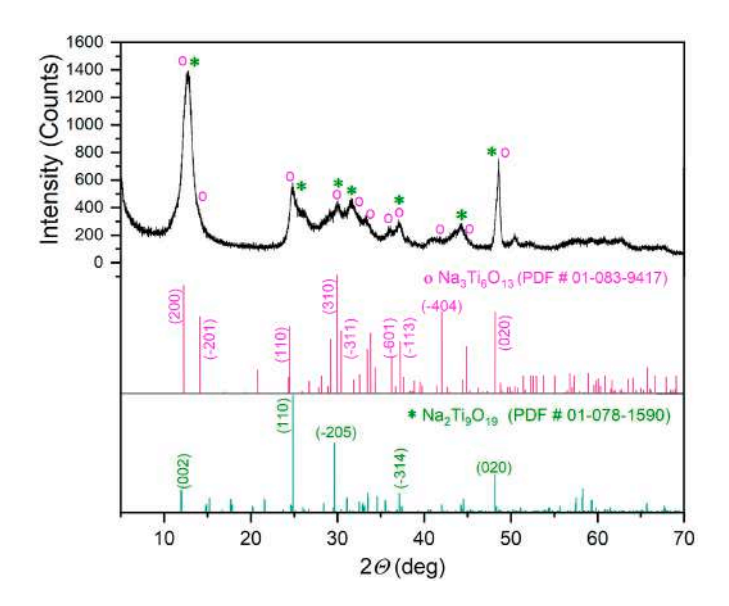


Fig. 4. Experimental XRPD pattern of annealed nanopowder. Peak positions and intensities for $Na_3Ti_6O_{13}$ (card number 01-083-9417) and $Na_2Ti_9O_{19}$ (card number 01-078-1590) (ICDD (PDF-2 Release 2016 RDB)) in blue and red respectively are shown below the experimental pattern. The most prominent peaks are denoted by symbols. (For interpretation of the references to color in this figure legend, the reader is referred to the Web version of this article.)

kinds of titanates are formed, $Na_3Ti_6O_{13}$ and $Na_2Ti_9O_{19}$ (Table 2). The refined lattice parameters are in good agreement with the unit cell parameter values reported in PDF cards. Relatively broad diffraction reflections may indicate somewhat disturbed crystallinity and/or small cristallyte sizes of sodium titanate phases, as indicated in SEM. As diffraction peaks highly overlap (Fig. 4) it is not possible to determine the anisotropic character of crystallites in $Na_3Ti_6O_{13}$ and $Na_2Ti_9O_{19}$ phases. For the crystalline phase $Na_3Ti_6O_{13}$, the analysis of diffraction line broadening shows that crystallite dimensions calculated from reflections (200), (020) and (006) are 67, 191 and 25 Å, respectively. For the crystalline phase $Na_2Ti_9O_{19}$, the analysis of diffraction line broadening shows that the dimensions of the crystallites calculated from reflections (002) and (020) (there are no reflections of type (h00) on the XRPD diagram) are 67 and 191 Å, respectively.

It should be noted that dominant broadening of XRPD reflections under the influence of crystallite size limits the analysis of the broadening of reflections due to microstrain. Consequently, reliable analysis of structural disorder from XRPD data is not possible.

To the best of our knowledge, Na₃Ti₆O₁₃ has not yet been recognized as a product of the hydrothermal treatment followed by annealing. Meng et al. [16] have reported that nanowires hydrothermally synthesized from both brookite and anatase phases can be attributed to Na₂Ti₆O₁₃ phase. They observed that the diffraction peak of those samples, which is denoted as reflection (2 0 0), shifts to a higher 2Θ position with an increasing NaOH/TiO2 molar ratio, and this shift is greater for the sample obtained from anatase than the one derived from brookite at the same NaOH/TiO2 molar ratio. According to these authors, the increase in diffraction angle 2Θ of the mentioned peak, i.e., the decrease in d-spacing of the corresponding (2 0 0) planes, has been related to the increase in Na amount intercalated into TiO2. On the other hand, Shen et al. [32] have investigated the structural changes in the $Na_{2+x}Ti_6O_{13}$ host structure due to Na-ion intercalation. By analyzing XRD patterns collected at samples with different sodium compositions between x =0 and x = 1 in Na_{2+x}Ti₆O₁₃, they have shown that the crystal structure possesses the same symmetry (monoclinic C2/m space group with a 3D tunnel structure). The continuous shift of some original reflections of Na₂Ti₆O₁₃ indicated a gradual change in the lattice parameters, most pronounced in the increase of the lattice parameters c and angle β . The XRPD pattern of our annealed sample (Fig. 4) does not match the XRPD pattern of neither $Na_2Ti_6O_{13}$ presented by Meng et al. nor the one for x = 0 given by Shen et al. Great discrepancies in position and width of diffraction peaks allowed us to conclude that sodium titanate with Na₂Ti₆O₁₃ as the dominant phase is not obtained as a product of the annealing process applied here. However, the refined unit cell parameters. Table 2 is the same within three estimated standard deviations with those reported by Shen et al. for x = 1, i.e., Na₃Ti₆O₁₃ [32].

3.1.3. TEM, HRTEM and STEM-EDS

The surface microstructure and phase composition of as-prepared TiO2 nanopowder, as well as sodium titanate samples before and after annealing, were investigated using transmission electron microscopy. The low- and high-resolution TEM micrographs, along with the corresponding selected area electron diffraction patterns, are summarized altogether and presented in Fig. 5. The bright-field TEM micrograph of the TiO₂ sample (Fig. 5(a)) reveals distinct nanocrystal morphologies among the two mixed phases, which is in accordance with SEM results. Thus, the predominantly anatase phase exhibits the morphology of quasi-spherical nanocrystallites of a few nanometers in size, whereas the spindle-like particles of brookite TiO₂ are up to 40 nm wide and typically 50-150 nm long. Indeed, the difference in the morphologies of the anatase and brookite phases is clearly visible in Fig. 5(b), which presents a TEM micrograph of the sample recorded at high magnification. Besides, the local crystal structure of two mixed TiO2 phases was confirmed by selected area electron diffraction; one SAED pattern of the TiO2

Table 2Phase composition, abundance and unite cell parameters of crystaline phases in sodium titanate after annealing.

Formula/PDF #	%	a (Å)	b (Å)	c (Å)	α (°)	β (°)	γ (°)	$V(\mathring{A}^3)$
Na ₃ Ti ₆ O ₁₃	59(8)	14.6(1)	3.77(3)	9.52(7)	90	100.1(4)	90	516(7)
PDF # 01-083-9417		14.8801	3.7570	9.4145	90	100.587	90	517.349
Na ₂ Ti ₉ O ₁₉	41(8)	12.11(8)	3.77(3)	15.3(1)	90	105.4(3)	90	673(9)
PDF # 01-078-1590		12.0799	3.7428	15.4464	90	105.0	90	675

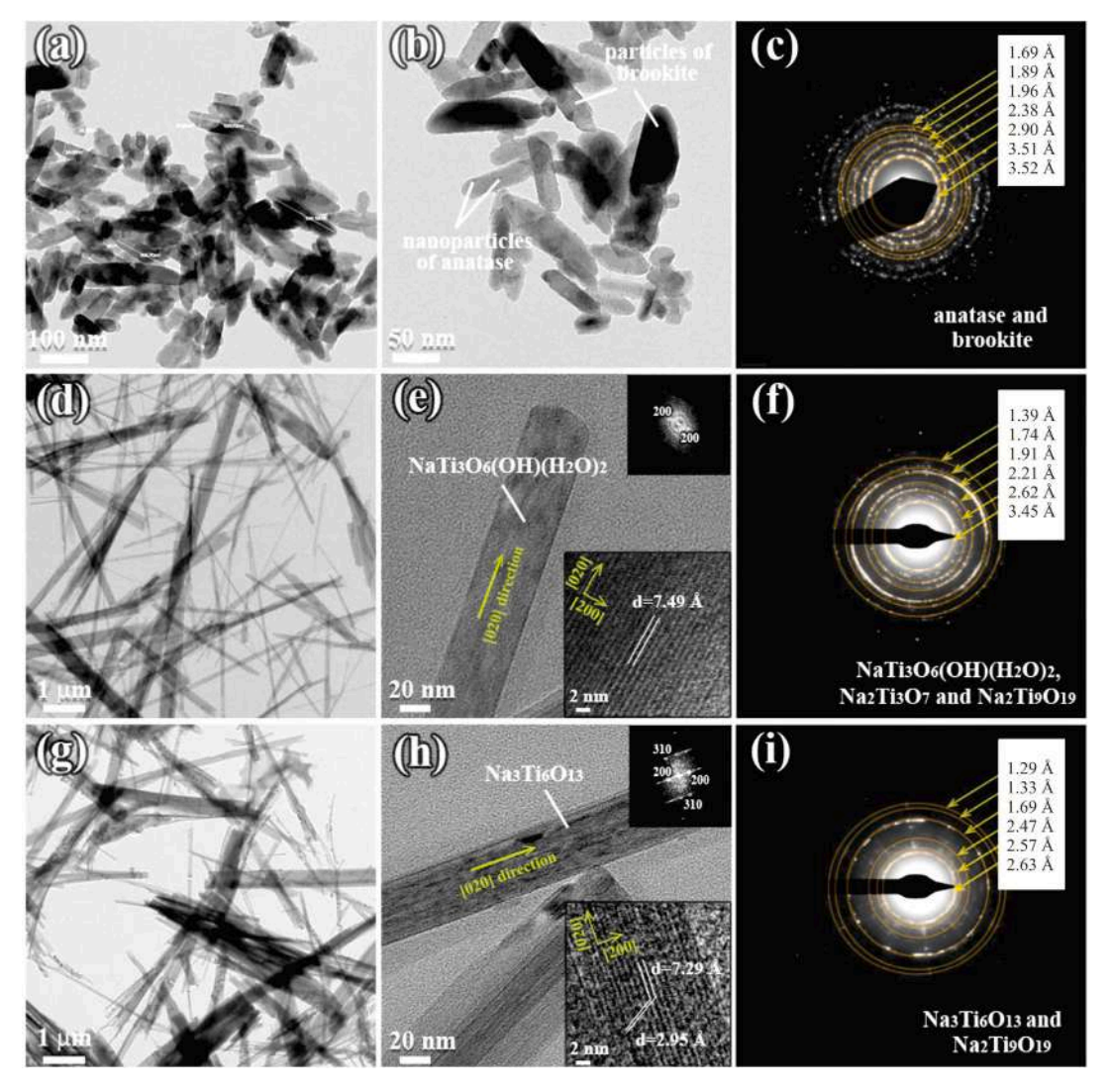


Fig. 5. Low- and high-magnification TEM micrographs and SAED patterns of the samples; each row corresponds to the following sample: (a–c) precursor TiO₂ nanopowder with major brookite phase, (d–f) sodium titanate before annealing, and (g–i) annealed sodium titanate. FFT's and HRTEM images with measured d-spacing of one isolated nanoribbon for sodium titanates before and after annealing, are given in the insets in (e) and (h), respectively.

sample is given in Fig. 5(c). The diffraction pattern is characterized by well-defined concentric rings, which is typical for a fine-grained nanocrystalline structure. According to the radii of the rings, d-spacings from different phases are calculated, hence providing indirect evidence of two mixed TiO_2 phases. The characteristic d-spacing of the anatase (101), (004), (200), and (105) plane is 3.52, 2.38, 1.89, and 1.69 Å, respectively, while the respective d-spacing for brookite (120), (121), and (032) was found to be 3.51, 2.90, and 1.96 Å, in accordance with the reference values [33].

For the sodium titanate before annealing, TEM analysis revealed quite different morphology as compared to the $\rm TiO_2$ sample. Fig. 5(d) shows a low-magnification bright-field TEM micrograph of this sample, presenting a large number of separately dispersed rod-like nanoribbon crystals with smooth morphology. The transparency of the nanoribbons indicates they are very thin. The width of the single crystals is around 50–300 nm, and their length varies from a submicron range to more than ten microns. A closer analysis of the microstructure was performed at higher magnifications, from which the distances between two adjacent planes were measured. Fig. 5(e) shows an enlarged section of one isolated nanoribbon, presenting an HRTEM image in the bottom inset. The HRTEM micrograph reveals clear and well-defined lattice planes, with a *d*-spacing of 7.49 Å. This value closely corresponds to the 7.47 Å reported for the (200) planes of $\rm NaTi_3O_6(OH)(H_2O)_2$ [34], as further

confirmed by the respective FFT analysis (top inset). Additionally, the HRTEM image indicates that the nanoribbons have grown as single crystals, elongated along the [020] direction (b axis). Fig. 5(f) shows a representative electron diffraction pattern obtained from a selected area of the sample, encompassing a large number of nanocrystals. The d-spacing values measured from the SAED pattern of 3.45, 2.62, 2.21, 1.91, 1.74, and 1.39 Å correlate closely with the theoretical interplanar distances for several phases. Specifically, these values match the $(\overline{6}$ 03), $(\overline{8}$ 04), $(\overline{4}$ 05), $(\overline{10}$ 06), $(\overline{9}$ 16), and $(\overline{14}$ 03) planes of NaTi₃O₆(OH)(H₂O)₂ (theoretical d-values of 3.47, 2.61, 2.21, 1.91, 1.74, and 1.39 Å) [34], (011), $(\overline{2}$ 03), $(\overline{3}$ 12), $(\overline{3}$ 04), $(\overline{2}$ 21), and $(\overline{4}$ 15) planes of Na₂Ti₃O₇ (theoretical d-values of 3.46, 2.62, 2.20, 1.90, 1.74, and 1.39 Å) [35], and (111), (311), $(\overline{2}$ 07), $(\overline{1}$ 17), $(\overline{2}$ 23), and (606) planes of Na₂Ti₉O₁₉ (theoretical d-values of 3.44, 2.60, 2.22, 1.92, 1.74, and 1.38 Å) [36], respectively.

Similar analyses were also performed for the annealed sample, and the results are presented in Fig. 5(g–i). Again, the morphology is characterized by a typical nanoribbon-shaped structure, although in this case the individual crystals are somewhat wider than for the sample before annealing. Besides, the image contrast suggests that the microstructure features distinctive stripes, a characteristic that has been previously observed in the sodium titanates synthesized at high temperatures [37,

38]. An exemplary HRTEM micrograph of one isolated nanoribbon is shown in the bottom inset of Fig. 5(h). Although the channel structure is difficult to clearly identify due to the complex atomic arrangement and uncertain HRTEM imaging conditions, the micrograph reveals a characteristic pattern of alternating bright and dark atomic planes that are typical for the tunnel-like structure. The nanoribbon exhibits a single-crystal structure oriented along the b-axis (i.e., the [020] crystallographic direction), displaying parallel (200) planes of Na₃Ti₆O₁₃. The measured interplanar spacing of approximately 7.29 Å matches the theoretically predicted d-value of 7.31 Å reported by Shen et al. [39]. Furthermore, fine stripes can be seen across the main crystalline planes, with a d-value of 2.95 Å corresponding to the interplanar distances between (310) crystal planes [39]. In a previous study, Zárate et al. reported similar results regarding the structure of Na₂Ti₆O₁₃ nanowires in single crystals [38]. This observation is further supported by the FFT pattern in the top inset of Fig. 5(h), which shows two sets of spots aligning with the [200] and [310] directions of $Na_3Ti_6O_{13}$. The SAED pattern of the sample, derived from a large number of nanoribbons, is presented in Fig. 5(i). The measured d-values of 2.63 Å and 2.47 Å correspond well to the (402) and ($\overline{6}$ 01) planes of Na₃Ti₆O₁₃ phase, with the theoretical d-spacings of 2.64 and 2.47 Å, respectively [39], thus confirming the presence of this phase. Additionally, the measured distance of 2.57 Å aligns with the predicted value of 2.60 Å for the (311) planes of Na₂Ti₉O₁₉ [36]. Furthermore, extra diffraction rings correspond to interplanar distances of 1.69, 1.33, and 1.29 Å, which can be attributed to the $(\overline{7}\ 13)$, (714), and $(\overline{4}\ 25)$, planes of Na₃Ti₆O₁₃ (theoretical d-values of 1.69, 1.33, and 1.30 Å) [39], as well as the (603), (028), and (607) crystal planes of Na₂Ti₉O₁₉ (theoretical d-values of 1.69, 1.33, and 1.29 Å) [36]. Interestingly, the rings that correspond to NaTi₃O₆(OH)(H₂O)₂ and Na₂Ti₃O₇ phases are missing, thus indicating that these phases are no longer stable after annealing. These results strongly support those obtained by the XRPD analysis.

In addition to conventional TEM analysis, the samples were also investigated by scanning transmission electron microscopy, together with EDS measurements. For example, in Fig. 6(a–d) the STEM/HAADF micrographs are presented together with corresponding elemental image maps obtained for sodium titanate sample before annealing. The elemental maps were acquired by using K and L line spectra, where different colors were associated with different elements. The green, red, and yellow color micrographs correspond to Na, Ti, and O elements, respectively. According to the EDS mapping images, it is clearly visible that sodium, titanium, and oxygen are evenly distributed over the sample. The EDS spectrum taken from the sample area, covering a large number of nanoribbons, is presented in Fig. 6(e). Apart from the C and Cu lines, which originate from the carbon-coated copper grid used during TEM observations, the spectrum shows that the sample is only composed of Na, Ti, and O elements.

In Table 3, we also provide the elemental composition from EDS analysis to evaluate the stoichiometry of sodium titanate samples both before and after annealing. The results show that, despite a minor variation in Na concentration, the atomic percent ratio of Na to Ti decreases from 0.44 in the hydrothermally treated sample to 0.38 after annealing. Considering the phase composition of sodium titanates revealed by XRPD measurements, this change in the Na/Ti ratio suggests that in the sample before annealing, some excess of Na may exist that was not incorporated into the sodium titanate structure. This could be the reason for the formation of the Na₃Ti₆O₁₃ phase after annealing, which has a higher Na ion content compared to the more common Na₂Ti₆O₁₃ hexatitanate [39].

Based on the literature data, and having in mind above analysis, transformation from NaTi $_3$ O $_6$ (OH)(H $_2$ O) $_2$ to Na $_2$ Ti $_6$ O $_1$ 3 upon heating is possible process [40]. In our case, the NaTi $_3$ O $_6$ (OH)(H $_2$ O) $_2$ with \sim 86 % represents the major form in sample before annealing process. Additionally, it has been reported that phase transition from sodium trititanate to sodium hexatitanate will occur through thermal treatment in

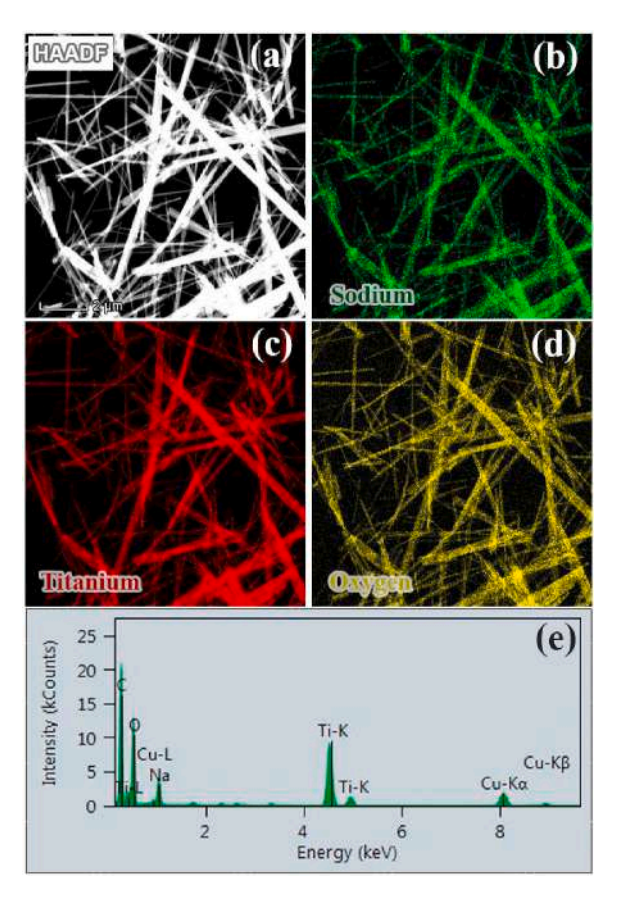


Fig. 6. STEM analysis of the sodium titanate before annealing: (a) STEM/ HAADF image of large area of the sample with corresponding EDS maps highlighting sodium (b), titanium (c) and oxygen (d) elements; (e) EDS spectrum taken from the sample area covering a large number of nanoribbons, as presented in HAADF image in (a).

Table 3EDS elemental composition analysis of sodium titanate samples before and after annealing.

Elemental composition (at.%)				
0	Na	Ti		
55.28 51.10	13.73 13.56	30.99 35.34		
	0	O Na 55.28 13.73		

3.2. Vibrational properties

3.2.1. Raman scattering

The Raman spectra of as-prepared TiO_2 , hydrothermally treated, and subsequently annealed samples are shown in Fig. 7. The measurements repeated on several locations of each sample have confirmed the homogeneity of all investigated samples. The modes in the spectrum of as-prepared TiO_2 (Fig. 7(a)) can be assigned to two titania crystalline phases - anatase and brookite [13,31], indicating that the as-prepared

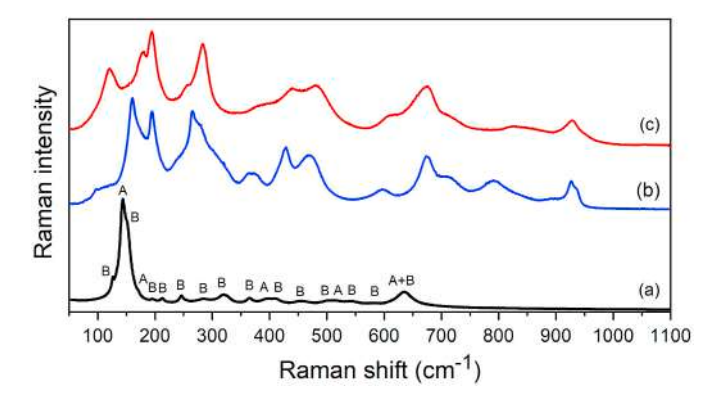


Fig. 7. Raman spectra of as-prepared ${\rm TiO_2}$ nanopowder (a), and sodium titanates before (b) and after (c) annealing. Anatase and brookite modes are denoted by A and B, respectively. The spectra are upshifted for clarity.

sample consists of these two polymorphs, which is in accordance with XRPD results.

The Raman spectrum in Fig. 8(a) shows that hydrothermal treatment of as-grown TiO2 nanopowder in NaOH solution leads to the transformation of TiO2 to sodium titanate phases. The absence of characteristic anatase and brookite Raman modes (see Fig. 7) and the appearance of a large number of modes, which may be ascribed to sodium titanates support this assumption. The spectrum of the sodium titanate sample before annealing has been fitted by the sum of Lorentzians in Fig. 8(a), where sodium titanate related modes were clearly distinguished at \sim 97. 112, 160, 175, 196, 239, 266, 283, 312, 370, 427, 470, 596, 674, 715, 792, 840, 895, 926, and 936 cm^{-1} . In the Raman spectra of sodium titanates, the modes occurring below 500 cm⁻¹ are generally ascribed to Na-O-Ti vibrations, those in the region of 600-800 cm⁻¹ to Ti-O vibrations in edge-shared and corner-shared TiO6 octahedra, and the features after 800 cm⁻¹ are related to Ti-O bonds of low coordination [44,45]. In several studies addressing the Raman spectroscopy of sodium titanates, the spectra with similar features to the one presented here have been related to Na₂Ti₃O₇ [24,44,45]. Regarding the shape and position of Raman modes, the spectrum shown in Fig. 8(a) matches to a great extent the one reported by Montecelo et al. [33]. These authors have claimed that most of the listed Raman peaks might be assigned to Na₂Ti₃O₇, except the mode observed at ~263 cm⁻¹, which they explained in terms of Na⁺/H⁺ exchange due to storing and manipulating their samples in water [44]. However, based on our FTIR spectrum (see Section 3.2.2) that confirms the presence of H_3O^+ ions in sample, we

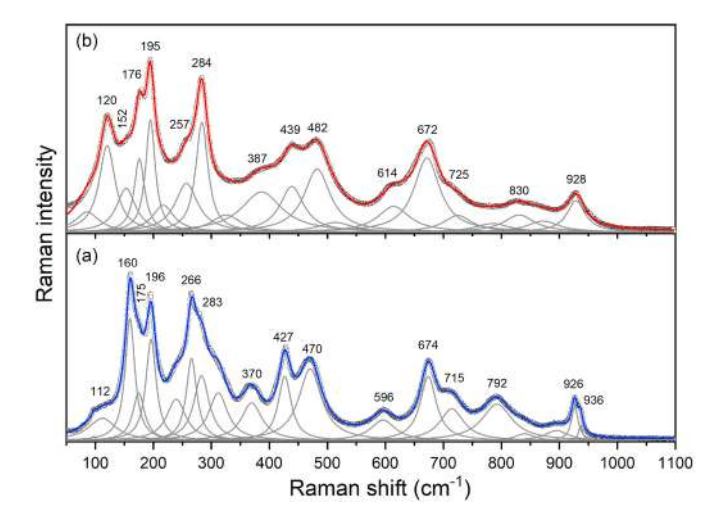


Fig. 8. Raman spectra of sodium titanates (a) before and (b) after annealing, fitted by the sum of Lorentzians.

believe that the $\mathrm{Na^+/H_3O^+}$ exchange gives the rise to the mentioned peak. In addition to this, it has been reported when replacement of $\mathrm{Na^+}$ ions with $\mathrm{H^+}$ ions take place, due to the smaller ionic radius the decrease of distance between adjacent layers will occur, which is consequently evident in XRD pattern [46,47]. Having in mind that $\mathrm{Na^+}$ and $\mathrm{H3O^+}$ ions have similar radius and no shift was observed in XRD pattern regarding this exchange, we can say that in our case this process is more likely to happen.

It should also be pointed out that the Raman spectrum of the sodium titanate sample (Fig. 8(a)) significantly deviates from the spectrum of $Na_2Ti_3O_7$ microcrystals, as presented in the Raman study by Silva et al. [48]. Although deviation in position and line width of some modes could be related to nanoribbon morphology [15], it is clear that the spectrum in Fig. 8(a) cannot be ascribed to $Na_2Ti_3O_7$, except if its structure is strongly disturbed, most probably due to the presence of interlayer water [23]. This assumption is supported by the results of XRPD analysis with $NaTi_3O_6$ (OH)(H_2O_{12} as the dominat phase in this sample, accompanied by $Na_2Ti_3O_7$ (Table 1). Although XRPD data point to the presence of a small amount of $Na_2Ti_9O_{19}$, evidence of this phase has not been found in the Raman spectra.

The Raman features in the spectrum of the annealed sample are registered at ~86, 120, 152, 176, 195, 217, 257, 284, 326, 387, 439, 482, 514, 614, 672, 725, 785, 830, 872, 928, and 1054 cm⁻¹ (as fitted in Fig. 8(b)). Structural change caused by annealing is confirmed by the variation in relative mode intensity as well as the disappearance of some Raman modes and the appearance of new ones in comparison to the spectrum before annealing (Fig. 7), indicating that the process of annealing has led to the dehydration of sodium hydroxititanate. The enhancement of representative peaks below 400 cm⁻¹ related to Na-O vibrations may be noticed. The increase of peaks at 195 and 284 cm⁻¹ characteristic for Na-Ti-O bonds suggests dehydration and good crystallinity of the sample after annealing [49]. Additionally, the peak at 176 cm⁻¹ most likely related to Na intercalated into TiO₂ [16], becomes sharp and well defined after annealing, as can be seen in Fig. 8. According to literature, the peaks at about 672 and 725 cm⁻¹ could be associated with the Ti-O-Ti stretch in edge-shared TiO6, whereas the weak feature at \sim 785 cm $^{-1}$ could be related to the Ti-O-Ti stretch in corner-shared TiO₆ octahedra [16]. The appearance of three bands (~872, 928, and 1054 cm⁻¹), which may be ascribed to short Ti-O stretching vibrations, Meng et al. attribute to the existence of multiple species of short Ti-O bonds, characteristic of sodium hexatitanates obtained from brookite as a precursor. Altogether, the spectrum of the annealed sample is quite similar to that reported by Meng et al. [16], but it also looks like those of Zhang et al. [40] and Kolenko et al. [50]. All these authors [16,30,40,50] state that the titanate structure obtained as a result of annealing at about 500 °C is close to Na₂Ti₆O₁₃, although their overall spectra are clearly different from Na₂Ti₆O₁₃ [51]. However, the spectrum of our annealed sample (Fig. 7(c)) obviously deviates from the spectrum of Na₂Ti₆O₁₃ microcrystals, as shown in a comprehensive Raman study by Silva et al. [52], pointing out that Na₂Ti₆O₁₃ cannot be the dominant titanate phase in this sample. On the other side, the Raman modes in the spectrum of the annealed titanate sample located at about 120, 153, and 831 cm⁻¹ could be ascribed to Na₂Ti₉O₁₉, whereas the modes at about 217, 387, 483, and 614 cm⁻¹ are somewhat shifted in comparison to those registered in pristine Na₂Ti₉O₁₉ and correspond more to sodiated/desodiated samples described in the work of Bhat et al. [53]. However, a prominent shoulder at \sim 250 cm⁻¹ and a peak at \sim 439 cm⁻¹ could hardly be related to both Na₂Ti₉O₁₉ structures mentioned above. Note that the features at these positions have been registered by Liu et al. [41], who noticed that the intensity of these modes changed during the structural transition from trititanate to hexatitanate due to heating. The behavior of these features in our samples (Figs. 7 and 8) is similar: the shoulder at $\sim 250 \text{ cm}^{-1}$ is more pronounced, whereas the peak at \sim 439 cm⁻¹ is decreased after annealing. It should also be noted that, to the best of our knowledge, there are no Raman modes of Na₃Ti₆O₁₃ reported yet. Although the analysis of the Raman spectra of annealed titanate supports the results obtained by XRPD, which suggests the combination of $Na_2Ti_9O_{19}$ and $Na_3Ti_6O_{13}$ phases for this sample, it is unable to fully confirm them.

3.2.2. FTIR

The FTIR spectra of all samples in the wave number range from 4000 to 700 cm⁻¹ are presented in Fig. 9. A broad band around 3500 cm⁻¹ together with one around 1600 cm⁻¹, assigned to fundamental vibrations (stretching and bending) of different O-H hydroxyl groups and water molecules, confirms the presence of water adsorbed on the surface [49,54,55]. These bands are the most pronounced in sodium titanate before annealing but are also present in the both annealed sample and the as-prepared precursor, indicating that some amount of physisorbed water remained in all samples. On the other side, the bands at 3150 cm⁻¹ and 1730 cm⁻¹, associated with the bending and stretching modes of the chemisorbed/interlamellar water molecules [45], exist only in sodium titanate sample (b) before annealing, pointing that interlamellar water has been removed by annealing. Moreover, based on literature data, these bands at 1730 cm⁻¹ and 3150 cm⁻¹, together with band around 3260 cm⁻¹ are ascribed to H₃O⁺ ions [56]. Unfortunately, due to the overlapping with the broad band around 3500 cm⁻¹, this last band can't be detected. The contribution of this band together with the band around 3150 cm⁻¹ is noticeable through the more pronounced widening in this region, compared to other two samples.

Several bands of low intensity in the range of $\sim 1100-1400~\rm cm^{-1}$ in the spectrum of the annealed sample (Fig. 9(c)), could be related to vibration of Ti-O and Ti-O-Ti bonds [57]. The band at $\sim 1385~\rm cm^{-1}$ is assigned to Ti-OH stretch [57] and here is more pronounced in the sample (c) annealed at 500 °C [58]. The peak at 870 cm⁻¹ should correspond to Ti-O bonds in TiO₆ octahedra, less pronounced in annealed sample [49]. The band at $\sim 910~\rm cm^{-1}$ clearly recognized in both sodium titanate samples (Fig. 9(b and c)) is related to Ti-O bonds in TiO₆ octahedra [45,49], whereas the shoulder at $\sim 1010~\rm cm^{-1}$, present only in the spectrum of the sample before annealing, might be ascribed to the bending vibrations of Ti-OH non-bridging bonds [45].

The FTIR spectra show that interlamellar water disappears due to the annealing, causing structural modifications. This is in accordance with the findings of XRPD about the $NaTi_3O_6(OH)(H_2O)_2$ as the dominant structure in the sample before annealing and the sodium titanate tunnel structures in the annealed sample.

Simultaneous thermogravimetric analysis (TGA) and differential thermal analysis (DTA) were carried out in air, in order to examine

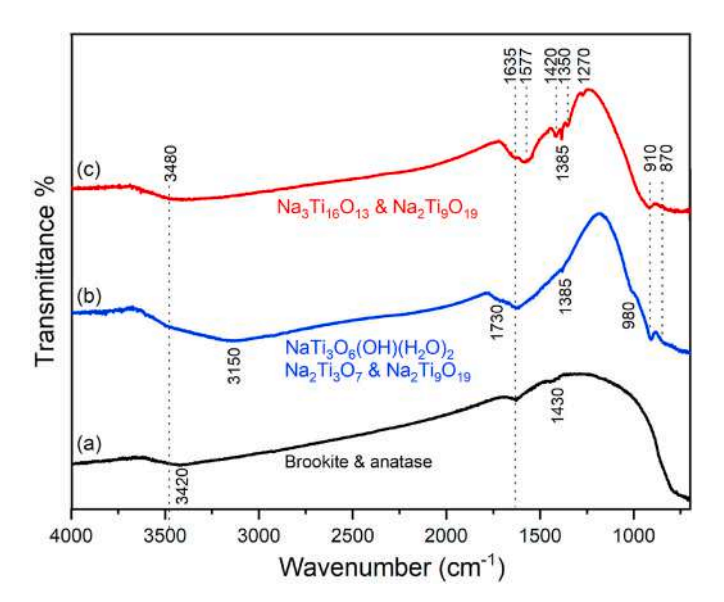


Fig. 9. FTIR spectra of as-prepared TiO_2 nanopowder (a), and sodium titanates before (b) and after annealing (c). The spectra are upshifted for clarity.

thermal behavior. Results are given in Fig. 10.

From TGA curve (Fig. 10), it could be noticed that overall weight loss, for the temperature range up to 500 °C is about 11 %. This is in a good agreement with the chemical composition of the material containing the NaTi₃O₆(OH)(H₂O)₂ as major phase. The corresponding DTA curve (Fig. 10) displays three endothermic peaks at about 50, 100, 150 °C, and one peak around 300 °C. A common endothermic peaks centered around 50 °C and 100 °C represent the release of moisture and surface adsorbed water molecules. The peak at about 150 °C originates from removal of water molecules bound to the surface of the sample. The last broad peak, around 300 °C, is due to phase transition and corresponds to desorption of interlayered water [40,43,49,59].

3.3. Photocatalytic activity

In order to evaluate the photocatalytic performance of the prepared samples, the dye solution of Reactive Orange (RO16) was used as a model pollutant. The effect of powders' structure, composition, and morphology on the photocatalytic activity is presented in Fig. 11.

As it can be noticed, all three samples were active in the degradation of RO16 dye. The nanopowder ${\rm TiO_2}$ with major brookite phase showed the highest photocatalytic activity, where only after 30 min, an almost complete degradation process took place. In the case of titanate before and after annealing, for the same time, around 39 % and 64 % of dye was removed, respectively. After 90 min the process of complete dye degradation was achieved in the case of annealed titanate, whereas for titanates before annealing, degradation was around 80 %.

The heterogeneous photocatalytic degradation reaction is usually described by the Langmuir-Hinshelwood kinetic model. This model relies on the assumption that a fast equilibrium sorption process is accompanied by a slow reaction at the solid-liquid interface [60–62].

At a lower dye concentration, much less than 10^{-3} M, the final form of the equation can be expressed as [62-64]:

$$\ln\left(\frac{C_0}{C_t}\right) = k_r K_{LH} t = k' t \tag{1}$$

where k_r is the reaction rate constant, C_0 is the initial dye concentration, K_{LH} represents the Langmuir-Hinshelwood equilibrium constant, and k' is the pseudo-first-order rate constant.

By presenting the $\ln (C_t/C_0)$ against irradiation time in Fig. 12, it can be clearly observed that good linear dependence shows that experimental data agree well with the first-order kinetic model for all three

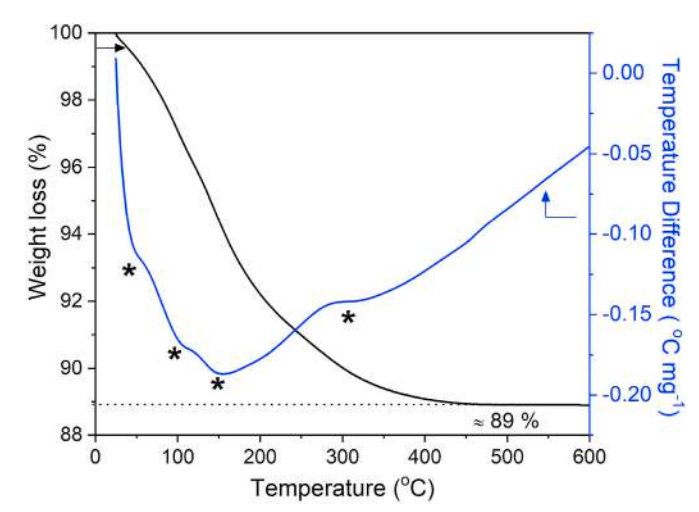


Fig. 10. TGA (black line) and DTA (blue line) during annealing process for titanates containing: $NaTi_3O_6(OH)(H_2O)_2$, $Na_2Ti_3O_7$, and $Na_2Ti_9O_{19}$. (For interpretation of the references to color in this figure legend, the reader is referred to the Web version of this article.)

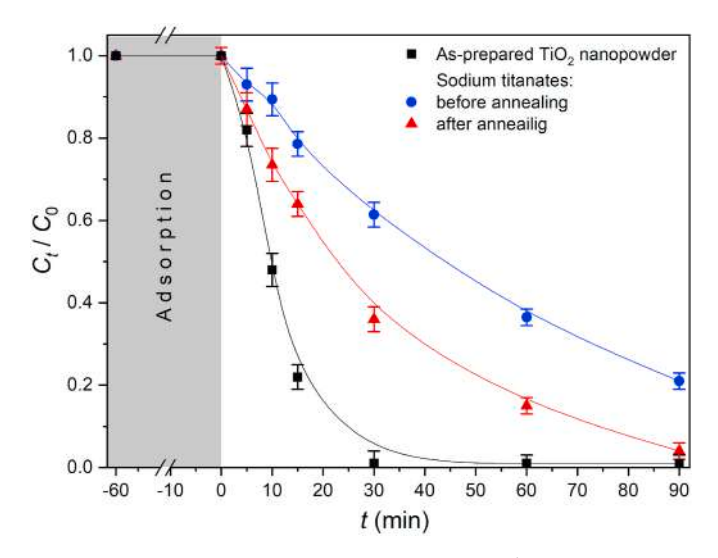


Fig. 11. Photocatalytic degradation of RO16 (50 mg l^{-1}) in the presence of mixed-phase TiO_2 nanopowder, and sodium titanate before and after annealing, under UV irradiation (the lines are only guides for the eyes).

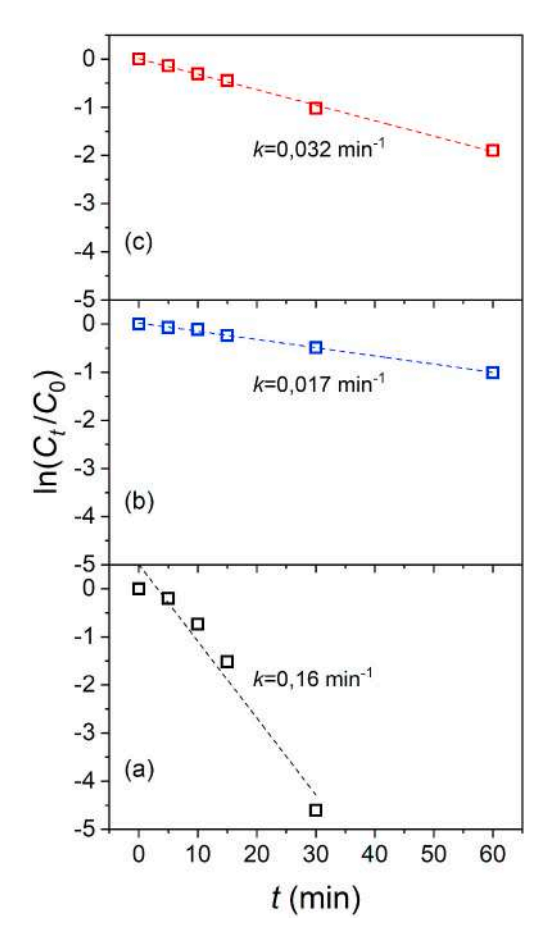


Fig. 12. Determination of the pseudo-first-order kinetic rate constant k' for the (a) mixed-phase TiO_2 nanopowder, and sodium titanate sample (b) before and (c) after annealing.

samples.

The values for k', calculated from the slope of Eq. (1), are given in Table 4. Together with these data, the high value of correlation coefficients (R^2) is also presented, confirming the adequacy of the pseudo-first-order model to describe the kinetics of RO16 dye degradation. From

Table 4Pseudo-first-order kinetic rate constant for all three samples.

Sample	Reactive Orange 16				
	k' - _{RO16} (min ⁻¹)	R ²			
mixed-phase TiO ₂	0.161	0.9550			
Titanate	0.017	0.9972			
Annealed titanate	0.031	0.9976			

this analysis, the lowest photocatalytic efficiency was recorded for titanate before annealing, whereas the most effective in the degradation process was mixed-phase TiO2 nanopowder. The reason for the high efficiency of the as-prepared nanopowder can be ascribed to the coexistence of brookite and anatase phases. Often, better photocatalytic efficiency of polymorph phases compared to a single crystalline phase of TiO₂ originates from better separation of photoinduced electrons and holes, and thus a slower process of recombination will occur. The advantages of the synergistic effect and interfacial contact of two-phase photocatalysts regarding the transfer of electrons have been reported [64–66]. The mechanism of photocatalysis is delicate field. Many factors have contribution such as: crystallinity, specific surface area, morphology, promotion of the active facets, the efficient charge carrier separation/slow recombination, and formation of different kind of radicals (the most important OH*). In addition to this, it has been reported that coupling of different crystals forms of TiO2, such as brookite/anatase mixed, can enhance the photocatalytic activity [39,64,67]. On the other hand, from the literature data, it has been reported that the sodium titanates are less photoactive. Namely, this was attributed to the presence of Na⁺ in the titanate, acting as a recombination center. The post-annealing treatment of the nanostructures plays an important role in determining photocatalytic activity, since the increase in this activity is related to corresponding changes in crystal phase and morphology. The improved performance can originate from the enhancement in crystallinity due to the calcination process. Consequently, this enables easier internal charge carrier transfer and also decreases charge recombination [47]. Furthermore, sodium titanates with a tunnel-like structure and nanoribbon morphology are formed as a result of the annealing process. The explanation for improved effectiveness is probably related to their tunnel structure, which is believed to promote electron/hole separation [47]. Although, the photocatalytic activity of obtained sodium titanates didn't outperform the activity of TiO2 regarding the decomposition of RO16 dye solution, their different structural and morphological properties together with possibility for modification opens the door for application in different fields, representing the topics of interest nowadays [46,68–70].

4. Conclusion

In the present study, different kinds of sodium titanates were prepared starting from the hydrothermally synthesized TiO2 brookite/ anatase mixed nanopowder, with the dominant brookite phase. Highly alkaline hydrothermal treatment has been used in both the synthesis of TiO₂ precursor and the preparation of sodium titanate. According to XRPD and HRTEM (also supported by FTIR and Raman results), asprepared sodium titanate with nanoribbon morphology appeared with NaTi₃O₆ (OH)(H₂O)₂ as a dominant phase. After subjecting this sample to annealing, the interlamellar water present in the sample before annealing disappeared, and phase transformation occurred. As a specific product of the annealing procedure under the condition of sodium excess, a unique combination of sodium hexatitanate (Na₃Ti₆O₁₃) and nonatitanate (Na2Ti9O19) appeared, which has been confirmed by the XRPD and HRTEM analyses. The Raman and FTIR spectra of these still insufficiently examined phases are analyzed in detail. The morphology has been maintained in the annealed sample, but with somewhat wider nanoribbons, implying that larger nanoribbons were growing at the expense of the smaller ones. The fastest photocatalytic degradation of an aqueous solution of RO16 dye was ascribed to ${\rm TiO_2}$ nanopowder with brookite and anatase phase, which could be explained by a synergistic effect. Hydrothermal synthesis of sodium titanate lowers photocatalytic efficiency, but subsequent annealing procedures make it better. The annealed sample, containing ${\rm Na_3Ti_6O_{13}}$ and ${\rm Na_2Ti_9O_{19}}$, represents a promising photocatalyst regarding the abatement of pollution caused by organic dyes.

CRediT authorship contribution statement

Nataša Tomić: Writing – original draft, Methodology, Investigation, Formal analysis, Conceptualization. Mirjana Grujić-Brojčin: Writing – original draft, Investigation, Formal analysis. Aleksandar Kremenović: Writing – original draft, Methodology, Investigation, Formal analysis. Mirjana Novaković: Writing – original draft, Investigation, Formal analysis. Vladimir Lazović: Investigation, Formal analysis. Maja Šćepanović: Writing – original draft, Supervision, Investigation, Formal analysis, Conceptualization.

Declaration of competing interest

The authors declare that they have no known competing financial interests or personal relationships that could have appeared to influence the work reported in this paper.

Acknowledgment

The authors acknowledge funding provided by the Institute of Physics Belgrade, through the grant by the Ministry of Science, Technological Development and Innovation of the Republic of Serbia, as well as by the Vinča Institute of Nuclear Sciences (contract No. 451-03-66/2024-03/200017) and Faculty of Mining and Geology, University of Belgrade (contract No. 451-03-66/2024-03/200126). Authors acknowledge Judith Oro from Institute of Material Science Barcelona, Spain (ICMAB-CSIC) for support in experimental assistance during TEM observation.

References

- [1] A. Di Paola, M. Bellardita, L. Palmisano, Brookite, the least known TiO₂ photocatalyst, Catalysts 3 (2013) 36–73. https://doi:10.3390/catal3010036.
- [2] J. Xie, X. Lü, J. Liu, H. Shu, Brookite titania photocatalytic nanomaterials: synthesis, properties, and applications, Pure Appl. Chem. 81 (2009) 2407–2415. http://doi:10.1351/PAC-CON-08-11-12.
- [3] A. Di Paola, G. Cufalo, M. Addamo, M. Bellardita, R. Campostrini, M. Ischia, R. Ceccato, L. Palmisano, Photocatalytic Activity of Nanocrystalline TiO₂ (Brookite, Rutile and Brookite-Based) powders prepared by thermohydrolysis of TiCl₄ in aqueous chloride solutions, Colloids Surf. A Physicochem. Eng. Asp. 317 (2008) 366–376, https://doi.org/10.1016/j.colsurfa.2007.11.005.
- [4] M.N. Iliev, V.G. Hadjiev, P. Litvinchuk, Raman and infrared spectra of brookite (TiO₂): experiment and theory, Vib. Spectrosc. 64 (2013) 148–152, https://doi. org/10.1016/j.vibspec.2012.08.003.
- [5] B.I. Lee, X. Wang, R. Bhave, M. Hu, Synthesis of brookite TiO₂ nanoparticles by ambient condition sol process, Mater. Lett. 60 (2006) 1179–1183. https://doi:10 .1016/j.matlet.2005.10.114.
- [6] R.C. Bhave, B.I. Lee, Experimental variables in the synthesis of brookite phase TiO₂ nanoparticles, Mater. Sci. Eng. A 467 (2007) 146–149. https://doi:10.1016/j.meeg.2007.03.002
- [7] J.H. Lee, Y.S. Yang, Synthesis of TiO₂ nanoparticles with pure brookite at low temperature by hydrolysis of TiCl₄ using HNO₃ solution, J. Mater. Sci. 41 (2006) 557–559. https://doi:10.1007/s10853-005-2152-z.
- [8] Y. Zheng, E. Shi, S. Cui, W. Li, X. Hu, Hydrothermal preparation of nanosized brookite powders, J. Am. Ceram. Soc. 83 (2000) 2634–2636, https://doi.org/ 10.1111/i.1151-2916.2000.tb01605.x.
- [9] Z. Yanqing, S. Erwei, C. Suxian, L. Wenjun, H. Xingfang, Hydrothermal preparation and characterization of brookite-type TiO₂ nanocrystallites, J. Mater. Sci. Lett. 19 (2000) 1445–1448, https://doi.org/10.1023/A:1011010306699.
- (2000) 1445–1448, https://doi.org/10.1023/A:1011010306699.
 [10] S. Okano, S. Yamamuro, T. Tanaka, Synthesis of brookite-typed titania from chloride solution, Sci. China Ser. E-Tech Sci. 52 (2009) 190–192, https://doi.org/10.1007/s11431-009-0024-5
- [11] T.-D. Nguyen-Phan, E.J. Kim, S.H. Hahn, W.-J. Kim, E.W. Shin, Synthesis of hierarchical rose bridal bouquet- and humming-top-Like TiO₂ nanostructures and their shape-dependent degradation efficiency of dye, J. Colloid Interface Sci. 356 (2011) 138–144. https://doi:10.1016/j.jcis.2010.12.073.

- [12] H. Lin, L. Li, M. Zhao, X. Huang, X. Chen, G. Li, R. Yu, Synthesis of high-quality brookite TiO₂ single-crystalline nanosheets with specific facets exposed: tuning catalysts from inert to highly reactive, J. Am. Chem. Soc. 134 (2012) 8328–8331, https://doi.org/10.1021/ia3014049.
- [13] N. Tomić, M. Grujić-Brojčin, N. Finčur, B. Abramović, B. Simović, J. Krstić, B. Matović, M. Šćepanović, Photocatalytic degradation of alprazolam in water suspension of brookite type TiO₂ nanopowders prepared using hydrothermal route, Mater. Chem. Phys. 163 (2015) 518–528, https://doi.org/10.1016/j.matchemphys.2015.08.008.
- [14] S. Papp, L. Korosi, V. Meynen, P. Cool, E.F. Vansant, I. Dekany, The Influence of temperature on the structural behaviour of sodium tri- and hexa-titanates and their protonated forms, J. Solid State Chem. 178 (2005) 614–1619. https://doi:10.1016/j.issc.2005.03.001.
- [15] V. Bellat, R. Chassagnon, O. Heintz, L. Saviot, D. Vandroux, N. Millot, A multi-step mechanism and integrity of titanate nanoribbons, Dalton Trans. 44 (2015) 1150–1160, https://doi.org/10.1039/c4dt02573c.
- [16] X.-d. Meng, D.-z Wang, J.-h. Liu, S.-y. Zhang, Preparation and characterization of sodium titanate nanowires from brookite nanocrystallites, Mater. Res. Bull. 39 (2004) 2163–2170. https://doi:10.1016/j.materresbull.2004.08.011.
- [17] A.-L. Papa, N. Millot, L. Saviot, R. Chassagnon, O. Heintz, Effect of reaction parameters on composition and morphology of titanate nanomaterials, J. Phys. Chem. C 113 (2009) 12682–12689, https://doi.org/10.1021/jp903195h.
- [18] C.-Y. Xu, J. Wu, P. Zhang, S.-P. Hu, J.-X. Cui, Z.-Q. Wang, Y.-D. Huang, L. Zhen, Molten salt synthesis of Na₂Ti₃O₇ and Na₂Ti₆O₁₃ one-dimensional nanostructures and their photocatalytic and humidity sensing properties, CrystEngComm 15 (2013) 3448–3454, https://doi.org/10.1039/C3CE27092K.
- [19] A. Baszczuk, M. Jasiorski, B. Borak, J. Wodka, Insights into the multistep transformation of titanate nanotubes into nanowires and nanoribbons, Mater. Sci. Poland 34 (2016) 691–702. https://doi:10.1515/msp-2016-0094.
- [20] D.M. da Silva, B.R.C. de Menezes, V.D. Nonato Bezzon, T.L. do Amaral Montanheiro, E.F. de Macedo, D.B. Tada, G. Petraconi, G.P. Thim, Phase transition of TiO₂ nanoparticles into titanate nanorods via hydrothermal reactions, SN Appl. Sci. 1 (2019) 945, https://doi.org/10.1007/s42452-019-1004-4.
- [21] L.N. Costa, F.X. Nobre, B.C.V. Neto, J.M.E. de Matos, Ion exchange in sodium titanate nanoribbons and its application in dye photodegradation of remazol blue, Mater. Sci. Forum 869 (2016) 795–799. https://doi:10.4028/www.scientific. net/MSF 869 795
- [22] D.S. Conceicão, D.P. Ferreira, C.A.L. Graca, M.F. Júlio, L.M. Ilharco, A.C. Velosa, P. F. Santos, L.F.V. Ferreira, Photochemical and photocatalytic evaluation of 1D titanate/TiO₂ based nanomaterials, Appl. Surf. Sci. 392 (2017) 418, https://doi.org/10.1016/j.apsusc.2016.09.067, 19.
- [23] B.C. Viana, O.P. Ferreira, A.G.S. Filho, J.M. Filho, O.L. Alves, Structural, morphological and vibrational properties of titanate nanotubes and nanoribbons, J. Braz. Chem. Soc. 20 (2009) 167–175. https://doi:10.1590/S0103-50532009000 100025
- [24] A.P.S. Souza, O.P. Ferreira, V.F. Nunes, A.F. Almeida, F.M. Lima, F.N.A. Freire, Performance evaluation of titanate nanotubes and nanoribbons deposited by electrophoresis in photoelectrodes of dye-sensitized solar cells, Mater. Res. 21 (2018) e20180110, https://doi.org/10.1590/1980-5373-MR-2018-0110.
- [25] D.L. Morgan, E.R. Waciawik, R.L. Frost, Relationship of titania nanotube binding energies and Raman spectra, in: International Conference on Nanoscience and Nanotechnology, Brisbane, QLD, Australia, 2006, pp. 60–63.
- [26] H. Yoshida, S. Mizuba, A. Yamamoto, Preparation of sodium hexatitanate photocatalysts by a flux method for photocatalytic steam reforming of methane, Catal. Today 334 (2009) 30–36, https://doi.org/10.1016/j.cattod.2019.02.055.
- [27] P. Ji, J. Zhang, P. Chen, M. Anpo, Study of adsorption and degradation of acid orange 7 on the surface of CeO₂ under visible light irradiation, Appl. Catal. B: Environmental 85 (2009) 148–154, https://doi.org/10.1016/j. apcatb.2008.07.004.
- [28] T.G. Venkatesha, R. Viswanatha, Y.A. Nayaka, B.K. Chethana, Kinetics and thermodynamics of reactive and vat dyes adsorption on MgO Nanoparticles, Chem. Eng. J. 198–199 (2012) 1–10, https://doi.org/10.1016/j.cej.2012.05.071.
- [29] M. Sahasrabudhe, G. Pathade, Biodegradation of azo dye C. I. Reactive orange 16 by an actinobacterium georgenia sp. CC-NMPTT3, Int. J. Adv. Res. 1 (2013) 91–99.
- [30] X.S. Wang, Y. Zhou, Y. Jiang, C. Sun, The removal of basic dyes from aqueous solutions using agricultural by-productst, J. Hazard Mater. 157 (2008) 374–385. https://doi:10.1016/j.jhazmat.2008.01.004.
- [31] A. Kremenović, M. Grujić-Brojčin, N. Tomić, V. Lazović, D. Bajuk-Bogdanović, J. Krstić, M. Šćepanović, Size–strain line-broadening analysis of anatase/brookite (TiO₂)-based nanocomposites with Carbon (C): XRPD and Raman spectroscopic analysis, Acta Crystallogr. B 78 (2022) 214–222, https://doi.org/10.1107/ S2052520622001731.
- [32] K. Shen, M. Wagemaker, Na_{2+x}Ti₆O₁₃ as potential negative electrode material for Na-ion batteries, Inorg. Chem. 53 (2014) 8250–8256, https://doi.org/10.1021/ ic5004269.
- [33] H.E. Swanson, H.F. McMurdie, M.C. Morris, E.H. Evans, B. Paretzkin, Standard X-Ray Diffraction Powder Patterns Monograph 25–Section 9, U.S. Government Printing Office, Washington, D.C., 1969.
- [34] I. Andrusenko, E. Mugnaioli, T.E. Gorelik, D. Koll, M. Panthöfer, W. Tremel, U. Kolb, Structure analysis of titanate nanorods by automated electron diffraction tomography, Acta Crystallogr. B: Structural Science, Crystal Engineering and Materials 67 (2011) 218–225, https://doi.org/10.1107/S0108768111014534.
- [35] O.V. Yakubovich, V.V. Kireev, Refinement of the crystal structure of Na2Ti3O7, Crystallogr. Rep. 48 (2003) 24–28, https://doi.org/10.1134/1.1541737.
- [36] F.R. Theobald, C.R.A. Catlow, A.N. Cormack, Lattice energy minimization as a complementary technique to refine structures obtained by high-resolution electron

- microscopy, J. Solid State Chem. 52 (1) (1984) 80-90, https://doi.org/10.1016/
- [37] L.-Y. Liu, Y. Ding, B. Zhou, N.-N. Jia, K. Wang, Z.-H. Zhang, M.-L. Su, Na2Ti7O15 nanowires with an oriented tunnel structure and high mechanical stability: a potential anode of sodium-ion batteries and gas sensing materials, Appl. Sci. 9 (2019) 1673, https://doi.org/10.3390/app9081673.
- [38] R.A. Zárate, S. Fuentes, A.L. Cabrera, V. Fuenzalida, Structural characterization of single crystals of sodium titanate nanowires prepared by hydrothermal process, J. Cryst. Growth 310 (2008) 3630–3637, https://doi.org/10.1016/j
- [39] X. Shen, B. Tian, J. Zhang, Tailored preparation of titania with controllable phases of anatase and brookite by an alkalescent hydrothermal route, Catal. Today 201 (2013) 151-158, https://doi.org/10.1016/j.cattod.2012.04.038
- [40] D.R. Zhang, C.W. Kim, Y.S. Kang, A study on the crystalline structure of sodium titanate nanobelts prepared by the hydrothermal method, J. Phys. Chem. C 114 (2010) 8294-8301, https://doi.org/10.1021/jp101482k
- [41] H. Liu, D. Yang, Z. Zheng, X. Ke, E. Waclawik, H. Zhu, R.L. Frost, A Raman spectroscopic and TEM study on the structural evolution of Na2Ti3O7 during the transition to Na₂Ti₆O₁₃, J. Raman Spectrosc. 41 (2010) 1331–1337, https://
- [42] J. Nava-Avendaño, A. Morales-García, A. Ponrouch, G. Rousse, C. Frontera, P. Senguttuvan, J.-M. Tarascon, M.E. Arroyo-de Dompablo, M. Rosa Palacín, Taking steps forward in understanding the electrochemical behavior of Na₂Ti₃O₇, J. Mater. Chem. A 3 (2015) 22280–22286, https://doi.org/10.1039/C5TA0517
- [43] L. Luo, Y. Zhen, Y. Lu, K. Zhou, J. Huang, Z. Huang, S. Mathur, Z. Hong, Structural evolution from layered Na₂Ti₃O₇ to Na₂Ti₆O₁₃ nanowires enabling a highly reversible anode for Mg-ion batteries, Nanoscale 12 (2020) 230-238, https://doi.
- [44] Y.N. Montecelo, M. Testa-Anta, L. Marín-Caba, M. Pérez-Lorenzo, V. Salgueiriño, M.A. Correa-Duarte, M. Comesaña-Hermo, Titanate nanowires as one-dimensional hot spot generators for broadband Au-TiO2 photocatalysis, Nanomaterials 9 (2019) 990. https://doi:10.3390/nano9070990.
- [45] M. Shirpour, J. Cabana, M. Doef, New materials based on a layered sodium titanate for dual electrochemical Na and Li intercalation systems, Energy Environ, Sci. 6 (2013) 2538-2547, https://doi.org/10.1039/c3ee41037d.
- [46] D.J. Yang, Z.F. Zheng, H.Y. Zhu, H.W. Liu, X.P. Gao, Titanate nanofibers as intelligent absorbents for the removal of radioactive ions from water, Adv. Mater. 20 (2008) 2777-2781, https://doi.org/10.1002/adma.200702055
- K. Kiatkittipong, A. Iwase, J. Scott, R. Amal, Photocatalysis of heat treated sodiumand hydrogen- titanate nanoribbons for water splitting, H2/O2 generation and oxalic acid oxidation, Chem. Eng. Sci. 93 (2013) 341-349, https://doi.org/ 10.1016/i.ces.2013.02.001.
- [48] F.L.R. e Silva, A.A.A. Filho, M.B. da Silva, K. Balzuweit, J.-L. Bantignies, E.W. S. Caetano, R.L. Moreira, V.N. Freire, A. Righi, Polarized Raman, FTIR, and DFT study of Na₂Ti₃O₇ microcrystals, J. Raman Spectrosc. 49 (2018) 538-548. https://doi:10.1002/irs.5316
- [49] Q. Zhang, T. Zhang, Y. Wei, T. Zhai, H. Li, Removing structural water from sodium titanate anode towards barrier-free ion diffusion for sodium ion batteries, J. Mater. Chem. A 5 (2017) 18691-18697, https://doi.org/10.1039/c7ta05217
- Y.V. Kolen'ko, K.A. Kovnir, A.I. Gavrilov, A.V. Garshev, J. Frantti, I. Lebedev, B. R. Churagulov, G. Van Tendeloo, M. Yoshimura, Hydrothermal synthesis and characterization of nanorods of various titanates and titanium dioxide, J. Phys. Chem. B 110 (2006) 4030-4038, https://doi.org/10.1021/jp055687u.
- [51] W. Yin, G. Barim, X. Peng, E.A. Kedzie, M.C. Scott, B.D. Mc Closkey, M.M. Doeff, Tailoring the structure and electrochemical performance of sodium titanate anodes by post-synthesis heating, J. Mater. Chem. A 10 (2022) 25178–25187, https://doi. 10.1039/D2TA07403F
- [52] F.L.R. e Silva, G.A.S. Ribeiro, K. Balzuweit, J.-L. Bantignies, R.L. Moreira, A. Righi, Vibrational and electronic properties of Na₂Ti₆O₁₃, J. Raman Spectrosc. 54 (2023) 551-561, https://doi.org/10.1002/jrs.6511.
- S.S.M. Bhat, B. Babu, M. Feygenson, J.C. Neuefeind, M.M. Shaijumon, Nanostructured Na2Ti9O19 for hybrid sodium-ion capacitors with excellent rate capability, CS Appl. Mater. Interfaces10 (2018) 437-447, https://doi.org 10.1021/acsami.7b13300.

- [54] I. Becker, I. Hofmann, F.A. Muller, Preparation of bioactive sodium titanate ceramics, J. Eur. Ceram. Soc. 27 (2007) 4547, https://doi.org/10.1016/j. eurceramsoc, 2007, 03, 024
- [55] F. Geng, H. Xin, Y. Matsushita, R. Ma, M. Tanaka, F. Izumi, N. Iyi, T. Sasaki, New layered rare-earth hydroxides with anion-exchange properties, Chem. Eur J. 14 (2008) 9255-9260, https://doi.org/10.1002/chem.200800127
- U. Mioč, M. Davidović, N. Tjapkin, Ph Colomban, A. Novak, Equilibrium of the protonic species in hydrates of some heteropolyacids at elevated temperatures, Solid State Ionics 46 (1991) 103–109, https://doi.org/10.1016/0167-2738(91)
- [57] M. Shaban, A.M. Ashraf, M.R. Abukhadra, TiO2 nanoribbons/carbon nanotubes composite with enhanced photocatalytic activity; fabrication, characterization, and application, Sci. Rep. 8 (2018) 781, https://doi.org/10.1038/s41598-018-19172-
- [58] V. Stengl, S. Bakardjieva, J. Subrt, E. Veeernikova, L. Szatmary, M. Klementova, V. Balek, Sodium titanate nanorods: preparation, microstructure characterization and photocatalytic activity, Appl. Catal. B Environ. 63 (2006) 20-30, https://doi. org/10.1016/j.apcatb.2005.09.006.
- [59] M. Zhang, Z. Jin, J. Zhang, X. Guo, J. Yang, W. Li, X. Wang, Z. Zhang, Effect of annealing temperature on morphology, structure and photocatalytic behavior of nanotubed H₂Ti₂O₄(OH)₂, J. M. Catal. A: Chem 217 (2004) 203-210, https://doi. org/10.1016/i.molcata.2004.03.032.
- [60] C.S. Turchi, D.F. Ollis, Photocatalytic degradation of organic water contaminants: mechanisms involving hydroxyl radical attack, J. Catal. 122 (1990) 178-192, https://doi.org/10.1016/0021-9517(90)90269-P.
- [61] A.V. Emeline, V. Ryabchuk, N. Serpone, Factors affecting the efficiency of a photocatalyzed process in aqueous metal-oxide dispersions Prospect of distinguishing between two kinetic models, J. Photochem. Photobiol., A: Chem 133 (2000) 89-97, https://doi.org/10.1016/S1010-6030(00)00225
- [62] N. Daneshvar, M.H. Rasoulifard, A.R. Khataee, F. Hosseinzadeh, C.I. Removal of, Acid Orange 7 from aqueous solution by UV irradiation in the presence of ZnO Nanopowder, J. Hazard Mater. 143 (2007) 95–101, https://doi.org/10.1016/j.
- [63] B. Pare, S.B. Jonnalagadda, H. Tomar, P. Singh, V.W. Bhagwat, ZnO assisted photocatalytic degradation of acridine orange in aqueous solution using visible irradiation, Desalination 232 (2008) 80–90, https://doi.org/10.1016/j desal.2008.01.007.
- [64] Y. Jiao, F. Chen, B. Zhao, H. Yung, J. Zhang, Anatase grain loaded brookite nanoflower hybrid with superior photocatalytic activity for organic degradation, Colloids Surf. A Physicochem. Eng. Asp. 402 (2012) 66-71, https://doi.org/ 10.1016/j.colsurfa.2012.03.020.
- [65] Q. Tay, X. Liu, Y. Tang, Z. Jiang, T.C. Sum, Z. Chen, Enhanced photocatalytic hydrogen production with synergistic two-phase anatase/brookite TiO2 nanostructures, J. Phys. Chem. C 117 (2013) 14973–14982, https://doi.org/ 10.1021/ip4040979
- [66] Q. Tay, Z. Chen, Effective charge separation towards enhanced photocatalytic activity via compositing reduced graphene oxide with two-phase anatase/brookite TiO₂, Int. J. Hydrogen Energy 41 (2016) 10590–10597, https://doi.org/10.1016/j
- [67] M. Khazaei, M.R. Mohammadi, Y. Li, Dye-sensitized solar cells based on anataseand brookite-TiO2: enhancing performance through optimization of phase composition, morphology and device architecture, Nanotechnology 35 (2024) 385602, https://doi.org/10.1088/1361-6528/ad5aa1, 14pp.
 S. Dong, N. Lv, Y. Wu, Y. Zhang, G. Zhu, X. Dong, Titanates for sodium-ion storage,
- Nano Today 42 (2022) 101349, https://doi.org/10.1016/j.nantod.2021.101349
- H. Ji, J. Ni, D. Zhao, W. Liu, Application of titanate nanotubes for photocatalytic decontamination in water: challenges and prospects, ACS EST Engg. 2 (2022) 1015-1038, https://doi.org/10.1021/acsestengg.1c00451
- X. Zhu, A. Anzai, A. Yamamoto, H. Yoshida, Silver-loaded sodium titanate photocatalysts for selective reduction of carbon dioxide to carbon monoxide with water, Appl. Catal. B Environ. 243 (2019) 47-56, https://doi.org/10.1016/j. apcatb.2018.10.021.

ARTICLE IN PRESS

Ceramics International xxx (xxxx) xxx

ELSEVIER

Contents lists available at ScienceDirect

Ceramics International

journal homepage: www.elsevier.com/locate/ceramint



Cation-induced structural/morphological control of ZnO under alkaline hydrothermal conditions: Influence on photocatalytic activity

Bojana Kuzmanović ^{a,*} ⁰, Milica Vujković ^b, Bojana Paskaš Mamula ^a ⁰, Mirjana Medić Ilić ^a ⁰, Katarina Batalović ^a, Benjamin Martínez Perea ^c ⁰, Nataša Tomić ^d

- ^a Department of Nuclear and Plasma Physics, Centre of Excellence for Hydrogen and Renewable Energy, "Vinča" Institute of Nuclear Sciences National Institute of the Republic of Serbia, University of Belgrade, POB 522, 11000, Belgrade, Serbia
- ^b Faculty of Physical Chemistry, University of Belgrade, Studentski trg 12-16, Belgrade 118, 11158, Serbia
- ^c Institute of Materials Science of Barcelona CSIC, Campus UAB, Bellaterra, 08193, Spain
- d Center for Solid State Physics and New Materials, Institute of Physics, University of Belgrade, 118 Pregrevica Street, Zemun, Serbia

ARTICLE INFO

Handling Editor: P. Vincenzini

Keywords: ZnO nanoparticles Alkaline cations Crystal growth Photocatalysis

ABSTRACT

This study investigates the hydrothermal synthesis of ZnO nanopowders using three different alkaline reagents: KOH, NaOH, and NH₄OH, focusing on their morphological, structural, and photocatalytic properties. The resulting ZnO powders displayed distinct morphologies - from hexagonal rods and prismatic structures to a 3D butterfly-nebula-like morphology - depending on the base employed. Phase purity and structural characteristics were confirmed via X-ray diffraction (XRD) and Raman spectroscopy, while scanning and transmission electron microscopy (SEM/TEM) revealed significant morphological differences at multiple magnifications. When hydrothermally produced using KOH and NaOH, ZnO crystallizes into hexagonal prismatic rods along the [0001] direction, starting from a zinc hydroxide precipitate. However, its transition to Zn ammine complex occurs by replacing K⁺ or Na⁺ with NH₄⁺ ions during hydrothermal reaction, which changes the preferential crystal growth, favoring the lateral direction. As a result, ZnO nanostructures with a 3D butterfly-nebula-like morphology are formed. This alteration influences the photocatalytic activity, which is assessed by monitoring the degradation of Reactive Orange 16 (RO16) dye under UV irradiation. The ZnO nanopowder synthesized using NaOH exhibited the highest photocatalytic efficiency, achieving complete degradation of the dye within 90 min. The sample prepared with KOH showed a faster degradation rate than the one synthesized with NH₄OH, but still lower than that of the NaOH-based sample. These findings highlight the crucial influence of base selection during hydrothermal synthesis on the morphology, crystallite size, and photocatalytic behavior of ZnO nanostructures, providing insights for the design of more efficient materials for environmental remediation applications.

1. Introduction

Thanks to their unique physicochemical properties—chemical inertness, thermal stability, a wide band gap (3.37 eV), high transparency, and high electron mobility—ZnO nanoparticles have found broad application in photocatalysis [1], chemical sensing [2], solar energy conversion [3], piezoelectric devices [4], biomedical applications [5], as well as in many other advanced technologies. They have attracted particular attention due to their biocompatibility, biodegradability, and non-toxicity, making them especially suitable for applications in medicine and environmental remediation [6,7]. Although TiO₂ is the most widely studied photocatalyst, research has shown that ZnO exhibits

higher photocatalytic efficiency [8], primarily due to more effective generation and separation of photoinduced electrons and holes [9].

Through various synthesis procedures [10–15], diverse morphologies of ZnO particles have been successfully obtained, including nanoparticles, nanodots, nanoneedles, nanotubes, nanoflowers, nanoplates, nanopyramids, and others [16–18]. Moreover, the literature also describes more complex morphologies of ZnO, such as flower-like, star-like, or cauliflower-like structures [19]. Compared to other methods, hydrothermal synthesis stands out because it allows the production of highly crystalline materials with controlled shape and particle size, as well as the possibility of targeted morphology modification according to desired applications.

E-mail address: kuzmob@vinca.rs (B. Kuzmanović).

https://doi.org/10.1016/j.ceramint.2025.09.347

Received 22 May 2025; Received in revised form 20 September 2025; Accepted 23 September 2025 Available online 30 September 2025

0272-8842/© 2025 Elsevier Ltd and Techna Group S.r.l. All rights are reserved, including those for text and data mining, AI training, and similar technologies.

^{*} Corresponding author.

The characteristics of the obtained ZnO are determined by a range of factors, including the pH of the reaction mixture, the type and concentration of the precursor, reaction temperature and calcination process, synthesis duration, and the choice of solvent [20,21]. According to most available studies, the pH of the solution has a decisive influence on the size and morphology of the synthesized ZnO nanoparticles [22-26]. In the scope of this, additional control can be achieved by selecting the initial precursor and introducing surfactants [27]. On the other hand, different zinc salts (Zn(CH₃COO)₂, ZnCl₂, Zn(NO₃)₂, ZnSO₄) [28-31], used as precursors in ZnO nanoparticle synthesis, significantly affect the morphology while having little or no effect on the crystallite size, according to results summarized by Shaba and colleagues [20]. Furthermore, even small changes in the concentration of these reactants can lead to particles of different shapes and compositions [32]. It has also been shown that the particle shape largely depends on the nature of the added base, indicating specific cation adsorption on the surfaces of crystal seeds [33]. Parameters such as the rate, location, and direction of ZnO crystal growth are crucial for controlling their morphology [34]. Using strong bases (NaOH, KOH) forms a larger number of species that act as crystal seeds for ZnO formation, which slows down the growth rate compared to the weaker base (NH₄OH) [35].

Although numerous studies have examined the influence of pH, precursor type, and base nature on the morphology and crystal structure of ZnO (e.g., NaOH in solvothermal and microwave procedures by Anžlovar and Katiyar [36,37], NH₄OH in sol–gel processes by Santra and co-workers [33], and KOH under hydrothermal conditions by Kumaresan [26]), in most of these studies multiple synthesis parameters are varied simultaneously — pH, type and concentration of precursor, method/solvent, presence of surfactants, temperature, and/or reaction time. This makes it difficult to isolate and quantitatively assess the specific contribution of individual alkaline cations (Na $^+$, K $^+$, NH $^+$) to ZnO growth and morphology.

In contrast, in this work we present comparative study and systematically investigate solely the effect of the cation, under strictly identical conditions: pH $\sim\!9$, the same Zn^{2+} precursor (ZnCl₂), identical reagent concentration, temperature, time, solvent, and without any surfactants; the only variable is the nature of the basic cation (NaOH, KOH, NH₄OH). Such an experimental design enables a direct and reliable attribution of the observed differences in crystallinity, size, and morphology of ZnO specifically to the type of cation.

At the same time, the photocatalytic degradation of organic dyes using ZnO has been extensively studied, but most works focused on dyes such as Reactive Red F3B, Auramine O-A, and Acid Red 14, Acid Brown 14 [38–41]. Only a few studies have addressed the degradation of Reactive Orange 16 (RO16) [10,42], even though it is widely used in the textile industry, resistant to natural degradation, and classified as a hazardous environmental pollutant.

To the best of our knowledge, such system, where differences in properties are established and further correlated with photocatalytic activity, has not been previously reported. This approach clearly highlights the influence of alkaline cations on nucleation and crystal growth, enabling a direct correlation between structural and morphological characteristics implying the variety in the field of adsorption and the photocatalytic performance of RO16 degradation.

2. Experimental

2.1. Synthesis of ZnO materials

ZnO nanoparticles were synthesized via a hydrothermal method from ZnCl $_2$ salt in the presence of three different bases: KOH, NaOH, and NH $_4$ OH. The preparation procedure was identical for all three bases. In a typical procedure, a certian amount of ZnCl $_2$ was dissolved in 100 mL of distilled water, and the selected base, each one with concentration of 2M, was added dropwise under constant stirring using a magnetic stirrer, in order to achieve pH $_2$ O. The resulting solution was transferred to

a 100 mL Teflon-lined stainless steel autoclave, where the hydrothermal synthesis was performed at a controlled temperature of 150 $^{\circ}\text{C}$ for 20 h. After the reaction, the autoclave was allowed to cool naturally to room temperature. The supernatant solution was then decanted to separate the precipitate, which was washed several times with distilled water and ethanol, followed by filtration and drying in an oven at a temperature of 60 $^{\circ}\text{C}$ overnight.

2.2. Characterization methods

The structural properties, phase composition, and crystallinity of ZnO nanopowders synthesized with the three different bases were analyzed using X-ray diffraction (XRD) on a Siemens D5000 diffractometer with Cu K α radiation ($\lambda=1.5406$ Å) over a 2θ range from 10° to 100° , with a step size of 0.02° . Phase identification was performed using the JCPDS database, Card No. 36-1451 (ZnO).

Raman spectra of the samples were collected using a commercial NTegra Spectra system from NT–MDT. The measurements were conducted in the spectral range of $100-1500~{\rm cm}^{-1}$ at room temperature, using a 532 nm laser source set to 2 mW power. The spectral resolution was $1~{\rm cm}^{-1}$, and the exposure time was 300 s.

Surface morphology was characterized using Scanning Electron Microscopy (QUANTA FEI 200 FEG-ESEM) operated at 20 kV. Prior to imaging, the samples were ultrasonically dispersed in ethanol.

Crystallinity, morphology, and particle size were further examined using transmission electron microscopy (TEM), with an FEI Talos F200X microscope operated at 200 keV. For TEM analysis, samples were ultrasonically dispersed in ethanol and drop-cast onto carbon-coated grids. Both conventional and high-resolution TEM (HRTEM) analyses were performed, along with imaging in high-angle annular dark-field (HAADF) mode. Scanning transmission electron microscopy (STEM) was coupled with energy-dispersive X-ray spectroscopy (EDS). Phase composition was also examined by selected area electron diffraction (SAED), with further analysis using the Fast Fourier Transform (FFT) method. The optical properties of ZnO samples were characterized by UV-Vis spectroscopy. The diffuse reflectance spectra were recorded at room temperature in the range of 300-800 nm with BaSO₄ as an internal standard, using a Shimadzu UV-2600i spectrophotometer with an integrating sphere. Zeta potentials of ZnO samples were measured using a 0.1 mg/mL suspension of ZnO nanoparticles at (25 \pm 0.1) $^{\circ}$ C in a disposable zeta cell (DTS 1070) of a NanoZS90 (Malvern, UK) apparatus. The measurements were performed under optimal scattering conditions in the pH range from 6 to 12, adjusted by adding HNO3 and KOH solutions.

The photocatalytic activity of all three samples was evaluated through the photodegradation of Reactive Orange 16 (RO16) solution. The reaction was conducted in a batch-type Pyrex reactor equipped with a magnetic stirrer and a water-circulating jacket. The initial RO16 concentration was 50 mg/L, and the catalyst loading was 2 g L $^{-1}$. A 125 W mercury lamp, wich served as the UV light source, was placed 15 cm above the reaction mixture. Experiments were conducted using 25 mL of dye solution. Prior to irradiation, the suspension was stirred in the dark for 60 min to ensure uniform dispersion of the photocatalyst and to establish adsorption—desorption equilibrium. At predetermined time intervals, aliquots of 0.5 mL were withdrawn, centrifuged to remove catalyst particles, and the supernatant was analyzed using a UV–Vis spectrophotometer (DU 720) to monitor dye concentration at 494 nm, the absorption maximum of RO16.

3. Results and discussions

3.1. Investigation of crystal structure, vibrational, and optical properties

3.1.1. XRD analysis

The X-ray diffraction patterns of ZnO_KOH, ZnO_NaOH, and ZnO_NH_4OH powders synthesized from precursor solutions at pH $\sim\!9$ are

shown in Fig. 1. Analysis of all three diffractograms confirmed that all diffraction peaks could be indexed to a hexagonal unit cell of the wurtzite type (space group $P6_3$ mc, JCPDS Card No. 36–1451).

The values obtained for the observed relative intensities, peak positions (2θ) , and interplanar spacings were compared with data for pristine ZnO from the crystallographic database and are presented in Table 1. Analysis of the obtained XRD results reveals that, regardless of particle size or shape, all synthesized ZnO powders exhibited very similar diffraction patterns. No additional diffraction peaks were observed in the recorded diffractograms, indicating the absence of impurities and confirming the high purity of the synthesized ZnO samples. All samples exhibit hexagonal symmetry typical of the wurtzite structure.

A detailed analysis of the recorded XRD patterns revealed variations in the relative intensities of certain reflections, as well as changes in the intensity ratios of the ($10\overline{1}0$):(0002):($10\overline{1}1$) reflections. These variations are attributed to differences in preferential crystal growth along specific crystallographic planes in the individual ZnO samples.

Using Eq. (1), as described by Singh et al. (2015) [43], the interplanar spacing (d) was estimated and is presented in Table 1, while the lattice constants a and c of the wurtzite structure, defined by Eqs. (2) and (3) [44], are provided in Table 2.

$$\frac{1}{d^2} = \frac{4}{3} \left(\frac{h^2 + hk + k^2}{a^2} \right) + \frac{l^2}{c^2}$$
 (1)

$$a = \frac{\lambda}{\sqrt{3}\sin\theta} \tag{2}$$

$$c = \frac{\lambda}{\sin \theta} \tag{3}$$

Assuming first-order approximation (n = 1), the following equation is obtained:

$$\sin^2 \theta = \frac{\lambda^2}{4} \left(\frac{4}{3} \left(\frac{h^2 + hk + k^2}{a^2} \right) + \frac{l^2}{c^2} \right) \tag{4}$$

By applying Equations (2) and (3) for the ($10\overline{10}$) orientation and using 20 values of approximately 31.74° for ZnO_KOH, 31.76° for ZnO_NaOH, and 31.86° for ZnO_NH₄OH, the calculated lattice constant a values are: $a_{\text{KOH}}=3.252$ Å, $a_{\text{NaOH}}=3.251$ Å and $a_{\text{NH4OH}}=3.241$ Å. Similarly, for the (0002) orientation and 20 values of approximately 34.39° (ZnO_KOH), 34.40° (ZnO_NaOH), and 34.52° (ZnO_NH₄OH), the calculated lattice constants c are: $c_{\text{KOH}}=5.211$ Å, $c_{\text{NaOH}}=5.210$ Å i

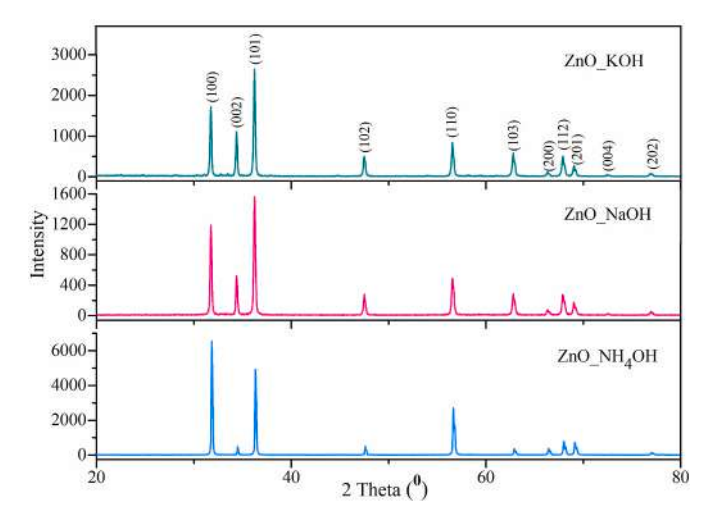


Fig. 1. Diffraction patterns of ZnO powders synthesized by the hydrothermal processing method: ZnO_KOH, ZnO_NaOH and ZnO_NH₄OH.

 $c_{NH4OH} = 5.193 \text{ Å}.$

To determine how the pH ~ 9 value of the reaction mixture together with the persence of different cations of base solution affect the crystallinity of ZnO particles, XRD data were used to calculate the crystallite sizes (D_Scherrer) along the crystallographic planes (1010), (0002), and (1011) for all synthesized samples. Using the Scherrer equation, with appropriate corrections and peak broadening considerations, the average crystallite sizes were calculated and presented in Table 2, based on Eq. (5):

$$D = \frac{k\lambda}{\beta\cos\theta} \tag{5}$$

where k is a shape factor (0.9), λ is the X-ray wavelength (1.5406 Å), β is the full width at half maximum (FWHM) of the diffraction peak in radians, and θ is the Bragg diffraction angle [45]. The average crystallite size along the (10 $\overline{10}$) plane was estimated to be 43.3 nm for ZnO_KOH, 42.5 nm for ZnO_NaOH, and 54.1 nm for ZnO_NH4OH. The FWHM values remained fairly consistent, except in the case of ZnO synthesized in the presence of NH4OH, where noticeable deviation was observed. The corresponding values are listed in Table 1.

The Zn–O bond lengths were calculated using Eq. (6) as described by Bindu et al. [46], where a and c are the lattice parameters, and u is the positional parameter that defines the relative displacement of atoms along the c-axis. The positional parameter u was determined using Eq. (7):

$$L = \sqrt{\left(\frac{a^2}{3} + \left(\frac{1}{2} - u\right)^2 c^2\right)} \tag{6}$$

$$u = \frac{a^2}{3c^2} + 0.25\tag{7}$$

The calculated Zn–O bond lengths for the ZnO_KOH, ZnO_NaOH, and ZnO_NH₄OH samples were 1.979 Å, 1.978 Å, and 1.970 Å, respectively. The calculated atomic packing values were consistent across the samples, showing agreement up to the third decimal place.

In addition, the strain values (ε) caused by crystal imperfections and lattice distortions in the powders were estimated using the Williamson–Hall (W–H) method, which considers the broadening of diffraction peaks due to both crystallite size and internal stresses within the material. According to this method, the total peak broadening in the diffraction pattern can be attributed to contributions from the size of the coherent scattering regions and microstrain within the crystal structure.

The Williamson–Hall approach enables a clear differentiation between peak broadening caused by crystallite size and that caused by lattice strain (stress). This is achieved by analyzing the peak width as a function of the diffraction angle, under the assumption that the contributions from size and strain are independent and can be expressed through mathematical functions dependent on the diffraction angle [46].

The peak broadening due to strain can be calculated using a formula that relates microstrain to peak width, while the contribution from crystallite size is inversely proportional to the size of the coherent crystalline domains. The total peak broadening, β_{hkl} , represents the sum of the contributions from crystallite size β_D and strain β_ε Eq. (8) [47]:

$$\beta_{hkl} = \beta_D + \beta_{\varepsilon} \tag{8}$$

Taking into account the instrumental broadening correction, this sum can be further expressed as a function of the X-ray wavelength, shape factor, crystallite size, and microstrain, yielding the final form of the Williamson–Hall equation (Eq. (9)):

$$\beta_{hkl}\cos\theta_{hkl} = \frac{k\lambda}{D} + 4\varepsilon\sin\theta_{hkl} \tag{9}$$

This equation represents the so-called Uniform Deformation Model (UDM), which assumes that strain is uniformly distributed in all

Table 1
As compared ZnO NPs (ZnO_KOH, ZnO_NaOH and ZnO_NH4OH) and JCPDS data values.

$2\theta_{\text{JCPDS}}$ (°)	$2\theta_{XRD}$			d_{XRD} (Å)	ZnO rela	ZnO relative intensity		$FWHM_{XRD}$			(hkil)	
					I_{JCPDS}	I _{XRD}			β(°)			
31.79	31.74(4)	31.76(4)	31.86(0)	2.819(4)	61.25	66.67	75.07	100	0.19(1)	0.19(1)	0.15(0)	1010
34.44	34.39(7)	34.40(8)	34.52(4)	2.608(6)	45.26	42.17	32.57	6.88	0.20(2)	0.20(2)	0.15(4)	0002
36.27	36.23(3)	36.24(3)	36.34(0)	2.479(3)	100	100	100	73.93	0.21(1)	0.22(1)	0.17(0)	$10\overline{1}1$
47.56	47.51(2)	47.52(2)	47.63(5)	1.914(1)	19.06	18.52	15.55	6.44	0.25(5)	0.26(4)	0.20(5)	$1\overline{0}12$
56.63	56.58(1)	56.59(1)	56.70(1)	1.627(1)	23.29	28.84	30.12	35.63	0.28(3)	0.29(3)	0.26(1)	$11\overline{2}0$
62.89	62.83(2)	62.85(2)	62.96(2)	1.479(1)	19.42	19.65	15.75	4.18	0.33(5)	0.33(5)	0.28(1)	$10\overline{1}3$
66.37	66.36(5)	66.37(8)	66.48(8)	1.409(2)	3.89	3.36	16.17	4.50	0.30(5)	0.32(1)	0.30(8)	$20\overline{2}0$
67.96	67.93(2)	67.95(2)	68.05(4)	1.378(1)	23.26	16.94	8.20	12.15	0.36(2)	0.36(2)	0.31(4)	$11\overline{2}2$
69.10	69.07(5)	69.08(4)	69.19(4)	1.359(2)	11.09	8.48	8.88	6.83	0.36(1)	0.35(1)	0.31(4)	$20\overline{2}1$
72.55	72.53(3)	72.56(2)	72.66(3)	1.303(1)	1.83	1.03	3.92	10.60	0.26(3)	0.23(1)	0.27(1)	0004
76.95	76.95(3)	76.98(3)	77.06(3)	1.239(1)	3.92	2.18	4.96	5.99	0.34(4)	0.35(2)	0.32(4)	$20\overline{2}2$
	(КОН)	(NaOH)	(NH ₄ OH)			(KOH)	(NaOH)	(NH ₄ OH)	(KOH)	(NaOH)	(NH ₄ OH)	

Table 2
X-ray diffraction parameter values of the sample ZnO KOH, ZnO NaOH and ZnO NH₄OH.

Sample	Lattice Parameter Values (Å)		Atomic packing factor (c/a)	Position parameter (u)	Average crystallite size		Bond length Zn-O	Lattice Strain	(hkil)
	a	c			DScherrer (nm)	DW-H	L (Å)		
ZnO (KOH)	3.252(2)	5.211(1)	1.732	0.380(2)	43.3(2) 42.2(4) 39.6(1)	75.4(10)	1.979(3)	0.00132(2)	$(10\overline{1}0)$ (0002) $(10\overline{1}1)$
ZnO (NaOH)	3.251(2)	5.210(1)	1.732	0.380(2)	42.5(0) 44.2(4) 38.6(1)	72.3(8)	1.978(3)	0.00133(1)	$ \begin{array}{c} (10\overline{1}0) \\ (0002) \\ (10\overline{1}1) \end{array} $
ZnO (NH4OH)	3.241(5)	5.193(9)	1.732	0.380(6)	54.1(2) 57.2(4) 49.8(3)	200.9(10)	1.97(1)	0.0016(2)	$(10\overline{1}0)$ (0002) $(10\overline{1}1)$

crystallographic directions and that the crystal is isotropic, meaning its properties do not depend on the measurement direction. Based on a plot of $\beta_{hkl}\cos\theta_{hkl}$ versus $4\sin\theta_{hkl}$, linear parameters are obtained the y-intercept corresponds to the crystallite size, while the slope of the line gives the microstrain value. The Williamson–Hall plots for all three samples, including the calculated values of slope and intercept, are presented in Fig. 2.

The strain values (ε), calculated from the slope of the Williamson–Hall plots, are presented in Table 2 for all samples. Similarly, the crystallite sizes (D_{H-W}) were calculated from the y-intercepts of the Williamson–Hall plots using the relation $D=k\lambda/intercept$, and the reported values correspond to the average of ten reflections, as summarized in Table 2.

3.1.2. Raman spectroscopy

Wurtzite-type ZnO belongs to the $C6v^4$ ($P6_3mc$) symmetry group, with two formula units per primitive cell. According to group theory, single-crystal ZnO possesses eight sets of optical phonon modes at the Brillouin zone center: two A_1 , two E_1 , two E_2 , and two B_1 modes [48,49]. The E_1 and A_1 modes are polar, both Raman- and infrared-active, and each splits into transverse optical (TO) and longitudinal optical (LO) phonons ($A_{1(TO)}$, $E_{1(TO)}$, and $A_{1(LO)}$, $E_{1(LO)}$). The E_2 mode is non-polar and consists of low-frequency (E_2^{low}) and high-frequency (E_2^{high}) phonons. The B_1 modes are Raman inactive (silent modes), whereas the E_2 modes are Raman active [50].

It is reasonable to assume that the low-frequency E_2^{low} mode mainly originates from the vibration of the heavy Zn sublattice, while the high-

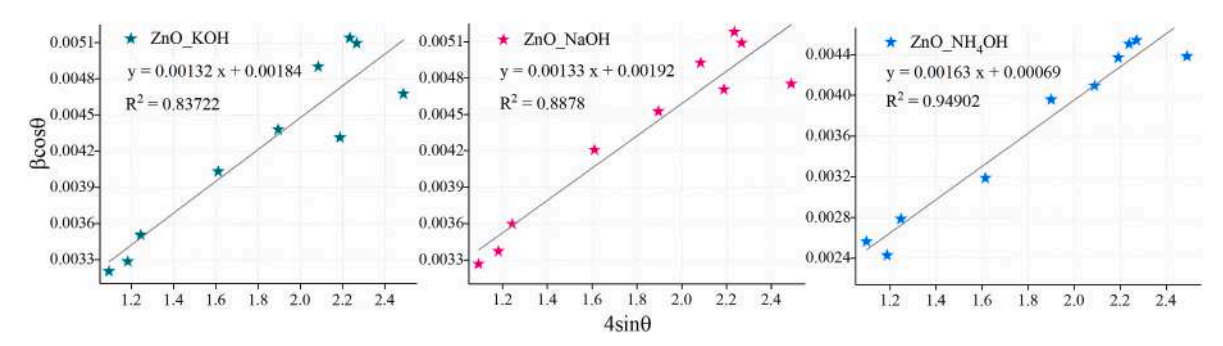


Fig. 2. Plot of $\beta_{hkl}\cos\theta_{hkl}$ versus $4\sin\theta_{hkl}$.

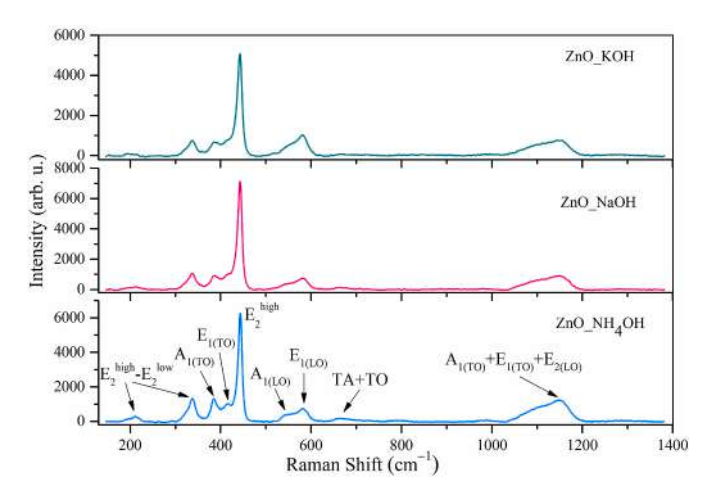


Fig. 3. Raman spectra of the ZnO_KOH, ZnO_NaOH and ZnO_NH4OH samples.

frequency E_2^{high} mode is associated with the vibration of the oxygen sublattice [51,52]. All three Raman spectra of ZnO powders synthesized using KOH, NaOH, and NH₄OH (Fig. 3) exhibit seven prominent peaks at approximately: ~209 cm⁻¹, ~335 cm⁻¹, ~382 cm⁻¹, ~412 cm⁻¹, ~438 cm⁻¹, ~542 cm⁻¹, ~584 cm⁻¹, as well as a broad and intense band in the range of 1050 to 1200 cm⁻¹. Our results are in good agreement with previously published Raman studies [52,53].

The dominant high-intensity peak observed at approximately \sim 438 cm⁻¹ is attributed to the E_2^{high} mode, indicating that all synthesized powders possess a highly crystalline wurtzite structure [54,55]. The lower-intensity peaks at \sim 209 cm⁻¹ and \sim 335 cm⁻¹ are assigned to second-order Raman scattering ($E_2^{high} - E_2^{low}$ mode), which arises from zone-boundary phonons of hexagonal ZnO [50,56]. The Raman peaks at

 ${\sim}382~\text{cm}^{-1}$ and ${\sim}412~\text{cm}^{-1}$ correspond to the polar $A_{1(TO)}$ mode, dominated by oxygen, and the $E_{1(TO)}$ mode, which is associated with Zn-O stretching vibrations, respectively [47] and reflect the strength of polar lattice bonds [57]. The peak located at ${\sim}584~\text{cm}^{-1}$ is attributed to the $E_{1(LO)}$ mode, which may appear due to nanorod misalignment or the presence of structural defects such as zinc interstitials and oxygen vacancies. The peak at 542 cm $^{-1}$ is assigned to the $A_{1(LO)}$ mode, in accordance with theoretical predictions [49,58,59]. In the region between 1050 and 1200 cm $^{-1}$, a broad and intense band labeled as $A_{1(TO)}+E_{1(TO)}+E_{2(LO)}$ is observed, which is attributed to second-order features involving longitudinal optical (LO) phonon combinations and overtones [52,60].

Notably, the ZnO_NH₄OH sample exhibits stronger peak intensities at ${\sim}382~\text{cm}^{-1}$ and ${\sim}412~\text{cm}^{-1}$ compared to the ZnO_KOH and ZnO_NaOH samples, where these peaks are less prominent. Furthermore, the intensity of the E_2^{high} mode in the ZnO_NaOH sample is relatively higher compared to that in the ZnO_NH₄OH and ZnO_KOH samples. These observations indicate differences in the structural and morphological properties, which will be analyzed further.

3.1.3. Optical analysis

The UV–Vis spectra of zinc oxide samples in the diffuse reflectance mode (R) are shown in Fig. 4(a)). The highest reflectance in the visible light region is observed for the ZnO_NaOH sample. The direct band gap energy (Eg) was determined using modified Kubelka–Munk function (F (R)=K/S), where K is the absorption coefficient defined as $(1-R)^2$, while S represents the scattering factor defined as 2R. By plotting $(F(R)h\nu)^2$ versus photon energy $(h\nu)$ (See Fig. 4(b)), the band gap values were estimated by the conventional Tauc's plot as the x-axis intercept, using the extrapolation of the linear fitting to the linear portion of the curve (Fig. 4(b)). Consequently, comparing the results it has been revealed that band gap is not significantly influenced by changing the base solution during synthesis.

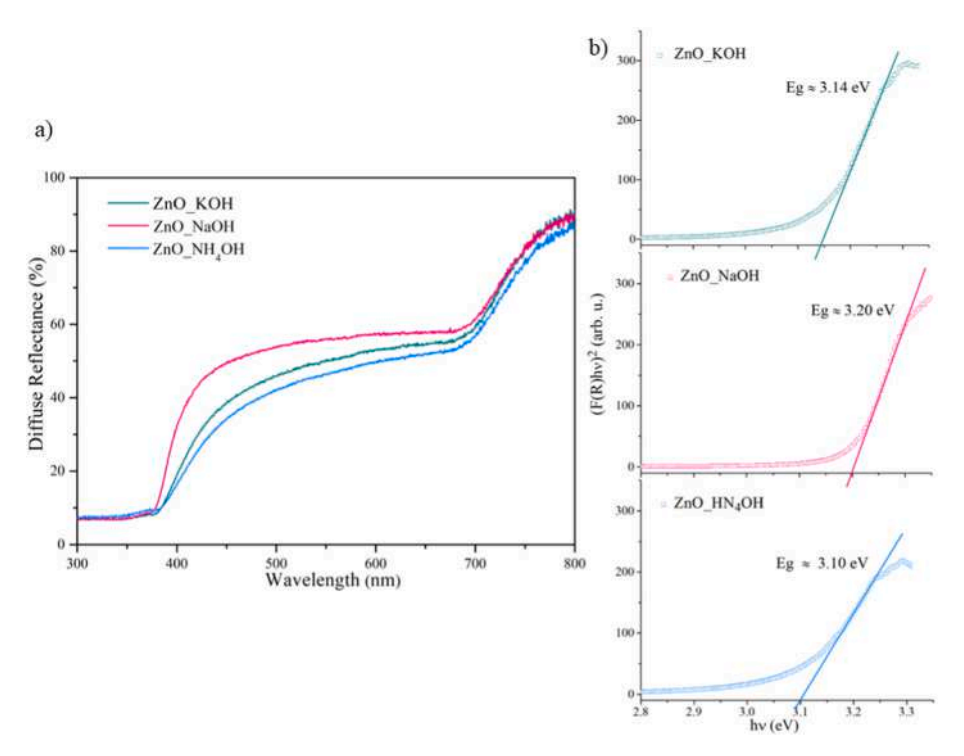


Fig. 4. Diffuse Reflectance spectra (a), and Tauc plot of (F(R)hν)² versus energy (b) of ZnO_KOH, ZnO_NaOH, and ZnO_NH₄ samples.

3.2. Morphological study

3.2.1. FESEM analysis

To determine the morphology and particle size of the hydrothermally synthesized ZnO powders, field emission scanning electron microscopy (FESEM) was employed. The FESEM results for the ZnO powders are presented in Fig. 5. Based on the obtained micrographs, a clear dependence of ZnO morphology and particle size on the choice of base solution used during synthesis, can be observed implying the role of different cations.

Fig. 5(a–c) presents the FESEM micrographs of ZnO samples synthesized using different alkaline reagents. The ZnO_KOH and ZnO_NaOH powders exhibit similar morphologies, consisting of randomly oriented hexagonal prismatic rods with relatively smooth surfaces and shallow central notches. In the ZnO_KOH sample, rod lengths ranged from 0.62 to 3.32 μm , with an average of 1.77 \pm 0.94 μm , while rod diameters (measured at the widest part of the prism) ranged from 0.22 to 0.65 μm

(average 0.36 \pm 0.09 μm). For the ZnO_NaOH sample, the rods were generally thinner and exhibited more pronounced but incompletely developed hexagonal pyramidal tips. Rod lengths ranged from 0.53 to 2.37 μm (average 1.47 \pm 0.72 μm), with rod diameters ranging from 0.20 to 0.43 μm (average 0.35 \pm 0.04 μm).

In contrast, the ZnO_NH₄OH sample (Fig. 5(c)) exhibits a markedly different morphology, with significantly larger prismatic rods branching from a central region; lengths range from 2.81 to 25.74 μm (average 11.71 \pm 9.26 μm) and diameters from 0.71 to 3.62 μm (average 1.90 \pm 1.12 μm), reflecting the pronounced heterogeneity of these branched rods. These structures exhibit pronounced surface roughness with numerous irregularities and a growth pattern involving beveled ends shaped like truncated pyramids. As a result, prismatic rods branch from a central region, and form a 3D butterfly-nebula-like morphology at the microscale. This complex, laterally developed morphology indicates a distinct crystal growth mechanism compared to the ZnO_KOH and ZnO NaOH samples.

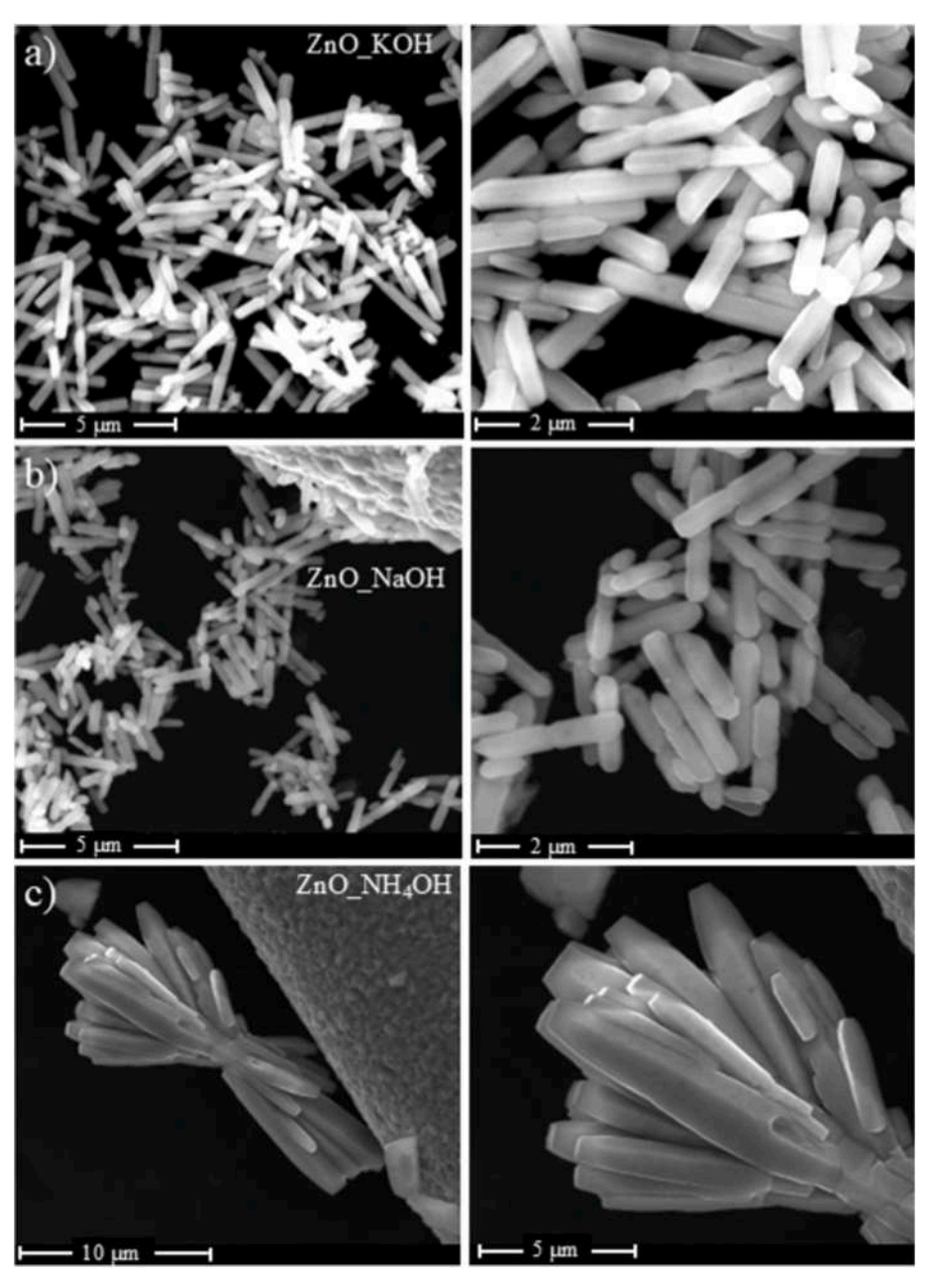


Fig. 5. FESEM images of (a) ZnO_KOH, (b) ZnO_NaOH and (c) ZnO_NH₄OH samples at different magnifications.

The pronounced differences in morphology and crystallographic orientation among the three samples highlight the significant influence of the alkaline reagent on the ZnO crystallization pathway. The transition from isolated prismatic rods (KOH/NaOH) to branched, laterally developed 3D butterfly-nebula-like structures (NH₄OH) suggests the involvement of distinct reaction mechanisms, likely governed by differences in the basicity and complexation behavior of the cations, as well as the formation of hydroxide and complex intermediates, despite all samples being synthesized from the same zinc precursor (ZnCl₂) under identical hydrothermal conditions (pH 9, 2 M base, 150 °C/20 h).

3.2.2. TEM

Transmission electron microscopy was employed to examine the morphology and crystallographic structure of the synthesized ZnO nanopowders (ZnO_KOH, ZnO_NaOH, and ZnO_NH₄OH). Fig. 6(a)_{1,2}, (b)_{1,2} and (c)_{1,2} show representative low- and high-magnification TEM micrographs of the samples, with the corresponding selected area electron diffraction (SAED) patterns given in Fig. 6(a)₃, (b)₃, and (c)₃.

In the ZnO_KOH sample, the low-magnification TEM images reveal

micrometer-sized hexagonal rod-like particles with well-defined facets, averaging $2.14\pm1.03~\mu m$ in length and $0.38\pm0.09~\mu m$ in diameter. These particles exhibit central notches and partially formed tips. The particles are randomly oriented in the projection plane, and occasional overlaps arise from sample preparation rather than a specific tendency to agglomerate. This morphology is consistent with SEM observations, although fine surface textures are less discernible in TEM due to the two-dimensional projection of relatively thick particles.

Similarly, the ZnO_NaOH sample exhibits a prismatic morphology, consisting of micrometer-sized hexagonal particles but with a broader size distribution, having lengths of $1.63\pm2.01~\mu m$ and diameters of $0.35\pm0.31~\mu m$ on average. Particle ends are generally flat or slightly tapered, and no intrinsic clustering tendency is observed; apparent groupings result from random particle overlap. Facets are clearly visible, and some particles display shallow notches or terminations resembling partially formed hexagonal pyramids. In contrast, low-magnification TEM images of the ZnO_NH4OH sample reveal significantly larger prismatic rods, with average lengths of 7.25 \pm 7.60 μm and diameters of 1.84 \pm 2.01 μm . Many particles exhibit irregular terminations and

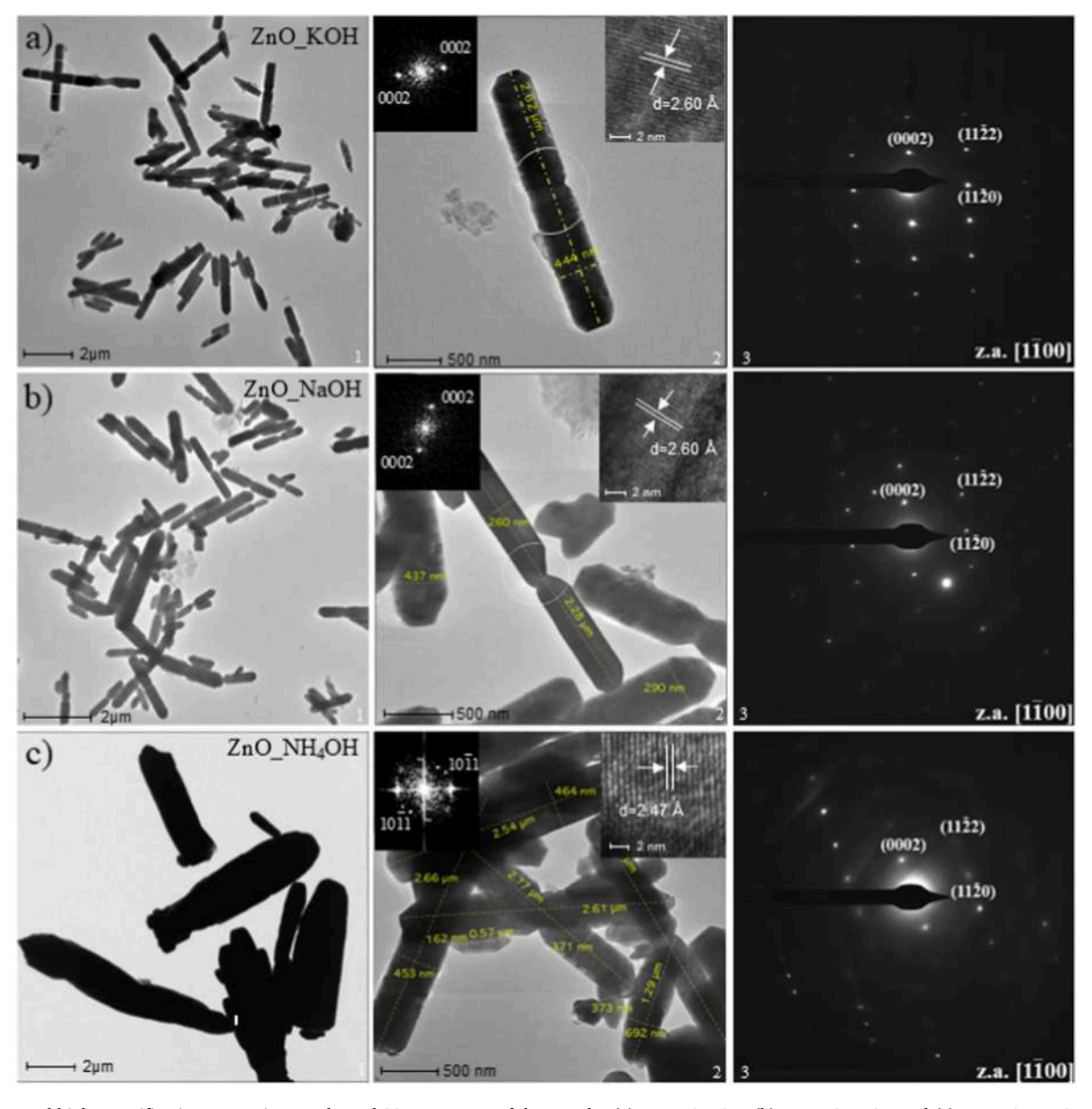


Fig. 6. Low- and high-magnification TEM micrographs and SAED patterns of the samples $(a)_{1,2,3}$ ZnO_KOH, $(b)_{1,2,3}$ ZnO_NaOH and $(c)_{1,2,3}$ ZnO_NH₄OH. FFT's and HRTEM images with measured d-spacing of one isolated, are given in the insets (top - right for HRTEM, top - left for FFT) in $(a)_2$, $(b)_2$ and $(c)_2$, respectively.

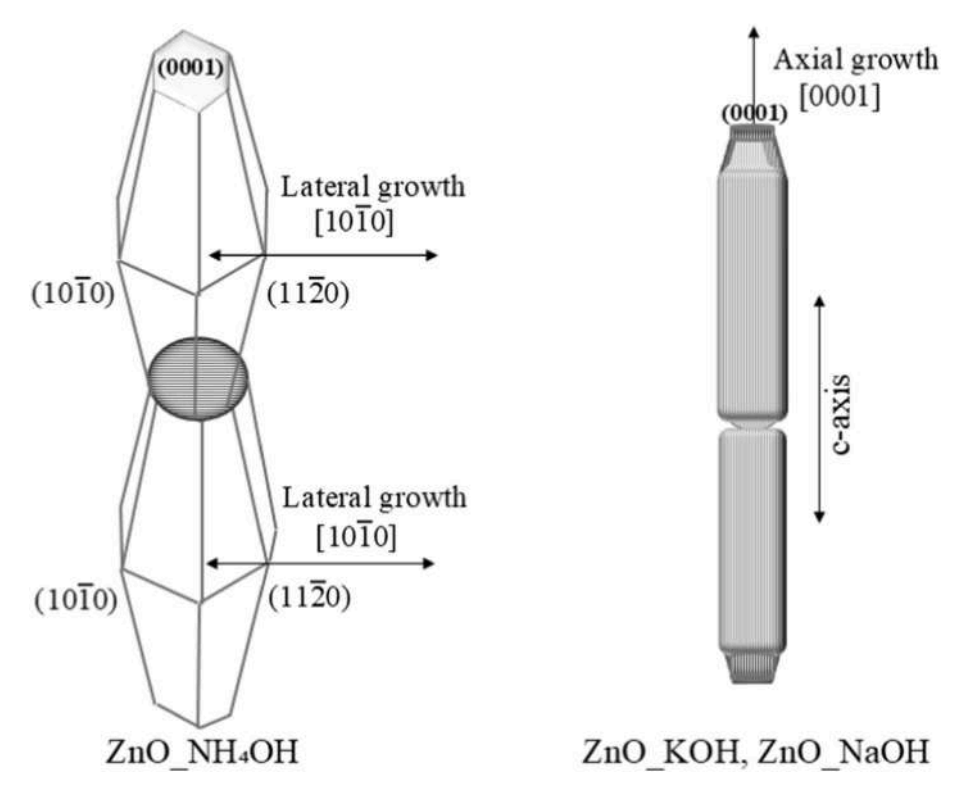


Fig. 7. Schematic representation of ZnO crystal growth orientations under different synthesis conditions. ZnO_KOH and ZnO_NaOH samples exhibit axial growth along the c-axis ([0001]), while ZnO_NH₄OH samples show suppressed axial growth and dominant lateral extension along [1010].

surface microcracks. Although SEM highlights complex surface structuring, such features remain hidden in TEM images, as the signal is integrated over the particle thickness, concealing finer topographical details. Nevertheless, the TEM observations clearly confirm that NH $_4$ OH promotes the growth of considerably larger ZnO rods compared to powders synthesized with KOH and NaOH.

At higher magnifications, HRTEM was employed to analyze the crystal structure in greater detail and to determine interplanar spacings. Representative HRTEM micrographs of single-crystalline ZnO nanorods, together with the corresponding FFT patterns, are presented as insets in Fig. $6(a)_2$, $(b)_2$, and $(c)_2$ (top-right for HRTEM, top-left for FFT). For the ZnO_KOH and ZnO_NaOH samples, the measured lattice spacing was 2.60 Å, corresponding to the (0002) planes of wurtzite ZnO, (JCPDS Card No. 36-1451), suggesting that the nanorods exhibit preferential growth along the c-axis, ([0001] direction). In comparison, the ZnO_NH₄OH sample showed a spacing of 2.47 Å, assigned to the $(10\overline{1}0)$ planes of ZnO, indicating that the particles predominantly grow along the $[10\overline{1}0]$ direction. The FFT patterns reinforce this structural interpretation, revealing lattice periodicities consistent with (0002) planes in ZnO KOH and ZnO NaOH, and (1010) planes in ZnO NH4OH. These findings are further supported by XRD results, which show changes in relative reflection intensities, particularly a reduced (0002) peak and enhanced non-polar plane reflections in ZnO_NH4OH. A schematic depiction of the proposed growth orientations is provided in Fig. 7, highlighting the contrast between the vertical (c-axis) alignment in ZnO_KOH and ZnO_NaOH, and the lateral growth tendency observed in ZnO NH₄OH.

To further verify the crystal structure and phase composition of the ZnO nanorods, selected area electron diffraction (SAED) patterns were acquired from individual nanorods in each sample. The resulting patterns (Fig. $6(a)_3$, $(b)_3$, and $(c)_3$) display well-defined, sharp diffraction spots arranged in a regular array, characteristic of single-crystalline materials. Interplanar spacings (d-values) were calculated from the measured distances relative to the central spot and compared with

standard reference data for ZnO (JCPDS Card No. 36-1451). The observed reflections were successfully indexed to the (0002), ($11\overline{2}0$), and ($11\overline{2}2$) planes, confirming the hexagonal wurtzite structure of ZnO. The measured d-spacings were 2.60 Å, 1.62 Å, and 1.38 Å for both the KOH and NaOH samples, and 2.59 Å, 1.61 Å, and 1.37 Å for the NH₄OH sample, corresponding to the aforementioned reflections. Although the differences between the samples are minor and within the expected experimental uncertainty, the slightly reduced values in the NH₄OH sample may suggest a subtle lattice contraction. This effect could tentatively be attributed to a lower oxygen content, as indicated later by EDS analysis. Nevertheless, this variation does not compromise the overall crystallinity or phase purity. In all cases, the sharpness and symmetry of the SAED reflections confirm the well-preserved wurtzite structure and the single-crystalline nature of the ZnO nanorods.

To complement the structural characterization, scanning transmission electron microscopy (STEM) combined with energy-dispersive X-ray spectroscopy (EDS) was employed to investigate the elemental distribution and composition homogeneity. Fig. 8(a-c) show STEM/ HAADF micrographs along with the corresponding elemental distribution maps obtained using K and L spectral lines (zinc in red, oxygen in green). For all three ZnO samples, the elemental maps reveal a uniform spatial distribution of Zn and O, indicating good compositional homogeneity at the microscale. Quantitative EDS analysis was conducted on larger regions containing multiple ZnO nanorods to determine the atomic percentages of Zn and O and to assess the overall stoichiometry. Signals of carbon and copper, originating from the carbon-coated copper TEM grid, were also detected but excluded from the analysis. The measured contents were 56 at.% Zn and 44 at.% O for the ZnO KOH sample, and 53 at.% Zn with 47 at.% O for the ZnO_NaOH sample (Fig. 9). Notably, the ZnO_NH4OH sample exhibited significantly elevated zinc content of 79 at.%, accompanied by only 21 at.% oxygen. This elevated Zn/O ratio may be attributed to several factors, including the surface morphology characterized by rough textures and surface pores observed in SEM images (Fig. 5(c), as well as the possible presence

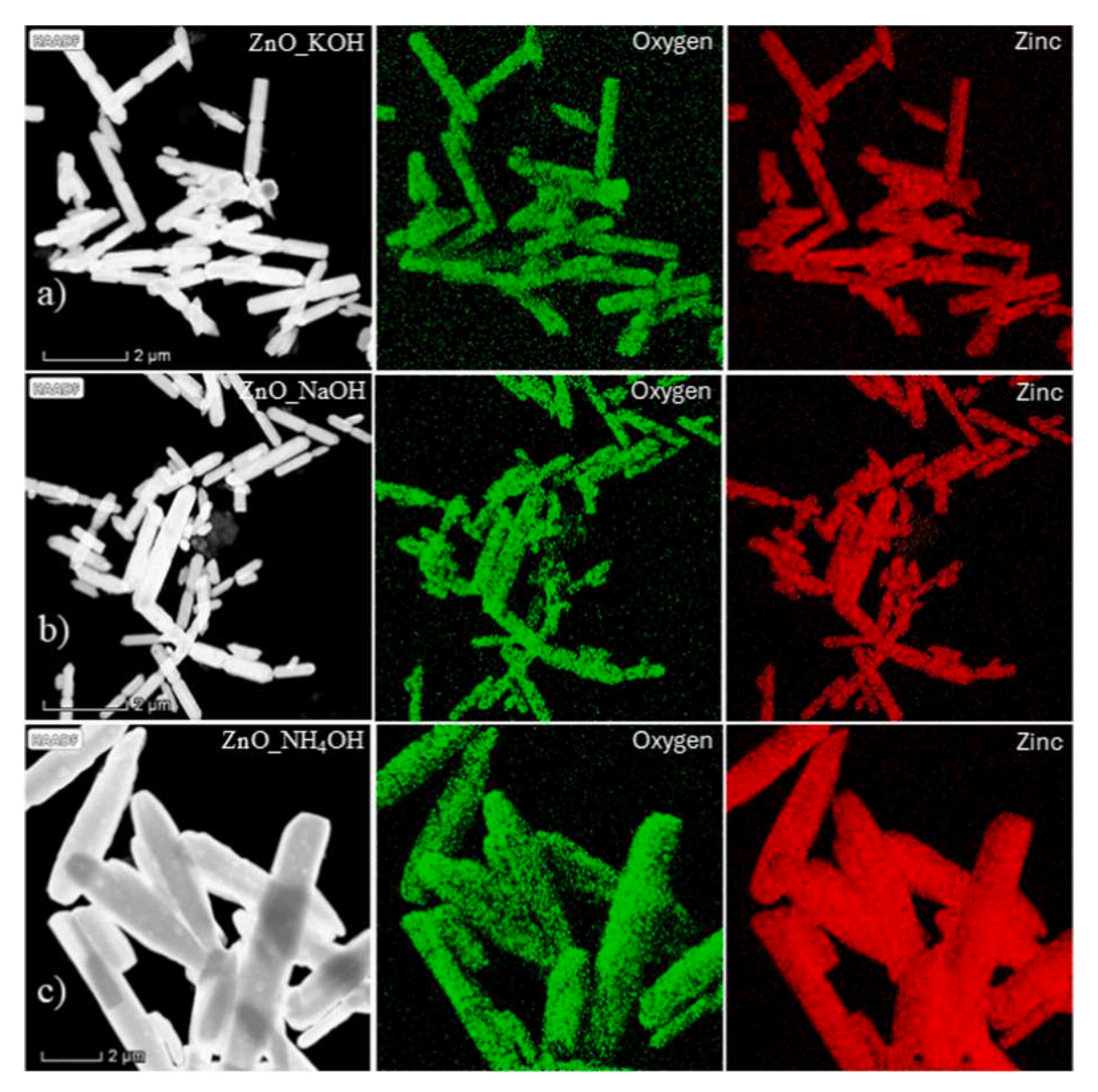


Fig. 8. STEM analysis of the zinc oxide: (a)₁, (b)₁ and (c)₁ STEM/HAADF image of large area of the sample with corresponding EDS maps highlighting oxygen (a)₂, (b)₂ and (c)₂ and zinc elements (a)₃, (b)₃ and (c)₃ in ZnO_KOH, ZnO_NaOH and ZnO_NH₄OH.

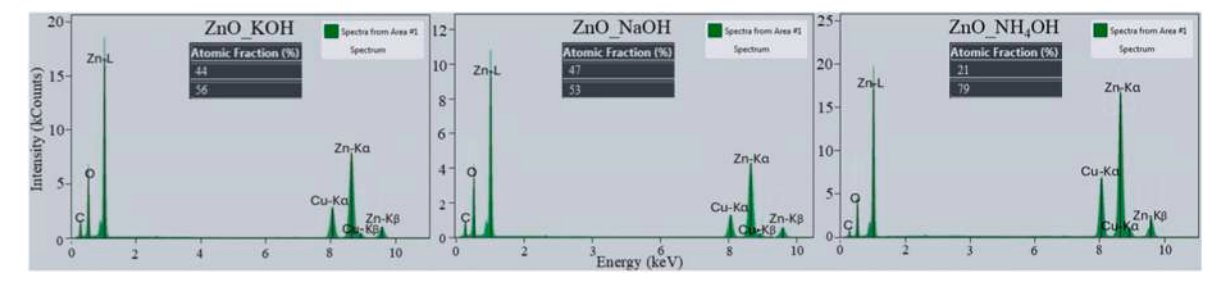


Fig. 9. EDS spectrum taken from the sample area covering a large number of particles, as presented in HAADF image in Fig. 8(a, b and c).

of internal voids. The reduced oxygen content might also reflect the formation of oxygen vacancies, residual $\rm Zn(OH)_2$ species, or adsorbed $\rm Zn^{2+}$ ions on particle surfaces. According to literature, the ideal stoichiometric $\rm Zn/O$ atomic ratio in $\rm ZnO$ is 1:1 (i.e., approximately 50 at.% of each element) [61], a ratio most closely achieved in the $\rm ZnO_NaOH$ sample. Overall, the combined microscopy and spectroscopy analyses illustrate that the alkaline environment used during synthesis has a

pronounced effect on the elemental distribution and $\mbox{Zn/O}$ ratio in the final \mbox{ZnO} structures.

In summary, TEM analysis confirms that the ZnO particle morphology is strongly influenced by the choice of base during synthesis. While KOH and NaOH promote the formation of micrometer-sized hexagonal prisms with well-faceted surfaces and moderate size distributions, NH_4OH leads to a significant increase in particle

dimensions, with widths exceeding 2 μm and lengths over 11 μm . Although fine surface features are more clearly resolved in SEM, TEM observations demonstrate unambiguously that NH₄OH induces more pronounced axial growth and results in particles with irregular terminations and internal cracking. This trend correlates well with the basicity and complexing ability of the respective hydroxides, which govern the nucleation and growth kinetics of ZnO crystals. The pronounced increase in particle size and altered growth direction in the NH₄OH sample likely stem from the distinct basicity and complexation behavior of the ammonium ion compared to K⁺ and Na⁺, affecting nucleation and crystal growth kinetics. These findings are consistent with previous reports highlighting the crucial role of OH⁻ ions not only in the formation of ZnO crystallites but also in directing their growth along specific crystallographic planes [62–64].

3.2.3. Cation-controlled crystal growth

The formation of ZnO nanostructures under hydrothermal conditions from aqueous solutions of $ZnCl_2$ and alkaline sources (KOH, NaOH, NH₄OH) occurs through two main stages: nucleation and crystal growth. These processes, which directly influence the structural and morphological characteristics of the resulting nanostructures, are based on the initial formation of Zn-hydroxide species in the solution, whose development further depends on the nature of the alkaline cation and the types of complex species formed during synthesis.

 $Zn(OH)_2$ is the dominant species in the reaction of $ZnCl_2$ with an OH^- -based solvent under moderate alkaline conditions (pH \sim 9) [65]. These species further react with OH^- ions and form $ZnO_2^{2^-}$, according to reactions (10) and (11) [35], while the OH^- concentration is insufficient to trigger for the formation of typical $Zn(OH)_4^{2^-}$ units required for crystal growth.

$$Zn(OH)_2 + 2OH^- \rightarrow ZnO_2^{2^-} + 2H_2O$$
 (10)

$$ZnO_2^{2^-} + 2H_2O \rightarrow ZnO + 2OH^-$$
 (11)

In this process, OH^- ions attach to the terminal vertices of the coordination polyhedron of $Zn(OH)_2$, and ZnO_2^{2-} intermediates act as growth units, promoting crystal elongation along the [0001] direction in KOH and NaOH samples. This mechanism complements the observed formation of elongated prismatic morphologies.

ZnO nanorods synthesized in the presence of KOH and NaOH thus exhibit preferential axial growth along the c-axis ([0001]), resulting in elongated nanorods or prismatic morphologies. This anisotropic growth is promoted under alkaline hydrothermal conditions (pH \sim 9), where

 Zn^{2+} ions predominantly exist as $Zn(OH)_4^{2-}$ complexes [65–67]. These negatively charged species selectively adsorb on the positively charged Zn-terminated polar (0001) surface of ZnO, thereby promoting elongation along the [0001] direction [64]. As a result, well-dispersed nanorods or prisms are formed, as confirmed by HRTEM and SEM analyses.

In contrast, in samples synthesized in the presence of NH₄OH, nucleation is slowed because the Zn-hydroxide precipitate further interacts with ammonium ions. NH₄⁺ ions in the solution also act as a buffering system, stabilizing the pH during synthesis and maintaining a constant level of supersaturation [35]. This buffering effect enables control over the nucleation rate and crystal growth kinetics of ZnO, preventing uncontrolled precipitation. At the same time, the formation of stable $[\text{Zn}(\text{NH}_3)_4]^{2+}$ complexes reduces the concentration of free Zn²⁺ ions available for instantaneous nucleation and passivates the polar (0001) surface, thereby inhibiting axial growth along the [0001] direction and favoring lateral elongation, particularly along the [10 $\overline{10}$] or [11 $\overline{20}$] directions, corresponding to nonpolar planes such as (10 $\overline{10}$) and (11 $\overline{20}$) [35]. The ZnO growth mechanism, as influenced by different alkaline agents under hydrothermal conditions, is schematically presented in Fig. 10.

Although growth along [0001] also occurs in NH_4OH samples, it is significantly less pronounced than in the KOH and NaOH systems. The typical morphology includes bipolar growth along [0001] and [000 $\overline{1}$] directions, with a characteristic central notch from which lateral structures branch. This formation of the notch and dual growth direction can be explained by localized stress and defects formed during early nucleation, consistent with previous reports on hydrothermally synthesized hexagonal twin-rod ZnO structures [68] with a schematic representation provided in the TEM section (Fig. 7). The lower ionic strength and weaker basicity of NH_4OH compared to NaOH and KOH slow ion diffusion and increase local supersaturation around the nuclei, further favoring radial and defect-mediated growth [69]. As a result, broader, more complex, and often branched particles with a 3D butterfly-nebula-like morphology at the micro-scale are formed, as clearly visible in SEM images (Fig. 5).

The size of the hexagonal prisms in all samples indicates that the crystallization rate follows the order $\mathrm{NH_4OH} > \mathrm{KOH} > \mathrm{NaOH}$. The formation of zinc-amine complexes accelerates the crystallization rate. Consequently, a smaller fraction of particles below the critical radius may dissolve under $\mathrm{NH_4OH}$ conditions (due to Ostwald ripening), leading to reduced particle uniformity. In contrast, crystallization initiated by Zn-hydroxide precipitate is slower, reflected in the smaller

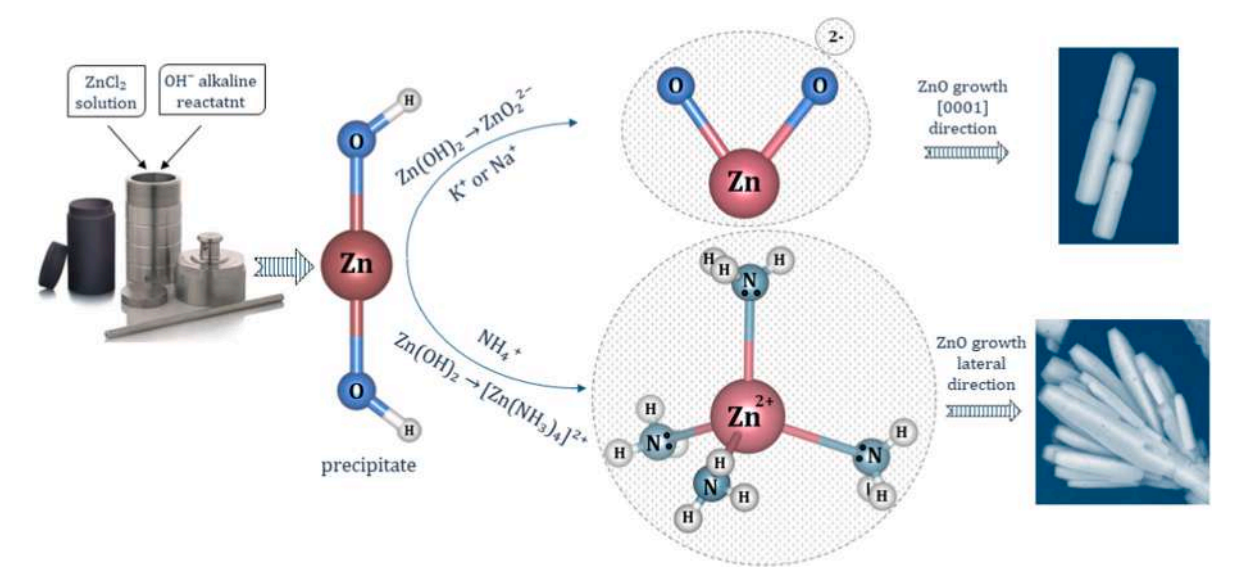


Fig. 10. ZnO growth mechanism influenced by various alkaline agents under hydrothermal conditions.

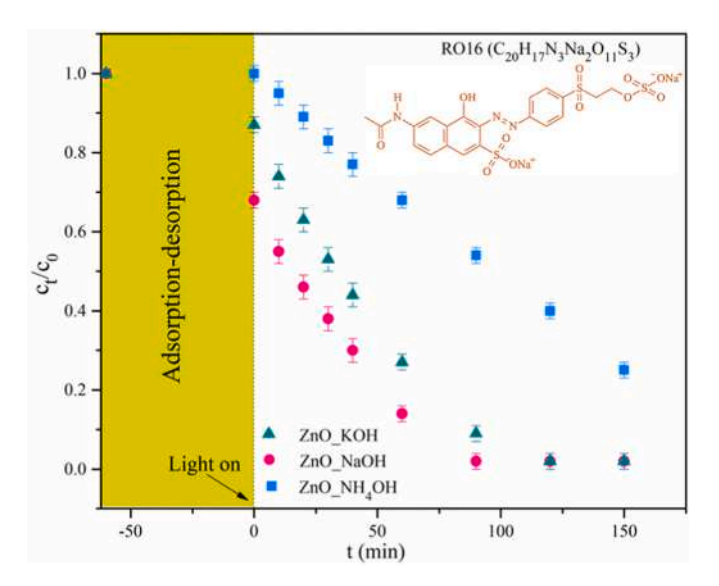


Fig. 11. Photocatalytic degradation of RO16 (50 mg/l) in the presence of ZnO nanopowders, prepared with the three different bases, under UV irradiation.

size of prismatic rods, while adsorption of Na $^+$ and K $^+$ ions suppress lateral crystal growth. Stronger binding of Na $^+$ compared to K $^+$, due to its higher charge density ($r_{Na+} \approx 102$ p.m. $< r_{K+} \approx 138$ p.m.), slows the elongation of the prismatic rods [35,67].

3.3. Photocatalytic activity

To assess the photocatalytic performance of the prepared samples, a solution of Reactive Orange 16 (RO16) dye was employed as a model pollutant. The influence of particle morphology induced by using different bases such as KOH, NaOH, and $\rm NH_4OH$ on photocatalytic activity is presented in Fig. 11. As previously reported by Xu et al. [70], ZnO nanostructures exhibit high sensitivity to growth conditions, which can significantly influence their morphology and physicochemical properties.

Based on the data presented in Fig. 11, it is important to note that the ZnO powder synthesized in the alkaline environment using NH_4OH showed no dye adsorption after stirring in the dark, whereas the other two powders, prepared using NaOH and KOH, exhibited adsorption levels of approximately 30 % and 10 %, respectively. Having in mind that these oxides are placed in aqueous solution, it is reasonable to assume that hydroxyl groups are present on the surface of ZnO nanopowders [71–73]. Experimentally determined zero point charge (pHZPC)) values were \sim 6.85, 6.80, and 6.56 for ZnO_NaOH, ZnO_KOH, and ZnO NH_4OH , respectively.

Since the pH value of the RO16 dye solution, pH \sim 4.6, is lower than pHZPC of ZnO nanopowders, from Fig. 12(a and b) we can conclude that the surface of hydroxyls will be protonated:

$$Zn-OH+H^+ \rightarrow Zn-OH_2^+ \tag{12}$$

In aqueous solution, the sulfonate groups of dye $(R-SO_3Na)$ dissociate and will be converted to $R-SO^{3-}$ anions (R represents the rest of the molecule). The adsorption process can be explained throuh the electrostatic attraction between two oppositely charged ions - positively charged surface of ZnO nanoparticles and negatively charged dye ions:

$$Zn-OH_2^+ + R-SO_3^- \rightleftarrows Zn-OH_2^+ \dots {}^-O_3S-R$$
 (13)

Furthermore, it is worth mentoning that samples ZnO_NaOH and ZnO_KOH have more drastical increase of Zeta potential (see Fig. 12(a) and inset in Fig. 12(a), implying that for the pH value of the RO16 solution the positive charge surface of these samples will be higher compared to ZnO_NH4OH. The difference in the level of adsorption can

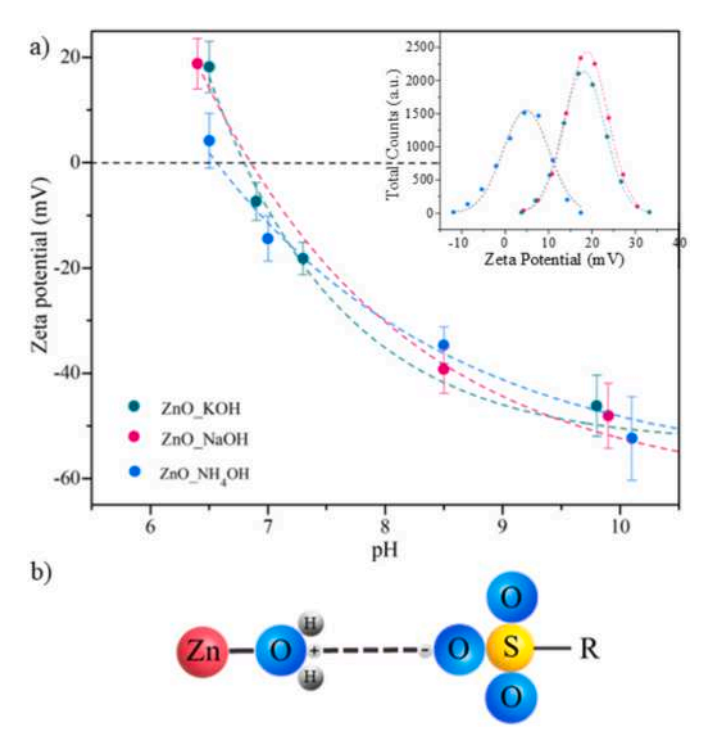


Fig. 12. Zeta potential values of ZnO samples vs. pH (a) and corresponding adsorption mechanism (b). The value of zeta potential at pH=6.5 is presented for each sample as Inset in (a).

be aligned very well with the different positive charge surface of three samples. The illustration of the adsorption mechanism is given in Fig. 12 (b).

All three ZnO nanopowders demonstrated photocatalytic activity in the degradation of RO16 dye. The ZnO_NaOH sample exhibited the highest photocatalytic efficiency, achieving complete degradation of the dye within 90 min. In the case of ZnO_KOH and ZnO_NH4OH, approximately 90 % and 45 % of the dye was removed after the same exposure time, respectively. Complete degradation for the ZnO_KOH sample was observed after 120 min, while the ZnO_NH4OH sample reached approximately 75 % degradation after 150 min. The Langmuir–Hinshelwood kinetic model is commonly applied to describe heterogeneous photocatalytic degradation reactions. This model assumes that a fast adsorption–desorption equilibrium is followed by a slower surface reaction at the solid-liquid interface [40,74,75]. The final form of the model is typically expressed as Eq. (14) [40,76]:

$$ln\left(\frac{C_{0}}{C_{t}}\right) = k_{r}K_{LH}t = k^{'}t \implies ln\left(\frac{C_{t}}{C_{0}}\right) = -k^{'}t \tag{14}$$

where k_r is reaction rate constant, C_0 and C_t are the initial and time-dependent concentration of dye, K_{LH} represents Langmuir–Hinshelwood equilibrium constant, and k' is the pseudo-first-order rate constant.

By plotting $\ln(C_t/C_0)$ as a function of irradiation time (Fig. 13), a clear linear dependence was observed, indicating that the experimental data fit well with the pseudo-first-order kinetic model for all three samples.

The k' values, calculated from the slope of Equation (14), are presented in Table 3. Along with these values, the corresponding high correlation coefficients (R^2) are also included, confirming the suitability of the pseudo-first-order kinetic model in describing the degradation kinetics of RO16 dye. Based on this analysis, the lowest photocatalytic efficiency was observed for the zinc oxide sample synthesized using NH₄OH as the base. A slight advantage in degradation performance was recorded for ZnO synthesized with NaOH, compared to the nanopowder

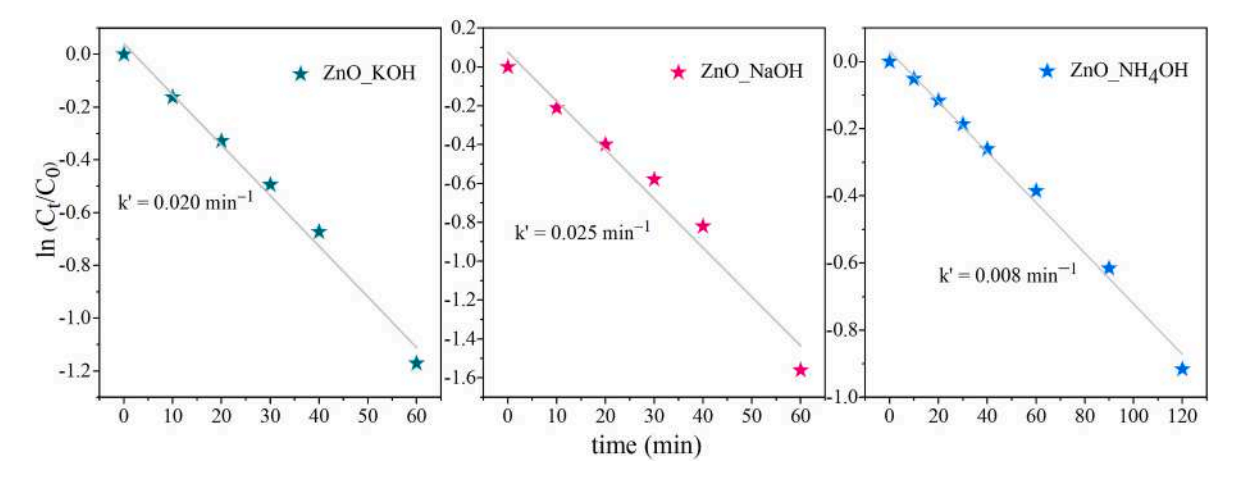


Fig. 13. Determination of the pseudo-first-order kinetic rate constant k' for the ZnO_KOH, ZnO_NaOH and ZnO_NH₄OH.

Table 3Pseudo-first-order kinetic rate constant for all three samples.

Sample	Reactive Orange 16			
	$k'{RO16} (min^{-1})$	R^2		
ZnO_KOH	0.020	0.9853		
ZnO_NaOH	0.025	0.9625		
ZnO_NH ₄ OH	0.008	0.9910		

prepared with KOH.

The ZnO as a direct wide band gap semiconductor, for the photocatalytic application can be excited by ultraviolet light [77]. Consequently, the band gap energy is considered as an important parameter in analysis of photocatalytic activity and efficiency. Having in mind values of band gap energies obtained in Section 3.13., we can observe that ZnO_NH₄OH even with the little bit lower band gap value of 3.10 eV, didn't provide more efficient degradation of the dye. The complex nature of photocatalysis can be explained by interplay of parameters such as: particle size, crystallinity, morphology, promotion of the active facets, the efficient charge carrier separation/slow recombination, density of hydroxyl groups on the catalyst surface, and formation of different kind of radicals (the most important OH) [72,78-80]. In addition to this, it has been reported that for the maximum photocatalytic efficiency exists an optimal particle size [78]. Furthermore, these factors can influence the adsorption behavior [80], which aligns very well with the variations in measured zeta potentials data. The ZnO NaOH and ZnO KOH samples with similar morphology, crystallite and particle size, together with comparable adsorption values outperformed activity of ZnO NH₄OH sample with larger crystallite and particle size with no adsorption ability.

The common mechanism [81,82] for the degradation of organic pollutants in the presence of metal oxides starts with the generation of $e^- - h^+$ pair upon UV irradiation:

$$ZnO + h\nu(UV) \rightarrow e_{cb}^{-} + h_{vb}^{+}$$
 (15)

These electron-hole pairs can recombine:

$$e_{cb}^- + h_{vb}^+ \to heat \tag{16}$$

Or, interact separately with other molecules:

$$e_{cb}^- + O_2 \to O_2^{\bullet -}$$
 (17)

$$h_{\nu h}^+ + H_2 O \rightarrow H^+ + O H^{\bullet} \tag{18}$$

$$h_{\nu b}^{+} + OH^{-} \rightarrow OH^{\bullet} \tag{19}$$

$$h_{vb}^+ + dye \rightarrow oxidative \ products$$
 (20)

Besides hydroxyl and superoxide radicals, the formation of various oxygen species is also possible

$$O_2^{\bullet -} + H^+ \to HO_2^{\bullet} \tag{21}$$

$$O_2^{\bullet -} + HO_2^{\bullet} + H^+ \rightarrow H_2O_2 + O_2$$
 (22)

All these reactive species represent the strong oxidants that can attack chromophoric azo bond -N=N-, aromatic rings in RO16, C–S bond between the aromatic ring and the sulfonate group, C–C, and C–N bonds breaking them down into smaller and less harmful molecules [83, 84]. Very often the most significant contribution to the degradation of organic pollutants is attributed to OH $^{\bullet}$ radicals, known as very strong and non-selective oxidizing agent [74,82,85]. It is expected that after complete mineralization of RO16 dye, the products will appear in form of CO₂, H₂O, Na $^+$, SO 2_4 , NO $^-_3$ and Cl $^-$ [84].

4. Conclusion

The hydrothermal synthesis of ZnO nanopowders using different alkaline sources resulted in distinct particle morphologies, which significantly influenced their photocatalytic performance. The type of cation controls the preferential crystal growth of ZnO under alkaline hydrothermal conditions and consequently its photocatalytic activity. Specifically, the presence of K⁺ and Na⁺ ions leads to the formation of prismatic, rod-shaped ZnO crystals, whereas NH₄ facilitates the development of a 3D butterfly-nebula-like morphology at the microscale under the same pH conditions. These differences can be attributed to distinct hydrothermal reaction pathways, including the nature of nucleation sites and crystal growth units. Consequently, these morphological variations cause different photocatalytic activity. Among the samples, ZnO synthesized using NaOH exhibited the highest photocatalytic efficiency, achieving complete degradation of RO16 dye within 90 min. The smaller rod-like particles of ZnO_NaOH enhance its photocatalytic performance when compared to ZnO_KOH. In contrast, ZnO synthesized with NH₄OH shows the lowest photocatalytic activity, likely due to its larger particle size, increased surface roughness, and altered crystallographic orientation. This study highlights the critical role of synthesis parameters, particularly the type of alkaline cation, in tailoring the morphology, surface structure, and photocatalytic behavior of ZnO nanoparticles. The results suggest that controlled hydrothermal synthesis at pH ~9 enables the formation of nanostructures with favorable properties for environmental applications.

CRediT authorship contribution statement

Bojana Kuzmanović: Writing – review & editing, Writing – original draft, Visualization, Validation, Methodology, Investigation, Formal analysis, Conceptualization. Milica Vujković: Writing – review & editing, Visualization, Supervision. Bojana Paskaš Mamula: Formal analysis, Data curation. Mirjana Medić Ilić: Methodology, Formal analysis, Data curation. Katarina Batalović: Visualization, Validation, Investigation. Benjamin Martínez Perea: Validation, Conceptualization. Nataša Tomić: Writing – original draft, Methodology, Investigation, Data curation, Conceptualization.

Declaration of competing interest

The authors declare that they have no known competing financial interests or personal relationships that could have appeared to influence the work reported in this paper.

Acknowledgement

This research was supported by funding through grant number 451-03-136/2025-03/200017 provided by the Ministry of Science, Technological Development and Innovation of the Republic of Serbia.

This research was supported by the Science Fund of the Republic of Serbia, Grant No. 372, Harnessing Machine Learning for Green Energy Materials: Insights into Mxene/Polyaniline Composite Surface – GEMComp.

This project has received funding from the European Union's Horizon 2020 research and innovation programme under grant agreement No 101007417 having benefited from the access provided by Institute of Material Science of Barcelona in Barcelona within the framework of the NFFA–Europe Pilot Transnational Access Activity, proposal ID543.

We sincerely thank Dr. Mirjana Novaković for her generous assistance with the additional electron microscopy measurements, careful analysis of the results, and valuable advice, which greatly contributed to the quality of this work.

We also wish to express our gratitude to Dr. Miloš Milović and Dr. Dragana Jugović for their helpful discussions and valuable advice.

References

- [1] Y. Sun, W. Zhang, Q. Li, H. Liu, X. Wang, Preparations and applications of zinc oxide based photocatalytic materials, Adv. Sensor Energy Mater 2 (2023) 100069, https://doi.org/10.1016/j.asems.2023.100069.
- [2] R. Sha, A. Basak, P.C. Maity, S. Badhulika, ZnO nano-structured based devices for chemical and optical sensing applications, Sens. Acutators Rep. 4 (2022) 100098, https://doi.org/10.1016/j.snr.2022.100098.
- [3] R. Dash, C. Mahender, P.K. Sahoo, A. Soam, Preparation of ZnO layer for solar cell application, Mater. Today Proc. 41 (2021) 161–164, https://doi.org/10.1016/j. mater. 2020.08.448.
- [4] A.T. Le, M. Ahmadipour, S.-Y. Pung, A review on ZnO-based piezoelectric nanogenerators: synthesis, characterization techniques, performance enhancement and applications, J. Alloys Compd. 844 (2020) 156172, https://doi.org/10.1016/j. iallcom.2020.156172.
- [5] C. Pushpalatha, J. Suresh, V.S. Gayathri, S.V. Sowmya, D. Augustine, A. Alamoudi, B. Zidane, N. Hassan, M. Albar, N.H.M. Albar, S. Patil, Zinc oxide nanoparticles: a review on its applications in dentistry, Front. Bioeng. Biotechnol. 10 (2022) 917990. https://doi.org/10.3389/fbice.2022.917990.
- [6] Z. Chen, N. Zhang, Y.J. Xu, Synthesis of graphene–ZnO nanorod nanocomposites with improved photoactivity and anti-photocorrosion, CrystEngComm 15 (2013) 3022–3030, https://doi.org/10.1039/C3CE27021A.
- [7] Z. Han, L. Liao, Y. Wu, H. Pan, S. Shen, J. Chen, Synthesis and photocatalytic application of oriented hierarchical ZnO flower-rod architectures, J. Hazard. Mater. 217–218 (2012) 100–106. https://doi.org/10.1016/j.jhazmat.2012.02.074.
- [8] A.A. Khodja, T. Sehili, J.F. Pilichowski, P. Boule, Photocatalytic degradation of 2phenylphenol on TiO₂ and ZnO in aqueous suspensions, J. Photochem. Photobiol. Chem. 141 (2001) 231–239, https://doi.org/10.1016/S1010-6030(01)00423-3.
- [9] Q. Wan, T.H. Wang, J.C. Zhao, Enhanced photocatalytic activity of ZnO nanotetrapods, Appl. Phys. Lett. 87 (2005) 083105, https://doi.org/10.1063/ 1.2034092.
- [10] B. Simović, A. Golubović, I. Veljković, D. Poleti, J. Zdravković, D. Mijin,
 A. Bjelajac, Hydro- and solvothermally-prepared ZnO and its catalytic effect on the

- photodegradation of reactive Orange 16 dye, J. Serb. Chem. Soc. 79 (2014) 1433–1443. https://doi.org/10.2298/JSC140520077S.
- [11] D. Raoufi, Synthesis and microstructural properties of ZnO nanoparticles prepared by precipitation method, Renew. Energy 50 (2013) 932–937, https://doi.org/ 10.1016/j.renene.2012.08.076.
- [12] L. Xu, X. Li, Y. Chen, F. Xu, Structural and optical properties of ZnO thin films prepared by sol-gel method with different thickness, Appl. Surf. Sci. 257 (2011) 4031–4037, https://doi.org/10.1016/j.apsusc.2010.11.170.
- [13] O. Milosević, D. Uskoković, B. Jordović, Preparation of fine spherical ZnO powders by an ultrasonic spray pyrolysis method, Mater. Lett. 19 (1994) 165–170, https://doi.org/10.1016/0167-577X(94)90063-9.
- [14] A. Dodd, T. Tsuzuki, M. Saunders, A comparative evaluation of the photocatalytic and optical properties of nanoparticulate ZnO synthesised by mechanochemical processing, J. Nanoparticle Res. 10 (2008) 243–248, https://doi.org/10.1007/ s11051-008-9412-1.
- [15] S.D.G. Ram, M.A. Kulandainathan, G. Ravi, On the study of pH effects in the microwave enhanced rapid synthesis of nano-ZnO, Appl. Phys. A 99 (2010) 197–203. https://link.springer.com/article/10.1007/s00339-009-5496-4#citeas.
- [16] A. Geetha, R. Sakthivel, J. Mallika, R. Kannusamy, R. Rajendran, Green synthesis of antibacterial zinc oxide nanoparticles using biopolymer Azadirachta indica gum, Orient. J. Chem. 32 (2016) 955–963, https://doi.org/10.13005/ojc/320222.
- [17] S.B. Eadi, S. Kim, S.O. Jeong, Efect of surfactant on growth of ZnO nanodumbbells and their characterization, J. Chem. (2017), https://doi.org/10.1155/2017/ 1728345.
- [18] G. Meenakshi, A. Sivasamy, Synthesis and characterization of zinc oxide nanorods and its photocatalytic activities towards degradation of 2,4-D, Ecotoxicol. Environ. Saf. 135 (2017) 243–325, https://doi.org/10.1016/j.ecoenv.2016.10.010.
- [19] W. Zhao, X. Song, Z. Yin, C. Fan, G. Chen, S. Sun, Self-assembly of ZnO nanosheets into nanoflowers at room temperature, Mater. Res. Bull. 43 (2008) 3171–3176, https://doi.org/10.1016/j.materresbull.2007.11.013.
- [20] E.Y. Shaba, J.O. Jacob, J.O. Tijani, M.A.T. Suleiman, A critical review of synthesis parameters afecting the properties of zinc oxide nanoparticle and its application in wastewater treatment, Appl. Water Sci. 11 (2021) 48, https://doi.org/10.1007/ s13201-021-01370-z.
- [21] S. Hajiashaf, N. Motakef-Kazemi, Green synthesis of zinc oxide nanoparticles using parsley extract, Nano Res. J 3 (2018) 44–50, https://doi.org/10.22034/ nmri.2018.01.007.
- [22] P. Shende, P. Kasture, R.S. Gaud, Nanofowers: the future trend of nanotechnology for multi-applications, artificial cells, nanomed, Biotechnol. 46 (2018) 413–422, https://doi.org/10.1080/21691401.2018.1428812.
- [23] M.J. Chitha, M. Sathya, K. Pushpanathan, Efect of pH on crystal size and photoluminescence property of ZnONPs prepared by chemical precipitation method, Acta Metall. Sin. 28 (2015) 394–404, https://doi.org/10.1007/s40195-015-0218-8.
- [24] A.H.S. Rana, S.-B. Chang, H.-S. Kim, NH₄OH-Oriented and pH-Dependent growth of ZnO nanostructures via microwave-assisted growth method, J. Nanosci. Nanotechnol. 18 (2018) 2125–2127. https://doi.org/10.1166/inn.2018.14961.
- [25] R. Wahab, Y.-S. Kim, H.-S. Shin, Synthesis, characterization and effect of pH variation on zinc oxide nanostructures, Mater. Trans. 50 (2009) 1999–2003, https://doi.org/10.2320/matertrans.M2009099.
- [26] N. Kumaresan, K. Ramamurthi, R.R. Babu, K. Sethuraman, S.M. Babu, Hydrothermally grown ZnO nanoparticles for effective photocatalytic activity, Appl. Surf. Sci. 418 (2017) 138–146, https://doi.org/10.1016/j. apsusc.2016.12.231.
- [27] A. Kołodziejczak-Radzimska, T. Jesionowski, Zinc oxide-from synthesis to application: a review, Materials 7 (2014) 2833–2881, https://doi.org/10.3390/ ma7042833.
- [28] V.R.V. Gopal, S. Kamila, Efect of temperature on the morphology of ZnO nanoparticles: a comparative study, Appl. Nanosci. 7 (2017) 75–82, https://doi. org/10.1007/s13204-017-0553-3.
- [29] K. Chitra, G. Annadurai, Antibacterial activity of pH-Dependent biosynthesized silver nanoparticles against clinical pathogen, BioMed Res. Int. 2014 (2014) 725165, https://doi.org/10.1155/2014/725165.
- [30] F. Zahedi, R.S. Dariani, Effect of precursor concentration on structural and optical properties of ZnO microrods by spray pyrolysis, Thin Solid Films 520 (2012) 2132–2135, https://doi.org/10.1016/j.tsf.2011.09.006.
- [31] D.E. Motaung, G.H. Mhlongo, I. Kortidis, S.S. Nkosi, G.F. Malgas, B. W. Mwakikunga, S. Ray, G. Kiriakidis, Structural and optical properties of ZnO nanostructures grown by aerosol spray pyrolysis: candidates for room temperature methane and hydrogen gas sensing, Appl. Surf. Sci. 279 (2013) 142–149, https://doi.org/10.1016/j.apsusc.2013.04.056.
- [32] A. Chittofrati, E. Matijević, Uniform particles of zinc oxide of different morphologies, Colloids Surf. 48 (1990) 65–78, https://doi.org/10.1016/0166-6622(90)80219-T.
- [33] P.K. Santra, S. Mukherjee, D.D. Sarma, Growth kinetics of ZnO nanocrystals in the presence of a base: effect of the size of the alkali cation, J. Phys. Chem. C 114 (2010) 22113–22118, https://doi.org/10.1021/jp108613f.
- [34] T. Kawano, H. Imai, Nanoscale morphological design of ZnO crystals grown in aqueous solution, J. Ceram. Soc. Jpn. 118 (2010) 1383, https://doi.org/10.2109/ icersi2.118.969.
- [35] S. Baruah, J. Dutta, Hydrothermal growth of ZnO nanostructures, Sci. Technol. Adv. Mater. 10 (2009) 013001, https://doi.org/10.1088/1468-6996/10/1/ 013001.
- [36] A. Anžlovar, K. Kogej, Z.O. Crnjak, M. Žigon, Impact of inorganic hydroxides on ZnO nanoparticle formation and morphology, Cryst. Growth Des. 14 (2014) 4262–4269, https://doi.org/10.1021/cg401870e.

- [37] A. Katiyar, N. Kumar, R.K. Shukla, A. Srivastava, Influence of alkali hydroxides on synthesis, physico-chemical and photoluminescence properties of zinc oxide nanoparticles, Mater. Today Proc. 29 (2020) 112–116, https://doi.org/10.1016/j. mator.2020.05.112.
- [38] A. Akyol, M. Bayramoglu, Photocatalytic degradation of remazol red F₃B using ZnO catalyst, J. Hazard Mater. 124 (2005) 241–246, https://doi.org/10.1016/j.ihazmat.2005.05.006.
- [39] A. Pandurangam, P. Kamala, S. Uma, M. Palanichamy, V. Murugesan, Degradation of basic yellow auramine OA textile dye by semiconductor photocatalysis, Indian J. Chem. Technol. 8 (2001) 496–499, https://doi.org/10.1166/sam.2011.1151.
- [40] N. Daneshvar, D. Salari, A.R. Khataee, Photocatalytic degradation of azo dye acid red 14 in water: investigation of the effect of operational parameters, J. Photochem. Photobiol., A 157 (2003) 111–116, https://doi.org/10.1016/S1010-6030(03)00015-7.
- [41] S. Sakthivel, B. Neppolian, M.V. Shankar, B. Arabindoo, M. Palanichamy, V. Murugesan, Solar photocatalytic degradation of azo dye: Comparison of photocatalytic efficiency of ZnO and TiO₂, Sol. Energy Mater. Sol. Cells 77 (2003) 65–82, https://doi.org/10.1016/S0927-0248(02)00255-6.
- [42] L.S. Roselin, R. Selvin, Photocatalytic degradation of reactive Orange 16 dye in a ZnO coated thin film flow photoreactor, Sci. Adv. Mater. 3 (2011) 251–258, https://doi.org/10.1166/sam.2011.1151.
- [43] A. Singh, H.L. Vishwakarma, Study of structural, morphological, optical and electroluminescent properties of undoped ZnO nanorods grown by a simple chemical precipitation, Mater. Sci.-Poland 33 (4) (2015) 751–759, https://doi.org/ 10.1515/msp-2015-0112.
- [44] P.G. Devi, A.S. Velu, Synthesis, structural and optical properties of pure ZnO and Co doped ZnO nanoparticles prepared by the co-precipitation method, J. Theor. Appl. Phys. 10 (2016) 233–240, https://doi.org/10.1007/s40094-016-0221-0.
- [45] A.K. Zak, W.H. Abd. Majid, M.E. Abrishami, R. Yousefi, X-ray analysis of ZnO nanoparticles by WilliamsoneHall and sizeestrain plot methods, Solid State Sci. 13 (2011) 251–256, https://doi.org/10.1016/j.solidstatesciences.2010.11.024.
- [46] P. Bindu, S. Thomas, Estimation of lattice strain in ZnO nanoparticles: X-ray peak profile analysis, J. Theor. Appl. Phys. 8 (2014) 123–134, https://doi.org/10.1007/ s40094-014-0141-9.
- [47] T. Pandiyarajan, B. Karthikeyan, Cr doping induced structural, phonon and excitonic properties of ZnO nanoparticles, J. Nano Res. 14 (2012) 647–656, https://doi.org/10.1007/s11051-011-0647-x.
- [48] A. Khan, Raman spectroscopic study of the ZnO nanostructures, J. Pak. Mater. Soc. 4 (2010) 5–9. http://142.54.178.187;9060/xmlui/handle/123456789/18648.
- [49] A. Umar, B. Karunagaran, E.-K. Suh, Y.B. Hahn, Structural and optical properties of single-crystalline ZnO nanorods grown on silicon by thermal evaporation, Nanotechnology 17 (2006) 4072–4077, https://doi.org/10.1088/0957-4484/17/ 16/013.
- [50] A.J. Reddy, M.K. Kokila, H. Nagabhushana, J.L. Rao, C. Shivakumara, B. M. Nagabhushana, R.P.S. Chakradhar, Combustion synthesis, characterization and raman studies of ZnO nanopowders, Spectrochim. Acta Mol. Biomol. Spectrosc. 81 (2011) 53–58, https://doi.org/10.1016/j.saa.2011.05.043.
- [51] J.M. Calleja, M. Cardona, Resonant Raman scattering in ZnO, Phys. Rev. B 16 (1977) 3753–3761, https://doi.org/10.1103/PhysRevB.16.3753.
- [52] C.X. Xu, X.W. Sun, X.H. Zhang, L. Ke, S.J. Chua, Photoluminescent properties of copper-doped zinc oxide nanowires, Nanotechnology 15 (2004) 856–861, https:// doi.org/10.1088/0957-4484/15/7/026.
- [53] R. Cuscó, E. Alarcón-Lladó, J. Ibáñez, L. Artús, Temperature dependence of Raman scattering in ZnO, Phys. Rev. B 75 (2007) 165202, https://doi.org/10.1103/ Phys. P. 75 (16520)
- [54] M.J. Šćepanović, M. Grujić-Brojčin, K. Vojisavljević, S. Bernik, T. Srećković, Raman study of structural disorder in ZnO nanopowders, J. Raman Spectrosc. 41 (2010) 914–921, https://doi.org/10.1002/jrs.2546.
- [55] R. Thangavel, R.S. Moirangthem, W.S. Lee, Y.C. Chang, P.K. Wei, J. Kumar, Cesium doped and undoped ZnO nanocrystalline thin films: a comparative study of structural and micro-raman investigation of optical phonons, J. Raman Spectrosc. 41 (2010) 1594–1600, https://doi.org/10.1002/jrs.2599.
- [56] K.A. Alim, V.A. Fonoberov, M. Shamsa, A.A. Balandin, Micro-Raman investigation of optical phonons in ZnO nanocrystals, J. Appl. Phys. 97 (2005) 124313, https://doi.org/10.1063/1.1944222.
- [57] N. Ashkenov, B.N. Mbenkum, C. Bundesmann, V. Riede, Infrared dielectric functions and phonon modes of high-quality ZnO films, J. Appl. Phys. 93 (2003) 126–133, https://doi.org/10.1063/1.1526935.
- [59] V.A. Fonoberov, A.A. Balandin, Polar optical phonons in wurtzite spheroidal quantum dots: theory and application to ZnO and ZnO/MgZnO nanostructures, J. Phys. Condens. Matter 17 (2005) 1085–1097, https://doi.org/10.1088/0953-8984/17/7/003.
- [60] R. Cuscó, E.A. Llado, J. Ibañez, L. Artús, Temperature dependence of raman scattering in ZnO, Phys. Rev. B Condens. Matter 75 (2007), https://doi.org/ 10.1103/PhysRevB.75.165202.
- [61] H. Morkoç, Ü. Özgür, Zinc Oxide: Fundamentals, Materials and Device Teechnology, Copyright © 2009 Wiley-VCH Verlag GmbH & Co. KGaA, 2009, https://doi.org/10.1002/9783527623945.

- [62] W.Y. Wu, W.Y. Kung, J.M. Ting, Effect of pH values on the morphology of zinc oxide nanostructures and their photoluminescence spectra, J. Am. Ceram. Soc. 94 (2011) 699–703, https://doi.org/10.1111/j.1551-2916.2010.04146.x.
- [63] R. Wahab, S.G. Ansari, Y.S. Kim, M. Song, H.-S. Shin, The role of pH variation on the growth of zinc oxide nanostructures, Appl. Surf. Sci. 255 (2009) 4891–4896, https://doi.org/10.1016/j.apsusc.2008.12.037.
- [64] B. Wang, W. Zhong, Y. Zhiwen, Morphological characteristics of ZnO crystallites under hydrothermal conditions, Chin. Sci. Bull. 42 (1997) 1041–1046, https://doi. org/10.1007/BF02882630.
- [65] Y. Zhang, J. Mu, Controllable synthesis of flower- and rod-like ZnO nanostructures by simply tuning the ratio of sodium hydroxide to zinc acetate, Nanotechnology 18 (2007) 075606, https://doi.org/10.1088/0957-4484/18/7/075606.
- [66] S. Xu, Z.L. Wang, One-dimensional ZnO nanostructures: solution growth and functional properties, Nano Res. 4 (2011) 1013–1098, https://doi.org/10.1007/ s12274-011-0160-7
- [67] C.-H. Lu, Y.-C. Lai, R.B. Kale, Influence of alkaline sources on the structural and morphological properties of hydrothermally derived zinc oxide powders, J. Alloys Compd. 477 (2009) 523–528, https://doi.org/10.1016/j.jallcom.2008.10.076.
- [68] L. Tan, X. Yu, L. Zhang, P. Yang, Growth of "Waist" ZnO twin rods through hydrothermal synthesis, J. Nanosci. Nanotechnol. 14 (2014) 3233–3238, https:// doi.org/10.1166/jnn.2014.8595.
- [69] S. Baruah, J. Dutta, pH-dependent growth of zinc oxide nanorods, J. Cryst. Growth 311 (2009) 2549–2554, https://doi.org/10.1016/j.jcrysgro.2009.01.135.
- [70] L. Xu, G. Zheng, J. Wang, M. Lai, J. Miao, F. Xian, F. Gu, T. Sun, Leaf-like ZnO nanostructure and its excellent photocatalytic activity, Mater. Lett. 122 (2014) 1–4, https://doi.org/10.1016/j.matlet.2014.01.182.
- [71] N. Tomić, Z. Dohčević-Mitrović, N. Paunović, D. Mijin, N. Radić, B. Grbić, S. Aškrabić, B. Babić, D. Bajuk-Bogdanović, Nanocrystalline CeO_{2.8} as effective adsorbent of azo dyes, Langmuir 30 (2014) 11582–11590, https://doi.org/ 10.1021/la502969w.
- [72] N. Tomić, M. Grujić-Brojčin, A. Kremenović, M. Novaković, V. Lazović, M. Šćepanović, From mixed brookite/anatase TiO₂ nanopowder to sodium titanates: insight into morphology, structure and photacatalytic performance, Ceram. Int. 50 (2024) 51465–51475, https://doi.org/10.1016/j. ceramint.2024.10.063.
- [73] A. Degen, M. Kosec, Effect of pH and impurities on the surface charge of zinc oxide in aqueous solution, J. Eur. Ceram. Soc. 20 (2000) 667–673, https://doi.org/ 10.1016/S0955-2219(99)00203-4.
- [74] C.S. Turchi, D.F. Ollis, Photocatalytic degradation of organic water contaminants: mechanisms involving hydroxyl radical attack, J. Catal. 122 (1990) 178–192, https://doi.org/10.1016/0021-9517(90)90269-P.
- [75] A.V. Emeline, V. Ryabchuk, N. Serpone, Factors affecting the efficiency of a photocatalyzed process in aqueous metal-oxide dispersions: prospect of distinguishing between two kinetic models, J. Photochem. Photobiol., A: Chem 133 (2000) 89–97, https://doi.org/10.1016/S1010-6030(00)00225-2.
- [76] B. Pare, S.B. Jonnalagadda, H. Tomar, P. Singh, V.W. Bhagwat, ZnO assisted photocatalytic degradation of acridine orange in aqueous solution using visible irradiation, Desalination 232 (2008) 80–90, https://doi.org/10.1016/j. desal.2008.01.007.
- [77] S. Moungsrijun, S. Sujinnapram, S. Sutthana, Synthesis and characterization of zinc oxide prepared with ammonium hydroxide and photocatalytic application of organic dye under ultraviolet illumination, Monatsh. Chem. 148 (2017) 1177–1183, https://doi.org/10.1007/s00706-017-1959-z.
- [78] Z. Zhang, C. Wang, R. Zakaria, J. Ying, Role of particle size in nanocrystalline TiO₂-Based photocatalysts, J. Phys. Chem. B 102 (1998) 10871–10878, https://doi.org/10.1021/jp982948+.
- [79] X. Chen, S. Mao, Titanium dioxide nanomaterials: synthesis, properties, modifications, and applications, Chem. Rev. 107 (2007) 2891–2959, https://doi. org/10.1021/cr0500535.
- [80] S. Ahmed, M. Rasul, W. Martens, R. Brown, M. Hashib, Heterogeneous photocatalytic degradation of phenols in wastewater: a review on current status and developments, Desalination 261 (2010) 3–18, https://doi.org/10.1016/j. desal.2010.04.062.
- [81] S. Rabindranathan, S. Devipriya, S. Yesodharan, Photocatalytic degradation of phosphamidon on semiconuctor oxides, J. Hazard. Mater. B 102 (2003) 217–229, https://doi.org/10.1016/s0304-3894(03)00167-5.
- [82] N. Daneshvar, M.H. Rasoulifard, A.R. Khataee, F. Hosseinzadeh, C.I. Removal of, Acid Orange 7 from aqueous solution by UV irradiation in the presence of ZnO nanopowder, J. Hazard. Mater. 143 (2007) 95–101, https://doi.org/10.1016/j. ibazmat.2006.08.072.
- [83] C.-Y. Chen, Photocatalytic degradation of azo dye reactive Orange 16 by TiO₂, Water Air Soil Pollut. 202 (2009) 335–342, https://doi.org/10.1007/s11270-009-9980-4.
- [84] R. Shahzad, M. Muneer, R. Khalid, H.M.A. Amin, ZnO-Bi2O3 heterostructured composite for the photocatalytic degradation of Orange 16 reactive dye: synergistic effect of UV irradiation and hydrogen peroxide, Catalysts 13 (2023) 1328, https://doi.org/10.3390/catal13101328.
- [85] I.K. Konstantinou, T.A. Albanis, Photocatalytic transformation of pesticides in aqueous titanium dioxide suspensions using artificial and solar light: intermediates and degradation pathways, Appl. Catal. B Environ. 42 (2003) 319–335, https:// doi.org/10.1016/S0926-3373(02)00266-7.

The Serbian Society for Ceramic Materials
Institute for Multidisciplinary Research (IMSI), University of Belgrade
Institute of Physics, University of Belgrade

Center of Excellence for the Synthesis, Processing and Characterization of Materials for use in Extreme Conditions "CEXTREME LAB" - Institute of Nuclear Sciences "Vinča", University of Belgrade

Faculty of Mechanical Engineering, University of Belgrade

Center for Green Technologies, Institute for Multidisciplinary Research, University of Belgrade

Faculty of Technology and Metallurgy, University of Belgrade Faculty of Technology, University of Novi Sad

PROGRAMME and the BOOK of ABSTRACTS

5CSCS-2019

5th Conference of the Serbian Society for Ceramic Materials June 11-13.2019. Belgrade Serbia

Edited by:

Branko Matović Zorica Branković Aleksandra Dapčević Vladimir V. Srdić Programme and Book of Abstracts of The Fifth Conference of The Serbian Society for Ceramic Materilas publishes abstracts from the field of ceramics, which are presented at international Conference.

Editors-in-Chief

Dr. Branko Matović Dr. Zorica Branković Prof. Aleksandra Dapčević Prof. Vladimir V. Srdić

Publisher

Institute for Multidisciplinary Research, University of Belgrade Kneza Višeslava 1, 11000 Belgrade, Serbia

For Publisher

Prof. Dr Sonja Veljović Jovanović

Printing layout

Vladimir V. Srdić

Press

Faculty of Technology and Metallurgy, Research and Development Centre of Printing Technology, Karnegijeva 4, Belgrade, Serbia

Published: 2019

Circulation: 150 copies

СІР - Каталогизација у публикацији - Народна библиотека Србије, Београд

666.3/.7(048) 66.017/.018(048)

DRUŠTVO za keramičke materijale Srbije. Konferencija (5; 2019; Beograd)

Programme; and the Book of Abstracts / 5th Conference of The Serbian Society for Ceramic Materials, 5CSCS-2019, June 11-13, 2019, Belgrade, Serbia; [organizers] The Serbian Society for Ceramic Materials ... [et al.]; edited by Branko Matović ... [et al.]. - Belgrade: Institute for Multidisciplinary Research, University, 2019 (Beograd: Faculty of Technology and Metallurgy, Research and Development Centre of Printing Technology). - 139 str.: ilustr.; 24 cm

Tiraž 150. - Str. 6: Welcome message / Branko Matovic. - Registar.

ISBN 978-86-80109-22-0

- а) Керамика Апстракти
- b) Наука о материјалима Апстракти
- с) Наноматеријали Апстракти

COBISS.SR-ID 276897292

area, mean pore diameter, pore volume and PSD), the presence of catalytically active mixed crystal phases and appropriate morphology provided efficient photocatalytic activity, especially when chemically modified catalyst was used.

- 1. M. Vasic, et al., *Process. Appl. Ceram.*, **10** [3] (2016) 189
- 2. G. Shao, et al., Powder Technol., 258 (2014) 99

P-18

PHASE TRANSITION FROM TiO₂ BROOKITE-BASED NANOPOWDER TO TITANATE: EFFECT OF ANNEALING TEMPERATURE ON MORPHOLOGY AND PHOTOCATALYTIC BEHAVIOR

Nataša Tomić¹, Mirjana Grujić-Brojčin¹, Aleksandar Kremenović², Vladimir Lazović³, Maia Šćepanović¹

Center for Solid State Physics and New Materials, Institute of Physics,
University of Belgrade, 11080 Belgrade, Serbia
Laboratory of Crystallography, Faculty of Mining and Geology, University of
Belgrade, Đušina 7, 11001 Belgrade, Serbia
Photonics Center, Institute of Physics, University of Belgrade,
11080 Belgrade, Serbia

TiO₂ nanopowder based on brookite phase was synthesized using sol-gel hydrothermal method, with TiCl used as a precursor [1]. For the purposes of preparing one-dimensional (1D) nanoribbons, the obtained TiO₂ nanopowder was used as a precursor following an alkaline hydrothermal approach [2, 3], after which an annealing process took place. The structural properties of the synthesized nanomaterials were analyzed by X-ray powder diffraction (XRPD). Besides the XRPD pattern, the structural and morphological characteristics of obtained nanopowder and nanoribbon were also investigated by Raman spectroscopy and Emission Scanning Electron Microscopy (FESEM). nanostructures were tested in photocatalytic degradation of Reactive Orange (RO16) azo-dye, since these dyes represent the most toxic ones among various types of dyes. The TiO₂ brookite-based nanopowder showed the best photocatalytic efficiency, whereas the titanate after annealing were much faster in degradation in comparison with titanate obtained after hydrothermal process.

- [1] N. Tomić, Mater. Chem. Phys., 163 (2015) 518
- [2] V. Bellat, R. Chassagnon, O. Heintz, L. Saviot, D. Vandroux, N. Millot, *Dalton Trans.* 44 (2015) 1150
- [3] A. Souza, O. Ferreira, V. Nunes, Aet al., *Mater. Res.*, **21** (2018) e20180110



The 20th Symposium on Condensed Matter Physics

BOOK OF ABSTRACTS





Faculty of Physics









Conference Chair

Cedomir Petrovic, *Brookhaven* National Laboratory, USA

Željko Šljivančanin, Vinča Institute of Nuclear Sciences Serbia

Organizing Committee

Jelena Pešić, Institute of Physics
Belgrade
Andrijana Šolajić, Institute of Physics
Belgrade
Petar Mali, Faculty of Sciences,
University of Novi Sad
Jelena Pajović, Faculty of Physics,
University of Belgrade, Serbia
Srđan Stavrić, Vinča Institute of Nuclear
Sciences
Svetislav Mijatović, Faculty of Physics,
University of Belgrade, Serbia
Božidar Nikolić, Faculty of Physics,
University of Belgrade, Serbia – chair

Organized by

Institute of Physics Belgrade

Faculty of Physics, University of Belgrade

Vinča Institute of Nuclear Sciences

Serbian Academy of Sciences and Arts

Program Committee

Ivan Božović, Brookhaven National Laboratory, USA Vladimir Dobrosavljević, Florida State University, USA Milan Damnjanović, Faculty of Physics, University of Belgrade, Serbia Vladimir Djoković, Vinča Institute, University of Belgrade, Serbia Gyula Eres, Oak Ridge National Laboratory, USA Laszló Forró, Ecole Polytechnique Fédérale de Lausanne, Switzerland Radoš Gajić, Institute of Physics Belgrade, University of Belgrade, Serbia Igor Herbut, Simon Fraser University, Canada Zoran Ikonić, University of Leeds, UK Ivanka Milošević, Faculty of Physics, University of Belgrade, Serbia Branislav Nikolić, University of Delaware, USA Cedomir Petrovic. Brookhaven National Laboratory, USA Dragana Popović, National High Magnetic Field Laboratory USA Zoran S. Popović, Vinča Institute, University of Belgrade, Serbia Zoran V. Popović, Institute of Physics, University of Belgrade, Serbia Zoran Radović, Faculty of Physics, University of Belgrade, Serbia Miljko Satarić, Faculty of Technical Sciences, University of Novi Sad, Serbia Vojislav Stamenković, Argonne National Laboratory, USA Željko Šljivančanin, Vinča Institute, University of Belgrade, Serbia Bosiljka Tadić, Jožef Štefan Institute, Slovenia Milan Tadić, School of Electrical Engineering, University of Belgrade, Serbia Darko Tanasković, Institute of Physics, University of Belgrade, Serbia

XX SYMPOSIUM ON CONDENSED MATTER PHYSICS SFKM 2019

Conference presentations cover full range of research topics within the experimental, theoretical and computational condensed matter physics, including but not limited to the following:

Semiconductor physics. Electronic structure, Quantum dots and wires, Photonic crystals, High magnetic fields phenomena, Ultra-fast phenomena.

Surface, interface and low-dimensional physics. Graphene, Carbon and other nanotubes, Topological insulators, Complex oxide interfaces, Transport in nanostructures.

Magnetism. Magnetic materials and phase transitions, Magneto-electronics and spintronics, Magnetic nanoparticles.

Superconductivity. Conventional, high *Tc*, and heavy-fermion superconductors: Materials and mechanisms, Heterostructures: Proximity effect and transport phenomena.

Strongly correlated and disordered systems. Materials with strong correlations and disorder, Dynamical properties from time-resolved experiments, Quantum fluids, Cold atoms and BEC.

Phase transitions, phase ordering and structural ordering of condensed matter. Equilibrium and dynamic phenomena, Ferroelectricity, Multiferroics, Quasi-Crystals, Crystal surface morphology and dynamics, Crystal growth.

Soft and biological matter. Polymers, Liquids and gels, Liquid crystals, Elastomers, Membranes, Living cells and living matter.

Statistical physics of complex systems. Networks and other structures.

Conference venue:

Serbian Academy of Sciences and Arts, Knez Mihailova 35, Belgrade

Conference website: http://www.sfkm.ac.rs

Pure Brookite Nanopowder: Photocatalytic Properties Before and After Annealing

Nataša Tomić^a, Mirjana Grujić-Brojčin^a, Bojana Višić^a, Jugoslav Krstić^b, and Maja Šćepanović^a

Abstract. TiO₂ nanopowder with pure brookite phase was synthesized using sol-gel hydrothermal method, with TiCl₄ as a precursor [1]. After this alkaline hydrothermal approach an annealing process at 860 K took place. The structural properties of the as synthesized and annealed nanopowders were analyzed by X-ray powder diffraction (XRPD). The structural, morphological and texture characteristics of both nanopowders were also investigated by Raman spectroscopy, Scanning Electron Microscopy (SEM) and N₂ physisorption at 77 K. Efficiency of photocatalytic degradation of Reactive Orange (RO16), one of the most toxic azo-dye among various types of dyes, was investigated for both nanopowders. As synthesized brookite nanopowder showed the fast photocatalytic degradation of RO16, whereas the annealed nanopowder was slower in degradation under the same conditions. Lower degradation efficiency could be related to decrease of the textural parameters (specific surface area, mesopore volume, and maximum pore diameter) of brookite nanopowder due to annealing.

REFERENCES

1. Tomic, N., et al., Mater. Chem. Phys. 163, 518-528 (2015).

^aCenter for Solid State Physics and New Materials, Institute of Physics, University of Belgrade, 11080 Belgrade, Serbia

^bInstitute of Chemistry, Technology and Metallurgy, Department of Catalysis and Chemical Engineering, University of Belgrade, Njegoševa 12, 11000 Belgrade, Serbia

Bulletin of the American Physical Society

Fall 2019 Meeting of the Ohio-Region Section and the Michigan Section of the American Association of Physics Teachers

Volume 64, Number 15

Friday-Saturday, October 11-12, 2019; Flint, Michigan

Session A02: OSAPS Poster Session

4:15 PM, Friday, October 11, 2019

Kettering University Academic Building Room: 3342

Chair: Corneliu Rablau, Kettering University

Abstract: A02.00006 : Formation of Palladium (II) Oxide within Titanium Dioxide Electrospun Nanofibers: Combined Raman and X-ray Diffraction Study

Preview Abstract → Abstract →

Authors:

Daniel Isaacs

(University of Wisconsin Oshkosh)

Patrick McManus

(University of Wisconsin Oshkosh)

Nenad Stojilovic

(University of Wisconsin Oshkosh)

Maja Scepanovic

(Institute of Physics, University of Belgrade)

Mirjana Grujic-Brojcin

(Institute of Physics, University of Belgrade)

Natasa Tomic

(Institute of Physics, University of Belgrade)

Laila Shahreen

(The University of Akron)

George Chase

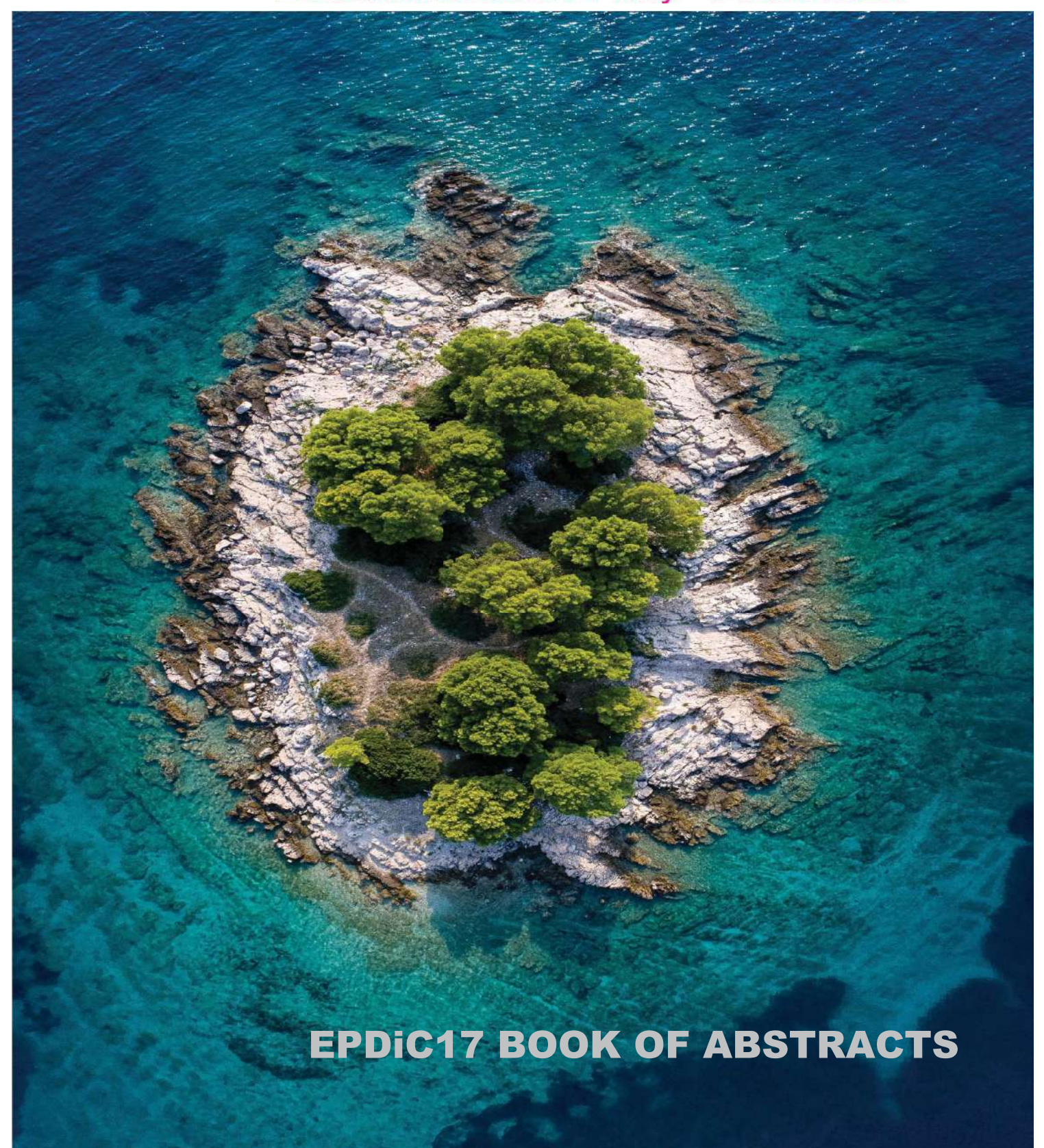
(The University of Akron)

 TiO_2 -PdO composite submicron fibers were produced using electrospinning method. The morphology of the fibers was probed using Scanning Electron Microscopy, whereas Raman Spectroscopy and powder X-Ray Diffraction experiments were used for probing the crystalline phases of pure TiO_2 and TiO_2 –PdO fibers. In particular, the effects of annealing time (at $600\,^{\circ}$ C) on the crystal structure and the role of embedded PdO were investigated. The results of Raman scattering measurements have shown dominant anatase TiO_2 phase in all samples. The crystallinity of anatase phase, as well as the appearence of rutile and brookite phases, depend on annealing and doping conditions. The existence of PdO within TiO_2 stabilizes its anatase phase, and the Raman modes ascribed to PdO become more pronounced with annealing. The combination of Raman and X-Ray diffraction techniques proves to be a powerful tool in characterizing these materials.

This site uses cookies. To find out more, read our Privacy Policy.

I Agree





MS9-P5

Structural and microstructural study of brookite based TiO_2 nanocomposites with carbon black (C)

Aleksandar Kremenović ¹, Mirjana Grujić-Brojčin ², Nataša Tomić ², Maja Šćepanović ²

¹ Faculty of Mining and Geology, University of Belgrade, Belgrade, Serbia

² Institute of Physics, University of Belgrade, Belgrade, Serbia

■ aleksandar.kremenovic@rgf.bg.ac.rs

tructural and microstructural properties of TiO_2 -based nanocomposites with carbon black (C), synthesized by sol-gel-hydrothermal method, have been studied by XRPD and Raman scattering. Detailed size-strain analyses of XRPD and Raman scattering results are presented in order to investigate the influence of C content on brokite and anatase phase formation. The XRPD size-strain analyses have resulted in reliable structure and microstructure results for both anatase and brookite and their relative abundance ratio has been refined by Rietveld method. The brookite and anatase crystallite sizes are estimated by XRPD at \sim 27-29 and 14-17 nm, respectively. The Raman spectra of all samples are dominated by the most intensive modes of anatase (E_g) and brookite (A_{1g}). The analysis of anatase E_g mode by PCM (Phonon Confinement model) has revealed partial compensation of phonon confinement due to anatase nanocrystallite size and tensile deformation of anatase lattice. The refined unit cell parameters obtained from XRPD have shown that C atoms did not enter in the significant amounts into brookite and anatase crystal structures. On the other side, the Raman spectra have revealed features assigned to carbon. The results of both analyses imply that the presence of carbon could influence the formation of brookite and anatase phase in the TiO_2 -based nanocomposites synthesized by the hydrothermal method [1].

[1] A. Kremenović, M. Grujić-Brojčin, N. Tomić, V. Lazović, D. Bajuk-Bogdanović, J. Krstić, M. Šćepanović, Size-strain line broadening analysis of anatase/brookite (TiO_2) based nanocomposites with carbon (C) – XRPD and Raman spectroscopy, *Acta Crystallographica B*, in press.



ACADEMY OF SCIENCES AND ARTS OF THE REPUBLIC OF SRPSKA





XV МЕЂУНАРОДНИ НАУЧНИ СКУП САВРЕМЕНИ МАТЕРИЈАЛИ 2022

ПРОГРАМ РАДА И КЊИГА АПСТРАКАТА

XV INTERNATIONAL SCIENTIFIC CONFERENCE CONTEMPORARY MATERIALS 2022

PROGRAMME AND THE BOOK OF ABSTRACTS

Бања Лука, 8 – 9. септембар 2022. године Banja Luka, September 8th to 9th, 2022

ОРГАНИЗАТОР НАУЧНОГ СКУПА

Академија наука и умјетности Републике Српске

СУОРГАНИЗАТОРИ

Alma Mater Europaea Технички универзитет Габрово

ПОКРОВИТЕЉ НАУЧНОГ СКУПА

Министарство за научнотехнолошки развој, високо образовање и информационо друштво

ОДРЖАВАЊЕ СКУПА СУ ПОМОГЛИ

МХ Електропривреда Републике Српске Универзитетски Клинички центар Републике Српске Комора доктора медицине РС

ОРГАНИЗАЦИОНИ ОДБОР

Академик Драгољуб Мирјанић, предсједник Академик Рајко Кузмановић мр Срђан Рајчевић Академик Бранко Шкундрић Академик Неђо Ђурић Академик Есад Јакуповић Проф. др Илија Железаров Проф. др Лудвик Топлак Проф. др Зоран Рајилић Проф. др Владо Ђајић Проф. др Саша Вујновић

PY

presented. This paper presents forensic medical expertise of traces on the corpse in combination with trasological analyzes, both on the corpse and on the materials related to the specific case of the crime of murder, which all contributed to clarifying the cause of the murder. The murder happened at night, committed by several people, the victim was a young man who was ostracized by his family due to frequent consumption of alcoholic beverages in combination with narcotics. In the cross-section of the set of conclusions that emerged after the conducted analyzes, an indisputable fact "emerged" that helped clarify this case.

Key words: Forensics, Medical analysis, Micro traces.

irontribu-

reen's sche-

tained e spin entally

other erstan-

otropic

E)

egy and lysis is

REMOVAL OF NADOLOL USING COUPLED NANOMATERIALS BASED ON TITANIUM AND CARBON

Andrijana Vukojević¹, Maria M. Savanović¹, Nataša Tomić², Stevan Armaković¹, Svetlana Pelemiš³, Sanja J. Armaković¹

¹University of Novi Sad, Faculty of Sciences, Novi Sad, Serbia,

²Center for Solid State and New Materials, Institute of Physics Belgrade,

Belgrade, Serbia

³University of East Sarajevo, Faculty of Technology, Zvornik,

Republic of Srpska, Bosnia and Herzegovina

Abstract: Nadolol (NAD), one of the representatives of β-blockers, is used to treat cardiovascular diseases such as angina and hypertension. Due to its frequent use, it has been detected in hospital wastewater from which it is not removed efficiently enough, so it reaches natural waters. The lack of a satisfactorily efficient method for removing NAD from wastewater has created a need to find a more efficient way for its removal. This paper aims to investigate the efficiency of photocatalytic degradation of NAD by two TiO₂-C nanocomposites with different carbon content (9 and 20 wt%) under UV radiation. The applied nanocomposites, synthesized by the sol-gel hydrothermal method, showed significant efficiency in removing NAD compared to direct photolysis. Also, the reaction rate constant, according to which the decomposition of NAD in the presence of TiO₂-C takes place in the pseudo-first order, was calculated. The degradation of NAD was monitored by HPLC-PDA technique.

Key words: Nadolol, Photocatalytic degradation, Kinetics.





5th Edition of Nanotechnology and Nanomaterials Virtual

December 09, 2022



Contact us:

Contact: +91 9440424355 E-mail: v-ntnm2022@sciwideonline.com Website: https://sciwideonline.com/v-ntnm2022/



Speakers Timings

07:00 - 07:10

Introduction

U		Plendry Sessions
07:10 – 07:50	12:40 - 13:20	Title: Designing of Functional Nano-Materials for Hydrogen Production using Overall Water Splitting Phenomenon Tokeer Ahmad, Jamia Millia Islamia, India.
07:50 - 08:30	16:50 – 17:30	Title: A Pure Titania Photocatalyst: Preparation, Characterization and Photocatalytic Activity of Octahedral-Shaped Anatase Particles

NPO, Japan.

Bunsho Ohtani, Hokkaido University and Nonprofitable Organization touche

•		Keynote Sessions
08:30 - 00:05	16:30 – 17:05	Title: NANOGARD SC202 - Self Cleaning and Antifogging Coating for Automobile Industry
00.00		Vengadaesvaran Balakrishnan, UM Power Energy Dedicated Advanced Centre, Malaysia.
09:05 - 09:40	17:05 – 17:40	Title: Gold Nanoparticle-based colorimetric Sensors for Pesticides Detection: A Review
		Keat Khim Ong, National Defence University of Malaysia, Malaysia.
09:40 - 10:15	10:40 - 11:15	Title: Hetero-structure-based Catalyst Nanomaterials for Visible Light-driven Photocatalytic CO2 Reduction Reactions
09.40 - 10.15	10.40 – 11.15	Blaž Likozar, National Institute of Chemistry, Slovenia.
		,
		Title: Nanocrystalline Tungsten Trioxide Cathode Films Prepared by Ultrasonic
10:15 - 10:50	18:15 – 18:50	Spray Deposition for Electrochromic Applications

Chi-Ping Li, National United University, Taiwan.

10:50 – 11:25	13:50 - 14:25	Title: Improving the Reliability Design of Mechanical Systems such as Refrigerator Seongwoo Woo, Ethiopian Technical University, Ethiopia.
11:25 – 12:00	15:25 – 16:00	Title: Domain wall Stability switching in magnetic nanowires for nanomemory storage devices Mohammed Al Bahri, A'Sharqiyah University, Oman.
12:00 - 12:35	07:00 - 07:35	Title: Contactless Magnetic Sensing in Condition Monitoring and Anomaly Detection for Smart Grid: New Possibilities and Alternatives Philip Pong, New Jersey Institute of Technology, USA.
12:35 – 13:10	07:35 - 08:10	Title: Experimental Evolution of Magnetite Nanoparticle Resistance in Escherichia coli Akamu Jude Ewunkem, Winston Salem State University, USA.

1		Invited Sessions
13:10 - 13:30	16:10 – 16:30	Title: Cyclable carbon dot/chitin nanocrystal hybrid for selective detection and adsorption of Cr(VI) and Co(II) from aqueous media
		Elena F Krivoshapkina, ITMO University, Russian Federation.
13:30 – 13:50	16:30 – 16:50	Title: Nanocomposite semiconducting materials for efficient utilization of visible light in photocatalytic reactions Dmitry Selishchev, Boreskov Institute of Catalysis, Russian Federation.
13:50 - 14:10	10:50 – 11:10	Title: Biopolymeric hybrid nanocomposites materials 3D printing with nanotechnological applications in the water treatment Estefanía Baigorria, Sao Paulo State University, Brazil.
14:10 – 14:30	16:10 – 16:30	Title: Supercapacitive Effects of Multi-Walled Carbon Nanotubes-Functionalized Spinel Copper Manganese Oxide Christopher Nolly, University of the Western Cape, South Africa.

	•		E-poster Sessions
	14:30 – 14:40	15:30 – 15:40	Title: Application of single-crystal V2O5 in photodegradation of selected pharmaceutical products Maria Savanovic, University of Novi Sad, Serbia.
14:40 –	14:40 - 14:50	08:40 – 08:50	Title: In Vitro Ruminal Digestibility Test of Forage (Festuca arundinacea) biofortificated with Selenium Nanoparticles
			Gabriela Medina-Pérez, Universidad Autonoma del Estado de Hidalgo, Mexico.
	14:50 – 14:60	22:50 - 23:00	Title: Metal selenides as electrodes for sustainable energy storage materials Muhammad Sajjad, Zhejiang Normal University, China.

Closing Ceremony



V-NTNM2022 wish to thank

Prof/Dr/Mr/Ms. Maria Savanovic

University of Novi Sad, Serbia

for his/her worthy e-poster presentation at

"5th Edition of Nanotechnology and Nanomaterials Virtual"

held during December 09, 2022

Prof. Tokeer Ahmad
Jamia Millia Islamia, India







INTERNATIONAL CONFERENCE MEĐUNARODNA KONFERENCIJA

MEETING POINT OF THE SCIENCE AND PRACTICE IN THE FIELDS OF CORROSION, MATERIALS AND ENVIRONMENTAL PROTECTION STECIŠTE NAUKE I PRAKSE U OBLASTIMA KOROZIJE, ZAŠTITE MATERIJALA I ŽIVOTNE SREDINE

PROCEEDINGS KNJIGA RADOVA

Under the auspicies of the MINISTRY OF SCIENCE, TECHNOLOGICAL DEVELOPMENT AND INNOVATION OF THE REPUBLIC OF SERBIA

Pod pokroviteljstvom MINISTARSTVO NAUKE, TEHNOLOŠKOG RAZVOJA I INOVACIJA REPUBLIKE SRBIJE

May 28-31, 2023 : : Divčibare, Serbia

CIP - Каталогизација у публикацији Народна библиотека Србије, Београд

620.193/.197(082)(0.034.2) 621.793/.795(082)(0.034.2) 667.6(082)(0.034.2) 502/504(082)(0.034.2) 66.017/.018(082)(0.034.2)

INTERNATIONAL Conference YUCORR (24; 2023; Divčibare)

Meeting point of the science and practice in the fields of corrosion, materials and environmental protection [Elektronski izvor]: proceedings = Stecište nauke i prakse u oblastima korozije, zaštite materijala i životne sredine: knjiga radova / XXIV YuCorr International Conference, May 28-31, 2023, Divčibare, Serbia = XXIV YuCorr [Jugoslovenska korozija] Međunarodna konferencija = [organized by] Serbian Society of Corrosion and Materials Protection ... [et al.]]; [organizatori Udruženje inženjera Srbije za koroziju i zaštitu materijala ... [et al.]; [editors, urednici Miroslav Pavlović, Marijana Pantović Pavlović, Miomir Pavlović]. - Beograd: Serbian Society of Corrosion and Materials Protection UISKOZAM = Udruženje inženjera Srbije za koroziju i zaštitu materijala UISKOZAM, 2023 (Beograd: Serbian Society of Corrosion and Materials Protection UISKOZAM = Udruženje inženjera Srbije za koroziju i zaštitu materijala UISKOZAM). - 1 elektronski optički disk (CD-ROM); 12 cm Sistemski zahtevi: Nisu navedeni. - Nasl. sa naslovne strane dokumenta. - Radovi na engl. i srp. jeziku. - Tiraž 200. - Bibliografija uz većinu radova. - Abstracts.

ISBN 978-86-82343-30-1

а) Премази, антикорозиони -- Зборници b) Превлаке, антикорозионе -- Зборници v) Антикорозиона заштита -- Зборници g) Животна средина -- Заштита -- Зборници d) Наука о материјалима -- Зборници

COBISS.SR-ID 119553545

XXIV YUCORR – International Conference | Međunarodna konferencija

PUBLISHED BY | IZDAVAČ

SERBIAN SOCIETY OF CORROSION AND MATERIALS PROTECTION (UISKOZAM)

UDRUŽENJE INŽENJERA SRBIJE ZA KORZIJU I ZAŠTITU MATERIJALA (UISKOZAM),

Kneza Miloša 7a/II, 11000 Beograd, Srbija, tel/fax: +381 11 3230 028, office@sitzam.org.rs; www.sitzam.org.rs

FOR PUBLISHER | ZA IZDAVAČA Prof. dr MIOMIR PAVLOVIĆ, predsednik UISKOZAM SCIENTIFIC COMMITEE | NAUČNI ODBOR: Prof. dr M. G. Pavlović, Serbia – President

Prof. dr D. Vaštag, Serbia; Dr M. M. Pavlović, Serbia; Prof. dr D. Vuksanović, Montenegro; Prof. dr D. Čamovska, N. Macedonia; Prof. dr M. Antonijević, Serbia; Prof. dr S. Stopić, Germany; Prof. dr R. Zejnilović, Montenegro; Prof. dr L. Vrsalović, Croatia; Dr N. Nikolić, Serbia; Dr I. Krastev, Bulgaria; Prof. dr B. Grgur, Serbia; Prof. dr M. Gvozdenović, Serbia; Prof. dr S. Hadži Jordanov, N. Macedonia; Prof. dr R. Fuchs Godec, Slovenia; Prof. dr J. Stevanović, Serbia; Dr V. Panić, Serbia; Dr M. Mihailović, Serbia; Prof. dr V. Marić, B.&H.; Prof. Dr C. Stojanović, , B.&H.; Prof. dr J. Jovićević, Serbia; Prof. dr D. Jevtić, Serbia; Dr M. Pantović Pavlović, Serbia; Dr F. Kokalj, Slovenia; Prof. dr M. Gligorić, B.&H.; Prof. dr A. Kowal, Poland; Prof. dr M. Tomić, B.&H.; Prof. Dr B. Arsenović, B.&H., Dr S. Blagojević, Serbia

ORGANIZING COMMITEE | ORGANIZACIONI ODBOR: Dr Miroslav Pavlović – president Dr Nebojša Nikolić – vice president; Dr Marija Mihailović – vice president

Prof. dr Miomir Pavlović; Dr Vladimir Panić; Jelena Slepčević, B.Sc.; Prof. dr Milica Gvozdenović; Zagorka Bešić, B.Sc.; Gordana Miljević, B.Sc.; Miomirka Anđić, B.Sc.; Dr Marija Matić; Dr Marijana Pantović Pavlović; Dr Dragana Pavlović; Dr Sanja Stevanović; Lela Mladenović – secretary

EDITORS | UREDNICI: Dr Miroslav Pavlović, Dr Marijana Pantović Pavlović, Prof. dr Miomir Pavlović

SCIENTIFIC AREA | OBLAST: CORROSION AND MATERIALS PROTECTION | KOROZIJA I ZAŠTITA MATERIJALA

PAGE LAYOUT | KOMPJUTERSKA OBRADA I SLOG: Dr Marijana Pantović Pavlović

CIRCULATION | TIRAŽ: 200 copies | primeraka PUBLICATION YEAR | GODINA IZDANJA: 2023

ISBN 978-86-82343-30-1

The influence of the brookite/anatase TiO₂ nanoparticles on structural and electrochemical properties of conducting polyaniline form

Uticaj nanočestica brukit/anatas TiO₂ na strukturna i elektrohemijska svojstva provodne forme polianilina

Bojana Kuzmanović^{1,*}, Nenad Ivanović¹, Nataša Tomić², Bojana Paskaš Mamula¹, Katarina Batalović¹, Mirjana Medić Ilić¹, MilicaVujković³

¹Vinča Institute of Nuclear Sciences – National Institute of the Republic of Serbia, University of Belgrade, P.O. Box 522, 11001, Belgrade, Serbia

² Institute of Physics, University of Belgrade, Pregrevica 118, 11080 Belgrade, Serbia

³Faculty of Physical Chemistry, University of Belgrade, Studentski Trg 12-16, 11000 Belgrade, Serbia

*kuzmob@vinca.rs

Abstract

The emeraldine salt polyaniline/TiO₂ composite (PANI_ES@TiO₂_BA) was prepared by in situ chemical oxidation of aniline in the presence of the TiO₂ brookite(74%)/anatase(26%) nanoparticles. Raman spectroscopy and Cyclic Voltammetry were used to examine the properties of the obtained composites and their charge storage performances. A significant decrease of the composite charging/discharging capacity indicates that the incorporation of 33 wt% of the brookite/anatase TiO₂ nanoparticles into the PANI_ES matrix deteriorates the charge storage possibilities of the composite in comparison with the pure PANI_ES at a common scan rate of 20 mVs⁻¹.

Keywords: polyaniline; TiO₂; composite; Raman spectroscopy; Cyclic Voltammetry; Charge storage.

Izvod

Kompozit polianilina u formi emeraldin soli/TiO₂ (PANI_ES@TiO₂_BA) je sintetisan in situ hemijskom oksidativnom polimerizacijom anilina u prisustvu nanočestica TiO₂ brukit(74%)/anatas(26%). Za ispitivanje svojstava dobijenog kompozita i njegovih performansi za skladištenje naelektrisanja korišćena je metoda Ramanske spektroskopije i ciklična voltametrija. Značajno smanjenje kapaciteta punjenja/pražnjenja kompozita ukazuje na to da ugradnja 33 težinskih procenata (wt%) nanočestica brukit/anatas TiO₂ u PANI_ES matricu smanjuje sposobnost skladištenja naelektrisanja u kompozitu u poređenju sa čistim PANI_ES, pri brzini polarizacije od 20 mVs⁻¹.

Ključne reči: polianilin; TiO₂; kompozit; Ramanska spektroskopija; ciklična voltametrija; skladištenje naelektrisanja.

Introduction

Both organic and inorganic core-shell hybrid materials have been extensively studied in the literature [1]. The complementary characteristics of these materials and their synergistic attract much attention advocating them as promising candidates for potential applications in electronic and optical devices, photocatalysis, batteries, and protective coatings [2]. Among the most comprehensively studied combinations for hybrid nanocomposites production are those of conducting polyaniline (PANI) and numerous inorganic oxides (γ-Fe2O3, TiO₂, CeO₂, graphene oxide, ZnO, SiO₂) encapsulated inside the PANI shell [3-6]. A small amount of oxide nanoparticles (NP) incorporated into the PANI matrix can significantly modify its structural, morphological, electrical, and optical properties [7].

Most of the existing studies of PANI@TiO₂ composites have been focused on their applications in photocatalysts and gas sensors [8-10], but much less of them are focused on their possible use as electrode materials for supercapacitors [11].

In studies of the PANI@TiO₂ nanocomposites, the largest attention has been paid to the anatase TiO₂ crystal form [12,13], while the use of rutile and rutile/anatase TiO₂ crystal form nanocomposites is much less investigated [7,14]. Due to the difficulties encountered in the synthesis process, there is even less interest in the pure brookite TiO₂ crystal form nanocomposites.

In this work, brookite(74%)/anatase(26%) TiO₂ (TiO₂_BA) (NP) were synthesized using sol-gel hydrothermal method, while PANI was obtained in the form of emeraldine salt (ES) (PANI_ES) by typical chemical oxidation polymerization of aniline monomer under highly acidic conditions. The PANI_ES@TiO₂_BA dielectric material was developed by in situ chemical oxidative polymerization in order to investigate its charge storage capacity and to relate it to the influence of the anatase/brookite TiO₂ (NP) on properties of the conductive PANI_ES matrix.

Experimental details and characterisation

Synthesis of polyaniline

The PANI_ES form was synthesized by typical chemical polymerization of aniline in the presence of hydrochloric acid and ammonium persulfate as an oxidant, according to the procedure described in our previous paper [5]. 0.18 mL of aniline monomer was injected into 7 mL of 2 M HCl solution. Then, 0.45 g of (NH₄)₂SO₄, previously dissolved in 2 mL of deionized water, was added dropwise to the solution, with constant stirring on a magnetic stirrer. After washing with 2 M HCl, deionized water, and ethanol, the obtained precipitate was dried at 60 °C in an oven for 36 h.

Sol-gel hydrothermally synthesis of TiO₂_BA

The polymorphic brookite/anatase TiO_2 (NP) were synthesized by the sol-gel hydrothermal method, with $TiCl_4$ used as a precursor. An appropriate amount of $TiCl_4$ was dissolved in 50 mL of distilled water, with constant stirring in an ice bath. In order to form the hydrogel, the NaOH solution was gradually added until pH ~ 9. After 5 hours of aging, the V = 80 mL of hydrogel was transferred to an autoclave and treated at T = 200 °C for 24 hours. Using the XRD method, the brookite/anatase phases relation in the obtained nanopowder sample [15], was determined to be 74%/26%.

PANI@TiO₂_BA synthesis procedure

The PANI@TiO₂_BA composites were synthesized using the same procedure as for PANI_ES synthesis but in the presence of TiO₂_BA. Two times distilled aniline monomer was added to an aqueous solution of 2M HCl containing 33 wt% of TiO₂ (NP) of the brookite/anatase TiO₂ crystal structure synthesized in the previously described manner. In order to prevent aggregation, the solution was treated with ultrasound, after which (NH₄)₂SO₄ dissolved in deionized water was added with constant stirring. The resulting sample was washed with 2M HCl aqueous solution and deionized water and then dried in an oven.

Raman stady of PANI_ES@AB interaction

The Raman spectra of the PANI_ES and PANI_ES@TiO₂_BA samples were recorded using a DXR Raman microscope (Thermo Scientific) equipped with a research optical microscope and a CCD detector, and the results are presented in Fig.1. The PANI_ES Raman spectrum is typical for this protonated PANI form, and its peaks were assigned using literature data [16-18]. The TiO₂_BA Raman spectra were measured under the same conditions as those of PANI_ES and shown in the inset of Fig. 1. The PANI_ES@TiO₂_BA composite Raman spectrum shows all characteristic PANI vibration modes with a modified intensity of certain bands mainly (but not exclusively) in the range

of wave numbers characteristic for the incorporating oxide vibrations. Shifts of the PANI_ES Raman bands were not observed in the composite, which can be attributed to the stability of principal structural features of both individual components of the composite after its formation.

The assignment of the PANI_ES Raman bands in the 2000 cm⁻¹ to 200 cm⁻¹ range is given in Table 1. In the Raman spectrum of the mixed brookite/anatase TiO_2 phase, the bands that correspond to the brookite phase are: ~ 286 cm⁻¹ (B_{1g}), ~ 412 cm⁻¹ (A_{1g}), ~ 505 cm⁻¹ (B_{3g}), ~ 544 cm⁻¹ (A_{1g}) and ~ 640 cm⁻¹ (A_{1g}). The Raman modes of the anatase phase were observed at positions ~ 399 cm⁻¹ (B_{1g}), ~ 518 cm⁻¹ ($A_{1g}+B_{1g}$), and ~ 639 cm⁻¹ (B_{2g}) [19].

Analyzing the Raman spectrum of the composite, one can observe the influence of the TiO₂_BA oxide (NP) on the PANI_ES band of medium intensity recorded at ~1490 cm⁻¹, which is related to the C=N stretching vibrations of the quinonoid structures. The oxide influence is also evident on mode at ~1509 cm⁻¹, which is attributed to the N-H deformation vibrations of the semi-quinonoid ring. In addition, the splitting of the band recorded at 1336 cm⁻¹, which is associated with C~N⁺⁺ vibrations in the delocalized polaronic structure [20] into ~1344 cm⁻¹ and ~1326 cm⁻¹ lines is significantly more pronounced in the composite than in pure PANI_ES, and the ratio of their intensities increases in the composite. It is indicative that all affected modes mentioned above originate from various vibrations that include PANI_ES N-atoms, so the cause for their modification should be searched in various interactions of N-atom, probably with both O and Ti atoms forming the TiO₂ surface [21]. The assumption that oxide Ti-atoms form a coordination compound with PANI_ES N-atoms is also possible [22].

Changes in the vibrational mode's intensity due to the PANI_ES - TiO_2 _BA interaction are also pronounced in the wave number range in which the oxide modes appear. The intensity of the band at 718 cm⁻¹, which is associated to the deformation of the amine structure of the bipolaronic form of PANI_ES, decreases in the presence of oxide (partially overlapping brookite A_{1g} mode and the anatase E_g mode). This indicates the possible existence of the PANI - TiO_2 interaction involving the amine hydrogen, i.e., the NH-O-Ti interaction. Changes in the PANI_ES bands recorded at 585 cm⁻¹ and 520 cm⁻¹ are due to the interaction with A_{1g} and B_{3g} vibrational modes of the brookite phase, as well as with the $A_{1g}+B_{1g}$ and B_{1g} anatase phase modes. The decrease of intensity of the PANI_ES band at 421 cm⁻¹, and increase of intensity of the ~ 298 cm⁻¹ band can be attributed to the interaction of the brookite phase B_{1g} vibrational mode with these PANI_ES modes.

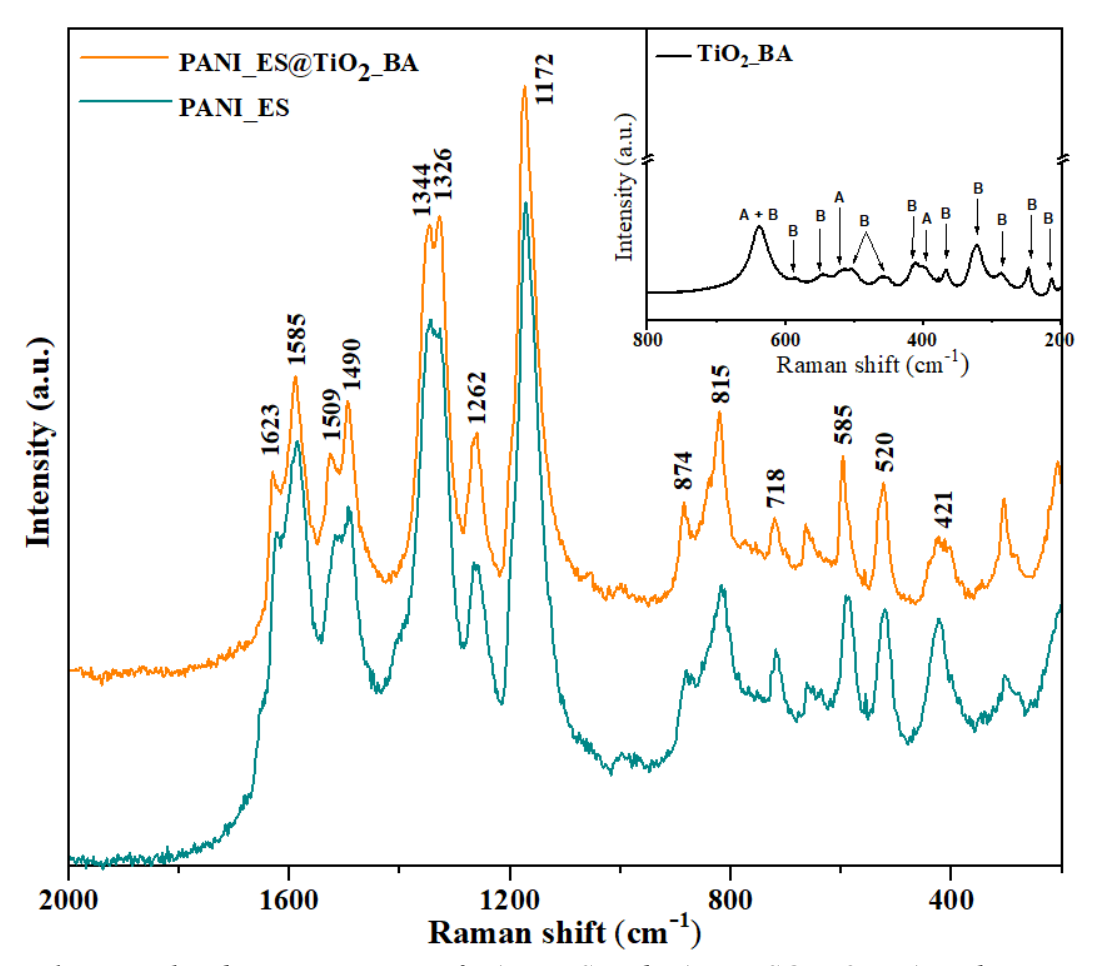


Figure 1. Normalized Raman spectra of PANI_ES and PANI_ES@TiO2_BA in the normalized scale. The spectrum of pure TiO2_BA oxide phase is given in the inset. The symbols A and B indicate bands corresponding to anatase, i.e., the brookite phase.

Table 1. The assignments of the PANI_ES Raman bands in the 2000 cm⁻¹ - 200 cm⁻¹ range. (ν)-stretching, (b)-bending, (w)-wagging, (τ)-torsion, (i-p) in plane, (o-p) out-of plane, (d) deformation, (r-d) deformation of ring, B: benzenoid, Q: quinonoid, SQ: semi-quinonoid rings.

Exp. frequencies (cm ⁻¹)	Assignments
1623	ν (C-C) _B
1585	$\nu(C=C)_Q; \nu(C\sim C)_{SQ}$
1509	δ(N-H)(i-p)
1490	ν(C=N) _Q
1344, 1326	$\nu(\text{C-N}^{+\bullet})_{\text{SQ}}$
1262	ν(C-N)
1172	b(CH)(i-p) _{SQ}
874	$w(C-H)(r-d)_B(i-p)$
815	$b(C-H)_Q(o-p), (r-d)_{SQ}$
718	$(r-d)_B(o-p)$
585	(o-p)(C-H)+(r-d)
520	τ(C-N-C)(o-p)
421	(CH)(o-p)

Electrohemical behavior

The influence of the brookite/anatase TiO₂ (NP) on the charge storage behavior of PANI_ES was studied by cyclic voltammetry method. The measurements were performed at Gamry PCI4/300 Potentiostat/Galvanostat in the typical three-electrode configuration. To examine the influence of the PANI_ES electrochemical over-oxidation, both samples were measured in an extended potential range of -0.2–1 V vs. SCE (Saturated Calomel Electrode) during ten consecutive cycles. The resulting cyclic voltammograms (CVs) are shown in Figure 2.

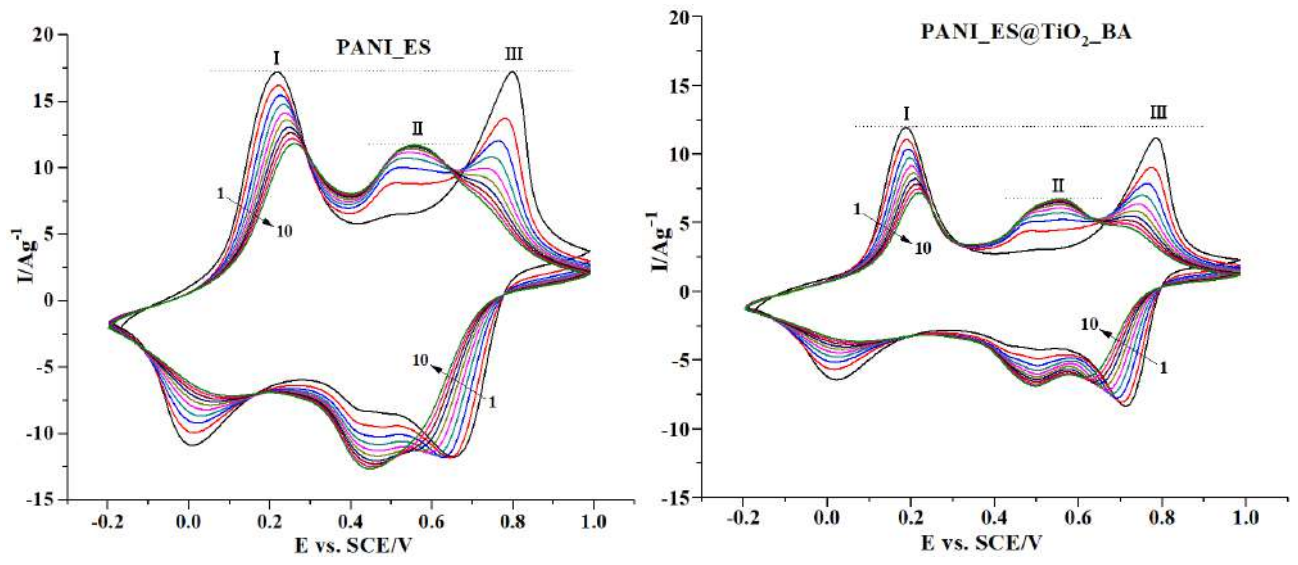


Figure 2. Cyclic voltamograms of PANI_ES, and PANI_ES@TiO₂_BA samples measured in HCl in potential range from -0.2 (the 1^{st}) to 1 V (the 10^{th}) cycle vs. SCE, at scan rate of 20 mVs⁻¹.

The first cycle anodic peak, which originates from oxidation of leucoemeraldine base (LB) into emeraldine salt (ES) is observed at 0.22 V, while the cathodic peak, which originates from reduction of (LB) to (ES), is observed at 0.001 V. The anodic peak of the second main redox pair originating from the oxidation of ES to pernigraniline salt (PNS) is positioned at 0.8 V, while the cathodic peak originating from reduction of PNS to ES is observed at 0.65 V. A low-intensity redox couple is positioned between these two main redox pairs of peaks, with the anodic peak at 0.55 V and the cathodic peak at 0.45 V. This pair of peaks is generally attributed to the formation of benzoquinone degradation products, leading to formation of the cross-linked PANI [23]. One can see that current of this middle peaks increase during the consecutive cycling of PANI within the extended water stability window, while the currents of redox peaks I and III decrease. This is in accord with previous observation that the formation of electrochemically inactive intermediates in preoxidized PANI leads to decrease of the current response during successive cycling [24].

The current responses of the anodic peaks in the first cycle is similar for processes I and III indicating similarity of the PANI_ES sample redox processes kinetics. After incorporation of the TiO_2 _BA (NP) into the PANI_ES matrix, the reduced current response was reduced. The anodic peak III is smaller than anodic peak I indicating that the (PNS) formation takes place more slowly in the composite than in pure PANI_ES. This behavior can be explained by the fact that the interaction of the TiO_2 _BA oxide with the PANI_ES chain hinders its deprotonation, which leads to a lower proportion of the (PNS) formed in the first anodic scan. Consequently, a slightly slower disappearance of the third peak was observed after the tenth cycle.

The charging/discharging capacitance of PANI is usually monitored in a narrower potential range (-0.2 to 0.6 V vs. SCE), in which the electrochemical preoxidation of PANI does not occur. In this regime, the calculated ratio of charging/discharging capacities was found to be 296/294 Fg⁻¹ for pure PANI_ES and 165/160 Fg⁻¹ for PANI_ES@TiO₂_BA. The significant decrease of the composite

capacity clearly shows that incorporation of 33 wt% of the TiO₂_BA (NP) into the PANI_ES matrix prevents the storage of significant amount of charge in the composite at a common scan rate of 20 mVs⁻¹.

Conclusion

The 33wt% of brookite(74%) and anatase(26%) TiO₂_BA nanoparticles (NP) mixture was incorporated into the PANI ES matrix during in situ chemical oxidative polymerization. The Raman spectra analysis of the obtained samples suggests that formation of the PANI_ES@TiO2_BA composite (NP) is accompanied by various interactions involving the N-atom from PANI ES, and most likely the O-atoms from the TiO₂_BA (NP) surfaces of the both involved TiO₂ phases. However, some kind of Ti-N interaction is also possible. The charging/discharging capacitance features of pure PANI ES and the composite were studied in 1M HCl using cyclic voltammetry at a common scan rate of 20 mV s⁻¹. In the -0.2 to 1 V SCE range, besides the two principle peaks pairs that correspond to the leucoemealdin base to emeraldine salt (0.22/0.001 V) and emeraldine salt to pernigraniline salt (0.8/0.65 V) oxidation/reduction, an additional pair of peaks (0.55/0.45 V) attributed to benzoquinone degradation products and subsequent PANI cross-linking appears. The relations between these peaks' current intensities in pure PANI ES and the PANI ES@TiO₂ BA composite and their changes during the consecutive cycling imply that interactions between the PANI_ES and TiO₂ BA (NP) in the PANI ES@TiO₂ BA composite hinders the PANI ES deprotonation and prevents about the half of the charge that could be stored in pure PANI_ES (in the -0.2 to 0.6 V SCE range) to be stored in the composite.

Acknowledgements

The funding for this research is provided by the Ministry of Science, Technological Development and Innovation of the Republic of Serbia, under Grant. No. 451-03-47/2023-01/200017.

References

- 1. S. H. Mir, L. A. Nagahara, T. Thundat, P. Mokarian-Tabari, H. Furukawa, A. Khosla, Review—Organic-Inorganic Hybrid Functional Materials: An Integrated Platform for Applied Technologies, *J. Electrochem. Soc.*, **165**, B3137-B3156, 2018.
- 2. C. Sanchez, B. Julian, P. Belleville, M. Popall, Applications of hybrid organic-inorganic nanocomposites, *J. Mater. Chem.*, 15, 3559–3592, 2005.
- 3. Y. Zhang, D. Jiang, Y. Wang, Y. Wang, T. C. Zhang, G. Xiang, Y.-X. Zhang, S. Yuan, Core-Shell Structured Magnetic γ-Fe₂O₃@PANI Nanocomposites for Enhanced As(V) Adsorption, *Ind. Eng. Chem. Res.*, **59**, 7554–7563, 2020.
- 4. H. Zhang, R. Zong, J. Zhao, Z.Zhu, Dramatic Visible Photocatalytic Degradation Performances Due to Synergetic Effect of TiO₂ with PANI, *Sci. Technol.*, **42**, 3803-3807, 2008.
- B. Kuzmanović, Milica J. Vujković, N. Tomić, D. Bajuk-Bogdanović, V. Lazović, B. Sljukić, N. Ivanović, S. Mentus, The influence of oxygen vacancy concentration in nanodispersed nonstoichiometric CeO_{2-δ} oxides on the physico-chemical properties of conducting polyaniline/CeO₂ composites, *Electrochim. Acta*, 306, 506-515, 2019.
- 6. S. Daikh, F. Z. Zeggai, A. Bellil, A. Benyoucef, Chemical polymerization, characterization and electrochemical studies of PANI/ZnO doped with hydrochloric acid and/or zinc chloride: differences between the synthesized nanocomposites, *J. Phys. Chem. Solids*, **121**, 78-84, 2018.
- 7. C. Bian, G. Xue, Nanocomposites based on rutile-TiO₂ and polyaniline, *Mater. Lett.*, **61**, 1299-1302, 2007.
- 8. G. Iinzhang, W. Shengying, Y. Wu, Z. Guohu, B. Lili, S. Li, Preparation and photocatalytic activity of PANI/TiO₂ composite film, *Rare Metals*, **26**, 1-7, 2007.
- 9. S. Min, F. Wang, Z. Kan, An investigation on synthesis and photocatalytic activity of polyaniline sensitized nanocrystalline TiO₂ composites, *J. Mater. Sci.*, **42**, 9966-9972, 2007.

- 10. H. Tai, Y. Jiang, G.g Xie, J. Yu, X. Chen, Z.Ying, Influence of polymerization temperature on NH₃ response of PANI/TiO₂ thin film gas sensor, *Sens. Actuators B*, **129**, 319-326, 2008.
- 11. M. B. Poudel, C. Yu, H. J. Kim, Synthesis of Conducting Bifunctional Polyaniline@Mn-TiO₂ Nanocomposites for Supercapacitor Electrode and Visible Light Driven Photocatalysis, *Catalysts*, **10**, 546, 2020.
- 12. S. Nasirian, H. M. Moghaddam, Hydrogen gas sensing based on polyaniline/anatase titania nanocomposite, *Int. J. Hydrog. Energy*, **39**, 630-642, 2014.
- 13. M. R. Nabid, M. Golbabaee, A. B. Moghaddam, R. Dinarvand, R. Sedghi, Polyaniline/TiO₂ Nanocomposite: Enzymatic Synthesis and Electrochemical Properties, *Int. J. Electrochem. Sci.*, **3**, 1117-1126, 2008.
- 14. R. Ganesan, A. Gedanken, Organic-inorganic hybrid materials based on polyaniline/TiO₂ nanocomposites for ascorbic acid fuel cell systems, *Nanotechn.*, **19**, 435709 (5pp), 2008.
- 15. A. Kremenović, M. Grujić-Brojčin, N. Tomić, V. Lazovic, D. Bajuk-Bogdanović, J. Krstić, M. Šćepanović, Size-strain line-broadening analysis of anatase/brookite (TiO₂)-based nanocomposites with carbon (C): XRPD and Raman spectroscopic analysis, *Acta Cryst.*, **B78**, 214-222, 2022.
- 16. M. Trchová, Z. Morávková, M. Bláha, J. Stejskal, Raman spectroscopy of polyaniline and oligoaniline thin films, *Electrochim. Acta.*, **122**, 28-38, 2014.
- 17. P. Colomban, S. Folch, A. Gruger, Vibrational study of short-range order and structure of polyaniline bases and salts, *Macromol.*, **32**, 3080-3092, 1999.
- 18. G. Ćirić-Marjanović, M. Trchová, J. Stejskal, The chemical oxidative polymerization of aniline in water: Raman spectroscopy, *J. Raman Spetrosc.*, **39**, 1375-1387, 2008.
- 19. T. Ohsaka, F. Izumi, Y. Fujiki, "Raman spectrum of anats, TiO₂", J. Raman Spectrosc. 7 (1978) 321-324.
- 20. M. Trchová, Z. Morávková, I. Šeděnková, J. Stejskal, Spectroscopy of thin polyanilin films deposited during chemical oxidation of aniline, *Chem. Pap.*, **66**, 415-445, 2012.
- 21. H. Lv, Y. Wang, L. Pan, L. Zhang, H. Zhang, L. Shang, H. Qu,N. Li, J. Zhao, Y. Li, Patterned polyaniline encapsulated in titania nanotubes for Electrochromism, *Phys. Chem. Chem. Phys.*, **20**, 5818-5826, 2018.
- 22. M. R. Nabid, M. Golbabaee, A. B. Moghaddam, R. Dinarvand, R. Sedghi, Polyaniline/TiO₂ Nanocomposite: Enzymatic Synthesis and Electrochemical Properties, *Int. J. Electrochem. Sci.*, **3**, 1117-1126, 2008.
- 23. R. Pauliukaite, C. M. A. Brett, A. P. Monkman, Polyaniline fibres as electrodes. Electrochemical characterisation in acid solutions, *Eelectrocim. Acta*, **50**, 159-167, 2004.
- 24. E. Song, J.-W. Choi, Conducting polyaniline nanowire and its applications in chemiresistive sensing, *Nanomater.*, **3**, 498-523, 2013.

Home > Sessions > Poster Session III (1pm-4pm CST)

V00: Poster Session III (1pm-4pm CST)

Session Tags:

Poster

Undergrad Friendly

	×
001	CONDENSED MATTER PHYSICS
002	Determining finite contact size corrections in the transport characterization of topological insulators
003	Topological phonons in two-dimensional materials
004	Control of Polarity in Kagome-NiAs Bismuthides
005	Constructing a device to study thermal transport properties of 2M-WS ₂ thin films and other topological materials.
006	Bottom-up Synthesis of Magnetic Topological Insulator
007	Theory of the spin-orbit coupling and topological flat band in the polyhedral π -conjugated molecules
800	Raman scattering from massive Dirac fermions in two dimensions
009	Structural evolution in SrRuO ₃ thin film at low temperature
010	Abstract Withdrawn
	Study of Fermi liquid behaviour in Kagome- semimetal Ni3In2S2

012 Broadband terahertz spectroscopy in reflection of three-dimensional Dirac semimetal Cd₃As₂

Electrospun titania-zinc oxide nanofibers

Hall BC

Electrospinning of sol-gel solutions containing polymers and metal precursors can be utilized to fabricate metal-oxide nanofibers whose properties depend on experimental conditions and chemical compositions. Composite metal-oxide nanofibers have properties that can be tailored by varying ratio of metal precursors or calcination temperature. The titania-based composite fibers are attractive candidates for numerous applications, from photocatalytic to medical. We present morphological investigation of titania-zinc oxide nanofibers calcined at different temperatures, using SEM and BET methods. Extensive studies of structural properties by XRD and Raman scattering measurements reveal the amorphous nature of as-spun fibers, whereas in calcined samples crystalline titania phases (anatase and rutile) emerge, with their ratio dependent on the calcination temperature. The optical characteristics of nanofibers are examined using UV-visible spectroscopy, yielding consistent values for energy band gaps through the analysis of transmission and diffuse reflectance.

Presented By

Connor P Jensen (University of Wisconsin Oshkosh)

Authors

- Nenad Stojilovic (University of Wisconsin Oshkosh)
- Connor P Jensen (University of Wisconsin Oshkosh)
- Sasa V Dordevic (University of Akron)
- Mira Grujić-Brojčin (Institute of Physics Belgrade, University of Belgrade)
- Maja Šćepanović (Institute of Physics Belgrade, University of Belgrade)
- Natasa Tomic (Institute of Physics Belgrade, University of Belgrade)
- Adria F Lotus (Southern Alberta Institute of Technology)
- George G Chase (The University of Akron)

2nd International Conference on Innovative Materials in Extreme Conditions

PROGRAM and BOOK OF ABSTRACTS

20-22 March 2024 Belgrade, Serbia Program and Book of Abstracts of the 2nd International Conference on Innovative Materials in Extreme Conditions (IMEC2024) publishes abstracts from the field of material science, physics, chemistry, earth, and computational science on the phenomena arising during the processing and/or exploitation of the innovative materials, which are presented at the international conference on innovative materials in extreme conditions.

Editors-in-Chief

Dr. Rer. Nat. Branko Matović

Dr. Ivana Cvijović-Alagić

Dr. Vesna Maksimović

Dr. Dejan Zagorac

Publisher

Vinča Institute of Nuclear Sciences - National Institute of the Republic of Serbia, University of Belgrade

Serbian Society for Innovative Materials in Extreme Conditions (SIM-EXTREME)

Printing layout

Dr. Ivana Cvijović-Alagić

Press

Donat Graf d.o.o., Vučka Milićevića 29, 11306 Grocka, Belgrade, Serbia

ISBN 978-86-7306-171-9

СІР - Каталогизација у публикацијиНародна библиотека Србије, Београд

66.017/.018(048)

INTERNATIONAL CONFERENCE ON INNOVATIVE MATERIALS IN EXTREME CONDITIONS

(2; 2024; BEOGRAD)

Program; and the Book of abstracts / 2nd International Conference on Innovative Materials in Extreme Conditions [i. e.] [(IMEC2024)], 20-22 March 2024 Belgrade, Serbia; [organizers Serbian Society for Innovative Materials in Extreme Conditions (SIM-EXTREME) [and] University of Belgrade, Vinča Institute of Nuclear Sciences - National Institute of the Republic of Serbia, Center of Excellence "Center for Synthesis, Processing and Characterization of Materials for Application in Extreme Conditions" (CEXTREME LAB) [and] University of Belgrade, Faculty of Mechanical Engineering]; [editors-in-chief Branko Matović ... [et al.]]. - Belgrade: University, Vinča Institute of Nuclear Sciences, National Institute of the Republic of Serbia: Serbian Society for Innovative Materials in Extreme Conditions [i. e.] (SIM-EXTREME), 2024 (Belgrade: Donat Graf). - 82 str.: ilustr.; 30 cm

Tiraž 70. - Str. 3: Preface / editors. - Bibliografija uz pojedine apstrakte. - Registar.

ISBN 978-86-7306-171-9 (VINS)

а) Наука о материјалима -- Апстракти б) Технички материјали -- Апстракти

COBISS.SR-ID 139413001

Two different paths to obtain pure nanosized Fe₃O₄: Morphology and Magnetic properties

Maria Čebela¹, Nataša Tomić², Milica Vujković³, Milena Rosić¹, Vesna Lojpur¹

Institute of Nuclear Sciences, Vinča", National Institute of the Republic of Serbia, University of Belgrade, 11001 Belgrade, Serbia

²The Institute of Physics Belgrade, National Institute of the Republic of Serbia, 11000 Belgrade, Serbia

³University of Belgrade - Faculty of Physical Chemistry, 11000 Belgrade, Serbia

The nanosized Fe₃O₄ was prepared in two different ways. Firstly, the precipitation method was used with iron (II) chloride as a precursor. After calcination at T=550 °C the pure Fe₂O₃ phase was obtained. In order to produce Fe₃O₄ nanopowder, consequently the annealing process in a mixed atmosphere (93% Ar and 7% H₂) was conducted. This transformation was confirmed by X-ray powder diffraction (XRPD) analysis, while morphology before and after annealing was investigated by Scanning Electron Microscopy (SEM). In the second procedure, hydrothermal method was used, where iron (II) and iron (III) chloride were used as precursors in a molar ratio 1:2. The temperature was kept at T=200 °C for t=1h. The structural and morphological characteristics were also investigated by XRPD and SEM. Furthermore, the influence of these two synthesis methods on magnetic properties will be presented. For this purpose the measurements on SQUID will be applied. It will be pointed out which kind of route and morphology enables better performance.









7th International Conference on Emerging Technologies in Materials Engineering



PROGRAMME and Book of Abstracts

No. 7 / 2024

2024, 30th- 31th October

GARDEN MARSHAL Hotel, Calea Dorobantilor 50B, Bucharest, Romania







7TH INTERNATIONAL CONFERENCE ON EMERGING TECHNOLOGIES IN MATERIALS ENGINEERING 30-31 October 2024, Bucharest, Romania

7th International Conference on Emerging Technologies in Materials Engineering EMERGEMAT

No.7 / 2024

30-31 October 2024 Bucharest, ROMANIA





7TH INTERNATIONAL CONFERENCE ON EMERGING TECHNOLOGIES IN MATERIALS ENGINEERING 30-31 October 2024, Bucharest, Romania

ISSN 2602-0424 ISSN-L 2602-0416

Print ISSN 2602-0416 ISSN-L 2602-0416

Editorial staff

Mirela PETRICEANU Mihaela-Georgia SIMA Florentina-Gabriela IONIȚĂ Paul STANCIU Ioan Albert TUDOR

Contact

MIRELA PETRICEANU

Specialist Proprietate Intelectuala CTT-AVANMAT

Centrul de Transfer Tehnologic
pentru Materiale Avansate,
Institutul National de Cercetare-Dezvoltare
pentru Metale Neferoase si Rare – IMNR

Bd. Biruintei nr. 102
Pantelimon, jud. Ilfov
T (+4021) 352 20 46 / 131
F (+4021) 352 20 49
mirela.petriceanu@imnr.ro





7TH INTERNATIONAL CONFERENCE ON EMERGING TECHNOLOGIES IN MATERIALS ENGINEERING 30-31 October 2024, Bucharest, Romania

GRAPHENE ENHANCEMENT OF V₂O₅ AS CATHODE MATERIAL

Nataša Tomić^{1*}, Ivana R. Milošević¹, Jasna Vujin¹, Bojana Kuzmanović², Milica Vujković³

¹Institute of Physics Belgrade, National Institute of the Republic of Serbia, University of Belgrade, Serbia

²Institute of Nuclear Sciences "Vinča", National Institute of the Republic of Serbia, University of Belgrade, Serbia

³Faculty of Physical Chemistry, University of Belgrade, Serbia

The pure V_2O_5 nanopowder, synthesized by acid-assisted hydrothermal method [1], was combined with water-based graphene dispersion in order to obtain the V_2O_5 -graphene nanocomposite. Previously, the simple and low-cost method known as liquid phase exfoliation (LPE) [2] was used to get desired graphene dispersion. The influence of graphene coupling with the vanadium oxide was analysed from the structural, morphological, and electrochemical point of view. The structural properties of the nanomaterials, before and after graphene modification, was analysed by X-ray powder diffraction (XRPD). The morphological characteristics were investigated by Field Emission Scanning Electron Microscopy (FESEM). These nanostructures were tested as an electrode material for Li-ion batteries using Gamry Potentiostat/Galvanostat. The influence of graphene on the capacity and its stability was evaluated and discussed. The applied graphene-based modification approach was found to be successful in improving the cathode performance of V_2O_5 .

References:

- 1. J. Liu, X. Wang, Q. Peng, Y. Li, Advanced Materials 17 (2005) 764.
- 2. T. Tomašević-Ilić, J. Pešić, I. Milošević, J. Vujin, A. Matković, M. Spasenović, R. Gajić, *Opt Quant Electron* 48 (2016) 319.

Acknowledgements:

The authors acknowledge funding provided by the Institute of Physics Belgrade, through the grant by the Ministry of Science, Technological Development and Innovation of the Republic of Serbia, as well as by the Innovation Fund of the Republic of Serbia - Proof of Concept (PoC) ID 5619, the Institute of Physics, University of Belgrade, Serbia.

^{*}Corresponding author: <u>natasat@ipb.ac.rs</u>



7TH INTERNATIONAL CONFERENCE ON EMERGING TECHNOLOGIES IN MATERIALS ENGINEERING 30-31 October 2024, Bucharest, Romania

ZnO NANOPOWDERS: EFFECT OF ALKALINE LIQUID CHEMISTRY ON THE MORPHOLOGY AND PHOTOCATALYTIC PROPERTIES

Bojana Kuzmanović^{1*}, Milica Vujković², Katarina Batalović¹, Mirjana Medić Ilić¹, Bojana Paskaš Mamaula¹, Nataša Tomić³

¹"Vinča" Institute of Nuclear Sciences, National Institute of the Republic of Serbia, University of Belgrade, Serbia

*Corresponding author: kuzmob@vinca.rs

Due to their exceptional properties, stability, cost-effectiveness, and especially their environmental friendliness, metal oxide nanoparticles are considered as promising material for the photocatalytic degradation of toxic dyes and organic solvents [1,2]. This study summarizes the preparation and application of ZnO nanoparticles with high catalytic performance. Zinc oxide powders were synthesized via a hydrothermal method in an alkaline environment using three different bases: NaOH, KOH, and NH₄OH. The phase purity, structural characteristics and morphology of the ZnO nanostructures were investigated using X-ray powder diffraction, Raman spectroscopy, Scanning electron microscopy and Transmission electron microscopy. The effects of different bases on morphology and the photocatalytic degradation of RO16 dye were evaluated and discussed. It was shown that the powder synthesized in the presence of NaOH exhibited the highest photocatalytic activity, while sample with KOH showed a slightly faster degradation rate compared to powder synthesized in the presence of NH₄OH.

References:

- 1. Manikanika, L. Chopra, Mater. Today Proc. 52 (2022) 1653-1656.
- 2. Y. Sun, W. Zhang, Q. Li, H. Liu, X. Wang, Adv. Sensor Energy Mater. 2 (2023) 100069.

Acknowledgements:

This research was supported by funding through grant number 451-03-66/2024-03/200017 provided by the Ministry of Science, Innovation and Technical Development.

²Faculty of Physical Chemistry, University of Belgrade, Serbia

³Institute of Physics Belgrade, National Institute of the Republic of Serbia, University of Belgrade, Serbia

BOOK OF ABSTRACTS



ДОСТИГНУЋА У ФИЗИЦИ ЧВРСТОГ СТАЊА И НОВИХ МАТЕРИЈАЛА

30 година Центра за физику чврстог стања и нове материјале Института за физику у Београду

ADVANCES IN SOLID STATE PHYSICS AND NEW MATERIALS

30 years of the Center for Solid State Physics and New Materials at the Institute of Physics Belgrade

19 - 23 May 2025Belgrade, Serbia











Conference Chairs

Nenad Lazarević, *Institute of Physics Belgrade, Serbia* Emil S. Božin, *Institute of Physics Belgrade, Serbia* Rudi Hackl, *IFW Dresden, Germany*

Zoran V. Popović, Serbian Academy of Sciences and Arts (SANU), Serbia – honorary chair

Organizing Committee

Jelena Pešić - chair Bojana Višić - chair

Ana Kanjevac

Ana Milosavljević

Andrijana Šolajić

Barbara Bekić

Bojan Stojadinović

Branka Hadžić

Ivana Milošević

Jasmina Lazarević

Jelena Mitrić

Jelena Trajković

Jovan Blagojević

Lenka Filipović

Marko Opačić

Milica Petrović

Nataša Tomić

Novica Paunović

Tea Belojica

Tijana Tomašević Ilić









Scientific Committee

Rudi Hackl, IFW Dresden, Germany
Nenad Lazarević, Institute of Physics Belgrade, Serbia
Emil S. Božin, Institute of Physics Belgrade, Serbia
Elena Gati, Max Planck Institute for Chemical Physics of Solids, Germany
John S. O. Evans, Durham University, UK
Zdeněk Sofer, UCT Prague, Czech Republic
Milorad Milošević, University of Antwerp, Belgium
Marija Drndić, University of Pennsylvania, USA
Simon J. L. Billinge, Columbia University, USA
Yann Gallais, Université Paris Cité, France

Advisory Committee

Bernd Büchner, IFW Dresden, Germany
Reshef Tenne, Weizmann Institute of Science, Israel
Zoran V. Popović, Serbian Academy of Sciences and Arts (SANU), Serbia
Dragana Popović, Florida State University, USA
Maja Remškar, Jožef Stefan Institute, Slovenia
Matthieu Le Tacon, Karlsruhe Institute of Technology, Germany
Wei Ku, Tsung-Dao Lee Institute & Shanghai Jiao Tong University, China

Advances in Solid State Physics and New Materials

The international conference "Advances in Solid State Physics and New Materials" is being organized to celebrate the 30th anniversary of the Center for Solid State Physics and New Materials at the Institute of Physics Belgrade (IPB). The conference, subtitled "30 Years of the Center for Solid State Physics and New Materials at the Institute of Physics Belgrade", will take place from May 19–23, 2025, as a joint endeavor of the Department of Natural Sciences of the Serbian Academy of Sciences and Arts (OTN SANU) and the Center for Solid State Physics and New Materials, IPB.

The event commemorates the founding of the Center on May 24, 1995, and highlights its recognition as one of the first centers of excellence in nanoscience and nanotechnology in Serbia. The Center has also been acknowledged as a European center of exceptional value for applications of optical spectroscopy in physics, materials science, and environmental protection (OPSA). The conference is also part of the activities of the **HIP-2D-QM project**, conducted under the Horizon ERA Chair call, independently executed by researchers at the Center.

The program will cover a broad spectrum of topics in solid-state physics, including:

- New quantum materials
- Strong correlations
- Ordering phenomena and phase transitions
- 2D materials
- Topology
- Magnetism
- Unconventional superconductivity
- Semiconductors

Conference venue:

Serbian Academy of Sciences and Arts (SANU), Knez Mihailova 35, 11000 Belgrade, Serbia

Conference website: https://www.advances25.solidstate.ipb.ac.rs/

Nanostructured thin films with strong spin-orbit interaction

M. Opačić ^a, B. Vasić ^a, N. Tomić ^a, M. Šćepanović ^a and Z. Konstantinović ^a V. Fuentes ^b, Ll. Balcells ^b, B. Martinez ^b and A. Pomar ^b

^aCenter for Solid State Physics and New Materials, Institute of Physics Belgrade, UB, Serbia ^bInstituto de Ciencia de Materiales de Barcelona, ICMAB-CSIC, Campus UAB, Bellaterra 08193, Spain

Abstract. Materials with strong spin-orbit coupling (SOC) position themselves at the frontline of spintronics, allowing generation and manipulation of pure spin-currents [1]. Perovskite iridates have received special interest as they exhibit a rich electronic phase diagram with exotic states, due to the delicate interplay between SOC and crystal field splitting. In particular, SrIrO₃ has been proposed as a topological semimetal, having band structures near the transition between semimetallic and insulating states, which can be finely tuned by strain and deposition conditions [2]. This electronic richness mixed with the inherent tendency of perovskite oxides towards self-organized growth offers an enormous and unexplored potential for engineering functional properties of thin films [3]. The influence of strain and nanostructured formation at the surface on electronic transport properties of SrIrO₃ is discussed (Figure 1).

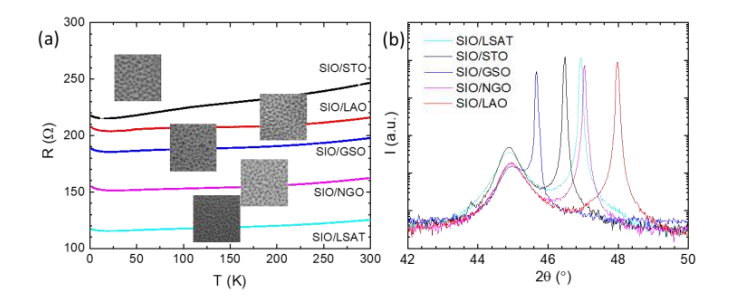


FIGURE 1. (a) Temperature dependent resistance of nanostructured SrIrO₃ thin films grown on different substrates (SrTiO₃ (STO), LaAlO₃ (LAO), NdGdO₃ (NGO), GdScO₃ (GSO), LaAlO₃) $_{0.3}$ -(Sr₂AlTaO₆) $_{0.7}$ (LSAT) with SEM images (2x2 μ m²) (b) θ -2 θ measurements of the corresponding films with similar thickness (25 nm<t<30 nm).

REFERENCES

- 1. Martin-Rio, S. et al., ACS Applied Materials and Interfaces 15, 37038-37046 (2023).
- 2. V. Fuentes et al., Nanomaterials 14, 242 (2024).
- 3. Konstantinović, Z. et al., Small 5, 265 (2009); Konstantinović, Z. et al., JMMM 509, 166898 (2020).

Strain-dependent vibrational properties of SrIrO₃ thin films

M. Opačić^a, N. Tomić^a, L. Balcells^b, B. Martinez^b, A. Pomar^b, M. Šćepanović^a and Z. Konstantinović^a

 ^aCenter for Solid State Physics and New Materials, Institute of Physics Belgrade, University of Belgrade, Pregrevica 118, 11080, Belgrade, Serbia
 ^bInstituto de Ciencia de Materiales de Barcelona, ICMAB-CSIC, Campus Universitario UAB, Bellaterra 08193, Spain

Abstract. Ruddlesden-Popper series of 5d strontium-irridates $(Sr_{n+1}Ir_nO_{3n+1})$ have been extensively studied in the past years due to its unique properties, including spin-orbit coupling, crystal field and electronic correlations. Interplay between these features facilitates transitions between different electronic states due to slight structural or chemical changes. In this work Raman spectra of SrIrO₃ thin films grown on different substrates (LAO, LSAT, STO, GSO) are investigated for various sample orientations and light polarizations. Our attention is focused on Raman mode appearing around 395 cm⁻¹, which is assigned as A_g symmetry mode by orientation-dependent measurements. A blue shift of this mode when going from SIO/GSO, through SIO/STO and SIO/LSAT, to SIO/LAO sample, was observed, which is a clear fingerprint of increasing compressive strain, induced by substrate.

The Morphological And Structural Changes Of V₂O₅ Cathode Film Upon Electrochemical Cycling

Nataša Tomić^a, Borislav Vasić^a, Milica Vujković^b, Benjamin Martinez^c and Zorica Konstantinović^a

^aCenter for Solid State Physics and New Materials, Institute of Physics Belgrade, UB, Serbia ^bFaculty of Physical Chemistry, University of Belgrade, Serbia ^cInstituto de Ciencia de Materiales de Barcelona, ICMAB-CSIC, Campus UAB, Bellaterra 08193, Spain

Abstract. Topics dealing with energy issues will always be of great importance. It has been known that vanadium oxide has potential application as a cathode material for the Li-ion batteries [1, 2]. The first step of this research is oriented towards designing the V_2O_5 thin film. For that purpose, the pulsed laser deposition technique [3] is used to deposit vanadium oxide thin film on a conductive substrate during heating at 400 °C. Post annealing treatment is needed in order to achieve crystalline nature of V_2O_5 film. Besides the intention to evaluate the lithium storage capability of the oxide as a cathode, the aim is to thoroughly explore the changes occuring in the material during consecutive Li⁺ insertion/deinsertion. The morphological and structural properties are investigated by Field Emission Scanning Electron Microscopy (FESEM), Atomic Force Microscopy (AFM) and Raman spectroscopy. Their correlation with the electrochemical performance is analyzed. The presented results will shed light on new insights into Li⁺ storage mechanism of the vanadium oxide.

REFERENCES

- Baddour-Hadjean, R., Pereira-Ramos, J.P., Navone, C., and Smirnov, M., Chem. Mater. 20, 1916-1923 (2008).
- Hevia, S. A., Orive, J., Guzman, F., Cisternas, E., Dietrich, F., Villarroel, R., and Lisoni, J., Appl. Surf. Sci. 576, 151710 (2022).
- 3. Nag, J., and Haglund Jr, R. F., J. Phys.: Condens. Matter. 20 264016 (14pp) (2008).